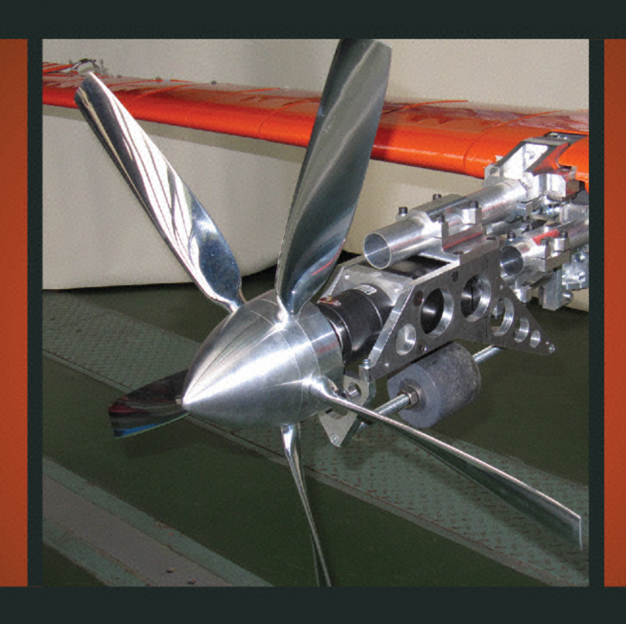
WOODHEAD PUBLISHING IN MECHANICAL ENGINEERING

Whirl Flutter of Turboprop Aircraft Structures

Jiří Čečrdle





Whirl Flutter of Turboprop Aircraft Structures

Related titles:

Materials and surface engineering: Research and development
Number 2 in the Woodhead Publishing Reviews: Mechanical Engineering Series
(ISBN 978-0-85709-151-2)

Machining and machine-tools: Research and development
Number 3 in the Woodhead Publishing Reviews: Mechanical Engineering Series
(ISBN 978-0-85709-154-3)

Whirl Flutter of Turboprop Aircraft Structures

Jiří Čečrdle



AMSTERDAM • BOSTON • CAMBRIDGE • HEIDELBERG • LONDON
NEW YORK • OXFORD • PARIS • SAN DIEGO
SAN FRANCISCO • SINGAPORE • SYDNEY • TOKYO
Woodhead Publishing is an imprint of Elsevier



Woodhead Publishing is an imprint of Elsevier
80 High Street, Sawston, Cambridge, CB22 3HJ, UK
225 Wyman Street, Waltham, MA 02451, USA
Langford Lane, Kidlington, OX5 1GB, UK

British Library Cataloguing-in-Publication Data
A catalogue record for this book is available from the British Library.

Library of Congress Control Number: 2014946711

ISBN 978-1-782421-85-6 (print)
ISBN 978-1-782421-86-3 (online)

For information on all Woodhead Publishing publications visit our website at http://store.elsevier.com/

Typeset by RefineCatch Limited, Bungay, Suffolk
Printed and bound in the United Kingdom

This book is dedicated to my children, Jan and Anna

This page intentionally left blank

Table of contents

List of figures

This page intentionally left blank

Acknowledgements

First, the author would like to acknowledge the Aeronautical Research and Test Institute (VZLU), Prague, Czech Republic (namely, Josef Kašpar, General Director, and Viktor Kušera, Technical Director), for granting permission for the use of the results of whirl flutter relating tasks performed by the author at the VZLU (within the framework of the Czech or European research projects as well as the aircraft certification projects) within the period 1999–2013 in this book, as well as for further support (namely, Josef Jironč, Head of Dept., Strength of Structures; Radek Doubrava, Head of Group, Structure Analyses; and Zuzana Šranková, Secretary, Structure Analyses).

Further acknowledgements are due to the outstanding whirl flutter achievers who performed the research work referred to in this book. Namely, Wilmer H. Reed III and Raymond G. Kvaternik (formerly NASA Langley Research Center, VA, USA), C. E. Hammond and H. L. Runyan (NASA Langley Research Center, VA, USA), William P. Rodden (formerly MSC.Software, CA, USA), Cecil W. Acree (NASA Ames Research Center, CA, USA), Omri Rand (Technion – Institute of Technology, Israel), Alireza Rezaeian and Wolf Krueger (DLR, Germany), Fritz Kiessling (formerly DLR, Germany), Alain Dugeai (ONERA, France), Robert E. Donham (formerly Lockheed Aeronautical Systems, CA, USA), K. V. Krishna Rao (formerly NAL, India), and many others.

Further acknowledgements are due to the aerospace research organisations and aerospace technical societies: National Aeronautical Laboratory (NAL), Bangalore, India (namely, J. S. Mathur, Chief Scientist); German Aerospace Research Centre (DLR), Germany (namely, Lorenz Tichy, Director, Institute of Aeroelasticity), French Aerospace Research Centre (ONERA), France; NASA Ames Research Center, CA, USA; American Institute of Aeronautics and Astronautics (AIAA), Reston, VA, USA (namely, Heather A. Brennan, Director, Publications); American Helicopter Society (AHS), Alexandria, VA, USA (namely, Mike Hirchsberg, Executive Director), and Elsevier Science, Ltd.

Special acknowledgement belongs to the NASA Langley Research Center, VA, USA (one of the greatest achievers in the whirl flutter branch), not only for granting permission to use their research (namely, Robin W. Edwards, Patent Counsel) but also for the effort spent in searching in the archive for the originals of aged photos (namely, Mary E. Garner).

My further thanks to aircraft spotters (Bill Hough, Orlando Suarez, Petr Kadlec, and Petr Štěrba) for granting permission to use their photographs; to Svatomír Slavík (Czech Technical University, Czech Republic); to Czech aircraft manufacturers Aero Vodochody Aerospace, a.s. (namely, Pavel Kučera, Head, Design Analysis); Evektor, spol. s.r.o., Kunovice (namely, Petr Štěrba, Deputy Director); Aircraft Industries, a.s., Kunovice (namely, Ilona Plšková, General Director); the Czech aircraft maintenance company Aeroservis, spol. s.r.o., Brno (namely, Jan Václavík, CEO) for granting permission to use the data of aircraft certification relating projects; and last, but not least, thanks to Evžen Šlechta for graphical processing of the hand-made sketches.

About the author

Jiří Čečrdle was born in 1969 in Prague, Czech Republic. He graduated from the Czech Technical University in Prague, Faculty of Mechanical Engineering. He completed his M.Sc. in Aircraft Design in 1993 and Ph.D. in Mechanics of Stiff and Deformable Bodies in 2003. He started his professional carrier in 1995 at the Aeronautical Research and Test Institute (VZLU) in Prague, Czech Republic, at the Strength of Structures Division as Research Assistant. Later, he was promoted to the Researcher (1996) and Scientist (2003) positions and finally, in 2004 to Senior Scientist position. Since that time, he has also been the head of the Workgroup of Aeroelasticity at the Strength of Structures Dept. In the meantime, he also completed four mid-term work stays at the German Aerospace Centre (DLR), Institute of Aeroelasticity in Goettingen, Germany within 2002–2005.

His spheres of scientific interest include the analytical and experimental dynamics and aeroelasticity of aircraft structures as well as aeroelastic optimisation and model updating. He participated in several projects of Czech aircraft development and certification (L-610G – twin-engine turboprop commuter for 40 passengers; L-159 – jet light attack aircraft; Ae 270 – single engine turboprop utility aircraft for eight passengers; Raven 257 – twin-piston engine utility aircraft for nine passengers; EV-55 / EV-55M – twin-engine turboprop utility aircraft for 9–13 passengers). He has been participating in the modernisation of the L-410 twin-engine turboprop commuter for 19 passengers. He also works as a Compliance Verification Engineer (CVE).

He was involved in several Czech and European research projects dealing with the topics of aeroelastic flutter, aeroelastic response analysis, the development of the nonlinear aeroelastic wind tunnel demonstrator, aeroelastic experiments of the active aeroelastic demonstrators, analytical methods for general aviation aircraft certification, aeroelastic sensitivity analysis, and dynamic model updating and optimisation methods. He also works as a research project evaluator.

He has been interested in the topic of whirl flutter since 1999. His experience includes aircraft certification issues, the development of

analytical tools and methods and the development of the whirl flutter aeroelastic wind tunnel demonstrator.

He is the author or co-author of approximately 60 conference papers and articles in technical and scientific journals. VZLU presented him with the Kaspar's award (2010). His biographical profile has been included in valuable databases such as Marquis Who's Who in the World. He is Associate Fellow of the American Institute of Aeronautics and Astronautics (AIAA).

The author may be contacted at:
Aeronautical Research and Test Institute (VZLU)
Beranových 130
199 05 Praha – Letňany
Czech Republic
e-mail: cecrdle@vzlu.cz
or
Zápy 94
250 01 Brandýs nad Labem
Czech Republic

1

Introduction to aircraft aeroelasticity and whirl flutter

DOI: 10.1533/9781782421863.1

Abstract: This chapter provides brief information regarding aeroelasticity. The chapter defines the scope of aeroelasticity and provides an overview of aerospace engineering, describing aeroelastic primary problems and achievements in the context of aviation history. Next, the physical principles of the most important static and dynamic aeroelastic phenomena, such as divergence, control surface reversion, flutter, and buffeting are outlined.

Key words: aeroelasticity, aeroelastic phenomena, divergence, control reversion, flutter, buffeting.

1.1 Scope of aeroelasticity

Aeroelasticity is a notably new branch of applied mechanics that studies the interaction between fluid matters and flexible solid bodies. The typical application of aeroelasticity is in the branch of aircraft engineering. However, aeroelastic issues are applicable also for civil engineering (e.g., slender buildings, towers, smokestacks, suspension bridges, electric lines, and pipelines) or transportation engineering (cars, ships, submarines). Also important are its applications in machine engineering (compressors, turbines).

In the following text we will focus on aerospace aeroelasticity. Aeroelasticity in regard to aircraft structures is defined as the branch that investigates the phenomena that emerge due to the interaction of aerodynamic (in particular unsteady), inertial and elastic forces emerging

during the relative movement of a fluid (air) and a flexible body (aircraft).

Aeroelastic phenomena may be divided according to the diagrammed definition of aeroelasticity (Collar's triangle of forces – Figure 1.1). The sides of the triangle represent the relationships among the particular pairs of forces representing specific areas of mechanics, including aeroelasticity, whereas the triangle's interior represents the interference of all three groups of forces typical for dynamic aeroelastic phenomena. Static aeroelastic phenomena that exclude inertial forces are characterised by the unidirectional deformation of the structure, whereas dynamic aeroelastic phenomena that include inertial forces are typical in their oscillatory property of structure deformation.

Problems with aeroelasticity have been occurring since the birth of aviation. The first famous event caused by an aeroelastic phenomenon was the crash of Langley's monoplane, which occurred only eight days before the Wright brothers' first successful flight. Thus, the Wrights became famous as the first fliers and Langley is only remarked in aeroelastic textbooks. The cause of the crash was the torsional divergence

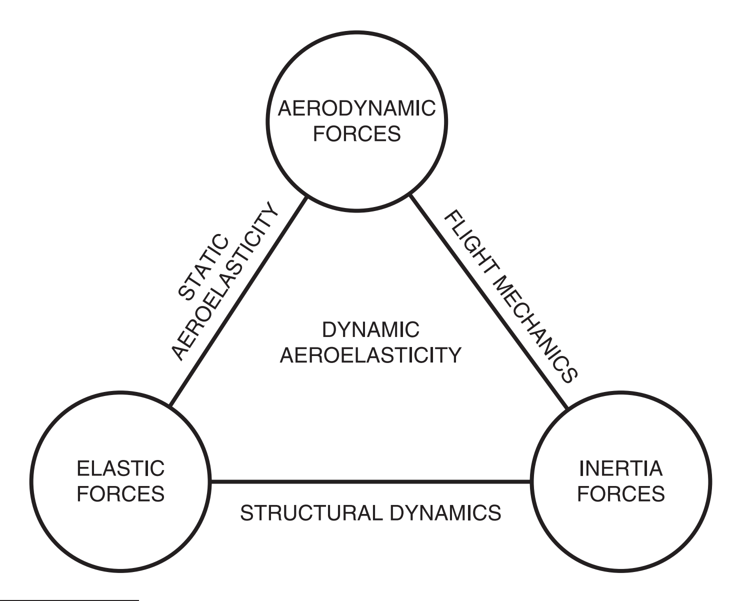


Figure 1.1 **Aeroelastic (Collar's) triangle of forces**

of the wing with low torsional stiffness. Therefore, the early stage of aviation is characterised by biplanes that allow for the design of a torsionally stiffer structure. At this time, torsional divergence was the dominant aeroelastic phenomenon. Torsional divergence was also the cause of several crashes of Fokker's high-wing monoplane D-8. The low stiffness of the fuselage and tail planes, as well as the unsuitable design of the control system, caused the crashes of the British Handley-Page O/400 twin-engine biplane bomber and the DH-9 biplane fighter during the First World War.

After the First World War, during tests in the USA, a further aeroelastic phenomenon emerged with the D-8 aircraft – wing aileron flutter. This phenomenon was eliminated using static balancing of the ailerons. With increasing flight velocities, as well as the design of monoplanes, the flutter phenomenon became increasingly important. The basic theories of flutter were formulated by Küssner in Germany and by Frazer and Duncan in the UK at the end of the 1920s. In the 1930s Theodorsen formulated the theory of unsteady forces distribution on a harmonically vibrating airfoil with a control surface. Similar problems were also solved in Russia.

With the attainment of sonic speed after the Second World War, qualitatively new aeroelastic issues, such as panel flutter or control buzz, gained prominence. These phenomena are caused by shock waves and pressure oscillations over the airfoil in the transonic region. In the supersonic velocity range, the aerodynamic heat effect also became an important contributing factor (aero-thermo-elasticity). Apart from this, further phenomena are connected to the effects of servo-systems in the control circuits (aero-servoelasticity). Currently, new aeroelastic problems are emerging in connection with the active control systems that are used for gust alleviation and the suppression of structural loads. Additionally, aeroelastic optimisation methods enable the potential of structural adjustments to, for instance, decrease mass and increase flight performance.

In general, a new aircraft design concept or a part or system may cause new aeroelastic problems. A typical example is the whirl fltter phenomenon that is the subject of this book. In the late 1950s, a new aircraft category (turboprop airliners) emerged. These aircraft were characterised by wing-mounted gas turbine engines and heavy propellers placed somewhat far in front of the wing. The gyroscopic effect of the rotating masses of the propeller, compressor and turbine combined with the wing dynamics, consequently created a new aeroelastic issue – whirl flutter.

1.2 Static aeroelastic phenomena

Static aeroelastic phenomena include the interaction of steady aerodynamic forces with elastic forces. Structural static deformation causes redistribution of the loads and related phenomena. Static aeroelastic phenomena may be important for small aircraft, gliders or for unconventional aircraft; nevertheless, conventional transport aircraft designed by modern methods should be safe with respect to static aeroelasticity. Occurrences of static phenomena are usually caused by insufficient analysis and evaluation.

The most important static aeroelastic phenomena are the following:

- Torsional divergence (redistribution of aerodynamic loads).
- Control surface reversion (decreasing of control effectiveness).
- Static stability of deformable aircraft.

1.2.1 Torsional divergence

The torsional divergence of the lifting surface is the first historically observed phenomenon. Torsional divergence represents the static loss of stability. Static load causes structural deformation, which, in turn, influences the load. The resulting deformation and load (i.e., the balance of the aerodynamic and elastic forces), determines the load redistribution. Torsional divergence is the critical state in load redistribution in which the internal elastic forces do not reach a balance with the external aerodynamic forces. The deformation becomes divergent, and as a consequence leads to structural destruction.

This principle is demonstrated in Figure 1.2 in the single degree-of-freedom system. The airfoil is exposed to the wind flow of velocity V_∞ with the angle of attack of α_T. The airfoil generates the lift force Y. This lift force causes the torsional deformation of the structure φ which increases the effective angle of attack and causes the additional lift force ΔY_φ. Again, the additional lift force increases the structural deformation, and the loop is closed. The structural deformation increases until the external aerodynamic moment is balanced with the internal elastic moment. As long as the moments' balance is kept, the phenomenon causes only the redistribution of the aerodynamic loads, and the structure is stable. The velocity at which the moments' balance is violated is the divergence velocity V_{DIV}. At this velocity, the structure becomes unstable, and the deformation becomes divergent.

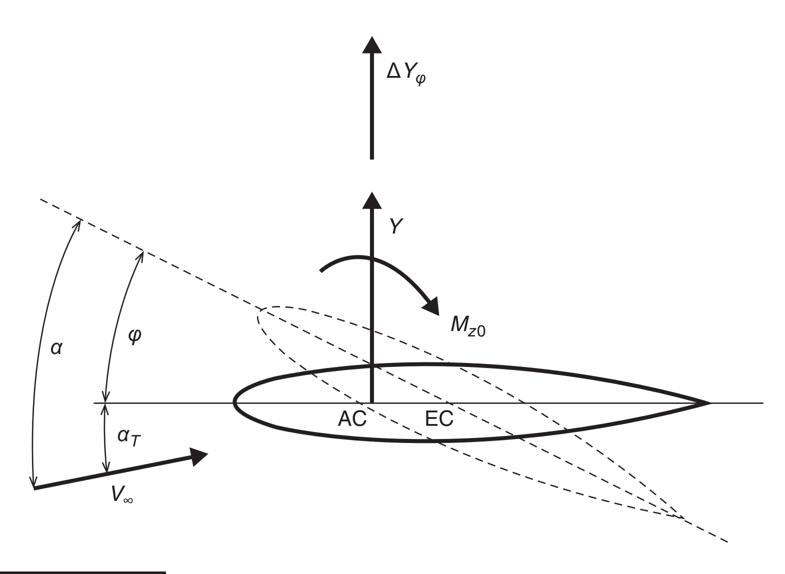


Figure 1.2 **Principle of airfoil torsional divergence**

1.2.2 Control surface reversion

Control surface reversion is the static aeroelastic phenomenon that, contrary to torsional divergence, does not cause the loss of stability but rather causes the loss of manoeuvrability. In general, this reversion may occur on any control surface; however, it is typical for the lateral control system (ailerons) because the ailerons are placed in the tip region of the relatively flexible wing. Another, but highly rare, option is the reversion of elevator due to the low stiffness of the fuselage, which may occur with unconventional aircraft with tail-booms.

Aerodynamic load redistribution due to control surface deflection causes the load on the main surface to move in the inverse direction, which decreases the efficiency of the control surface. The critical state occurs when the two forces are balanced, and the aerodynamic effect of the control surface is completely eliminated. In this case, the aircraft does not respond to the control surface deflection. When the velocity increases beyond the critical state, the aircraft's response becomes inverse with respect to its standard behaviour.

This principle is demonstrated in Figure 1.3 on the two degree-of-freedom system. The airfoil is exposed to the wind flow of velocity V_∞ with the angle of attack of α. The airfoil generates the lift force Y. The control surface is deflected by the angle of δ, which creates the additional

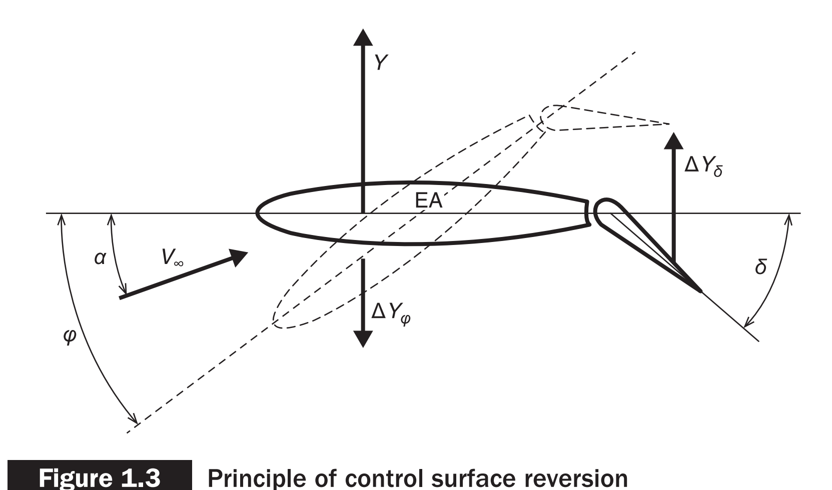


Figure 1.3 Principle of control surface reversion

force on the control surface ΔY_δ. This force causes the torsional deformation of the main surface by the angle of φ, which decreases the effective angle of attack and causes the additional force ΔY_φ in the inverse direction on the main surface. The state of ($\Delta Y_\delta > \Delta Y_\varphi$) represents the decrease of the control surface's effectiveness with respect to the rigid structure. The state of ($\Delta Y_\delta = \Delta Y_\varphi$) represents the critical state of reversion, when the aircraft does not respond to the control surface's deflection. The state of ($\Delta Y_\delta < \Delta Y_\varphi$) represents the control surface's reversion when the aircraft responds to the control surface's deflection in the inverse manner. The velocity of the critical state ($\Delta Y_\delta = \Delta Y_\varphi$) is the reversal velocity V_{REV}.

1.2.3 Static stability of deformable aircraft

The origin of the aerodynamic force (neutral point) of the deformable aircraft may differ with respect to the rigid structure, and it may influence the static stability of the aircraft. This phenomenon is usually investigated as part of flight mechanics.

1.3 Dynamic aeroelastic phenomena

Dynamic aeroelastic phenomena include the interactions of unsteady aerodynamic forces, elastic forces and forces of inertia. Dynamic

aeroelastic phenomena, particularly flutter, are the decisive phenomena for aircraft certification.

The most important dynamic aeroelastic phenomena are the following:

- Flutter
- Buffeting
- Aeroelastic response to dynamic load
- Dynamic stability and manoeuvrability of deformable aircraft
- Aero-servoelasticity.

1.3.1 Flutter

Flutter is the most important aeroelastic phenomenon applicable to aircraft structure. Flutter represents self-excited vibrations that are possible if a disturbance in the aeroelastic system gives rise to oscillatory aerodynamic loads. The energy is supplied from the airstream. At flutter speed, a critical phasing between the motion and the loading permits the extraction of the amount of energy that is equal to the energy dissipated by the internal damping, and therefore the system maintains neutrally stable periodic motion. At lower speeds, the disturbance is damped and the motion is stable, whereas at higher speeds (or at least in the range of higher speeds) the disturbances are amplified, and the motion is unstable. Classical flutter (potential flutter) arises under non-stall conditions from the critical coupling of two or more modes of motion, each of which is stable itself.

The specific type of flutter occurring under stall conditions is stall flutter with a single dominating degree of freedom. Other specific flutter types with a single degree of freedom may occur due to the shock effects in the transonic velocity range.

In the following text we will focus only on potential flutter. Standard potential flutter is most likely the most dangerous aeroelastic phenomenon. The amplitudes of self-excited motion are theoretically unlimited, and the rate of change is extremely high. This motion may cause the destruction of a structure in several seconds.

The principle of flutter is demonstrated in several simple examples. Figure 1.4 and Figure 1.5 show the harmonic motion of an airfoil with a single degree of freedom for torsional and bending deformations. The figures show the displacement during the complete cycle of motion and the energy during the cycle. The load and the displacement are in-phase,

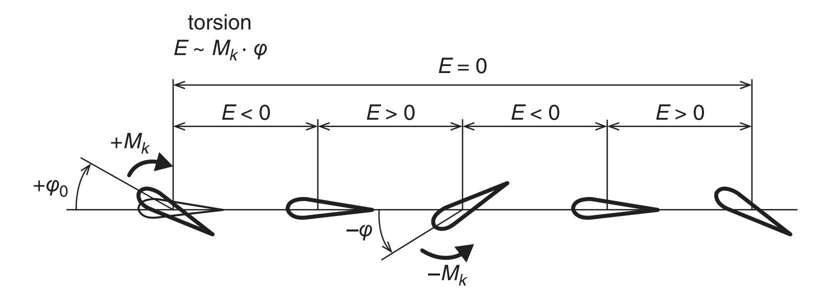


Figure 1.4 **Harmonic motion of airfoil with single DOF – torsion**

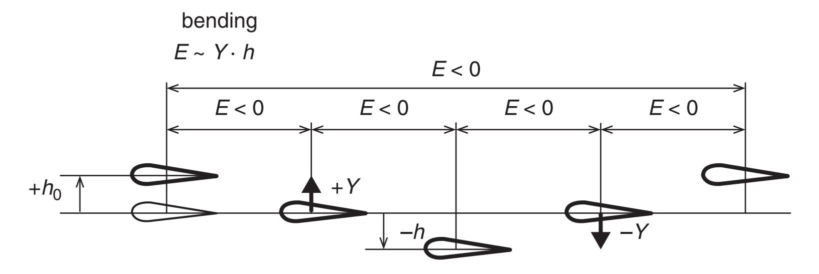


Figure 1.5 **Harmonic motion of airfoil with single DOF – bending**

and the resulting energy during the cycle is zero for the torsional deformation and negative for the bending deformation. This means that the system is stable; therefore, flutter cannot occur in the single degree of freedom case.

The mechanism of the classical two degree of freedom bending / torsional flutter is demonstrated in Figure 1.6 and Figure 1.7. These figures again show displacement during the complete cycle of motion and the energy during the cycle. Contrary to the single degree of freedom case, the load is shifted with respect to the displacement, and the magnitude is also changing. The primary contributing factor is the phase shift. Figure 1.6 presents the case of 'in-phase' bending and torsional displacements. In this case, the resulting energy during the cycle is zero, and flutter cannot occur. However, a completely different situation emerges in the case of the phase shift between both displacements. An example of the bending and torsion phase shift of $\pi/2$ is shown in Figure 1.7. The resulting energy is positive, and flutter may occur. In

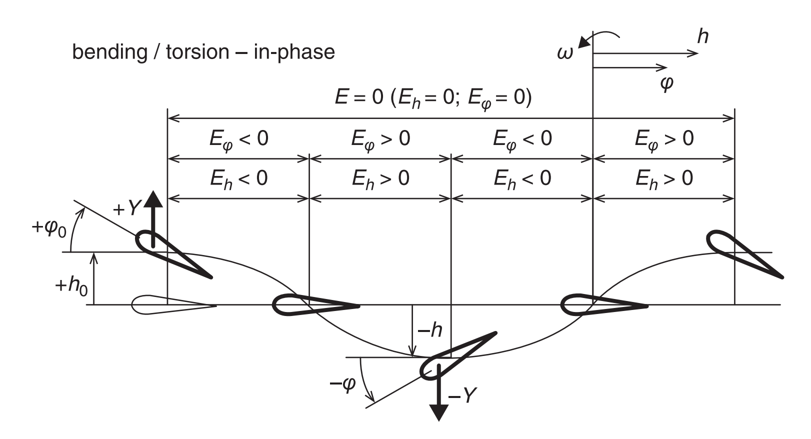


Figure 1.6 **Harmonic motion of airfoil with 2 DOFs (bending / torsion – 'in-phase')**

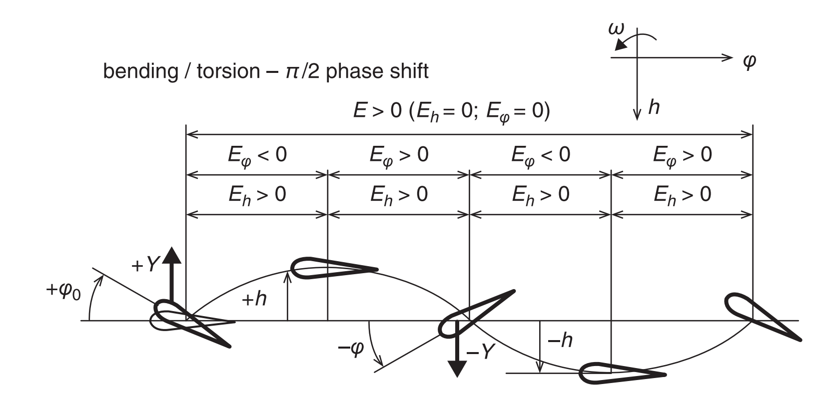


Figure 1.7 **Harmonic motion of airfoil with 2 DOFs (bending / torsion – 'out-of-phase' – shift $\pi/2$)**

fact, the bending deformation is excited by means of the torsional deformation.

In the general case, the motion may include two or more degrees of freedom, and the resulting energy may become either negative or positive. In the latter, flutter may occur.

The previous example considered that the control surfaces are vibrating as the integral part of the wing. Provided we consider the flapping motion of the control surface, the flutter mechanism become more complicated. Figure 1.8 and Figure 1.9 show an example of the wing bending mode coupled with the control surface (aileron) flapping mode. Similarly to the

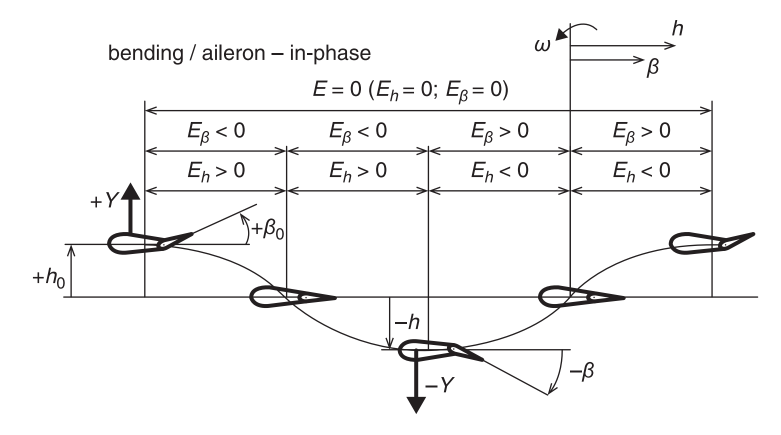


Figure 1.8 **Harmonic motion of airfoil with 2 DOFs (bending / aileron – 'in-phase')**

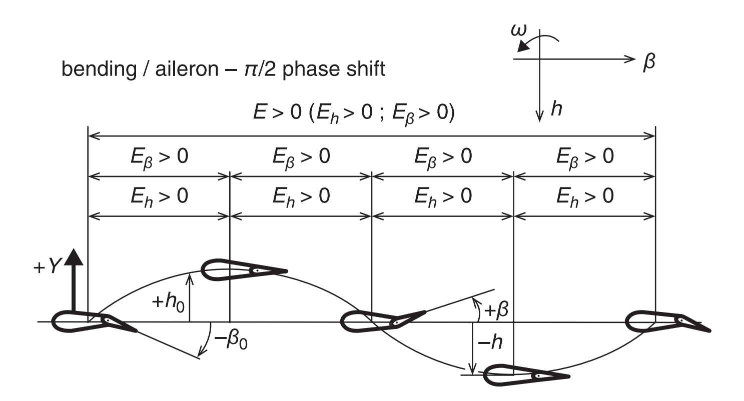


Figure 1.9 **Harmonic motion of airfoil with 2 DOFs (bending / aileron – 'out-of-phase' – shift $\pi/2$)**

former example, Figure 1.8 shows the case of the 'in-phase' wing bending and aileron flapping displacements where the energy during the cycle is zero, and Figure 1.9 shows the wing bending and aileron flapping phase shift of $\pi/2$ where the resulting energy during the cycle is positive. Therefore, the latter allows under specific conditions (aileron static under-balancing) the occurrence of flutter.

The examples presented show only essential flutter types. In practice, flutter mechanism may become much more complicated and may include

two or more degrees of freedom. Natural frequencies are dependent on the flow velocity, thus the phase relations are variable as well. In the general case, the energy during the cycle may be either negative or positive. In the latter, flutter may occur.

Considering the characteristics of the vibration modes contributing to flutter we distinguish the following flutter categories:

1. Bending / torsional surface flutter. The wing or tail surface vibrates with compound bending / torsional deformations. The control surface vibrates as an integral part of a main surface and causes no additional forces.
2. Bending / aileron flutter. This flutter combination includes wing bending and the aileron flapping mode. A similar case is the combination of a tail surface mode with a control flapping mode.
3. Bending / torsional / aileron flutter. This is combination of both of the previous cases. A flutter combination includes the wing bending mode, wing torsional mode and aileron flapping mode. A similar case is the combination of a tail surface bending and torsional mode with a control flapping mode.
4. Bending / torsional / aileron / tab flutter. This is a more complicated flutter case that includes the wing bending mode, wing torsional mode, aileron flapping mode and tab flapping mode.

In general a flutter combination may include any number of modes and usually includes either symmetrical or antisymmetrical modes.

1.3.2 Buffeting

Buffeting is the excited aeroelastic phenomenon caused by the vortices in the wake region behind the wing or other structural part. It is usually evaluated by means of stochastic or experimental methods. In most cases, buffeting does not cause structural destruction, but the vibrations may negatively affect structural fatigue life, aircraft control or the crew’s comfort.

1.3.3 Aeroelastic response to dynamic load

This is a response of deformable aircraft including unsteady aerodynamic forces to various dynamic loads, such as gust, turbulence, landing shock,

gun fire, rocket release, etc. It may cause additional structure loads, which may negatively influence the fatigue life, etc. It may also lead to flutter.

1.3.4 Dynamic stability and manoeuvrability

This includes controllability and manoeuvrability, including aircraft deformation.

1.3.5 Aero-servoelasticity

This includes the stability and controllability of a deformable aircraft with control servo-systems (e.g., fly-by-wire), active systems, etc.

1.4 References

1 Slavík, S.: *Aeroelasticita leteckých konstrukcí* (in Czech), Czech Technical University in Prague, Prague, Czech Republic, 1997, ISBN 80-01-01415-0.
2 Daněk, V.: *Aeroelasticita* (in Czech), Brno University of Technology, Brno, Czech Republic, 1987.
3 Kopřiva, Z. and Maleček, J.: *Aeroelasticita* (in Czech), Military Technical Academy, Brno, Czech Republic, 1982.
4 Rodden, W.P.: *Theoretical and Computational Aeroelasticity*, Crest Publishing, CA, USA, ISBN 978-0-692-01241-3, 2011.

2

Theoretical background of whirl flutter phenomenon

DOI: 10.1533/9781782421863.13

Abstract: This chapter provides basic information regarding the propeller whirl flutter phenomenon. It explains the physical principle of the phenomenon and outlines the fundamental solution by means of the quasi-steady theory. Next, the equations of motion and the solution are formulated. Finally, the influences of the most important parameters on whirl flutter characteristics are outlined.

Key words: whirl flutter, propeller whirl flutter, quasi-steady theory, gyroscopic system.

2.1 Physical principle

Whirl flutter, also called gyroscopic flutter, is a dynamic aeroelastic stability phenomenon that may occur in a flexibly mounted engine and propeller system. It takes into account the influence of the rotating masses, such as the propeller, compressor and turbine. Rotating masses increase the number of the system's degrees of freedom and produces additional forces and moments (centrifugal, Coriolis, gyroscopic moments). Furthermore, the propeller induces a complicated flow field that interferes with the nacelle and wing. The fundamental problem is an unsymmetrical distribution of the lift force on the transversely vibrating propeller. Whirl flutter may cause the propeller mounting to have unstable vibrations or even the failure of the engine, nacelle or whole wing. Whirl flutter was discovered analytically by Taylor and Browne [1] in 1938. However, practical interest in this phenomenon

started after the two fatal Lockheed L-188 C Electra II aircraft accidents in 1959 and 1960.

Whirl flutter may occur especially in turboprop aircraft, helicopters or tilt-rotor aircraft. This book is focused primarily on turboprop aircraft whirl flutter. The whirl flutter phenomenon relates to the mutual interactions of the rotating propeller with the aircraft deformations and the aerodynamic forces emerging during the aircraft's forward flight. The standard solution is based on the assumption of the rigid propeller. It is applicable for standard turboprop aircraft such as commuters, utility aircraft, military trainers, etc., for which the natural frequencies of the propeller blades are much higher than the frequencies of the engine system suspension vibrations. In large turboprops, in particular military transport aircraft with heavy multi-blade propellers, the solution requires taking into account the deformations of the propeller blades as well.

The whirl flutter of the tilt-rotor aircraft is much more complicated compared to turboprops. Obviously, the solution must include the deformations of the rotor blades. The solution must include all the flight regimes, i.e. the helicopter flight regime, transition flight regimes and, finally, the forward flight regime. The description of unsteady aerodynamic forces is very complicated and requires massive calculations or experimental data. Another important factor is that the nacelles of tilt-rotor aircraft are placed at the wing tips, which is a very sensitive region from the aeroelastic point of view. This placement causes strong interactions between the rotor and the wing's dynamics.

2.2 Propeller whirl flutter

Turboprop aircraft engine system flexible mounting can be substituted by the system of two rotational springs (stiffness constants K_Ψ, K_Θ) as illustrated in Figure 2.1. The propeller is considered as rigid, rotating with the angular velocity Ω. The system is exposed to the airflow of velocity V_∞.

Neglecting the propeller's rotation and the aerodynamic forces, two independent mode shapes (yaw – around vertical axis; pitch – around lateral axis) will emerge (Figure 2.2) with the angular frequencies ω_Ψ and ω_Θ.

Considering propeller rotation, the system motion changes to the characteristic gyroscopic motion. The gyroscopic effect makes the two independent mode shapes merge into the whirl motion (Figure 2.3). This

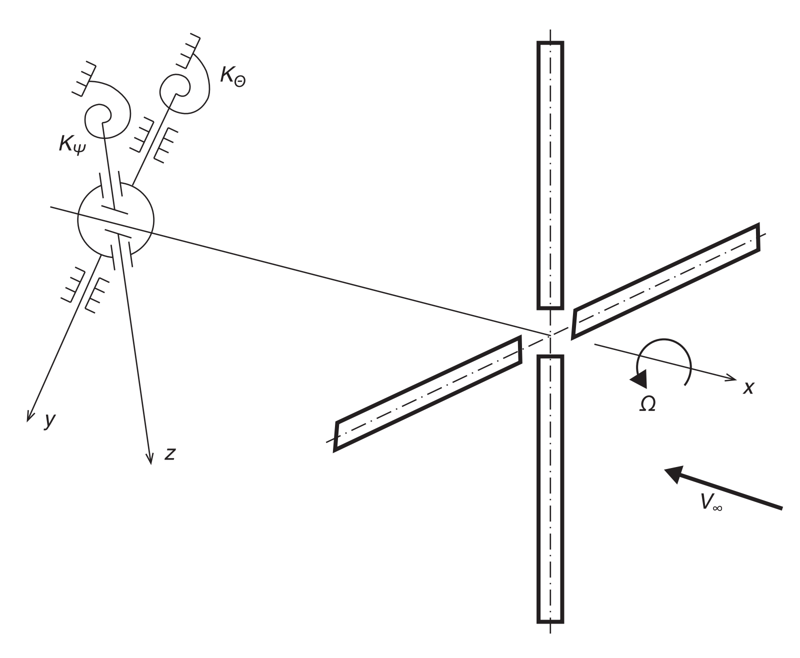


Figure 2.1 **Gyroscopic system with propeller [2]**

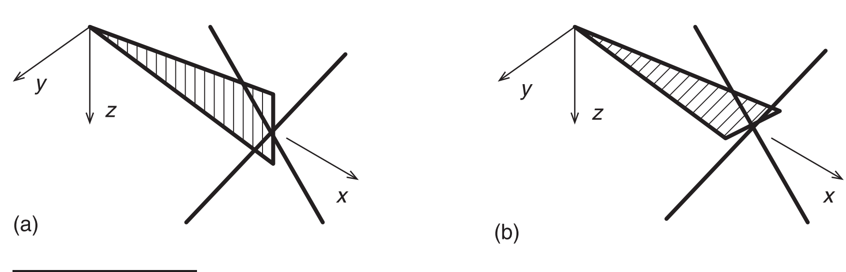


Figure 2.2 **Independent mode shapes ((a) pitch, (b) yaw) [2], [3]**

is caused by the fact that the angular velocity ω_Ψ (with respect to the *z*-axis) causes a reactive moment with respect to the *y*-axis and vice versa. The propeller axis shows an elliptical movement. The orientation of the propeller axis movement is backward relative to the propeller rotation for the mode with the lower frequency (backward whirl mode – Figure 2.3a) and forward relative to the propeller rotation for the mode with the higher frequency (forward whirl mode – Figure 2.3b). This

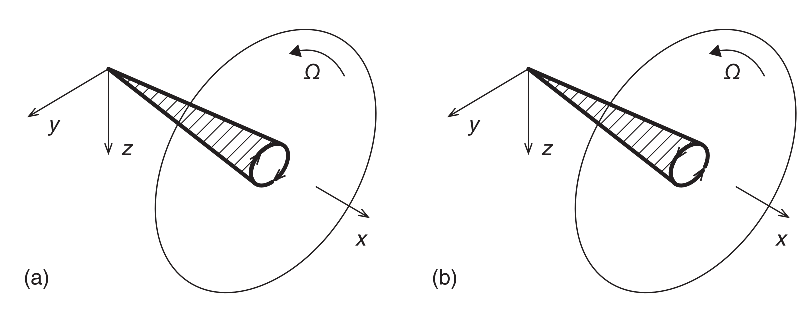


Figure 2.3 Backward (a) and forward (b) whirl mode [2], [3]

motion corresponds to the low-speed and high-speed precession of the gyroscopic system. Increasing the propeller revolutions increases the difference between both modes. The mode shapes of the described gyroscopic modes are complex, as yaw and pitch modes have a 90° phase shift. The condition of real mode shapes corresponds to the state of a non-rotating system.

The described gyroscopic mode shapes result in changes of the propeller blades' angles of attack. They give rise to non-stationary aerodynamic forces, which may under specific conditions induce flutter instability. Considering the rigid blades, the instability occurs inherently in the backward whirl mode. The possible states of the gyroscopic system from the flutter stability point of view for this backward mode are explained in Figure 2.4. Provided that the air velocity is lower than the critical value ($V_\infty < V_{FL}$), the system is stable and the motion is damped. If the airspeed exceeds the critical value ($V_\infty > V_{FL}$), the system becomes unstable, and motion is divergent. The limit state ($V_\infty = V_{FL}$), with no total damping, is called the critical flutter state, and V_{FL} is called the critical flutter speed.

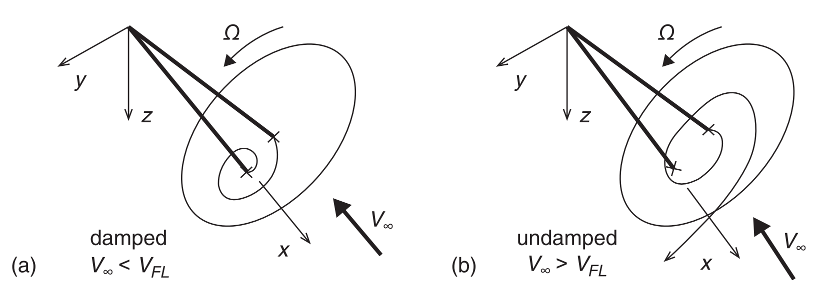


Figure 2.4 Stable (a) and unstable (b) state of gyroscopic vibrations for backward flutter mode [2], [3]

The specific case is a gyroscopic divergence, which occurs when the frequency becomes zero and the motion changes to a one-directional character.

The basic problem of the analytical solution is grounded in the determination of the aerodynamic forces caused by the gyroscopic motion for specific propeller blades. The solution is based on the assumption of no sideslip angle and the basic characteristics of aerodynamic forces are obtained using quasi-steady theory [2], [3].

Because both gyroscopic modes have the same character, we reduce the solution to the motion symmetrical with respect to the *x*-*z* plane. We use the system of coordinates *x*, *y*, *z* connected to the propeller. Let us consider the propeller inclined relative to the airflow V_∞ at the angle of Θ, as demonstrated in Figure 2.5a. We separate the components of V_∞ on the propeller axis and the propeller disc plane (perpendicular to the propeller axis). We can say that the right-hand side (looking in the *x*-axis direction) generates higher thrust than the left-hand side, as demonstrated in Figure 2.5c, d. The yaw moment $M_Z(\Theta)$ emerges. The vector of this

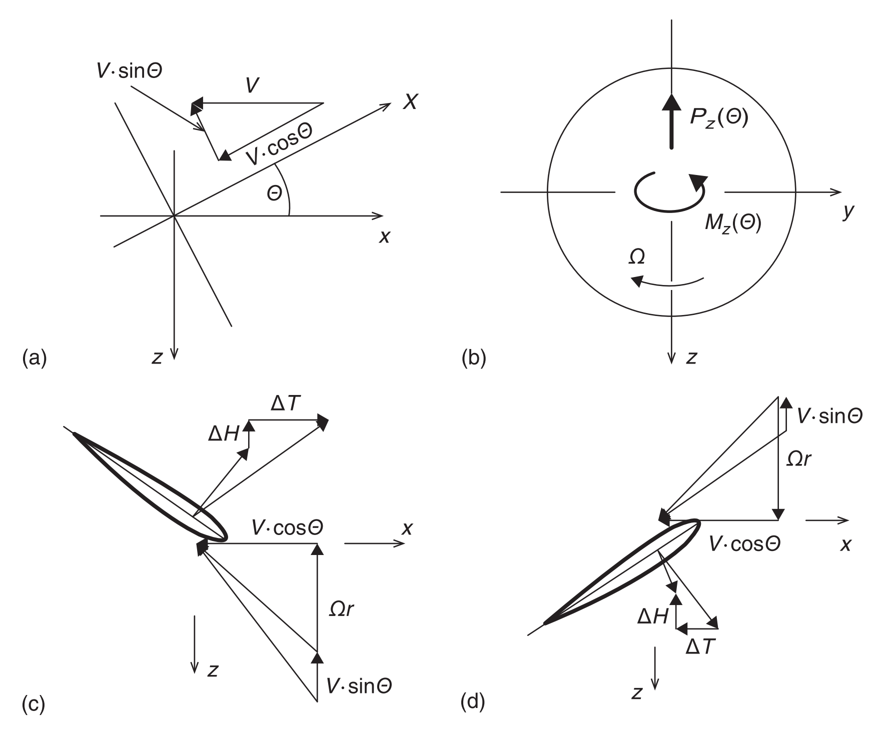


Figure 2.5 **Aerodynamic forces due to pitching deflection (angle Θ) [2]**

moment is acting in the direction of the -z axis (negative z-semiaxis). In the same (-z) direction, also acting is the vertical force $P_Z(\Theta)$ that is the result of the horizontal components ΔH. Considering the tractor propeller configuration, this force increases the Θ angle. This fact may cause static divergence instability of the system; however, in most cases, this phenomenon does not have a practical effect because the internal elastic forces are usually much higher than the $P_Z(\Theta)$ force. Static divergence results from the very low stiffness of the engine's suspension. The yawing moment due to pitch $M_Z(\Theta)$ is a cross stiffness term. It acts in the same direction as the yawing velocity for the backward whirl mode; therefore, it has a destabilising effect.

The quasi-steady approach leads to the same results for the forces emerging due to the propeller disc movement (velocity $\dot{z}$) as described in Figure 2.6. The aerodynamic yawing moment $M_Z(\dot{z})$ and the aerodynamic force $P_Z(\dot{z})$ are acting in opposition to the propeller disc motion and damp it.

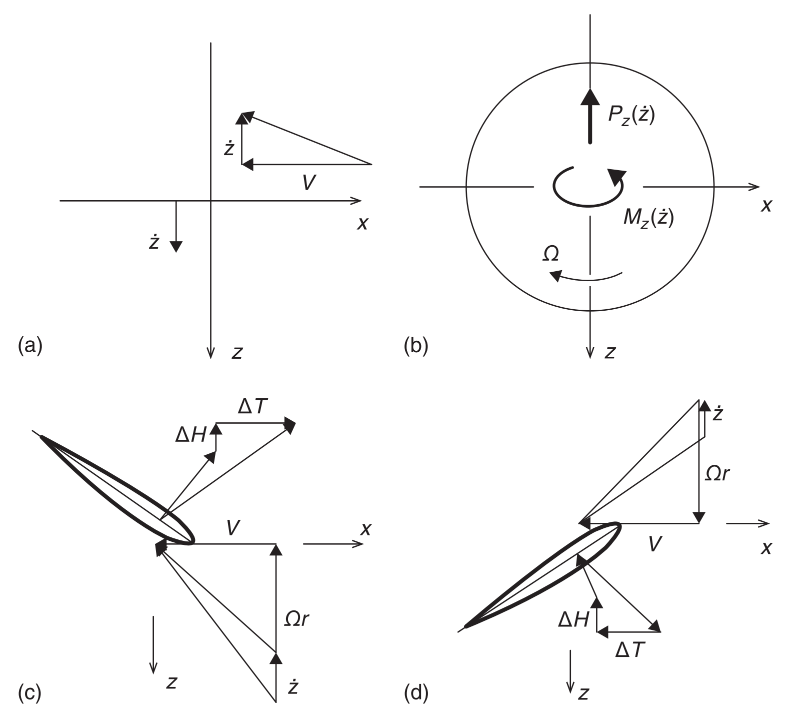


Figure 2.6 Aerodynamic forces due to the yawing velocity $\dot{z}$ (movement around vertical axis) [2]

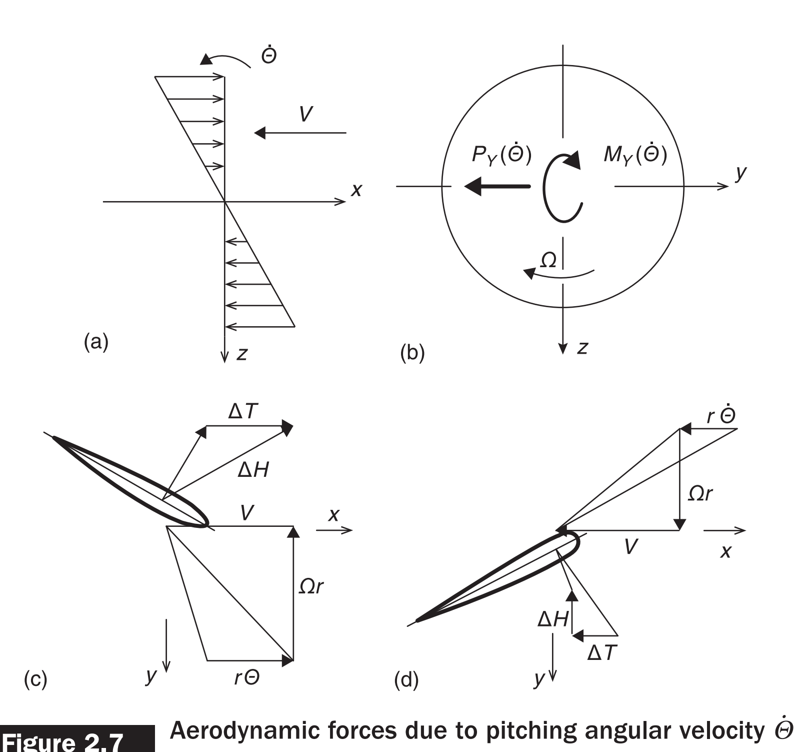


Figure 2.7 **Aerodynamic forces due to pitching angular velocity $\dot{\Theta}$ (movement around lateral axis) [2]**

Finally, Figure 2.7 demonstrates the aerodynamic reactive forces caused by the angular velocity $\dot{\Theta}$. The cross-sections of the blades that are in the vertical position are shown. The angular velocity $\dot{\Theta}$ influences the wind flow coming to the propeller blades as demonstrated in Figure 2.7 and causes moment $M_Y(\dot{\Theta})$, acting in opposition to the propeller disc motion and damping this motion. Furthermore, a force $P_Y(\dot{\Theta})$ emerges, acting in the direction of *-y* (negative *y*-semiaxis), which couples the movements around both vertical and lateral axes.

To summarise, the most important terms with regard to whirl flutter are yaw moment due to pitch $M_Z(\Theta)$, or similarly the pitch moment due to yaw $M_Y(\Psi)$. These moments are to be balanced by aerodynamic or structural damping terms.

The equations of motion were set up for the system described in Figure 2.1 by means of Lagrange's approach. The kinematical scheme, including the gyroscopic effects, is shown in Figure 2.8.

The independent generalised coordinates are three angles (φ, Θ, Ψ). Ranges for angle Θ are $<z;Z>$ and $<x;X>$, and ranges for angle Ψ are

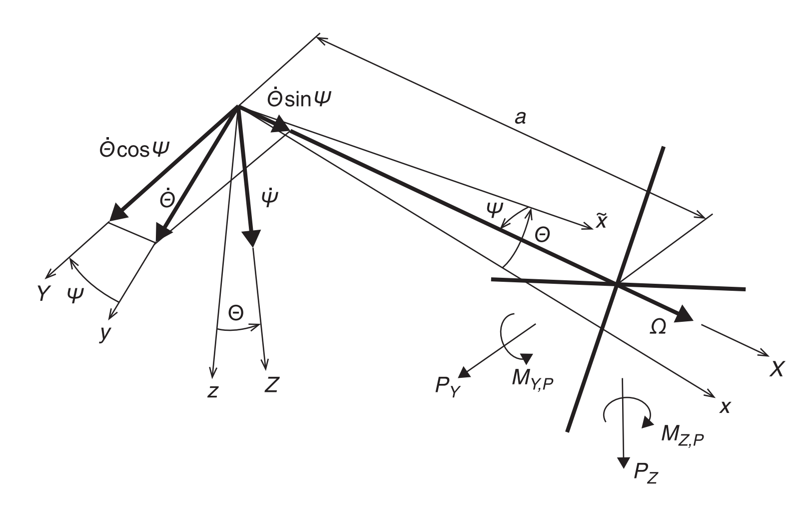


Figure 2.8 Kinematical scheme of the gyroscopic system [2], [4]

<$\tilde{x}$; X> and <y; Y>. We assume the propeller angular velocity constant ($\varphi = \Omega t$), the mass distribution symmetry around the X-axis and the mass moments of inertia $J_Z \neq J_Y$. We will use a coordinate system X, Y, Z linked to the system. Then, kinetic energy is:

$$E_K = \frac{1}{2} J_X \omega_X^2 + \frac{1}{2}\left(J_Y \omega_Y^2 + J_Z \omega_Z^2\right) \qquad [2.1]$$

The angular velocities in the coordinate system X, Y, Z will be:

$$\begin{aligned} \omega_X &= \Omega + \dot{\Theta}\sin\Psi \approx \Omega + \dot{\Theta}\Psi \\ \omega_Y &= \dot{\Theta}\cos\Psi \approx \dot{\Theta} \\ \omega_Z &= \dot{\Psi} \end{aligned} \qquad [2.2]$$

Considering the fact, that $\dot{\Theta}^2\,\dot{\Psi}^2 << \Omega^2$, the equation for the kinetic energy becomes:

$$E_K = \frac{1}{2} J_X \Omega^2 + J_X \Omega \Psi \dot{\Theta} + \frac{1}{2}\left(J_Y \dot{\Theta}^2 + J_Z \dot{\Psi}^2\right) \qquad [2.3]$$

The first part of Eqn. 2.3 is independent on both Θ and Ψ; thus, it does not appear in Lagrange's equation. Then potential energy becomes:

$$E_P = \frac{1}{2} K_\Theta \Theta^2 + \frac{1}{2} K_\Psi \Psi^2 \qquad [2.4]$$

To describe the structural damping, we assume here the structural damping commonly used in the flutter analyses, with the damping force proportional to the amplitude of displacement:

$$D = \frac{1}{2}\frac{K_\Theta \gamma_\Theta}{\omega}\dot{\Theta}^2 + \frac{1}{2}\frac{K_\Psi \gamma_\Psi}{\omega}\dot{\Psi}^2 \qquad [2.5]$$

Then, we obtain from Lagrange's equations and Eqns 2.3–2.5 the system of two mutually influencing differential equations:

$$\begin{aligned} &J_Y\ddot{\Theta} + \frac{K_\Theta \gamma_\Theta}{\omega}\dot{\Theta} + J_X\Omega\dot{\Psi} + K_\Theta\Theta = Q_\Theta \\ &J_Z\ddot{\Psi} + \frac{K_\Psi \gamma_\Psi}{\omega}\dot{\Psi} - J_X\Omega\dot{\Theta} + K_\Psi\Psi = Q_\Psi \end{aligned} \qquad [2.6]$$

Generalised propeller forces and moments (see Figure 2.8) can be expressed as:

$$\begin{aligned} &Q_\Theta = M_{Y,P} - aP_z \\ &Q_\Psi = M_{Z,P} + aP_Y \end{aligned} \qquad [2.7]$$

The index P means that the moment around the specific axis is at the plane of the propeller rotation. Employing the quasi-steady theory, the effective angles become:

$$\begin{aligned} &\Theta^* = \Theta - \frac{\dot{Z}}{V_\infty} = \Theta - \frac{a\dot{\Theta}}{V_\infty} \\ &\Psi^* = \Psi - \frac{\dot{Y}}{V_\infty} = \Psi - \frac{a\dot{\Psi}}{V_\infty} \end{aligned} \qquad [2.8]$$

Neglecting the aerodynamic inertia terms ($\dot{\Theta}^* \approx \dot{\Theta}$, $\dot{\Psi}^* \approx \dot{\Psi}$), we obtain the equations for the propeller's dimensionless forces and moments as follows:

$$\begin{aligned} &P_Y = q_\infty F_p\left(c_{y\Psi}\Psi^* + c_{y\Theta}\Theta^* + c_{yq}\frac{\dot{\Theta}^* R}{V_\infty}\right) \\ &P_Z = q_\infty F_p\left(c_{z\Theta}\Theta^* + c_{z\Psi}\Psi^* + c_{zr}\frac{\dot{\Psi}^* R}{V_\infty}\right) \\ &M_{Y,P} = q_\infty F_P D_P\left(c_{m\Psi}\Psi^* + c_{mq}\frac{\dot{\Theta}^* R}{V_\infty}\right) \\ &M_{Z,P} = q_\infty F_P D_P\left(c_{n\Theta}\Theta^* + c_{nr}\frac{\dot{\Psi}^* R}{V_\infty}\right) \end{aligned} \qquad [2.9]$$

where: F_P = propeller disc area; D_P = propeller diameter. The aerodynamic derivatives are defined as follows:

$$c_{y\Theta} = \frac{\partial c_y}{\partial \Theta^*} \quad c_{y\Psi} = \frac{\partial c_y}{\partial \Psi^*} \quad c_{yq} = \frac{\partial c_y}{\partial\left(\frac{\dot{\Theta} R}{V_\infty}\right)} \quad c_{yr} = \frac{\partial c_y}{\partial\left(\frac{\dot{\Psi} R}{V_\infty}\right)}$$

$$c_{z\Theta} = \frac{\partial c_z}{\partial \Theta^*} \quad c_{z\Psi} = \frac{\partial c_z}{\partial \Psi^*} \quad c_{zq} = \frac{\partial c_z}{\partial\left(\frac{\dot{\Theta} R}{V_\infty}\right)} \quad c_{zr} = \frac{\partial c_z}{\partial\left(\frac{\dot{\Psi} R}{V_\infty}\right)}$$

$$c_{m\Theta} = \frac{\partial c_m}{\partial \Theta^*} \quad c_{m\Psi} = \frac{\partial c_m}{\partial \Psi^*} \quad c_{mq} = \frac{\partial c_m}{\partial\left(\frac{\dot{\Theta} R}{V_\infty}\right)} \quad c_{mr} = \frac{\partial c_m}{\partial\left(\frac{\dot{\Psi} R}{V_\infty}\right)} \qquad [2.10]$$

$$c_{n\Theta} = \frac{\partial c_n}{\partial \Theta^*} \quad c_{n\Psi} = \frac{\partial c_n}{\partial \Psi^*} \quad c_{nq} = \frac{\partial c_n}{\partial\left(\frac{\dot{\Theta} R}{V_\infty}\right)} \quad c_{nr} = \frac{\partial c_n}{\partial\left(\frac{\dot{\Psi} R}{V_\infty}\right)}$$

These aerodynamic derivatives can be obtained analytically [5], [6]. Considering the symmetry, they can be expressed as follows:

$$c_{z\Psi} = c_{y\Theta};\, c_{m\Psi} = -c_{n\Theta};\, c_{mq} = c_{nr};\, c_{zr} = c_{yq};\, c_{z\Theta} = -c_{y\Psi};\, c_{n\Psi} = c_{m\Theta};$$
$$c_{mr} = -c_{nq};\, c_{yr} = -c_{zq} \qquad [2.11]$$

Neglecting the low value derivatives, we can consider:

$$c_{mr} = -c_{nq} = 0 \; ; \; c_{yr} = -c_{zq} = 0 \qquad [2.12]$$

Substituting from Eqn. 2.10 to the equations of motion Eqn. 2.6 and considering the harmonic motion:

$$\left[\Theta, \Psi\right] = \left[\bar{\Theta}, \bar{\Psi}\right] e^{j\omega t} \qquad [2.13]$$

We obtain the final whirl flutter matrix equation:

$$\left(-\omega^2 \left[M\right] + j\omega \left(\left[D\right] + \left[G\right] + q_\infty F_P \frac{D_P^2}{V_\infty}\left[D^A\right]\right) + \left(\left[K\right] + q_\infty F_P D_P \left[K^A\right]\right)\right) \begin{vmatrix} \bar{\Theta} \\ \bar{\Psi} \end{vmatrix} = \{0\} \qquad [2.14]$$

where the mass matrix becomes

$$[M]=\begin{bmatrix} J_Y & 0 \\ 0 & J_Z \end{bmatrix} \quad [2.15]$$

The structural damping matrix becomes

$$[D]=\begin{bmatrix} \frac{K_\Theta \gamma_\Theta}{\omega} & 0 \\ 0 & \frac{K_\Psi \gamma_\Psi}{\omega} \end{bmatrix} \quad [2.16]$$

The gyroscopic matrix becomes

$$[G]=\begin{bmatrix} 0 & J_X \Omega \\ -J_X \Omega & 0 \end{bmatrix} \quad [2.17]$$

The structural stiffness matrix becomes

$$[K]=\begin{bmatrix} K_\Theta & 0 \\ 0 & K_\Psi \end{bmatrix} \quad [2.18]$$

The aerodynamic damping matrix becomes

$$[D^A]=\begin{bmatrix} -\frac{1}{2}c_{mq}-\frac{a^2}{D_P^2}c_{z\Theta} & \frac{1}{2}\frac{a}{D_P}c_{yq}-\frac{a}{D_P}c_{n\Theta}-\frac{a^2}{D_P^2}c_{y\Theta} \\ -\frac{1}{2}\frac{a}{D_P}c_{yq}+\frac{a}{D_P}c_{n\Theta}+\frac{a^2}{D_P^2}c_{y\Theta} & -\frac{1}{2}c_{mq}-\frac{a^2}{D_P^2}c_{z\Theta} \end{bmatrix} \quad [2.19]$$

The aerodynamic stiffness matrix becomes

$$[K^A]=\begin{bmatrix} \frac{a}{D_P}c_{z\Theta} & c_{n\Theta}+\frac{a}{D_P}c_{y\Theta} \\ -c_{n\Theta}-\frac{a}{D_P}c_{y\Theta} & \frac{a}{D_P}c_{z\Theta} \end{bmatrix} \quad [2.20]$$

The solution of Eqn. 2.14 can be performed as an eigenvalue problem. The limit (flutter) state is attained when for a specific combination of the parameters V_∞ and Ω, the angular velocity ω becomes real. The whirl flutter characteristics are explained in Figure 2.9, which describes the influence of the propeller advance ratio ($V_\infty/(\Omega R)$) on the stability of an undamped gyroscopic system. Increasing the propeller advance ratio

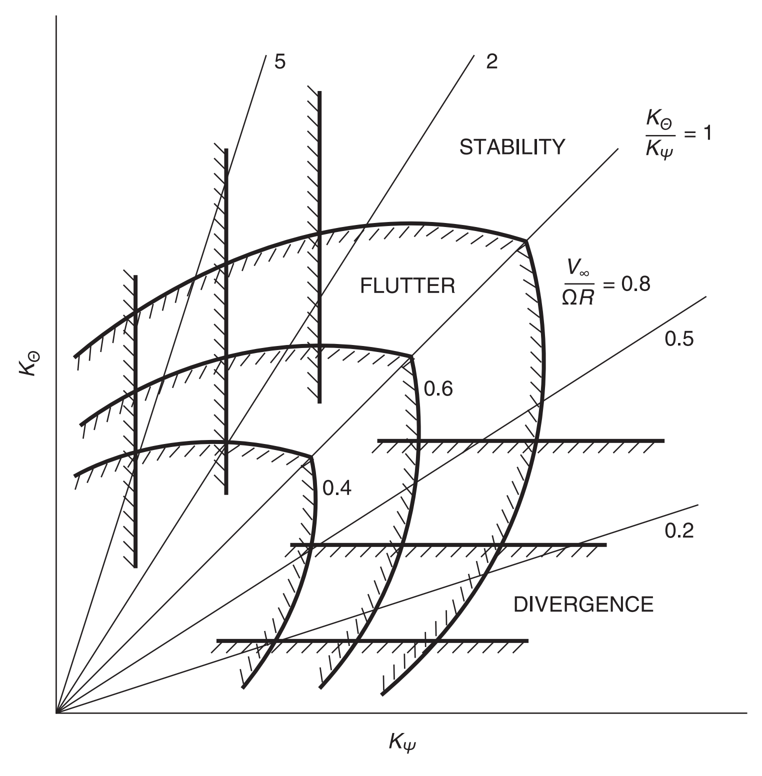


Figure 2.9 **Influence of the propeller advance ratio ($V_\infty/(\Omega R)$) on the stability of an undamped gyroscopic system [2], [7]**

increase the necessary stiffnesses K_Θ, K_Ψ. The influence of structural damping and the influence of the distance propeller–pivot point is described in Figure 2.10.

Considering the linear system, the whirl flutter appears at gyroscopic rotational vibrations, and the flutter frequency is the same as the frequency of the backward gyroscopic mode. The critical state may be reached by increasing either the air velocity or the propeller revolutions. Structural damping is a significant stabilisation factor. On the contrary, the propeller thrust influence is barely noticeable. The most critical state is $K_\Theta = K_\Psi$, which means that $\omega_\Theta = \omega_\Psi$ when the interaction of both independent motions is maximal. A special case of Eqn. 4.14 for $\omega = 0$ is gyroscopic static divergence.

$$\left([K] + q_\infty F_P D_P [K^A]\right) \begin{Bmatrix} \bar{\Theta} \\ \bar{\Psi} \end{Bmatrix} = \{0\} \qquad [2.21]$$

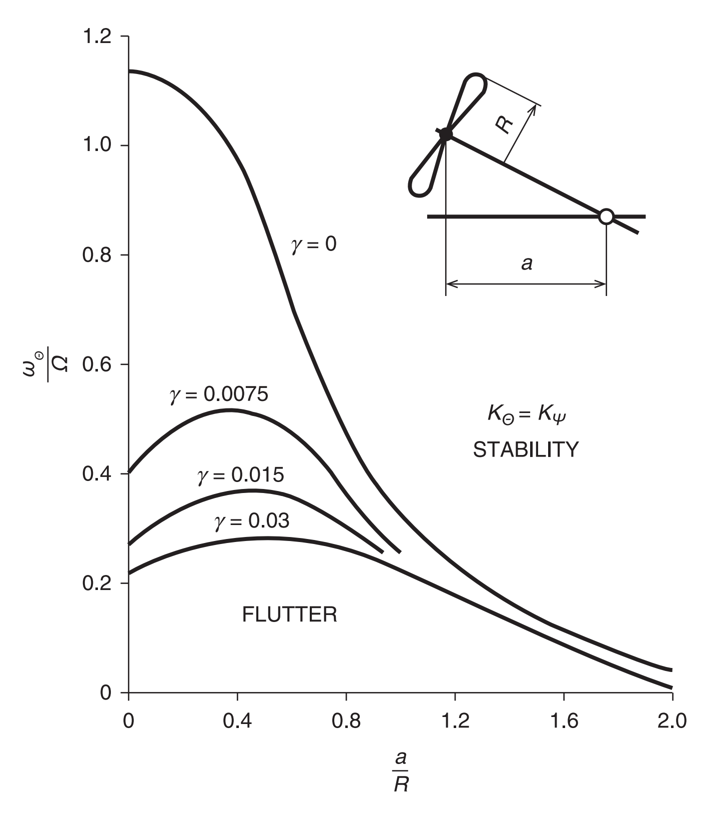


Figure 2.10 **Influences of structural damping and propeller – pivot point distance on whirl flutter stability [2], [7]**

The critical dynamic pressure for the divergence is obtained when the determinant of the whirl flutter matrix becomes zero:

$$\left|\left[K\right]+q_{\mathrm{DIV}}F_P D_P\left[K^A\right]\right|=0 \qquad [2.22]$$

Figure 2.11 describes the characteristics of static divergence. It is worth noting that for the stiffness values $K_\Theta \approx K_\Psi$, the divergence does not appear when approaching zero.

The most important structural and flight parameters influencing the whirl flutter are:

- effective stiffness of power unit attachment (K_Θ; K_Ψ);
- stiffness ratio (K_Θ/K_Ψ);
- structural damping of vibration modes (γ_Θ; γ_Ψ);

- propeller revolutions (Ω);
- propeller advance ratio ($J_o = (V_\infty/(\Omega R))$).

The influence of the stiffness of K_Θ and K_Ψ is shown in Figure 2.9. Increasing the stiffness increases the flutter velocity. However, another important factor is the stiffness ratio. The most critical stiffness ratio is $(K_\Theta/K_\Psi) = 1$, represented by the diagonal in Figure 2.9. The stability boundary may also be affected by the structural damping of both modes. As shown in Figure 2.10, it may become an important stabilising factor. For this reason, structural damping should not be neglected; otherwise, the flutter speed will be significantly underestimated. Figure 2.10 also shows the influence of the pivot point location. The pivot position influence the damping force $P_Z(\dot{z})$ due to the transverse velocity of the propeller hub (see Figure 2.6). Moving the pivot location aft causes an increase in the flutter speed and also makes the system less sensitive to structural damping due to the increasing aerodynamic damping.

Other stability boundaries are shown in the next figures. The stability boundary for the constant speed is shown in Figure 2.12, considering

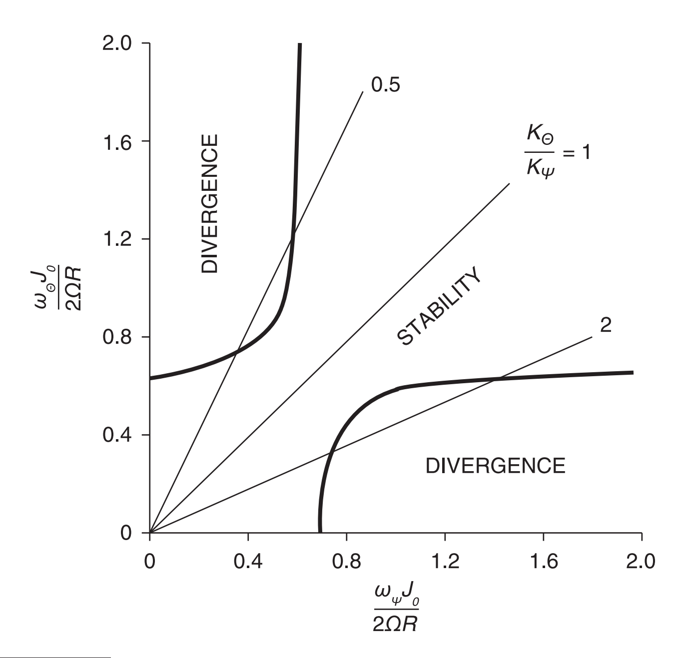


Figure 2.11 **Static divergence of the gyroscopic system [2], [7]**

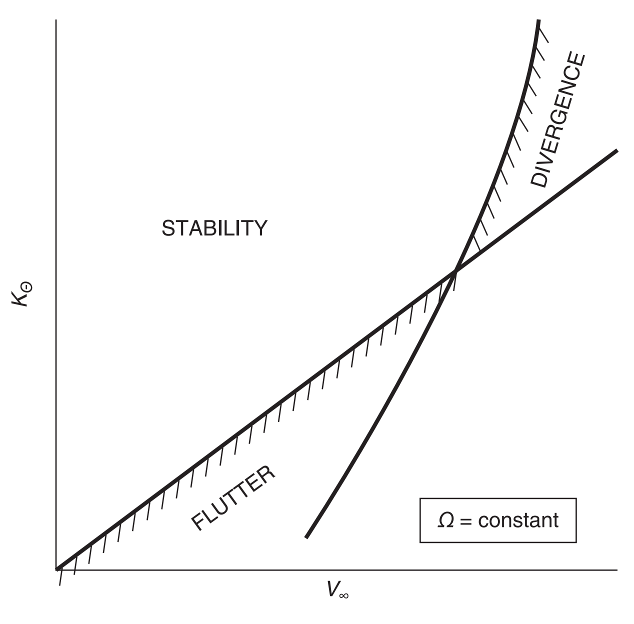


Figure 2.12 **Whirl flutter boundaries (Ω=const.) [3]**

the specific stiffness ratio (K_Θ/K_Ψ). It represents the constant-speed propeller during flight. For lower velocities, the required stiffness is lower, and the stability boundary is determined by the condition of flutter, whereas at higher velocities static divergence becomes the limiting factor.

Another type of stability boundary is shown in Figure 2.13. It considers the constant stiffnesses K_Θ and K_Ψ and shows the influence of the propeller revolutions. It may represent the influence of the propeller over-speed in the flight condition. For high propeller revolutions, the flutter velocity is not very sensitive to changes in propeller revolutions. On the other hand, for low propeller revolutions, the flutter speed does become sensitive; however, at this level divergence is the primary limiting factor.

The stability boundary for the constant advance ratio considering the specific stiffness ratio (K_Θ/K_Ψ) is shown in Figure 2.14. It represent the fixed blade angle propeller in the windmilling mode. Such propellers have frequently been used for wind tunnel tests. The required stiffness is proportional to the V_∞^2 (or linear with the dynamic pressure). In this case, divergence cannot occur.

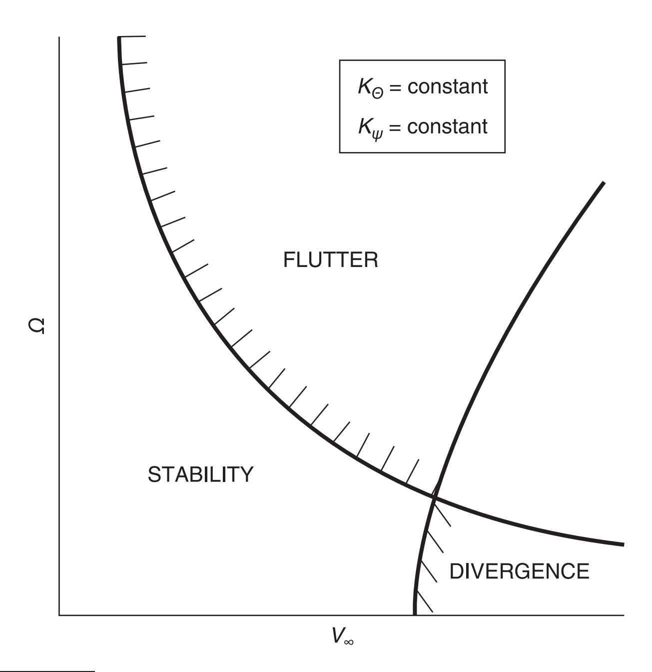


Figure 2.13 **Whirl flutter boundaries (K_{Θ} = const.; K_{Ψ} = const.) [3]**

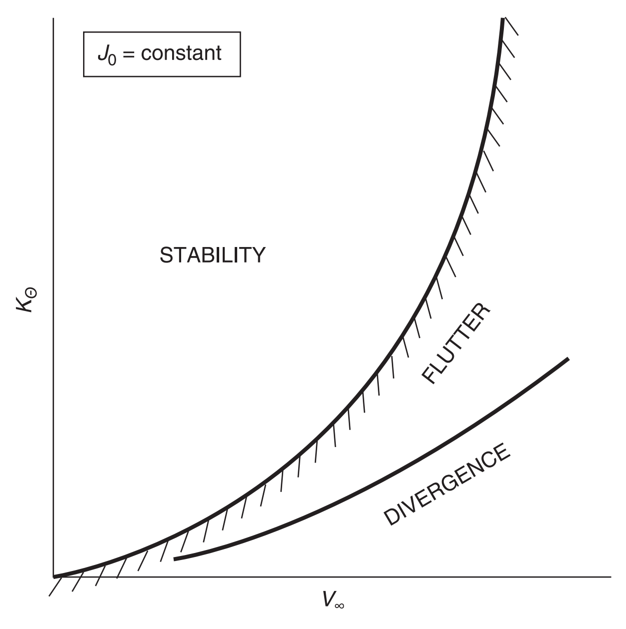


Figure 2.14 **Whirl flutter boundaries (J_o = const.) [3]**

2.3 Tilt-rotor whirl flutter

Tilt-rotor aircraft flight regimes include the helicopter flight regime, transition flight regime and the forward flight regime. Therefore, the inflow angle (α_T), which is the angle between the propeller axis and the airstream, may vary within the range of 0° and 90°. The aerodynamic derivatives at these high inflow angle regimes differ significantly from those of the forward flight regime. Despite that whirl flutter is expected at the high airspeeds that correspond to the forward flight regime of the tilt-rotor aircraft, it is necessary also to evaluate the possibility of whirl flutter occurrence at low-speed transition regimes. Considering the rigid rotor and the aerodynamic derivatives based on the experiments, the influence of the high inflow angle is slightly stabilising. This stabilising effect is higher for the thrusting propeller in comparison with the windmilling one, as shown in Figure 2.15.

The above-mentioned facts are limited by the assumption of the rigid propeller. This assumption is reasonable, for conventional propellers that provide thrust only. The eigen-frequencies of conventional propeller

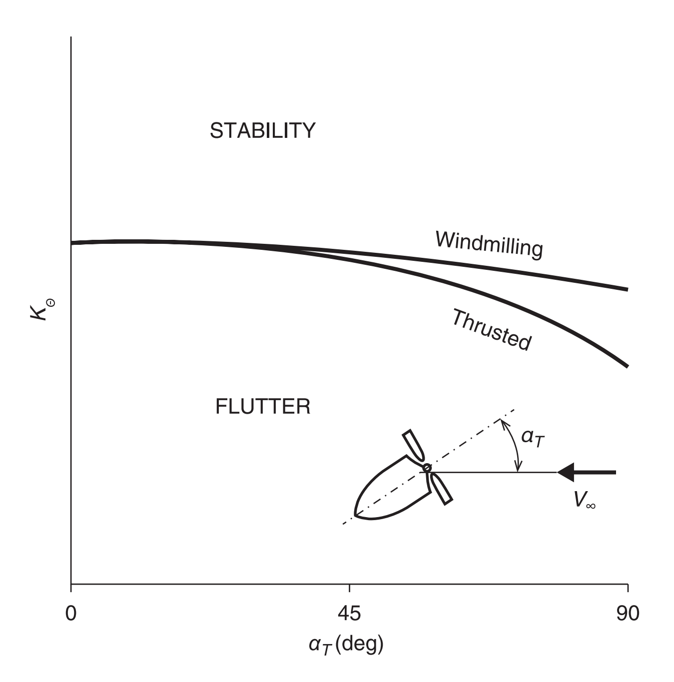


Figure 2.15 **Influence of inflow angle to whirl flutter boundaries [3], [8]**

blades are usually much higher with respect to the frequencies of the engine vibration modes. However, this assumption cannot be applied to the tilt-rotor aircraft rotors that provide thrust as well as lift (let alone the rotors of helicopters). Therefore, it is necessary to include the stiffness characteristics of the rotor's blades in the whirl flutter analysis. Obviously, this consideration makes the analysis more complicated. The additional degrees of freedom coming from the blades increase the number of equations of motion and also influence the inertial and aerodynamic characteristics of the system. Moreover, tilted flight regimes create additional forces due to the inflow angle and the aerodynamic interference effects. Thus, the equations of motion are different, the aerodynamic derivatives are time dependent and the solution of such a system of differential equations requires more complex methods than classical whirl flutter. The unsteady aerodynamic solution is complicated and requires massive calculations (typically CFD) or experimental data. Moreover, the rotors are placed in the wing tip region and cause strong interactions between the rotor and the wing's dynamics. For this reason, the solution for tilt-rotor aircraft whirl flutter is usually assigned to the specific aircraft's concept. Tilt-rotor related issues are described only briefly in this book. The detailed description is beyond our scope and can be found, for example, in reference [9].

Note that rigid blade consideration is sufficient for the standard propellers that are used on utility aircraft, commuters, etc. An analysis of turboprop systems with large multi-blade propellers used, for example on heavy military transport aircraft, should include the effects of the blades' flexibility as well.

2.4 References

1 Taylor, E. S. and Browne, K. A.: Vibration isolation of aircraft power plants, *Journal of Aerospace Sciences*, Vol. 6, no. 2, December 1938, pp. 43–49.
2 Försching, H.W.: *Grundlagen der Aeroelastik* (in German), Springer–Verlag, 1974, ISBN 0387065407, 9780387065403, also: Основы Аэроупругости (in Russian), Mašinostroenie, 1984.
3 Reed, W.H.: Review of Propeller – Rotor Whirl Flutter, NASA Technical Report, NASA TR R-264, 1967.
4 Reed, W.H. and Bland, S.R.: An Analytical Treatment of Aircraft Propeller Precession Instability, NASA Langley, Technical Note, TN D-659, 1961.
5 Ribner, H.S.: Propellers in Yaw, NACA Report 820, 1945.

6 Ribner, H.S.: Formulas for Propellers in Yaw and Charts of the Side – Force Derivatives, NACA Report 819, 1945.
7 Houbolt, J.C. and Reed, W.H.: Propeller – nacelle whirl flutter, *Journal of Aerospace Sciences*, Vol. 29, 1962.
8 Reed, W.H. and Bennett, R.M.: 'Propeller Whirl Flutter Considerations for V/STOL Aircraft', CAL/TRECOM Symposium, Buffalo, NY, USA, 1963.
9 Kiessling, F.: Zur Problematik von Whirl-Flatteruntersuchungen von V/STOL-Flugzeugen (in German), Forschungsbericht 74-11, German Aerospace Research Center (DLR), Institute of Aeroelasticity, Goettingen, Germany, 1974, also, Some Problems in Research on Whirl Flutter in V/STOL Aircraft, ESRO TT-160, 1975.

This page intentionally left blank

Whirl flutter occurrence in aerospace practice

DOI: 10.1533/9781782421863.33

Abstract: This chapter provides information regarding the occurrence of the whirl flutter phenomenon in aerospace practice. It provides information concerning the Lockheed L-188 C Electra II aircraft accidents in 1959 and 1960 as well as the Beechcraft 1900C aircraft accident in 1991. The chapter describes the investigation process and the outcomes. Additionally, further accidents, e.g., the Turbo Mallard GF73T in 2005, are outlined.

Key words: whirl flutter, Lockheed Electra II, Beechcraft 1900C, Grumman Turbo Mallard.

3.1 Introduction

As was described previously, whirl flutter is a stability phenomenon that may result in unstable vibrations of the propeller mounting, even to a failure of the engine, nacelle or whole wing. Whirl flutter was the direct cause of several aircraft accidents. The most famous instances are the crashes of two Lockheed L-188 C Electra II airliners in 1959 and 1960 and the crash of a Beechcraft 1900C commuter in 1991. Furthermore, whirl flutter most likely also contributes to other events.

3.2 Lockheed L-188C Electra II

The Lockheed L-188 C Electra II is a four-engine turboprop airliner for 98 passengers with a wingspan of 30.18 m, a length of 31.85 m and a maximal take-off weight of 51 256 kg (see Figure 3.1). The maiden flight was accomplished in 1957, and total of 170 aircraft were manufactured. Currently, several Electras are operated as freighters or water tankers. Most likely more successful was the modified Electra, known as the Lockheed P-3 Orion, which is operated by the navy as scout and anti-submarine aircraft.

Electra became famous because of two accidents in 1959 and 1960 that were directly caused by whirl flutter [1]. After these events, the fleet was restricted in speed, and the power unit attachments were reinforced and redesigned. We will explore these crashes in more detail because they were the first documented occurrences of whirl flutter and initiated the following large experimental research and analytical studies aimed at understanding this new phenomenon.

The Lockheed L-188 C Electra II was designed as a passenger airliner, with four Allison 501 turboprop wing-mounted power units. The concept of the aircraft was very new. These powerful engines were installed into the lengthy nacelles, with large propellers placed quite far forward of the wing. The maiden flight was accomplished in 1957, and the commercial outlook was promising. During the next two years, 144 orders were



Figure 3.1 Lockheed L-188 C Electra II aircraft (photo copyright Bill Hough, used with permission)

placed. Unfortunately, on 29 September 1959, a Braniff Airways' Electra lost the port wing during flight and crashed near Buffalo, Texas. A very similar incident occurred several months later, when on 17 March 1960, a Northwest Orient Airlines' Electra crashed near Cannelton, Indiana after losing the starboard wing during the flight. In both cases, everyone on board was killed, a total of 97 casualties.

After that event, the fleet of Electras was restricted in speed, and a large investigation was started. The investigational activities were shared by the FAA, Lockheed and the Allison gas turbine division of General Motors. The official conclusion reports the cause of the first event as 'failure of the port wing due to the forces coming from the undamped propeller whirl mode' and the cause of the second event as 'failure of the starboard wing due to the flutter caused by the vibration of the outboard engine'. Investigations of the former event determined that the outboard engine nacelle was vibrating at an amplitude of 35 degrees around the neutral position. The nacelle was designed considering a case of large unbalancing, e.g. due to the loosening of the propeller blade; however this was not the case. On the contrary, the whole wing had been torn away from the fuselage, but the nacelle attachment was undamaged. The cause was not the overload of the wing, as such a design failure would have been detected during the extensive tests conducted by Lockheed or during the earlier operational flights. However, the coupling of the propeller/engine whirl mode with the wing flutter mode had not been taken into account before, and the investigation was then directed towards this issue. The whirl mode was introduced into the analytical flutter solution, and the mechanism of the failure was discovered.

The whirl flutter occurrence was also demonstrated on the 1/8 scale aeroelastic wind tunnel model of the Electra, with the reduced stiffness of the engine attachment performed at the NASA Langley transonic wind tunnel.

The first Electra crash was caused by the effect of the propeller's overspeed, which was attested to by witnesses who verified the specific sound, and the loose and wobbly attachment of the port outboard propeller examined on the wreckage. The propeller's vibratory motion was transmitted to the wing, which as a consequence was torn away.

The second Electra crash was caused by a combination of the weakened engine mounts coming from the 'hard' intermediate landing, as described by the passengers who deplaned there, and the pilot's impulses to the control system that were intended to compensate for air turbulence during the flight.

It was found that the engine mounts were not strong enough to damp the outboard engine's whirl mode vibrations. These oscillations were transmitted to the wing, which resulted in the destructive outcome.

Later on the wings were strengthened, the nacelles were reinforced and the engine mounts were redesigned to be able to withstand much more stress. Electras were returned to operation free from the threat of whirl flutter. However, the Electra's unfortunate story continued. Several additional crashes have occurred since 1960, with other causes, such as bird strike, pilots' faults, maintenance faults, aircraft overloading or even a pilot's cardiac failure during the critical phase of the flight. A total of 58 of the 170 manufactured aircraft were lost in crashes and other incidents.

3.3 Beechcraft 1900C

The Beechcraft 1900C is a twin-turboprop commuter for 19 passengers that has a wingspan of 17.64 m, a length of 17.62 m and a maximal take-off weight of 7764 kg (see Figure 3.2). The maiden flight was accomplished



Figure 3.2 Beechcraft 1900C aircraft (photo copyright Orlando Suarez, used with permission)

in 1982, and a total of 695 aircraft were manufactured. Currently more than 400 of these aircraft are operated as regional commuters. The military version is marketted as the C-12J Huron. Beechcraft 1900C was the successor of the Beech model 200 that was designed as a pressurised twin turboprop regional commuter and powered by Pratt & Whittney PT6A-65B engines.

A Beech 1900C was involved in an accident in 1991 that was directly caused by whirl flutter. Contrary to the Electras' events, which revealed a new phenomenon, the Beech 1900C crash occurred at a time when the whirl flutter issue was already well known. This is evidence that the whirl flutter phenomenon is still important and in the forefront of aeroelasticity. We will explore the crash in more detail because it demonstrates the importance of the regulatory requirements to analyse failure states and also because of the interesting facts that accompanied the investigation.

On 28 December 1991 Business Express Airlines' 1900C crashed into the ocean off the coastline of Block Island in Rhode Island during a training mission. All three people aboard (the pilot trainer and two pilot trainees) were killed. Initially the investigation conducted by the NTSB [2], [3] assessed the cause as the pilot's loss of spatial orientation during the sharply descending flight. However, this conclusion was later questioned, and the follow-up investigation by the ALPA (Airline Pilots Association) [4] determined the true cause to be whirl flutter. The ALPA's investigation found that the structural failure occurred early during the flight. First, the starboard nacelle tore away and rammed into the horizontal tail. Consequently, the outer part of the starboard wing was torn away, the aircraft started to pitch and roll and finally fell into the ocean upside down. Several parts of the wreckage were recovered; unfortunately the black boxes were not found. In addition to the other things the investigators used to explain the causes and the course of the events, the voice record from the cabin was used. This record contained acoustic signals indicating the late stage of growing fatigue cracks and the subsequent structural destruction [5]. The voice record was closely scrutinised, and the specific frequency peaks characteristic of whirl flutter and the propellers were evaluated. Also important was the fact that the record did not contain any pilots' voices indicating the stress situation, so the destruction was suspected to have occurred rapidly with no warning.

It was already known that whirl flutter should not occur on an undamaged structure. Therefore, the ALPA initiated a large study of the 1900C's operational reliability. The characteristic fatigue life of the engine bed structure was analysed and reports of the structure checks

were assessed. The evaluation found fatigue cracks on six elements of the engine mounting. More than 70 cracks were documented, as well as the complete failures of the engine bed truss by one airline company. Although the interval between the engine bed checks was 100 hrs, as many as eight cracks were found during one check alone. Defects were found on the engine mount isolators as well. The study included a statistical evaluation of the failure modes, dealing with the danger and probability of the occurrence of particular failure modes.

The reliability study evidenced a much lower fatigue life of the engine mount with respect to the design life. The fatigue life of the most frequent operational mode was found to be 4282 hours, which was far removed from the design life of 30 000 hours.

Both the cracks on the engine bed truss and defects of the engine mount isolators may contribute to whirl flutter. Further activities were focused on this possibility. Analyses demonstrated that whirl flutter cannot occur if the engine bed is undamaged. However, considering the failure modes, the whirl flutter speed decreases, and flutter may occur inside the flight envelope at a speed of 96–250 knots and a frequency of 0.7–1.0 Hz. According to the radar record, the flight velocity of the aircraft at the moment of destruction was approximately 185–195 knots.

3.4 Other aircraft

Whirl flutter may have been a contributing factor of some other aircraft crashes that are outlined. One example is the twin-engine amphibious aircraft Grumman Turbo Mallard GF73T that crashed on 19 December 2005 shortly after take-off in Florida's Miami harbour and after losing the starboard wing during the flight. All 20 people aboard were killed. The cause was investigated as a fatigue crack in the aft wing's spar. The Mallard was designed shortly after the war, and some of them were later remotorised with Pratt & Whitney R-1340 or PT-6A-34 turboprop engines. The wing structure was not designed with regard to the modern fatigue philosophies, and it would be feasible that vibrations originating in the whirl mode might contribute to the propagation of wing fatigue cracks.

Another example is the twin-piston engine aircraft accident on 20 June 1997. The investigation after the crash [6] found the failure on the left engine mount truss structure. Despite that the most threatened aircraft category is the turboprops, with respect to the large rotating parts of the

gas turbine engines and heavy propellers, whirl flutter may also occur on piston engine aircraft. Again, failure of the engine mount is the key contributing factor.

3.5 References

1 Donham, R.E. and Watts, G.A.: 'Whirl flutter first case', in *The Revolution in Structural Dynamics*, ISBN 0-9659773-0-7, MIT memorial book to Dr Raymond Bisplinghoff (editor Dr Hugh Flomenhoft), 1997.

2 National Transportation Safety Board, Washington, D.C. 20594, Aircraft Accident / Incident, Summary Report: Loss of Control Business Express, Inc. Beechcraft 1900C N811BE Near Block Island, Rhode Island, December 28, 1991, adopted April 27, 1993.

3 Editorial Staff Report: Fatal Commuter Training Flight Cash Blamed On Spatial Disorientation, Poor Judgment, Flight Safety Foundation, *Accident Prevention*, Vol. 50, No. 10, October 1993.

4 Airline Pilots Association Report, Beechcraft 1900C N811BE, 1992.

5 Stearman, R.O., Schulze, G.H., Rohre, S.M. and Buschow, M.C.: 'Aircraft Damage Detection From Acoustic Signals Found By A Cockpit Voice Recorder', Acoustical Society of America 133rd Meeting, State College, PA, USA, 17 June 1997.

6 Donham, R.E.: 'Twin Piston Engine Aircraft Whirl Flutter Accident/Analysis', Aerospace Flutter and Dynamics Council Meeting, Sedona, AZ, USA, May, 2002.

This page intentionally left blank

Experimental research on whirl flutter

DOI: 10.1533/9781782421863.41

Abstract: This chapter describes the experimental research on the whirl flutter phenomenon. Includes a chronological list of the primary experimental accomplishments, including the early tests, primary developments in 1960s and recent activities. Both simple propeller models and more complex aircraft models (including tilt-rotor aircraft) activities are included. The descriptions of the experimental hardware, test methodologies, parameters and the main results are provided. Finally, the newly developed whirl flutter demonstrator (W-WING) from the VZLU, Prague is described.

Key words: whirl flutter experiment, whirl flutter demonstrator, wind tunnel, Lockheed Electra II, W-WING demonstrator.

4.1 Introduction

The complicated physical principle of whirl flutter required the experimental validation of the analytically gained results. Experimental research activities were required, especially because of the unreliable analytical solution of propeller aerodynamic forces; in particular, considering the high inflow angles of the tilt-rotor applications the experimental data are irreplaceable.

Another key issue was the influence of structural damping. A paper, reference [1], describes an experiment during which friction was deeply suppressed and whirl flutter occurred. However, the notably slight structural damping made the model stable. This represented important knowledge that whirl flutter is extremely sensitive to structural damping.

The validation of analytical results and obtaining reliable input data for analyses are feasible only experimentally.

The next sections provide a description of the whirl flutter experimental research activities in different time periods. Experimental research on whirl-flutter-related issues started in the 1930s. The primary activities were conducted in the 1960s after the Electras crashes. Recent activities were focused mainly on the tilt-rotor applications. Finally, the newly developed whirl flutter demonstrator (W-WING) is presented.

4.2 Early tests (1930s)

The test activities in the period before the war were focused on researching the aerodynamic interference characteristics among the propeller, nacelle and wing. At that time, the whirl flutter phenomenon was unknown. These tests precede the true whirl flutter tests in the later period when the phenomenon become known.

A report [2] describes the wing-nacelle-propeller interference tests made on the full-scale structures, which were accomplished at NACA Langley in 1936. These tests were intended to validate the previous tests conducted using scaled models. The model included the rectangular wing and the nacelle with the tractor propeller in the centre of the wing. The wing span was variable (4 variants) as well as the nacelle placement (3 variants – central, above and below the wing) – see Figure 4.1.

The nacelle placement was also variable in the chordwise direction. The model was measured using a balance and some pressure sensors. The measurement parameters included velocities up to 100 mph and various angles of attack. The measurements included both rotating and non-rotating propellers. Measurements were intended to assess the efficiency of the propulsion system, nacelle drag and the influence of the nacelle on wing pressure distribution.

The aerodynamic measurement of the propeller was performed at Stanford University [3]. A motor with the constant speed propeller (1800 rpm) on a pylon was attached to a balance (see Figure 4.2).

The forces on the propeller were measured, and the rolling, pitching, yawing and torque moments were evaluated. There were varied velocities, and the propeller yaw angles were up to 30 degrees. The resulting characteristics of the propeller show the slight decrease of the propeller thrust due to the yaw angle up to the angle of 10 degrees. For the angle of 30 degrees, the thrust reduction reached approximately 10%.

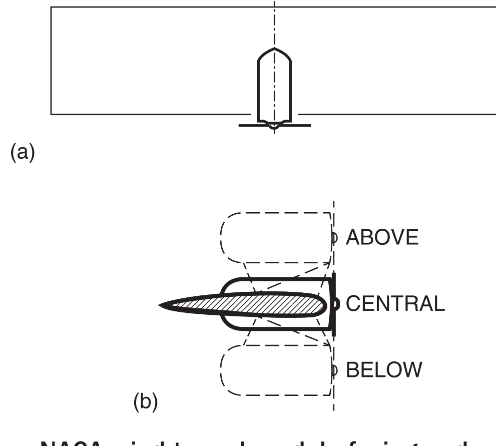


Figure 4.1 **NACA wind tunnel model of wing and nacelle [2]: (a) top-view, (b) side-view**

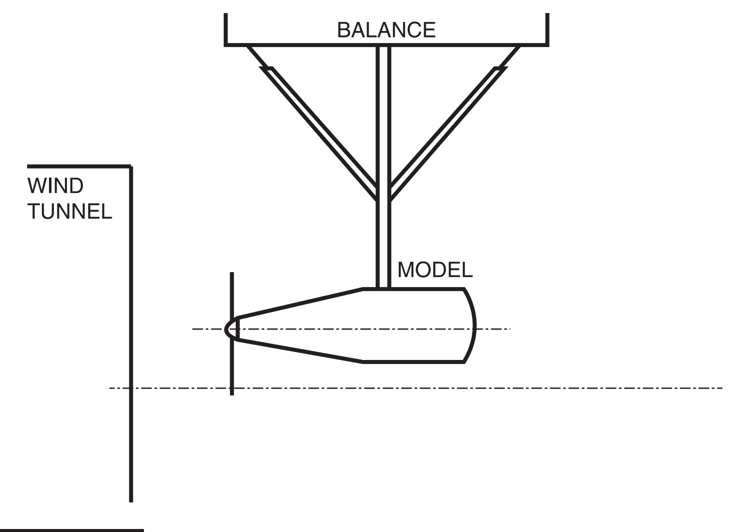


Figure 4.2 **Propeller wind tunnel model [3]**

4.3 Main developments (1960s)

The main developments in the experimental research on whirl flutter were accomplished in the early 1960s in direct connection with the Electras accidents. The experiments are divided into two main categories. In the first category are simple tests on the models of the flexibly attached propeller in the windmilling mode. The second category includes more complex tests on the aircraft models or parts of the aircraft.

4.3.1 Propeller demonstrators

The first experimental investigations of whirl flutter characteristics were accomplished by Houbolt and Reed [4] on the simple model of a propeller in the windmilling mode. The propeller was attached to the rod simulating the engine's inertia. This rod has freedom in the pitch and yaw. The stiffness of the attachment was adjustable by varying the springs and the tension of the springs. The hinge points were adjustable as well. This model is presented in Figure 4.3.

Regarding the pitch and yaw stiffness ratio, the model was close to unity. The experimental whirl flutter boundaries are shown in Figure 4.4 as the dependence of the required stiffness on the dynamic pressure.

The complex investigations were conducted by Bland and Bennett [5] in NASA Langley wind tunnel. They were investigating the aerodynamic forces on the propeller – nacelle model and measured the whirl flutter characteristics. The propeller rotating in the windmilling mode was attached by the shaft through a hinge allowing pitch and yaw with adjustable flexibilities. The propeller blade angles were also changeable. Structural damping was simulated by means of removable rubber blocks. This model is shown in Figure 4.5.

The comparison of the experimental results with theory demonstrated that the theoretical aerodynamic derivatives underestimated the whirl flutter speed. The application of the experimentally gained derivatives

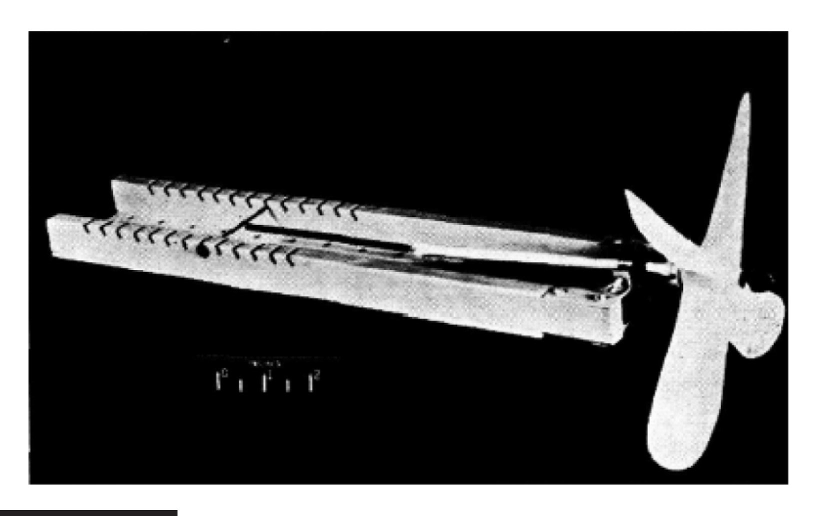


Figure 4.3 Propeller simple wind tunnel model [4]

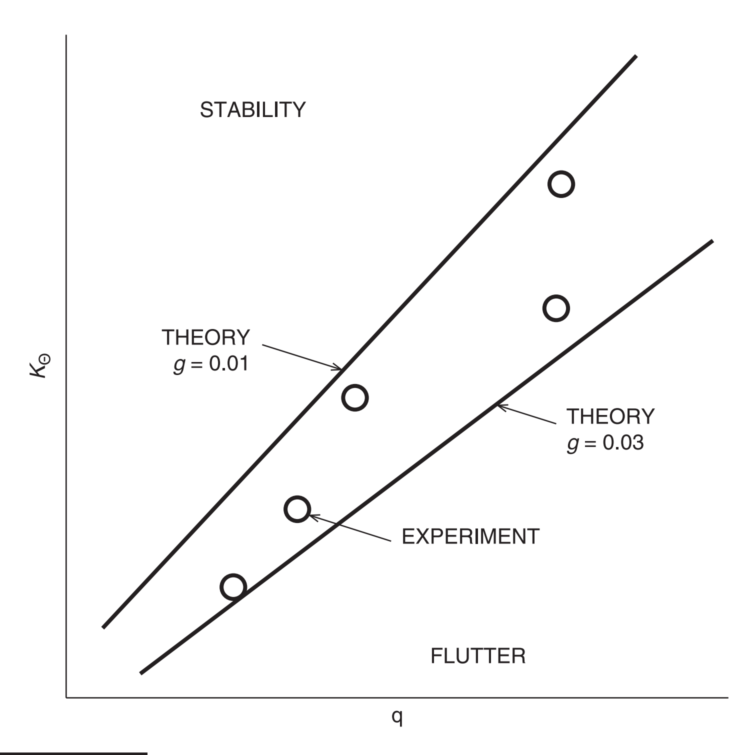


Figure 4.4 Experimental whirl flutter boundaries [4]

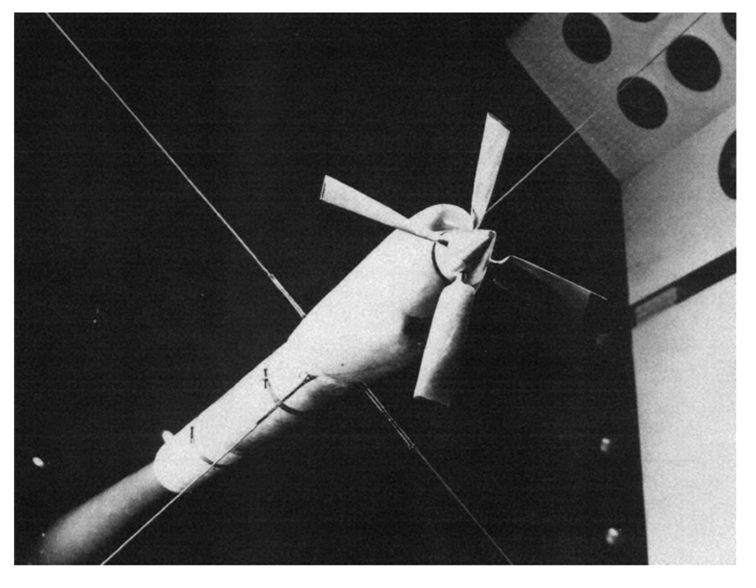


Figure 4.5 NASA propeller wind tunnel model [5]

(excluding the damping force due to the pitch) to the analytical solution made the solution much closer to the experimental results. A viscous model of structural damping was found to be realistic. A comparison of the theoretical and experimental results is provided in Figure 4.6 expressed as the whirl flutter velocity ratio's dependence on the structural damping.

The whirl flutter characteristics of the S/VTOL (tilt-rotor) aircraft were first studied by Reed and Bennett [7]. They focused on the flight regimes of high inflow angles. The results are shown in Figure 2.14. Increasing the inflow angle made the system more stable. This effect is stronger for thrusting propellers compared with windmilling propellers. The study utilised the experimental aerodynamic derivatives of Yaggi and Rogallo [8].

Propellers were rotated in the windmilling mode during the described tests. Windmilling propellers were frequently used, considering the low effect of the propeller thrust on the whirl flutter at high velocities. This effect is expressed in Figure 4.7 as the dependence of the required stiffness on the thrust coefficient. The usage of the windmilling propellers reduced the costs of the test because no motor was necessary.

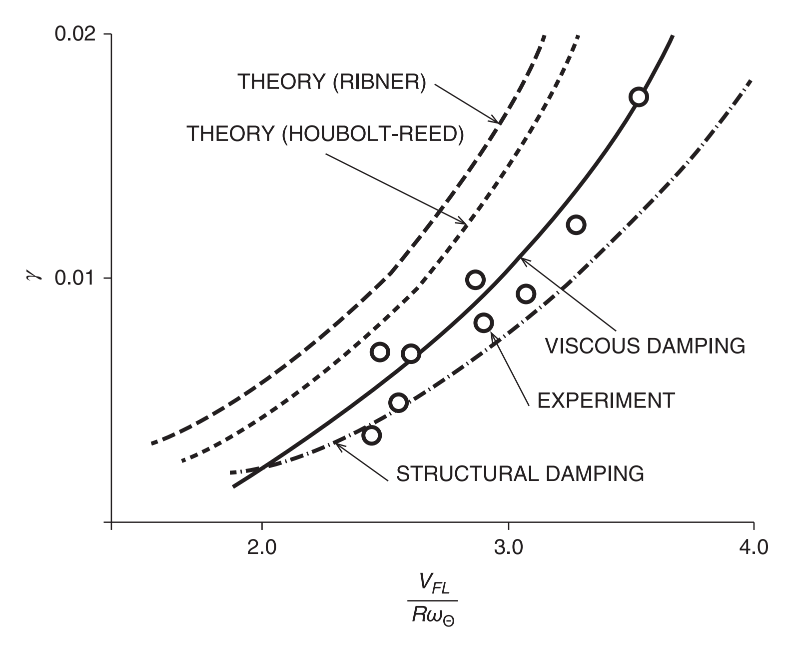


Figure 4.6 **Comparison of experimental aerodynamic derivatives [5] with theory [6], [4]**

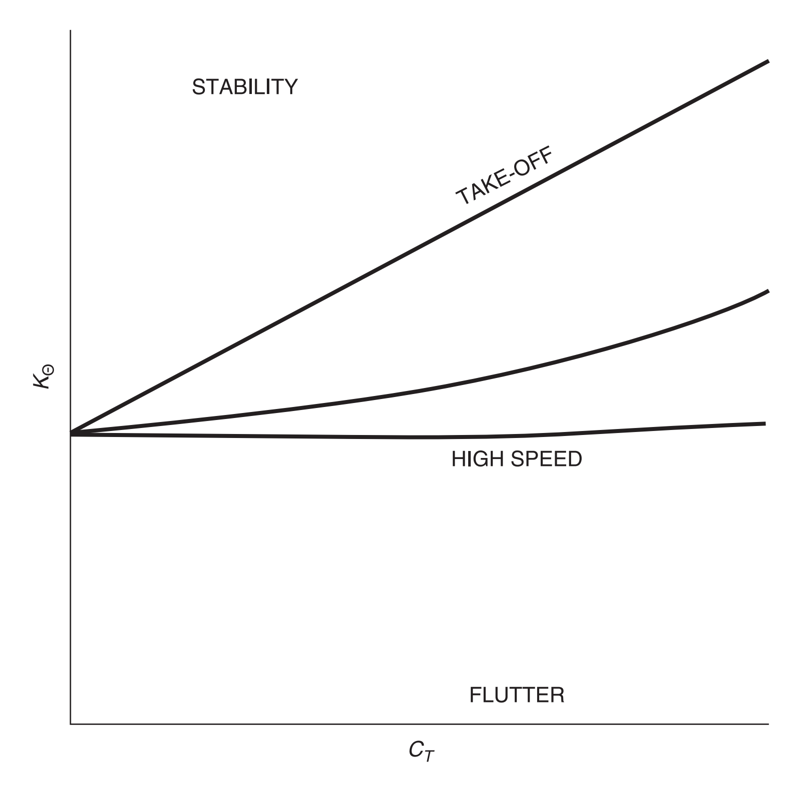


Figure 4.7 **Effect of thrust to whirl flutter stability [7]**

The above-mentioned models were equipped with rigid propellers. However, as mentioned in Chapter 2, some applications require an addition to account for the blades' flexibility. The experiment on the simple model with flapping blades is described in [7]. The model shown in Figure 4.8 was similar to the model shown in Figure 4.3.

Each blade was attached to the hub by two pins. If one of these pins was removed, the blade began to flap, with the hinge at the remaining pin (8% or 13%), whereas the use of both pins together made the blade fixed. During the test, both backward and forward whirl mode instabilities occurred. For the 13% hinge offset the instability had the characteristics of the backward whirl mode, whereas the 8% hinge offset resulted in forward whirl mode instability. In comparison with the fixed blades, the effect of the blades flapping was significantly stabilising for the former mode and destabilising for the latter mode. Both are presented in Figure 4.9 as the dependence of the required stiffness on the dynamic pressure.

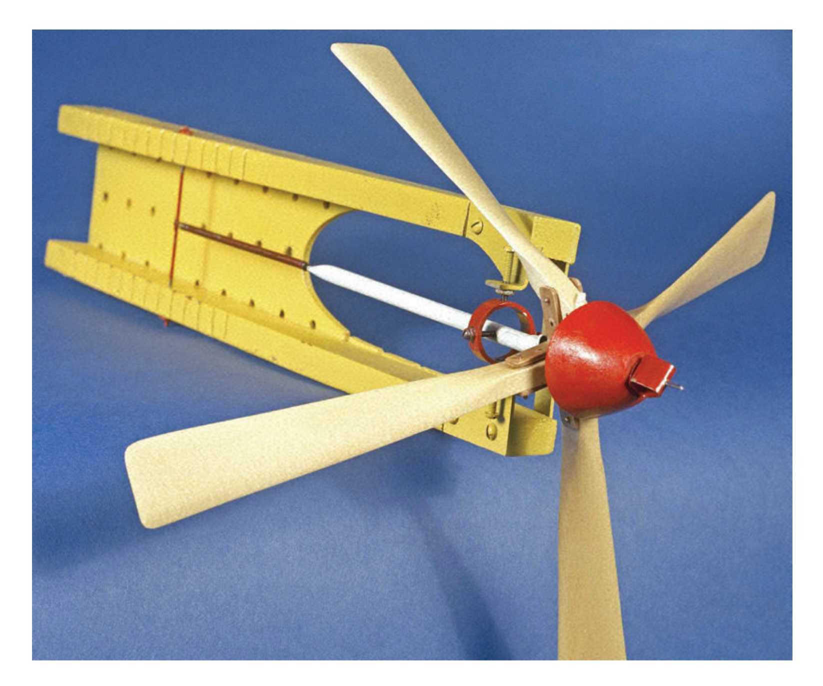


Figure 4.8 **Hinged blades propeller wind tunnel model [7]**

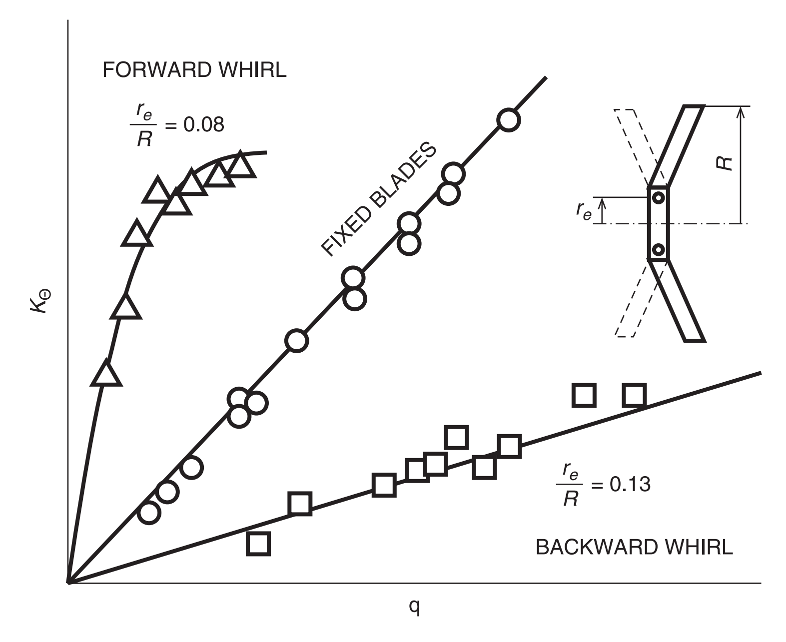


Figure 4.9 **Effect of blades flapping to whirl flutter stability [7]**

In addition, it was observed that backward instability can be predicted by linear theory, and forward whirl instability is characterised by the amplitude limited motions that may become excited when the disturbing force exceeds a specific threshold.

Note that the forward whirl instabilities were obtained by introducing a large phase lag between the displacement of the propeller axis and the associated aerodynamic forces on the blades as high as 45 degrees, which could not be rationally justified at that time. Later on, Donham [9] described that the phase angle of 25 degrees due to the blade dynamic response may be increased to 40–45 degrees because of the aerodynamic time delay. Such a phase angle produces a significant negative stiffness effect, which may also reduce the rotating stiffness. However, the typical bending and torsional stiffnesses result in much higher blade frequencies than represented by the tested model.

Other experiments of the flapped blade rotor system were performed by Krishna Rao and Sundararajan [10] in NAL Bangalore. The model of the rotor with four blades and the windmilling propeller was designed similarly to the formerly mentioned one, that is, the blades could be either locked or enabled to flap about any of the pins. The rotor was connected to the nacelle with the freedom to pitch and yaw about a set of gimbal axes. This model is shown in Figure 4.10.

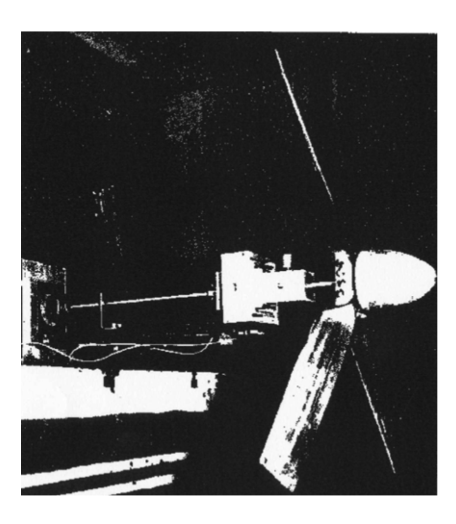


Figure 4.10 **NAL hinged blade propeller model [10]**

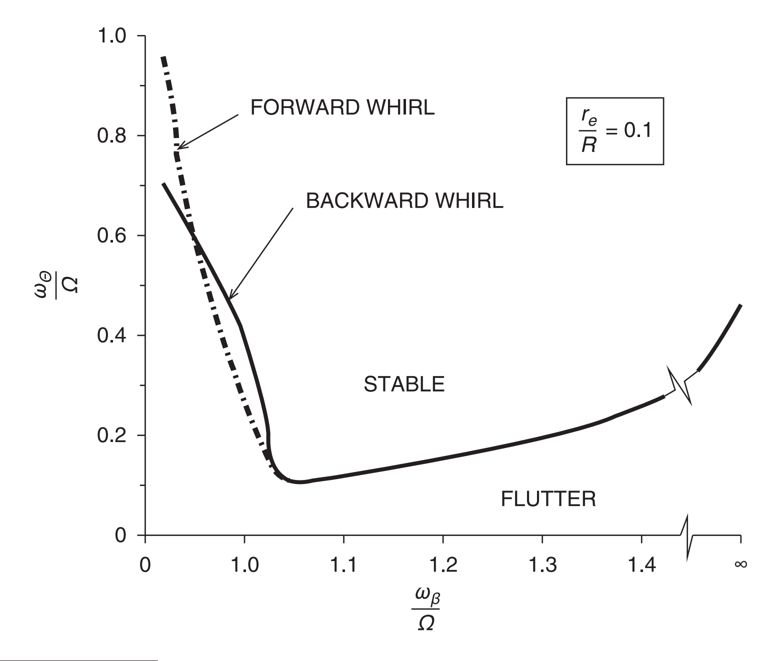


Figure 4.11 **Effect of blades flapping to whirl flutter stability [10]**

The low-speed wind tunnel experiments included three blade flapping hinge offsets. The results showed that starting from the rigid blade, the reduction of the flapping frequency decreased the nacelle frequency required for neutral stability. The flutter occurs in the backward mode. Provided that the flapping frequency to propeller revolutions ratio decreases roughly under 1.05, the backward whirl is followed by the forward whirl mode, and further reduction of the flapping frequency makes the forward whirl mode dominant. The flapping frequency of this transition increases as the hinge offset decreases. An example of this dependence is shown in Figure 4.11. Comparing the theoretical results with the experimental results, the theory considering rigid blades was found to be conservative (experiments above theory), whereas the results considering hinged blades were found to be unconservative (experiments below theory).

4.3.2 Aircraft demonstrators

The experimental investigations of whirl flutter characteristics were not limited only to the propeller demonstrators. Further investigations were

performed also employing demonstrators representing parts of the aircraft, and even the complete aircraft structure.

An experimental and analytical investigation of the power plant on the flexible wing was accomplished by Bland and Bennett [11], [5] in the NASA Langley wind tunnel. They used the model of the semispan wing with a single nacelle with a power plant and 4-blade windmilling propeller (see Figure 4.12). The model consisted of an aluminium spar with a varying cross-section modelling the stiffness and a balsa sectional structure to approximate the airfoil outline. The model also included the simulated half-cross-section of the fuselage. The engine model included four different configurations of the engine attachment varying the engine mass and the pitch and yaw stiffnesses. The model did not represent any specific aircraft; however the structural parameters were realistic. The measurements included variations of the noted parameters as well as two levels of damping. The results were compared with the results for the isolated nacelle model (see Section 4.2.1). The results showed a low effect of the wing structure on the whirl flutter boundaries. However, this is not typical; this low effect was caused by the fact that the nacelle was placed rather inboard because it was adapted from the former four-engine aeroelastic model [12]. Moreover the stiffness of the wing root part was rather high.

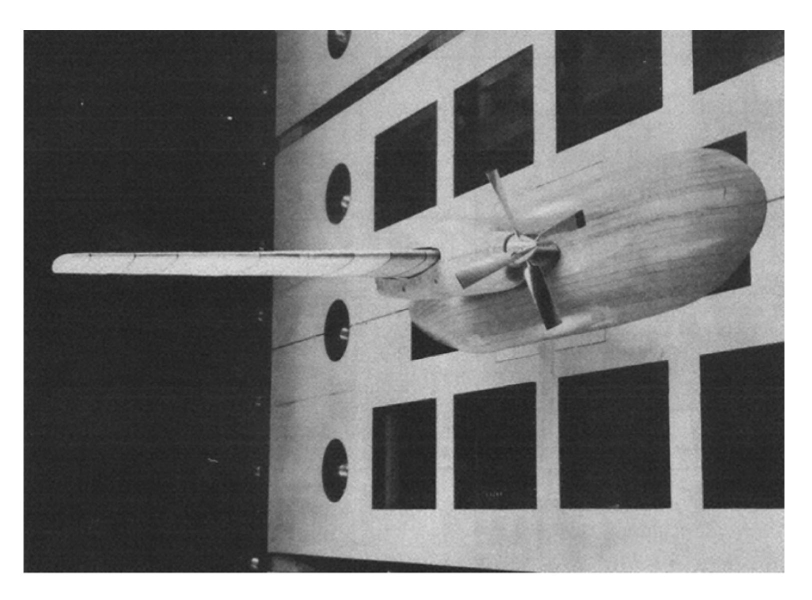


Figure 4.12 Semispan wing/engine component model (NASA Langley) [11], [5]

The largest experimental campaign was conducted using the aeroelastic model of the L-188 C Electra II aircraft. As mentioned in Chapter 3, this aircraft became famous due to the first occurrence of whirl flutter during its flight and the subsequent crashes of two aircraft in 1959 and 1960. After these events, additional experiments, including the whirl effect, were performed. These tests helped to determine the whirl flutter as the cause of the accidents. The experiments are summarised by Abbott, Kelly and Hampton in reference [12]. The aeroelastic model represented a full-span aircraft due to the investigation of the unsymmetrical phenomena. The model included four nacelles and propellers. The power plants were attached with independently variable pitch and yaw stiffnesses. The mass and inertia characteristics were fixed, simulating the relevant power plant characteristics. Four blade propellers were rotated in the windmilling mode. The wing structure was created as usual for the aeroelastic scaled models. The stiffness was simulated by an aluminium beam and the inertia by means of lead weights. The aerodynamic shape was created by a sectional balsa structure. The ailerons and flaps were not modelled. A similar structure was used also for the fuselage and the empennage structure. The model's characteristics represented regular aircraft, including the levels of fuel loading. The all-movable horizontal tail was remotely controlled and used as longitudinal trim. The vertical tail was not movable. The model could have been excited by electrically driven eccentrical weight in one of the engines or by the small aerodynamic oscillators placed at the horizontal tail tips. Another option was external excitation.

During the measurements, the model was flown with sufficient lift. The measurement was started with the model on the bottom wind tunnel wall. As the airspeed increased the model took-off and started to fly. At the same time, the trimmed flight was maintained by an operator controlling the horizontal stabiliser. The vertical motion was restrained and damped by the attachment rod and system of wires. The model during the wind tunnel measurement is shown in Figure 4.13 and Figure 4.14.

The measurement campaign included various combinations of the structural parameters. Note that the measurement regimes were limited by the windmilling propellers. The major tests were aimed at identifying the causes of the aircraft accidents; therefore various configurations with the reduced starboard outboard engine stiffnesses were performed. States with the reduced damping were also tested. The reduced stiffness parameters were also tested on the inboard power plant, and the combination of two engines was also tested. The variations in the

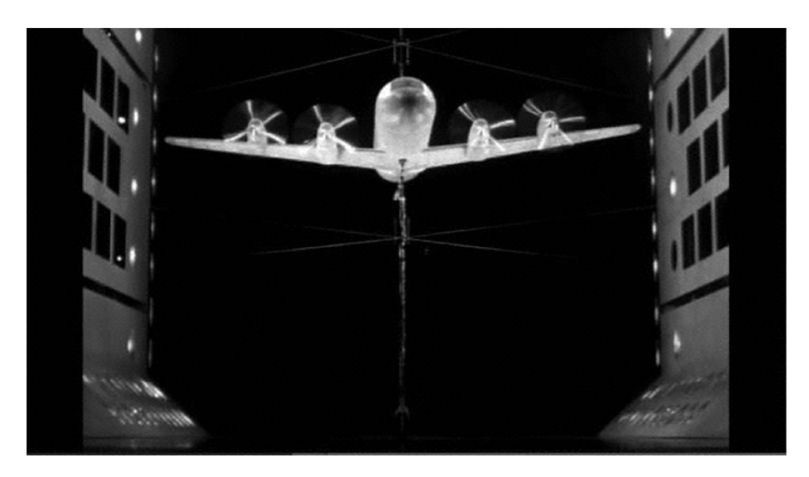


Figure 4.13 L-188 C Electra II aeroelastic model WT measurement (NASA Langley) [12]

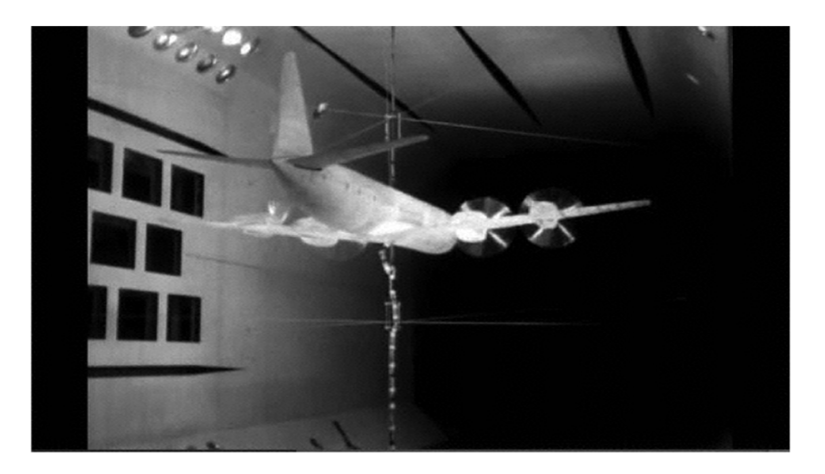


Figure 4.14 L-188 C Electra II aeroelastic model WT measurement (NASA Langley) [12]

structural damping for particular engines were also taken into account. In addition, measurements under the condition of inboard propeller overspeed were performed.

The results of the tests demonstrated the destabilising effect of the reduced stiffness of the engine attachment. Figure 4.15 shows the influence of the stiffness on the whirl flutter stability. With regard to

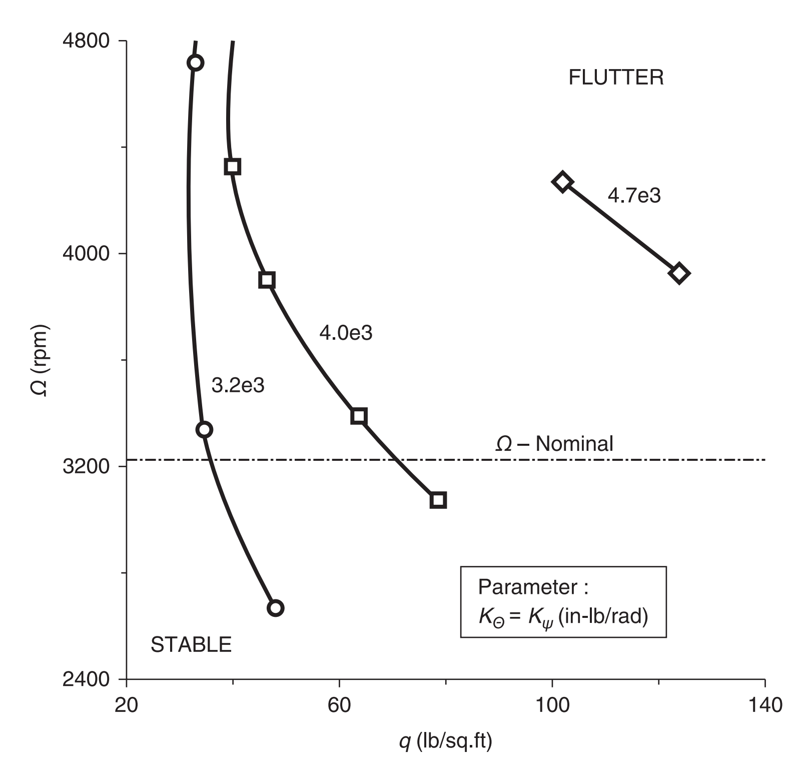


Figure 4.15 **Effect of stiffness reduction on the whirl flutter boundary for the starboard outboard engine, $(K_{\Theta}/K_{\psi})=1.0$; $g=0.014$ [12]**

the propeller, the windmilling mode is expressed as the dependence of the critical dynamic pressure on the propeller revolutions with the parameter of stiffness.

Although the problem of both crashed Electras was caused by the outboard engine, the inboard engine was found to be more sensitive to the reduction of the stiffness with respect to the whirl flutter stability. The worst case is the reduction of stiffness of multiple engines. Figure 4.16 shows the influence of stiffness reduction of different engines (starboard outer, starboard inner and both starboard engines) considering the different stiffness ratios. The influence is expressed as in previous examples.

Structural damping was also found to be an important contributing factor, as documented in Figure 4.17. The stability boundaries are expressed also as the dependence of the critical dynamic pressure on the propeller revolutions.

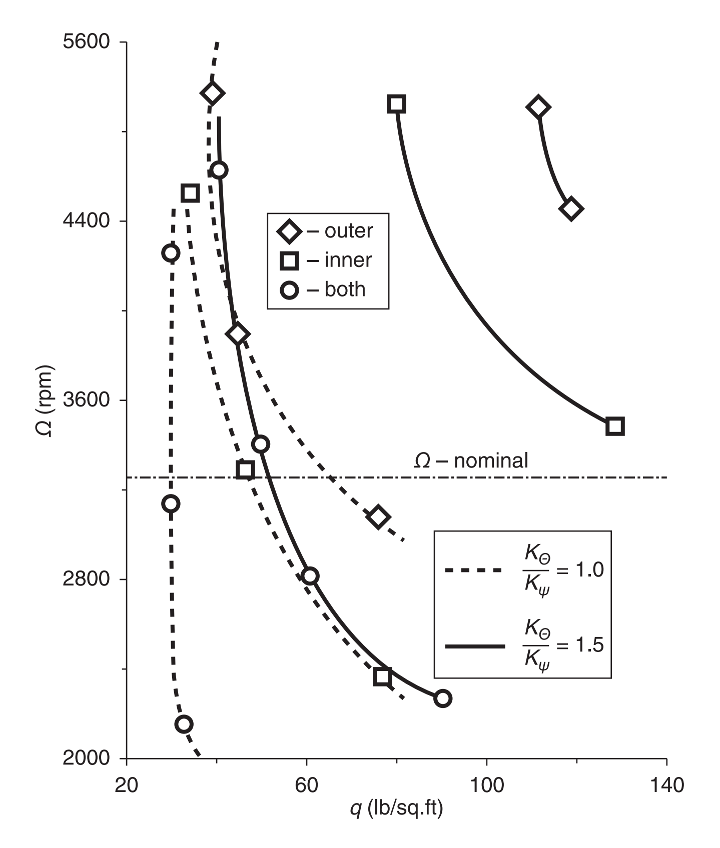


Figure 4.16 Effect of stiffness and damping reduction (K_Θ – 67%; g – 35% of nominal) on the whirl flutter boundary for various starboard engines, $(K_\Theta/K_\psi) = 1.0$ or 1.5 [12]

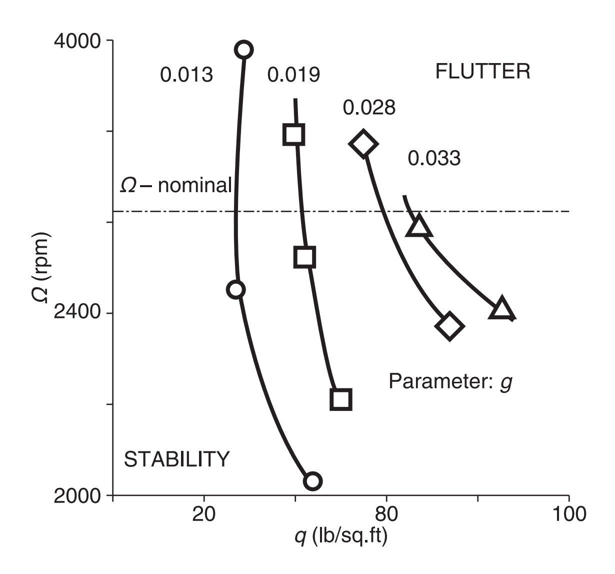


Figure 4.17 Effect of structural damping on the whirl flutter boundary, $K_\Theta = 3.6e3$ [in-lb/rad]; $(K_\Theta/K_\psi) = 1.8$ [12]

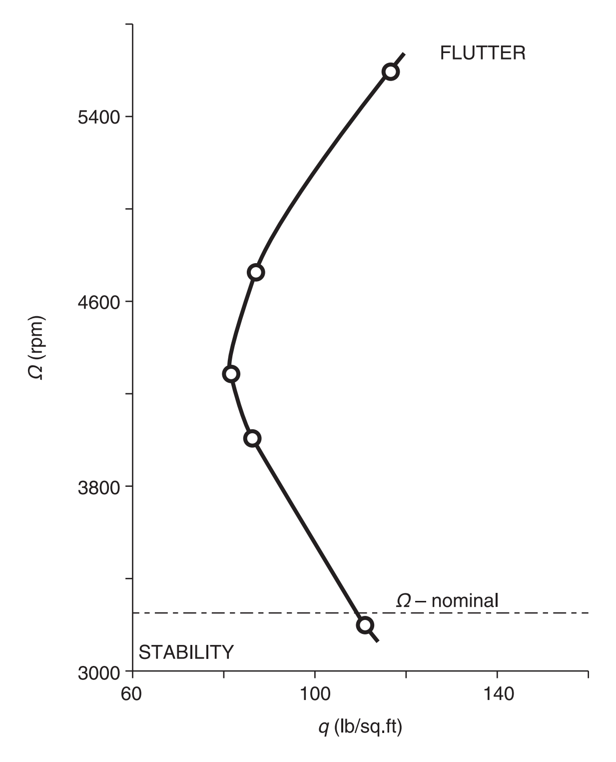


Figure 4.18 Effect of starboard inner propeller overspeed on the whirl flutter boundary (others at nominal rpm) [12]

Finally, Figure 4.18 shows the influence of the propeller overspeed, which was also found to be the destabilising factor.

During the test campaign many other tests were performed to investigate the level of fuel, etc. Low fuel levels were found to be less stable compared with full fuel loading. This fact is related to the influence of the wing modes on whirl flutter stability.

4.4 Recent activities

The activities in the experimental research on whirl flutter performed in the early 1960s as described in Section 4.5 were aimed at describing the fundamental characteristics, influences of parameters and other facts of the new phenomenon at that time. This section describes later experimental activities that are primarily focused on more specific issues, especially

those connected to the tilt-rotor aircraft applications, such as the Bell XV-3 or XV-15, Bell-Boeing V-22 Osprey, Agusta-Westland AW609, and XC-142A [13], [14]. The experiments are divided into two main categories. In the first category, there are tests on the propeller (or prop-rotor) models, and the second category includes experiments on the tilt-rotor aircraft component or complete models.

4.4.1 Proprotor demonstrators

The investigation of the prop-rotor with flapping blades was conducted by Kvaternik and Kohn [16]. As mentioned in Section 4.2.1, earlier experimental studies of the propeller with flapping blades found forward whirl mode instabilities, for which the blade flexibility had a significant destabilising effect compared with rigid blades. The motivation of further work was the necessity to establish an experimental database for prop-rotor whirl flutter prediction with sufficient confidence. The model was derived from the existing aircraft [16] aeroelastic model. The model included the prop-rotor with a nacelle attached to the wing structure. The prop-rotor was rotated in the windmilling mode. The model included four degrees of freedom – blade lateral flapping, blade in-plane flapping, nacelle pitching and nacelle yawing. The model also included the kinematical coupling of the nacelle pitch and blade flapping to reduce the latter. The blades were equipped with pins that formed the flapping hinge offset. With respect to actual aircraft, the stiffness of the nacelle attachments were reduced to reach the flutter boundaries within the low speed velocities. Therefore, the effect of the wing structure was eliminated, as the wing was stiff enough in comparison with the nacelle modes. In addition, the wing structure's airfoil coating was removed; thus, the wing generated no aerodynamic forces. In fact, the model represented an isolated prop-rotor with a nacelle. The variable parameters were the nacelle pitch and yaw stiffnesses, parameters of the kinematic pitch-flap link attachment and the blade hinge offset. The model in the wind tunnel test section is shown in Figure 4.19.

The wind tunnel measurements included the properties of the actual aircraft, and parametric studies were performed. A total of 50 forward whirl flutter states and 26 backward whirl flutter states were found. The backward mode of the whirl flutter appeared at low frequencies near the blade flapping (rotor mode), whereas the forward whirl mode occurred at higher frequencies near the nacelle pitch or yaw (nacelle mode). The resulting flutter states are summarised in Figure 4.20.

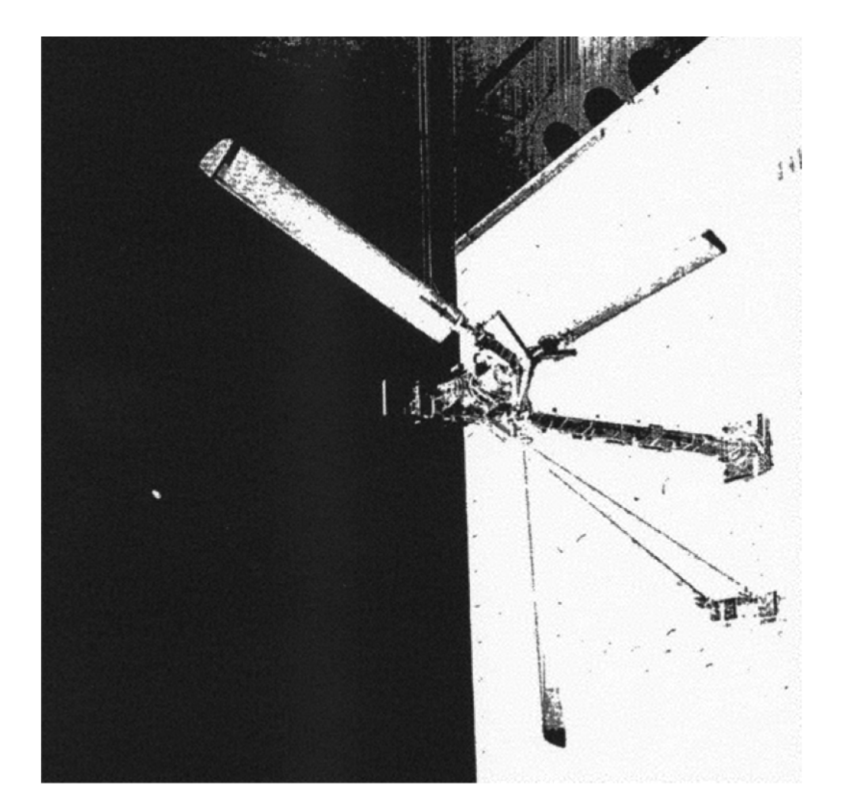


Figure 4.19 Flapping blades proprotor wind tunnel model [16]

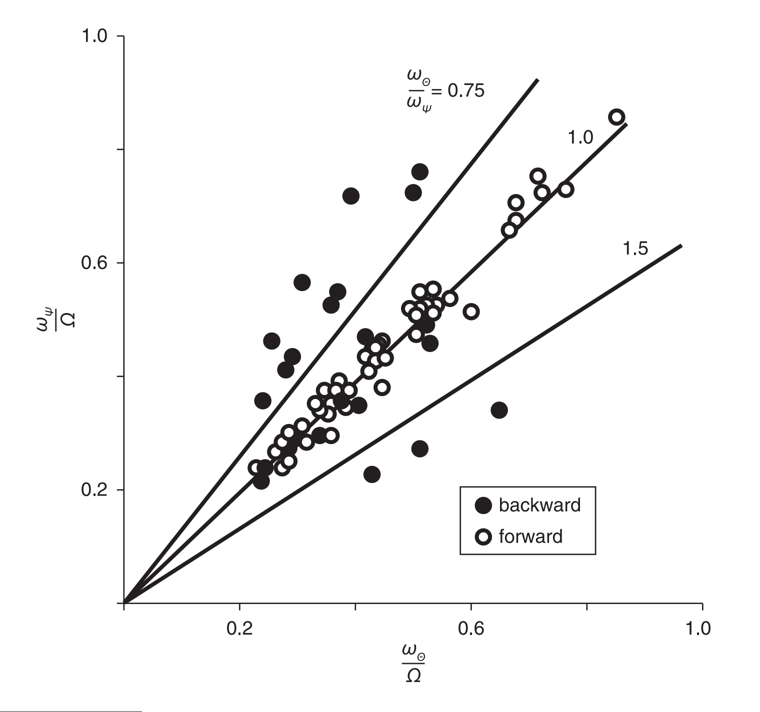


Figure 4.20 Flapping blades prop-rotor – results summary [16]

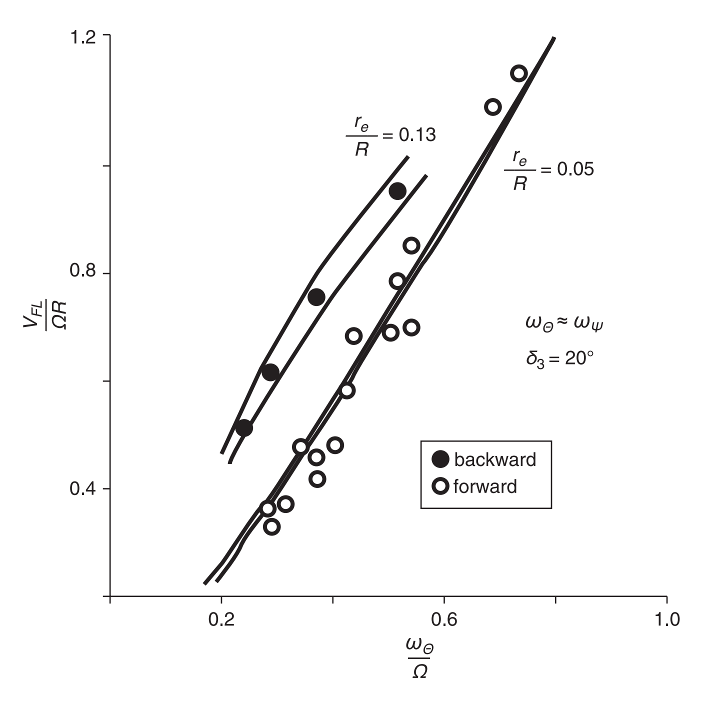


Figure 4.21 **Flapping blades prop-rotor results – influence of blade flapping hinge [16]**

The various dependences of the parameters on the whirl flutter were evaluated. Figure 4.21 summarises the effect of the blade flapping hinge offset. Considering the pitch / yaw stiffness ratio of unity, the low offset ratio causes the forward whirl mode instability, whereas the high offset ratio causes the backward whirl mode instability (for comparison see Section 4.2.1).

However, the character of the whirl mode is affected by other parameters as well, for example the stiffness ratio, as demonstrated in Figure 4.22

During the experiments, the influence of many further parameters were evaluated, e.g., pitch-flap coupling, etc. Some of the influences of damping were also evaluated, although most of the experiments included very low structural damping. The experimental results were compared with the analytical results predicted by the linear methods with quasi-steady aerodynamics. The agreement of the results was found to be quite good, as is apparent in the figures.

A very simple table-top model was used by Acree, Peyran and Johnson [17]. The model included a two-blade balsa windmilling rotor (see Figure 4.23). Windflow was provided by the fan. The model included

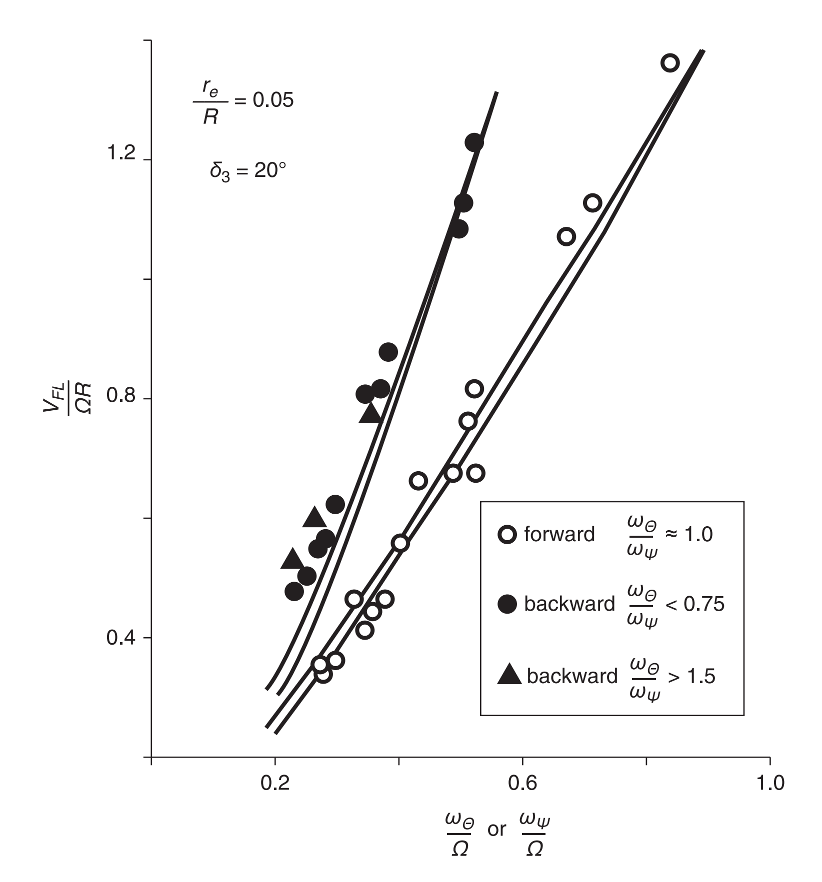


Figure 4.22 Flapping blades prop-rotor results – influence of stiffness ratio [16]

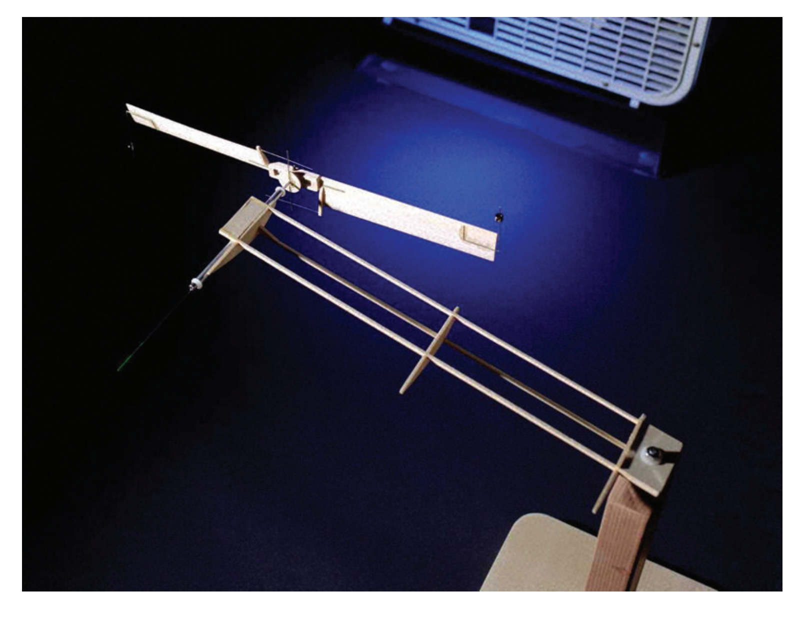


Figure 4.23 Simple table-top prop-rotor model [17]

weights in front of the leading edge of the blades' tips. Moving the weights chordwise produced significant changes in the whirl mode stability.

Further studies are represented by the experiments performed by Rand and Peyran [18]. The demonstrator included the prop-rotor in the windmilling mode attached to the wing structure; however the wing included only the structural dynamic characteristics and, it did not generate aerodynamic forces. The model allowed the variation of the beamwise / chordwise bending characteristics by means of tilting the wing and beamwise bending / twist characteristics by moving the nacelle. In fact it simulated the nacelle pitch, yaw and plunging motion. The prop-rotor axis was in the horizontal position at any time. The demonstrator that did not represent any actual aircraft structure is shown in Figure 4.24. The tests were aimed at assessing the effects of the noted structural characteristics couplings to the whirl flutter of the prop-rotor during forward flight and the possibility of suppressing the instability by means of the active control of the wing's structural characteristics.

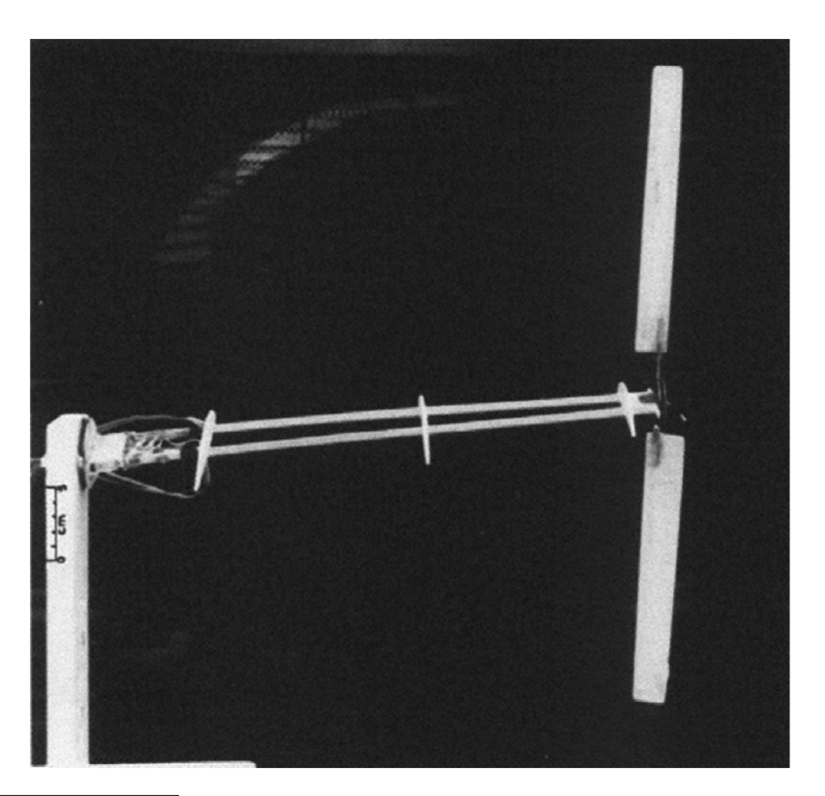


Figure 4.24 Prop-rotor model [18]

The more complex prop-rotor model was tested at DNW wind tunnel in the Netherlands [19]. The demonstrator included a four-blade windmilling prop-rotor and nacelle attached to the wing structure by springs. Both springs exhibited structural non-linearity given by the narrow operational range of springs. The wing structure was represented by the beam simulating the wing bending. The wing torsion was simulated by the pair of springs. The demonstrator was equipped with an excitation system located in the nacelle consisting of a pair of unbalanced masses. The demonstrator's installation is shown in Figure 4.25. The experimental



Figure 4.25 Four-blade prop-rotor model [19]

results included the structure's responses in certain combinations of parameters (windflow and rotor revolutions).

A similar experiment on the three-blade gimballed windmilling prop-rotor is outlined by Mueller and co-workers in reference [19]. The model is shown in Figure 4.26.

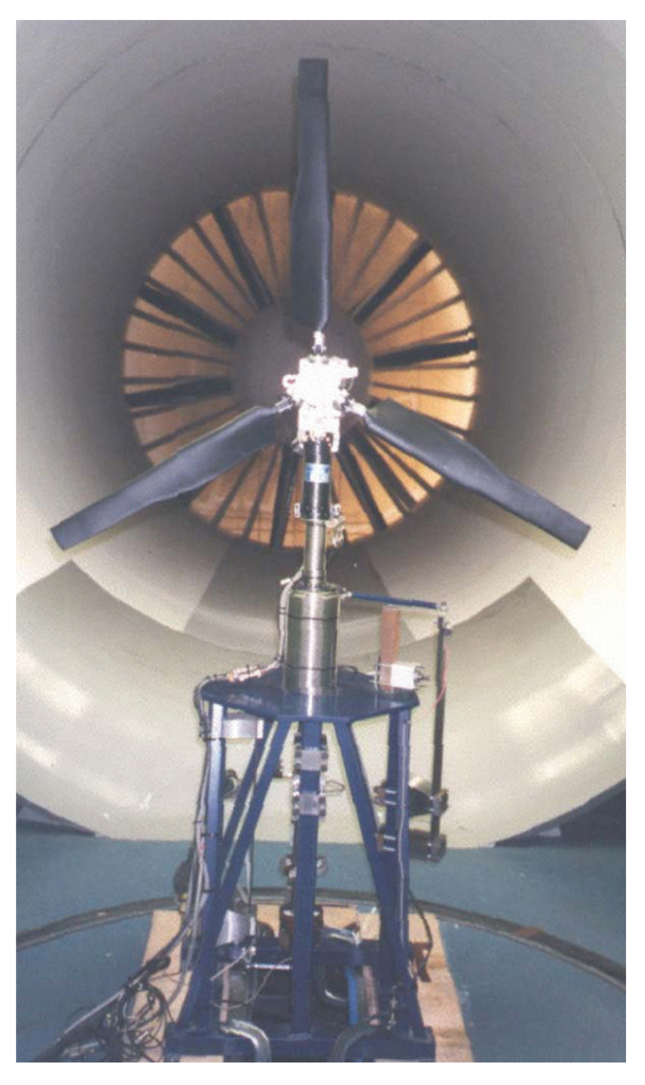


Figure 4.26 **Three-blade prop-rotor model [20]**

4.4.2 Tilt-rotor aircraft demonstrators

The experimental activities performed on aircraft components or on complete models were connected especially with the development work of the specific aircraft type. Most of the activities were conducted at NASA Langley. An in-depth review of this work is given, e.g., in reference [21]. As an example the work on the WRATS (Wing and Rotor Aeroelastic Test System) is presented here. WRATS-related activities are summarised by Piatak, Kvaternik *et al.* [22] or by Nixon *et al.* [23]. The model was based on the 1/5 size semispan aeroelastic model of the V-22 Osprey aircraft. The model was used during the development of the Osprey to improve the stability characteristics of the aircraft. Later on, the model was modified and utilised as the research demonstrator for active control research. The model included a windmilling prop-rotor connected to the wing structure and a half-cross-section of the fuselage. The rotor attachment allowed testing in both forward and hovering flight regimes. The rotor blades included the flapping degree of freedom as well. The model in the wind tunnel measurement section is shown in Figure 4.27.

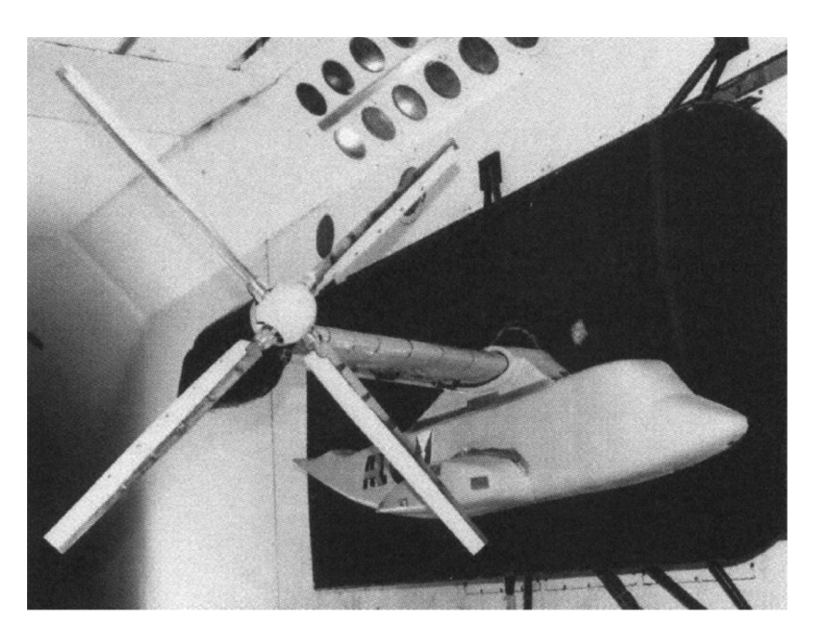


Figure 4.27 WRATS tilt-rotor aircraft component model [22]

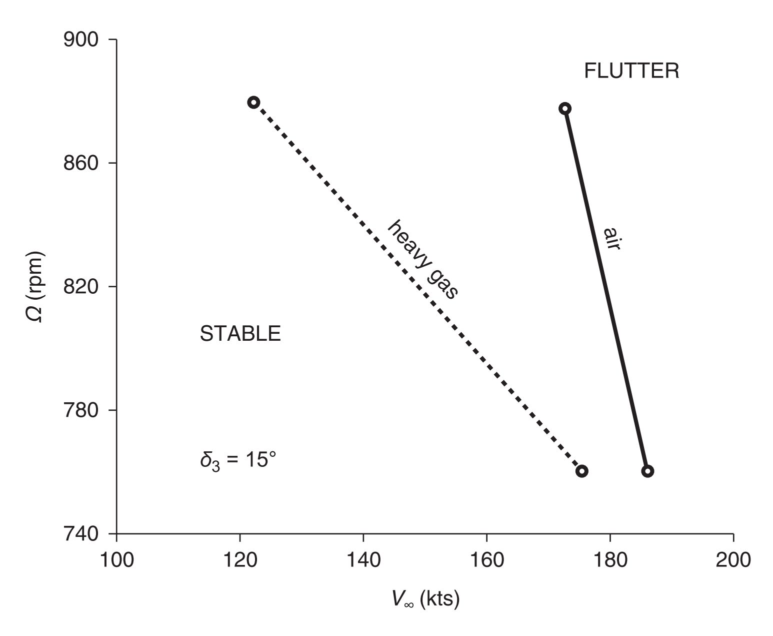


Figure 4.28 **WRATS measurement results – influence of WT medium [22]**

The WRATS tests were aimed at validating the analytical methods. These methods included the measurement of the baseline configuration and, following that, additional tests varying the rotor design variables, control system stiffness and pitch-flap coupling. The tests were conducted in both air and heavy gas wind tunnel test mediums. The aim of the heavy gas tests was to quantify the Mach number compressibility effect on the tilt-rotor system stability. Increasing the pitch-flap coupling was found to be destabilising, while the control system's stiffness had a small effect. As an example of the results, Figure 4.28 shows the comparison of both air and heavy gas measurements. As apparent from the figure, the effect of the Mach number was found to be destabilising.

4.5 W-WING whirl flutter demonstrator

The last section of the whirl flutter experimental research chapter describes one of the latest developments represented by the W-WING (Whirl-Wing) aeroelastic demonstrator developed by VZLU Prague. The demonstrator was adapted from the former aeroelastic model of the



Figure 4.29 L-610 commuter aircraft (photo copyright Aircraft Industries, a.s., used with permission)

L-610 commuter aircraft for 40 passengers (see Figure 4.29) developed by the Let Kunovice (currently Aircraft Industries) Company. The scale of the length of the aeroelastic model was 1/5, and the velocity scale was 1/6.

The aeroelastic model of the aircraft was used during the development of the aircraft for assessment of the flutter and the aeroelastic dynamic response issues. The complete model was tested at the T-104 wind tunnel (7 m diameter) in TsAGI, Russia (see Figure 4.30). The models for the wing component and tail component were tested at the VZLU wind tunnel (3 m diameter).

The starboard wing with a span of 2.56 m including the engine was later utilised as the research demonstrator (see Figure 4.31). This demonstrator no longer represents the aircraft due to the structural changes since then. Nevertheless, the structural parameters have been kept realistic.

The wing structure is modular. The wing stiffness is modelled by the duralumin spar with the variable H-cross-section; the aileron stiffness is modelled by the spar with a variable rectangular cross-section. The inertial characteristics are modelled by lead weights. The aerodynamic shape is covered by the modular balsa and paper segments (14 for wing and six for aileron). The aileron is actuated by the hydraulic actuator placed at the wing root via a push-pull rod. The aileron actuation stiffness is modelled by the steel spiral spring (see Figure 4.32). The aileron can

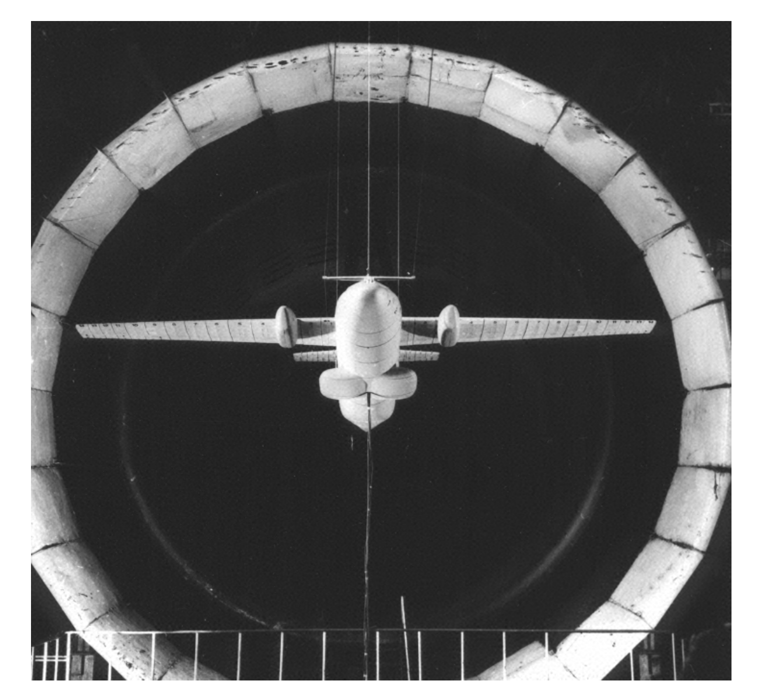


Figure 4.30 L-610 complete aeroelastic model at TsAGI T-104 wind tunnel test section

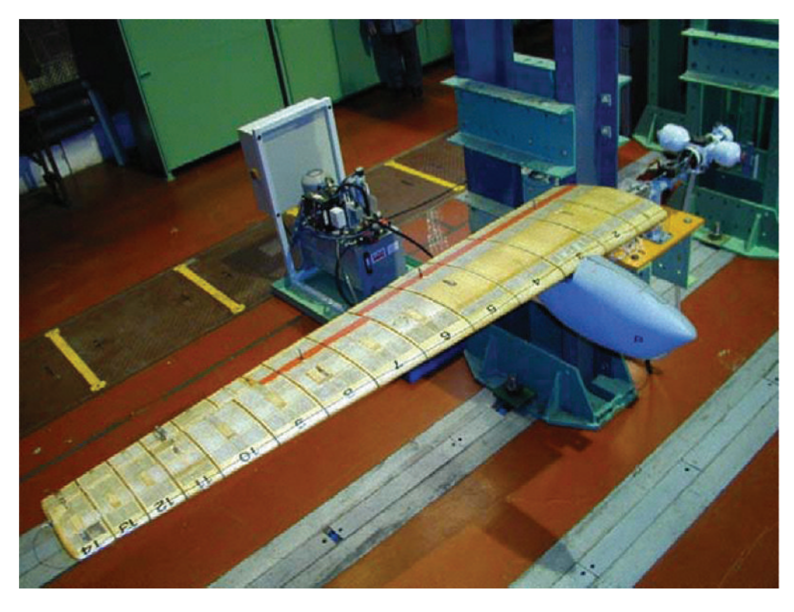


Figure 4.31 L-610 aeroelastic model starboard wing / engine component

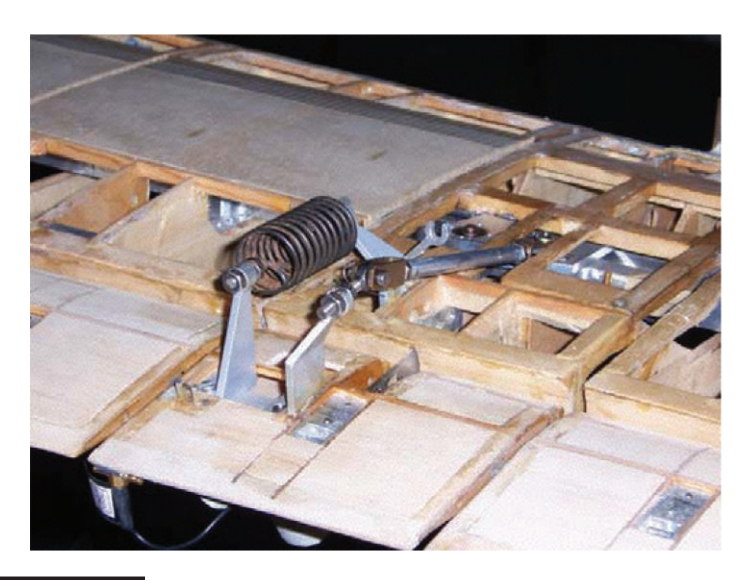


Figure 4.32 L-610 aeroelastic model aileron actuation

optionally be actuated by means of the active electromagnetic actuator [24], which is capable of simulating the nonlinear characteristics as well as the additional mass, damping or stiffness terms.

The nacelle structure is replaceable. The baseline nacelle includes the standard linear engine model with four degrees of freedom (L-WING), with three degrees of freedom in pitch and a single degree of freedom in yaw. This nacelle may optionally be equipped with a nonlinear element [24] such as a non-linear magnetic spring, ball rubber or flat rubber spring with plug to model nonlinear stiffness characteristics of the engine first pitch attachment (N-WING). The nonlinear engine arrangement is shown in Figure 4.33.

The W-WING demonstrator [25], [26] represents the optional nacelle structure that may be used either separately or attached to the described wing structure. W-WING does not represent any specific type of aircraft. However, the structural parameters are also realistic with respect to the structure of the commuter aircraft category. The demonstrator is capable of simulating changes of all of the important parameters influencing the whirl flutter of the commuter turboprop aircraft. The nacelle model has two degrees of freedom – engine pitch and yaw. The stiffness parameters in both pitch and yaw are modelled by means of cross-spring pivots. The spring leaves are changeable, and both stiffness constants are independently adjustable by replacing these spring leaves. Both pivots are independently

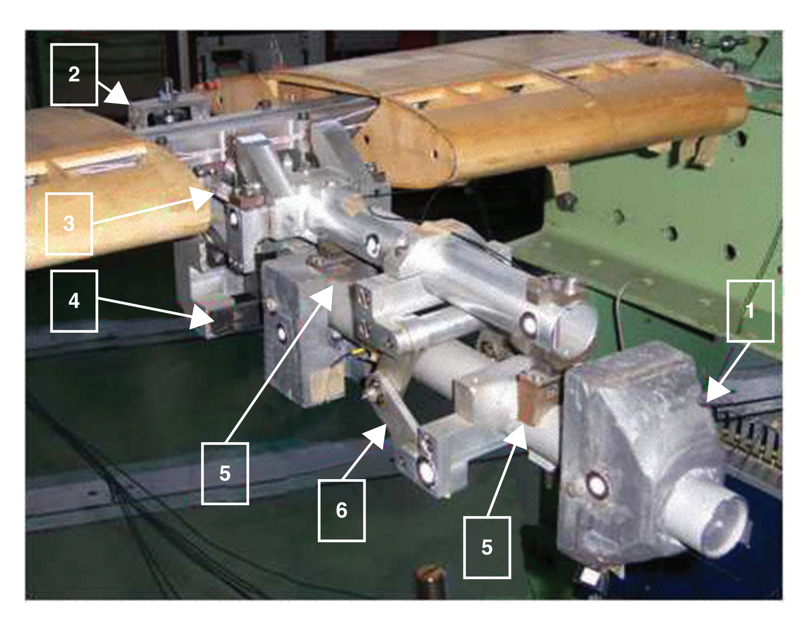


Figure 4.33 Aeroelastic model engine nonlinear attachment (1 – engine mass; 2 – nonlinear attachment; 3 – pitch 1st attachment; 4 – yaw attachment; 5 – pitch 2nd and 3rd attachments; 6 – hinge)

movable in the direction of the propeller axis to adjust the pivot points of both vibration modes. The inertia of the engine is modelled by means of the weight, which is also replaceable and movable to adjust the centre of gravity of the engine. The position of the nacelle centre of gravity with respect to the various combinations of changes that have been mentioned may be measured by means of the special tool. The position of the centre of gravity can also be obtained analytically using the special program.

Provided the nacelle is attached to the wing, the wing dynamic characteristics can also be adjusted using weights simulating the wing fuel to evaluate the influence of the wing structure on the whirl flutter. The demonstrator design drawing is shown in Figure 4.34. The nacelle coat is made of plastic manufactured using the 3D print technology. The photo of the uncoated nacelle attached to the wing spar is shown in Figure 4.35. The nacelle fixed to the wing is shown in Figure 4.36 and the overall view of the nacelle and wing is shown in Figure 4.37.

The wing is equipped with strain gauges in the root and half-span sections (see Figure 4.38) to measure the vertical bending, in-plane

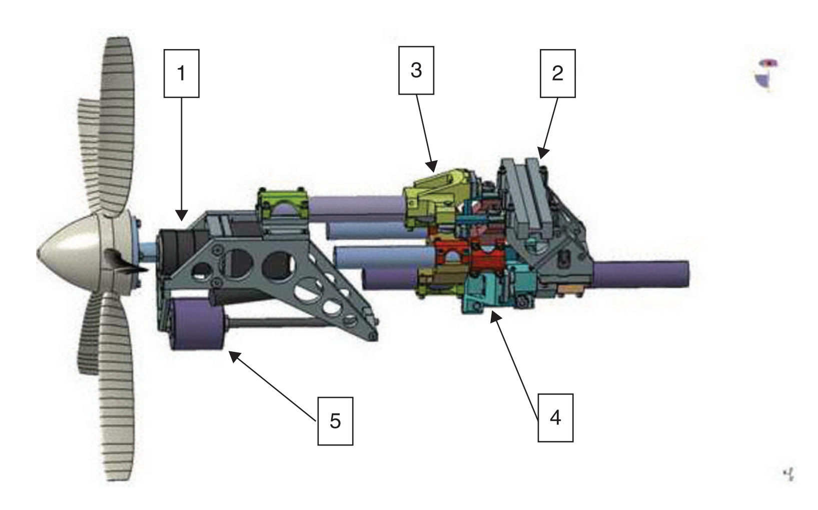


Figure 4.34 W-WING demonstrator nacelle design drawing (1 – motor and gearbox; 2 – wing spar; 3 – pitch attachment; 4 – yaw attachment; 5 – mass balancing weight)

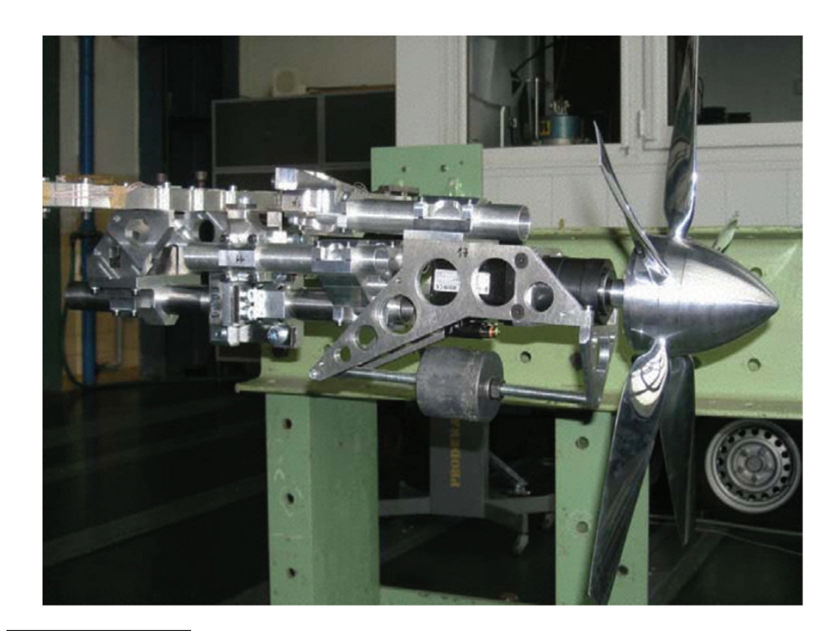


Figure 4.35 W-WING demonstrator, uncoated nacelle



Figure 4.36 W-WING demonstrator, uncoated nacelle integrated into wing structure



Figure 4.37 W-WING demonstrator wing and coated nacelle

bending and torsional deformations. The demonstrator is also equipped with accelerometers at the engine front part and the wing tip section providing signals of vertical and lateral acceleration.

The gyroscopic effect of the rotating mass is simulated by the mass of the propeller blades. At present, two sets of blades made of duralumin

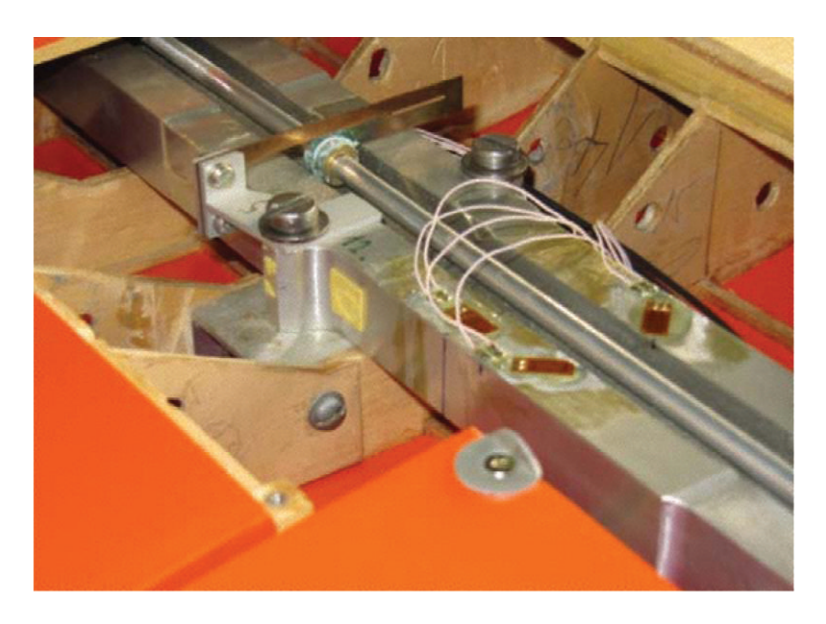


Figure 4.38 W-WING demonstrator wing – strain gauges in half-span section

and steel are available. The demonstrator propeller represents a scaled-down real five-blade Avia V-518 propeller.

Contrary to most applications mentioned in Chapter 4 with the windmilling propellers, the W-WING propeller is powered by an electric motor. Although the propeller thrust influence on the whirl flutter stability is low, the powered propeller solution was chosen to obtain wider options in the combinations of the windflow velocity and the propeller revolutions. The technical realisation of the powered propeller is not complicated at present due to the modern powerful electric motors that are available. The required motor power of 500 W was calculated considering a range of flow velocities up to 70 $m.s^{-1}$ with propeller revolutions up to 3000 min^{-1}. The selected maximal flow velocity corresponds to the top flow velocity of the VZLU low-speed 3-m-diameter wind tunnel, and the propeller maximal revolutions are more than sufficient with respect to the scaled down nominal revolutions of the real propeller. With regard to the power, mass and dimensions, the synchronic servomotor of type TGN3-0205-50-320/T1Y was chosen.

The motor is equipped with a servo-amplifier AKD-P00606-NAEC-E000 that allows management of the propeller revolutions. The

system is controlled by the special in-house SW tool (program 'regulator') prepared in the LabVIEW v2012 environment with the Real-Time and FPGA accessories. The program provides acquisition of measured quantities from the strain gauges, accelerometers and the propulsion system. The selected quantities that are used to manage the experiment are depicted in the time domain in real time as well as pre-processed into the form of the power spectral densities. The program also provides a safeguard preventing the destruction of the demonstrator due to the flutter by turning off the motor and the aerodynamic excitation, provided the response is exceeding the selected threshold.

The program provides the immediate power and propeller revolutions signal from which the torque of the propeller is evaluated. The propeller torque is the criterion for estimation of the necessity of re-adjusting the propeller blades to avoid the stall condition on the blades. The propeller blades are adjustable at the standstill by means of the special tool (see Figure 4.39). Several positions of the blade adjustment are applicable for the specific ranges of the flow velocity. When the rearrangement of the blades becomes necessary, the wind tunnel must be turned off, and the



Figure 4.39 Tool for the propeller blade adjustment

measurement is interrupted. Such a solution is obviously the feasible technical compromise.

The demonstrator configuration for the wind tunnel measurement is defined by the engine centre of gravity, pitch and yaw stiffness and hinge positions and finally the wing mass (fuel loading). The measurement can be managed either with constant propeller revolutions and gradually increased wind flow velocity or with constant wind flow velocity and gradually increased propeller revolutions. Both approaches can be applied until neutral stability is reached. The demonstrator may be excited either by the wind flow turbulence or aerodynamically by means of the aileron deflection using various excitation signals (harmonic, swept sine, impulse). An external excitation is also an option.

The measured quantities include propeller revolutions, propeller torque, wind flow velocity, aileron excitation system deflection, aileron excitation force, wing root and wing half-span stress (vertical bending, in-plane bending, torsion), engine vertical and lateral accelerations, wing tip leading and trailing edge accelerations and, finally, auxiliary signals as marker and voice records.

The analytical model for the FE flutter calculations was prepared in parallel with the demonstrator hardware. The model has a character of a dynamic stick model with concentrated masses. The model is based on the design data updated according to the results of the stiffness and modal tests. The components of the nacelle were also weighed prior to nacelle assembly. The model is parametric, and represents the feasible configurations with respect to the model parameters. The structural model is shown in Figure 4.40. The aerodynamic model is based on the Wing-Body Interference Theory. It includes the wing and splitter surfaces as well as the nacelle body representing the wind tunnel layout (see Figure 4.41).

The model was used for prediction of the demonstrator flutter behaviour. Large parametric analytical studies by means of the optimisation-based approach described in Section 6.2.2 have been accomplished. The parameters assessed include the wind flow velocity, propeller revolutions, propeller mass moment of inertia (duralumin or steel blades), engine vertical and lateral frequency order and ratio and, finally, engine vertical and lateral hinge positions. Based on the results of these calculations, the plan of the experiment will be defined.

The examples of the results are shown in Figures 4.42–4.44. The first example shows the required vertical and lateral stiffness for the neutral stability considering the particular configuration for the fixed propeller revolutions and variable flow velocity. Such drawings simulate the

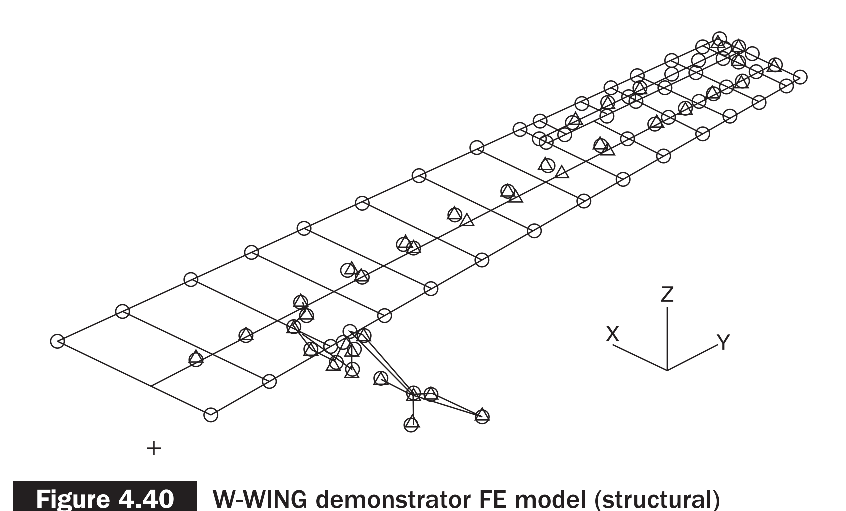


Figure 4.40 W-WING demonstrator FE model (structural)

Figure 4.41 W-WING demonstrator FE model (aerodynamic)

measurement approach with increasing of the flow velocity. The second example shows the comparison of the stability margins considering both light (duralumin – IP = 0.0266 kg·m^2) and heavy (steel – IP = 0.0659 kg·m^2) blades. The example demonstrates the influence of the propeller polar

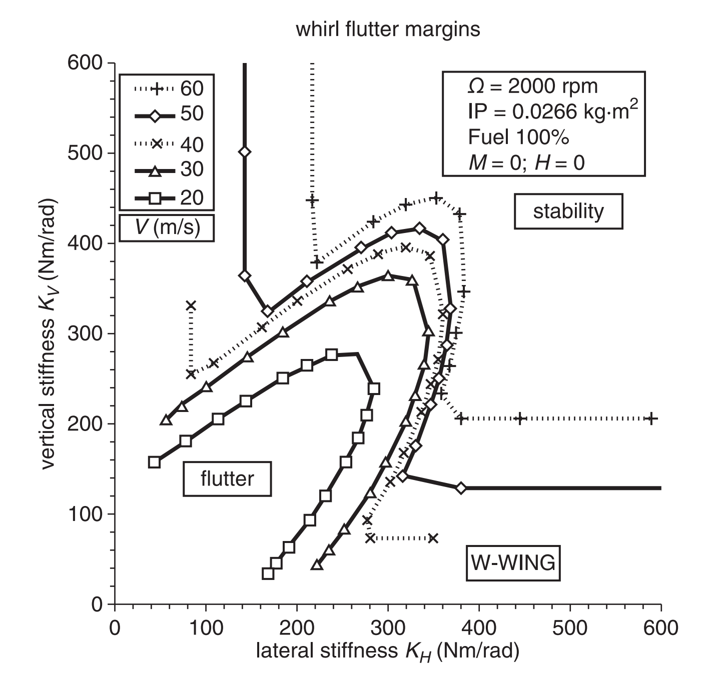


Figure 4.42 Example of W-WING analytical results – required stiffness for neutral stability ($\Omega = 2000$ rpm, light blades), parameter: flow velocity

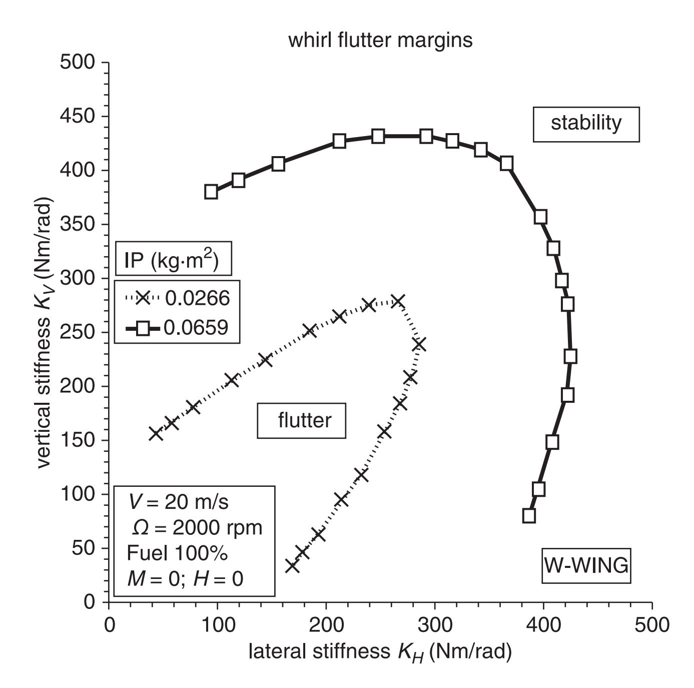


Figure 4.43 Example of W-WING analytical results – required stiffness for neutral stability ($V = 20\,\mathrm{m \cdot s^{-1}}$, $\Omega = 2000$ rpm), parameter: IP (light/heavy blades)

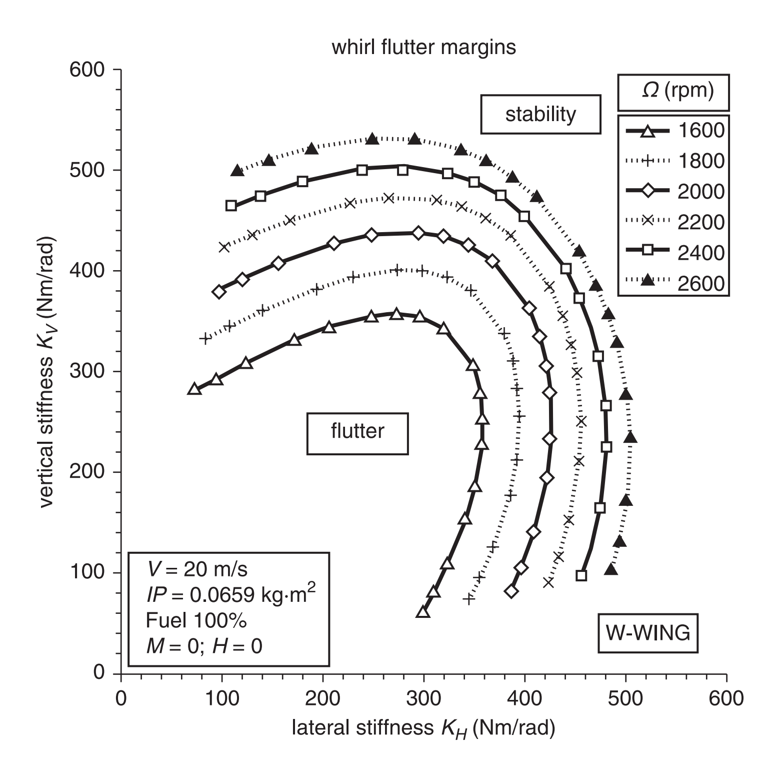


Figure 4.44 Example of W-WING analytical results – required stiffness for neutral stability ($V = 20\,m{\cdot}s^{-1}$, heavy blades), parameter: propeller revolutions

mass moment of inertia making the stability margin wider as well as the influence of the engine vertical and lateral mass moments of inertia increasing the required stiffness. The last example shows the required vertical and lateral stiffness for neutral stability considering the particular configuration for the variable propeller revolutions. Such drawings simulate the measurement approach with increasing of the propeller revolutions.

The first wind tunnel testing of the W-WING demonstrator is planned for the second half of 2014. Experiments will be aimed to reach the critical state and to evaluate the influence of specific parameters. The results will be utilised for verification of the analytical methods and tools that are used for the certification of turboprop aircraft structures according to the regulation standards of FAR/CS 23 and 25.

4.6 References

1 Taylor, E.S. and Browne, K.A.: Vibration isolation of aircraft power plants, *Journal of Aerospace Sciences*, Vol. 6, no. 2, December 1938, pp. 43–49.

2 Robinson, R.G. and Herrenstein, W.H., Jr.: 'Wing – Nacelle – Propeller Interference for Wings of Various Spans Force and Pressure Distribution Tests', Report No. 569, NACA, Langley Field, VA, USA, 1936.

3 Lesley, E.P., Worley, G.F. and Moy, S.: 'Air Propellers in Yaw', Report No. 597, Daniel Guggenheim Aeronautical Laboratory, Stanford University, CA, USA, 1936

4 Houbolt, J.C. and Reed, W.H.: Propeller – nacelle whirl flutter, *Journal of Aerospace Sciences*, Vol. 29, 1962.

5 Bland, S.R. and Bennett, R.M.: 'Wind-Tunnel Measurement of Propeller Whirl – Flutter Speeds and Static-Stability Derivatives and Comparison with Theory', NASA TN D-1807, 1963.

6 Ribner, H.S.: 'Propellers in Yaw', NACA Report 820, 1945.

7 Reed, W.H. and Bennett, R.M.: 'Propeller Whirl Flutter Considerations for V/STOL Aircraft', CAL/TRECOM Symposium, Buffalo, NY, USA, 1963.

8 Yaggi, P.F. and Rogallo, V.L.: 'A Wind-Tunnel Investigation of Three Propellers Through an Angle-of-Attack Range from 0° to 85°', NASA, Technical Note, TN D-318, 1960.

9 Donham R.E. and Watts, G.A.: 'Lessons Learned from fixed and Rotary Wing Dynamic and Aeroelastic Encounters', AIAA/ASME/ASCE/AHS/ASC Structures, Structural Dynamics and Materials Conference, Atlanta, GA, USA, April 2000, AIAA 2000–1599.

10 Krishna Rao, K.V. and Sundararajan, D.: 'Whirl Flutter of Flapping Blade Rotor Systems', NAL Technical Note, TN-18, National Aeronautical Laboratory, Bangalore, India, 1969.

11 Bennett, R.M. and Bland, S.R.: 'Experimental and Analytical Investigation of Propeller Whirl Flutter of a Power Plant on a Flexible Wing', NASA, Technical Note, TN D-2399, August 1964.

12 Abbott, F.T., Jr., Kelly, H.N. and Hampton, K.D.: 'Investigation of Propeller-Power Plant Autoprecession Boundaries for a Dynamic-Aeroelastic Model of a Four-Engine Turboprop Transport Airplane', NASA, Technical Note, TN D-1806, 1963.

13 Kvaternik, R.G.: A review of some tilt-rotor aeroelastic research at NASA-Langley, *Journal of Aircraft*, Vol. 13, No. 5, pp. 357–363, May 1976.

14 Head, A.L. and Smith, W.D.: 'Dynamic Model Testing of the XC-142A Aircraft', Proceeding of Symposium on Aeroelastic and Dynamic Modeling Technology, RTD-TDR-63–4197, Part I, March, 1964.

15 Kvaternik, R.G.: 'Some Remarks on the Use of Scale Models', NASA, Langley Research Center, Hampton, Virginia 23681, NASA/TP-2006–212490/Vol2/PART2, Document ID: 20070008392.

16 Kvaternik, R.G. and Kohn, J.S.: 'An Experimental and Analytical Investigation of Proprotor Whirl Flutter', NASA, Technical Paper, TP 1047, December 1977.

17 Acree, C.W., Jr., Peyran, R.J. and Johnson, W.: 'Rotor Design for Whirl Flutter: An Examination of Options for Improving Tiltrotor Aeroelastic Stability Margins', American Helicopter Society 55th Annual Forum, Montreal, QC, Canada, 25–27 May, 1999.
18 Rand, O. and Peyran, R.J.: Experimental demonstration of the influence of wing couplings on whirl–flutter instability, *Journal of Aircraft*, Vol. 37, No. 5, pp. 859–864, 2000.
19 Krueger, W.R.: 'Analysis of Whirl Flutter Dynamics on a Tiltrotor Wind Tunnel Model', International Forum of Aeroelasticity and Structural Dynamics, Seattle, WA, USA, 21–25 June, 2009.
20 Mueller, J.P., Gourinat, Y., Ferrer, R., Krzsinski, T. and Kerdreux, B.: 'A Numerical Study on Active Control for Tiltrotor Whirl Flutter Stability Augmentation, Revised version of the paper: A Multibody Study on Single- and Multi-Variable Control Algorithms for Tiltrotor Whirl Flutter Stability Augmentation', American Helicopter Society 4th Decennial Specialist's Conference on Aeromechanics, Fisherman's Wharf, San Francisco, CA, USA, 21–23 January, 2004.
21 Yeager, W.T., Jr. and Kvaternik, R.G.: 'A Historical Overview of Aeroelasticity Branch and Transonic Dynamics Tunnel Contributions to Rotorcraft Technology and Development', NASA Langley, NASA TM-2001–211054 ARL-TR-2564.
22 Piatak, D.J., Kvaternik, R.G., Nixon, M.W., Langston, Ch.V., Singleton, J.D., Bennett, R.L. and Brown, R.K.: 'A Wind-Tunnel Parametric Investigation of Tiltrotor Whirl-Flutter Stability Boundaries', American Helicopter Society 57th Annual Forum, Washington, DC., 9–11 May, 2001.
23 Nixon, M.V., Langston, Ch.W., Singleton, J.D., Piatak, D.J., Kvaternik, R.G., Corso, L.M. and Brown, R.: 'Aeroelastic Stability of a Four-bladed Semi-articulated Soft-inplane Tiltrotor Model', American Helicopter Society 59th Forum, Phoenix, AZ, 6–8 May, 2003.
24 Maleček, J., Hlavatý, V., Malínek, P. and Čečrdle, J.: 'Development of Wing / Engine Component Non-linear Aeroelastic Demonstrator', IFASD 11 (International Forum on Aeroelasticity and Structural Dynamics, International Conference, 26–30 June, 2011, Paris, France, IFASD-2011–012, CD-ROM.
25 Čečrdle, J. and Maleček, J.: 'Conceptual Design of Aeroelastic Demonstrator for Whirl Flutter Simulation', World Academy of Science, Engineering and Technology (WASET), International Conference, 13–14 August, 2012, Oslo, Norway, *Proceedings: WASET*, Issue 68, pp. 132–136, pISSN 2010–376X, eISSN 2010–3778.
26 Čečrdle, J. and Maleček, J.: 'Design and Development of New Whirl Flutter Aeroelastic Demonstrator', AIAA Science and Technology Forum and Exposition 2014: 55th AIAA/ASME/ASCE/AHS/SC Structures, Structural Dynamics and Materials Conference, National Harbor, MD, USA, 13–17 January, 2014.

This page intentionally left blank

5

Analytical methods for whirl flutter investigation

DOI: 10.1533/9781782421863.81

Abstract: This chapter addresses the analytical methods of the whirl flutter investigation. It describes both the basic and advanced analytical models of whirl flutter. First, the fundamental solution using two-degrees-of-freedom model and a rigid propeller is provided, and the influences of the major structural parameters are described. Then, the fundamental solutions of the propeller aerodynamic forces and the influences of the main aerodynamic parameters are described using Strip Theory. Next, the more complex mechanical models, such as the four-degrees-of-freedom model including wing flexibility or a model including blade flexibility with hinged blades or twisted blades, are described. Then, the more complex solution of the propeller aerodynamic forces is described using the lifting surface theory. The final part of the chapter addresses the comprehensive computational models utilising the experimental modal data, multi-body simulations or the CFD-based simulations.

Key words: whirl flutter, whirl flutter analysis, whirl flutter analytical models, rigid blade model, hinged blade model, twisted blade model, wing–engine whirl flutter model, CFD-based whirl flutter model.

5.1 Historical overview

The aero-mechanical phenomenon known as prop-whirl flutter was analytically discovered by Taylor and Browne in 1938 [1]. The next work in the field was performed by Ribner in 1945 [2], [3] who described the

basic formulae for the aerodynamic derivatives of propeller forces and moments due to the motions and velocities in pitch and yaw. Ribner's aerodynamic derivatives were frequently used and are still in use in the analytical solutions. After the Electra accidents, the whirl flutter phenomenon received practical application. In the early 1960s a lot of analytical and experimental works was performed. The important contributions from this period are the works of Houbolt and Reed [4] and Reed and Bland [5] using Strip Theory Aerodynamics [6], [7]. Further analytical studies of propeller whirl flutter are summarised in [8] as well. Analytical investigations of the tilt-rotor configuration have been carried out by Kvaternik and Kohn [9]. Later, these analytical methods were refined and worked out. The developments using Linear Lifting Surface Theory have been presented by Hammond, Runyan and Masson [10] using the results of Runyan [11]. The method was implemented to a rotor in forward flight by Runyan and Tai [12]. Recently, non-linear methods also appeared in connection with the growth of the FE-based methods and SW tools [13]. Comprehensive analytical tools, such as CAMRAD II [14], [15], as well as multibody simulation tools [16] were applied. For the description of the propeller aerodynamic forces, the complex CFD methods were used as well. Shiravastava and Reddy [17] developed the CFD code using the three-dimensional unsteady compressible Euler equations. The comprehensive tool based on the RANS and URANS equations was developed and used by ONERA [18].

5.2 Fundamental solution

The analytical solution of the whirl flutter stability issue was worked out by Reed and Bland [5]. A rigid propeller was assumed. The power plant was flexibly mounted in pitch and yaw to a fixed structure. The stability solution assumes small amplitudes of the pitching and yawing motions. The forces and moments are dependent on the inertia, elastic and damping characteristics as well as on the gyroscopic moment due to the rotating masses. Furthermore, the stability is influenced by the aerodynamic forces on the propeller. The wing structure was assumed rigid, and the aerodynamic interference effects between the propeller, nacelle and the wing were ignored. The fundamental facts regarding such a system and the derivation of the equations of motion were outlined in Section 2.2. Here, the solution is worked out in more detail. The coordinate system used is shown in Figure 2.8. Lagrange's formulation of the differential

equations of the motion is expressed using Eqns 2.1–2.5. From Lagrange's equation

$$\frac{d}{dt}\left(\frac{\partial E_k}{\partial q_i}\right)-\frac{\partial E_k}{\partial q_i}+\frac{\partial E_P}{\partial q_i}+\frac{\partial D}{\partial q_i}=Q_{q_i} \quad [5.1]$$

where the generalised coordinates q_i are the pitch and yaw angles (Θ, Ψ). We obtained the equations of motion expressed by Eqn. 2.6. The generalised aerodynamic forces are represented by the pitch and yaw moments about the pitch and yaw rotation axes, which are expressed by the propeller forces and moments in Eqn. 2.7. Thus, the final equations of motion from Eqn. 2.6 can be rewritten as

$$\begin{aligned} J_Y\ddot{\Theta}+\frac{K_\Theta\gamma_\Theta}{\omega}\dot{\Theta}+J_X\Omega\dot{\Psi}+K_\Theta\Theta &= M_{Y,P}-aP_Z \\ J_Z\ddot{\Psi}+\frac{K_\Psi\gamma_\Psi}{\omega}\dot{\Psi}-J_X\Omega\dot{\Theta}+K_\Psi\Psi &= M_{Z,P}+aP_Y \end{aligned} \quad [5.2]$$

Note that the formulation of Eqn. 5.2 express the mass moments of inertia in pitch and yaw as J_y and J_z, whereas [5] uses the common notation of J_y directly expecting $J_y = J_z$. The equations of motion in Eqn. 5.2 include the inertia term, damping term, gyroscopic term and stiffness term on the left side (ordered) and the aerodynamic term on the right side.

The aerodynamic forces and moments of the propeller are expressed using the dimensionless aerodynamic derivatives as in Eqn. 2.9. These aerodynamic derivatives can be obtained either from the analytical solution or from the experiments. The fundamental analytical solution of the aerodynamic derivatives is based on Ribner's work [2].

The solution employs the aerodynamic Strip Theory. The Strip Theory is an early and simple method. The two-dimensional solution was formulated by Theodorsen in 1935 [6]. The solution assumed that the motion of each spanwise station depended only on the motion of this station. Later developments of the method by Smilg and Wasserman in 1942 [7] extended the solution to three-dimensional structures. The wing was divided into a number of strips spanwise and the aerodynamic load on each strip was based on the 2D coefficients evaluated on the strip centreline. There were no interference effects among the strips considered, and thus, the aerodynamic matrix was diagonal. The aerodynamic loads could be corrected to account for the compressibility or aspect ratio effect. The Strip Theory may be accurate in many cases, especially for unswept high-aspect-ratio wings; therefore, it is still used for some applications today.

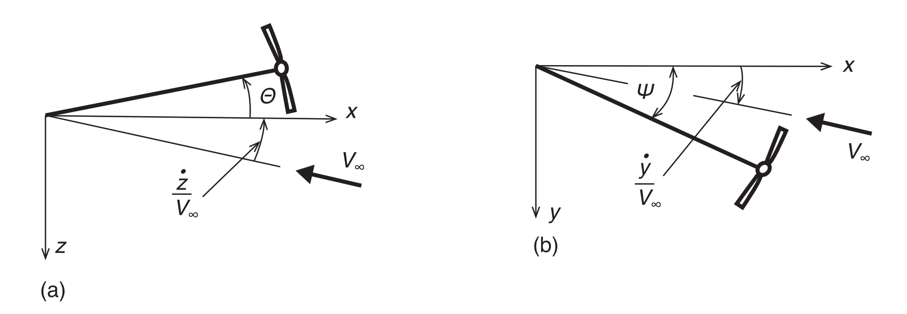


Figure 5.1 **Effective quasi-steady angles [19]**

The definitions of the aerodynamic derivatives are given in Eqn. 2.10. We have 16 derivatives in total (two forces and two moments with respect to two angular deformations and two angular velocities); however, we can reduce the number of derivatives by considering the symmetry, as expressed in Eqn. 2.11, and neglecting the ones with low values as expressed in Eqn. 2.12. In fact, we have six aerodynamic derivative variables that are based on [2], except for $c_{z\Psi}$ and $c_{y\Theta}$, which were obtained from experiments or the approximate solution of [5].

According the quasi-steady theory as described in Section 2.2, the effective angles can be expressed as in Eqn. 2.8. It consists of the geometric angle and the angle due to the translational velocity of the propeller hub, as expressed in Figure 5.1.

The solution is now laid out according to [5]. For the purpose of solution, the dimensionless parameters were defined. First, the dimensionless time τ is defined as

$$\tau = \frac{V_\infty t}{R} \qquad [5.3]$$

Putting τ into the equations of motions (5.2), they change to the form

$$J_Y \left(\frac{V_\infty}{R}\right)^2 \left(\frac{d^2\Theta}{d\tau^2}\right) + \left(\frac{K_\Theta \gamma_\Theta}{\omega}\right)\left(\frac{V_\infty}{R}\right)\left(\frac{d\Theta}{d\tau}\right) + J_X \Omega \left(\frac{V_\infty}{R}\right)\left(\frac{d\Psi}{d\tau}\right) + K_\Theta \Theta = M_{Y,P} - aP_Z$$

$$J_Z \left(\frac{V_\infty}{R}\right)^2 \left(\frac{d^2\Psi}{d\tau^2}\right) + \left(\frac{K_\Psi \gamma_\Psi}{\omega}\right)\left(\frac{V_\infty}{R}\right)\left(\frac{d\Psi}{d\tau}\right) - J_X \Omega \left(\frac{V_\infty}{R}\right)\left(\frac{d\Theta}{d\tau}\right) + K_\Psi \Psi = M_{Z,P} + aP_Y \qquad [5.4]$$

Now, we set up further dimensionless parameters which are:

Ratio of the polar moment of inertia of the propeller to the pitching moment of inertia of the power plant: $H = (\pi J_x / J_y)$;

Ratio of the yaw stiffness to the pitch stiffness: $\gamma^2 = (K_\Psi/K_\Theta) = (\omega_\Psi/\omega_\Theta)^2$;

Ratio of the yaw damping to the pitch damping: $G = (\gamma_\Psi/\gamma_\Theta)$

Ratio of the mass moment of inertia of the propeller air cylinder to the pitching moment of inertia of the power plant: $\kappa = (\pi\,\rho\,R^5/J_y)$;

Propeller reduced frequency defined as: $k_\Theta = (\omega_\Theta\ R/V_\infty)$;

Frequency ratio: $\lambda = (\omega/\omega_\Theta)$;

Propeller advance ratio: $J_0 = (\pi V_\infty/\Omega R)$.

Setting up these dimensionless parameters and making further algebraic adjustments the equations of motion change to the dimensionless form:

$$\left(\frac{d^2\Theta}{d\tau^2}\right)+\frac{\gamma_\Theta k_\Theta}{\lambda}\left(\frac{d\Theta}{d\tau}\right)+\left(\frac{H}{J_0}\right)\left(\frac{d\Psi}{d\tau}\right)+k_\Theta^2\ \Theta=\kappa\ f_\Theta$$
$$\left(\frac{d^2\Psi}{d\tau^2}\right)+\frac{\gamma_\Theta G k_\Theta \gamma^2}{\lambda}\left(\frac{d\Psi}{d\tau}\right)-\left(\frac{H}{J_0}\right)\left(\frac{d\Theta}{d\tau}\right)+\gamma^2 k_\Theta^2\ \Psi=\kappa\ f_\Psi \qquad [5.5]$$

where the generalised forces have the form

$$f_\Theta = a_0\Theta + a_1\left(\frac{d\Theta}{d\tau}\right)+a_2\left(\frac{d^2\Theta}{d\tau^2}\right)+b_0\Psi+b_1\left(\frac{d\Psi}{d\tau}\right)+b_2\left(\frac{d^2\Psi}{d\tau^2}\right)$$
$$f_\Psi = -b_0\Theta - b_1\left(\frac{d\Theta}{d\tau}\right)-b_2\left(\frac{d^2\Theta}{d\tau^2}\right)+a_0\Psi+a_1\left(\frac{d\Psi}{d\tau}\right)+a_2\left(\frac{d^2\Psi}{d\tau^2}\right) \qquad [5.6]$$

where the coefficients are only dependent on the propeller aerodynamic derivatives and the hinge locations. Note that these coefficients do not include the effect of the mass of the air around the propeller, which would influence the a_2 and b_2 coefficients.

$$a_0 = -\frac{1}{2}\cdot\frac{a}{R}\,c_{z\Theta}$$
$$a_1 = c_{mq}+\frac{1}{2}\left(\frac{a}{R}\right)^2 c_{z\Theta}$$
$$a_2 = -\frac{a}{R}\,c_{mq} \qquad [5.7]$$
$$b_0 = c_{m\Psi}-\frac{1}{2}\cdot\frac{a}{R}\,c_{z\Psi}$$
$$b_1 = -\frac{a}{R}\left(\frac{1}{2}\,c_{zr}+b_0\right)$$
$$b_2 = \frac{1}{2}\left(\frac{a}{R}\right)^2 c_{zr}$$

Now, we search for the critical (flutter) state, i.e., when the system will achieve the harmonic motion:

$$\Theta(t) = \Theta_0 e^{j\omega t};\ \Psi(t) = \Psi_0 e^{j\omega t} \quad [5.8]$$

In the dimensionless form, it becomes:

$$\Theta(\tau) = \Theta_0 e^{j\lambda k_\Theta \omega t};\ \Psi(\tau) = \Psi_0 e^{j\lambda k_\Theta \omega t} \quad [5.9]$$

We put Eqn. 5.9 into the equations of motion of Eqn. 5.5. The solution is a characteristic eigenvalue problem. The nontrivial solution is given when the determinant of coefficients is set to zero. By neglecting the second order terms, the real part becomes a quadratic in λ^2 and two roots λ_1 and λ_2 corresponding to the forward and backward whirl modes, respectively, are obtained.

The required damping of the critical flutter state for the both forward and backward whirl modes is given by setting the imaginary part of the determinant to zero and solving for the given λ:

$$\gamma_{\Theta FL} = \frac{\lambda_\kappa}{k_\Theta}\left(\frac{a_1\left(k_\Theta^2 - 2\lambda^2 k_\Theta^2 + \gamma^2 k_\Theta^2\right) + 2\frac{H}{J_0}\left(b_0 - b_2\lambda^2 k_\Theta^2\right) - 2\kappa\left(a_0 a_1 + b_0 b_1\right) + 2\kappa\left(a_1 a_2 + b_1 b_2\right)\lambda^2 k_\Theta^2}{k_\Theta^2\left(\gamma^2 - \lambda^2\right) + k_\Theta^2\left(1 - \lambda^2\right)\gamma^2 G + \kappa\left(a_2\lambda^2 k_\Theta^2 - a_0\right)\left(1 + \gamma^2 G\right)}\right) \quad [5.10]$$

Figure 5.2 shows the typical dependence of λ_1 and λ_2 and the corresponding critical damping $\gamma_{\Theta 1FL}$ and $\gamma_{\Theta 2FL}$ on the parameter $(V_\infty/R\omega_\Theta)$. The other structural parameters considered are $G = (\gamma_\Psi/\gamma_\Theta) = 1.0$ and $\gamma^2 = (K_\Psi/K_\Theta) = 1.4$.

Figure 5.2 shows the damping of the system to reach the critical state. Provided the damping is higher, the system is stable and vice versa. It is apparent from Figure 5.2 that (considering the rigid propeller) the instability may occur only on the backward whirl mode. The reason is that the damping of the physical system is always positive, and thus always in the stable region with respect to the forward whirl mode stability boundary (above the boundary).

5.3 Influences of major parameters

Now, the influences of the major parameters on the whirl flutter stability are evaluated. For this purpose the special case of $G = (\gamma_\Psi/\gamma_\Theta) = 1.0$ (symmetric damping) and $\gamma^2 = (K_\Psi/K_\Theta) = 1.0$ (symmetric stiffness) are

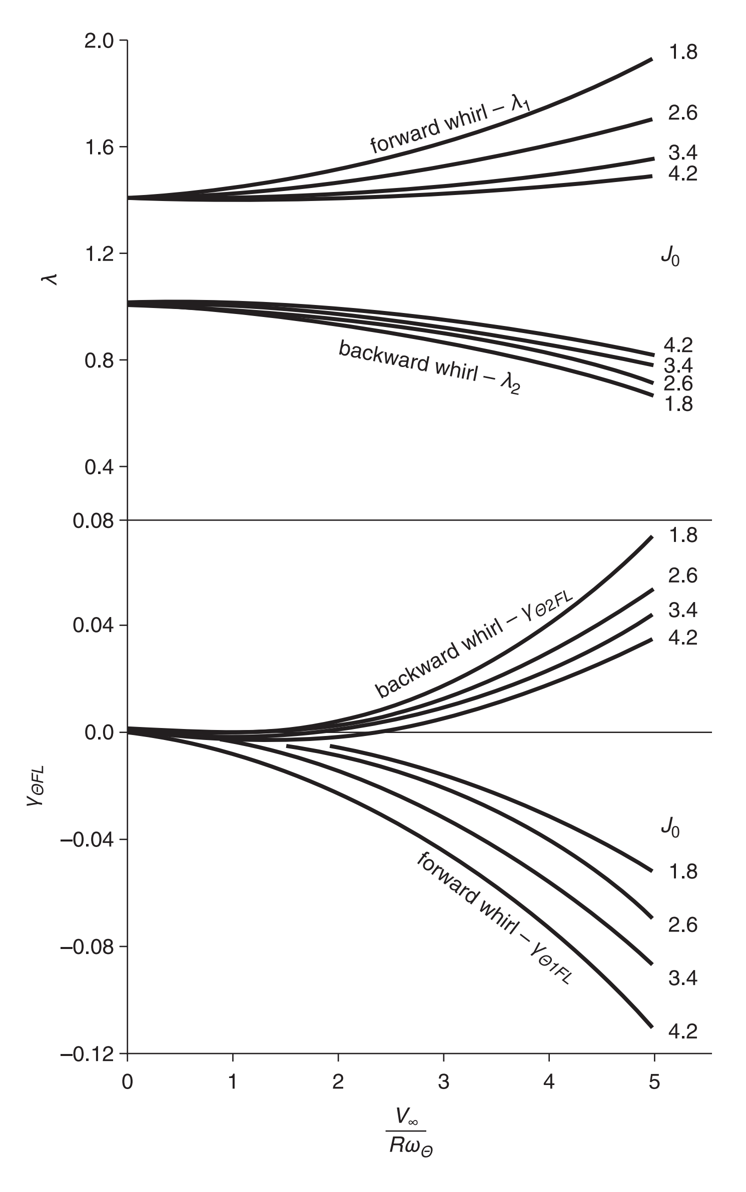


Figure 5.2 **Whirl flutter critical dimensionless frequency and damping ($G = (\gamma_\Psi/\gamma_\Theta) = 1.0$ and $\gamma^2 = (K_\Psi/K_\Theta) = 1.4$) according to [5]**

considered. In this case, the dimensionless frequency relation can be approximated as

$$\lambda_1 \approx 1 + \frac{J_X \Omega}{2\, J_y \omega_\Theta}; \quad \lambda_2 \approx 1 - \frac{J_X \Omega}{2\, J_y \omega_\Theta} \qquad [5.11]$$

and from Eqn. 5.10 we obtain the approximate expression for the critical damping as

$$\begin{aligned} \gamma_{\Theta 1FL} &\approx \frac{\kappa}{k_\Theta} \left(\left(1 + \frac{J_X \Omega}{2\, J_y \omega_\Theta} \right) a_1 - \frac{b_0}{k_\Theta} \right) \\ \gamma_{\Theta 2FL} &\approx \frac{\kappa}{k_\Theta} \left(\left(1 - \frac{J_X \Omega}{2\, J_y \omega_\Theta} \right) a_1 - \frac{b_0}{k_\Theta} \right) \end{aligned} \qquad [5.12]$$

where the coefficients a_1 and b_0 are the ones from Eqn. 5.7. Because the aerodynamic derivatives c_{mq} and $c_{z\Theta}$ are always negative, and at the same time the derivatives $c_{m\Psi}$ and $c_{z\Psi}$ are always positive [5], a_1 must become negative, and b_0 must be positive. Therefore, the required critical damping of Eqn. 5.12 can become positive only for the $\gamma_{\Theta 2FL}$ and so the instability may occur on the backward whirl mode only. Therefore, the following paragraphs that describe the influences of the variation of the parameters on the stability only account for the backward whirl mode. Also note that these descriptions are valid only for the critical state of the whirl flutter, thus the ratio between the $\gamma_{\Theta FL}$ and real damping of the structure does not indicate the rate of the reserve in terms of the whirl flutter stability.

The influence of the air density can be evaluated from the approximate solution of Eqn. 5.12. It is simply proportional to the dimensionless parameter $\kappa = (\pi\, \rho\, R^5 / J_y)$.

As mentioned previously, the influence of the propeller thrust is very small. This small influence comes from the fact that the aerodynamic derivatives of the thrusted propeller and windmilling propeller variance can be high in the low speed region, but at high velocities (where whirl flutter is expected), the variance is less than 5%. This fact is also good justification for the usage of the windmilling propellers for experiments.

It was also mentioned in Section 2.2 that increasing the distance from the propeller hub to the vibration mode hinge point has a stabilising effect. This distance is represented by the dimensionless propeller hub distance (a/R). Figure 5.3 shows the influence of the (a/R) variation on the critical damping of the backward whirl mode. Note that the variation

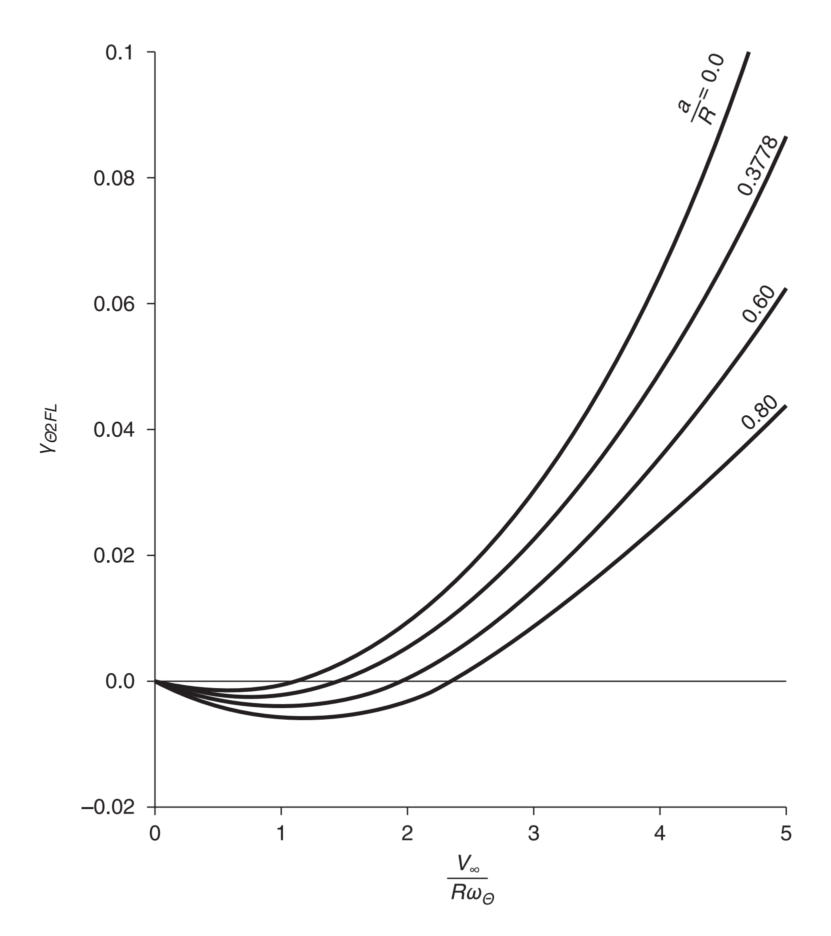


Figure 5.3 **Influence of the propeller hub distance on the backward whirl mode critical damping ($G = (\gamma_\Psi/\gamma_\Theta) = 1.0$ and $\gamma^2 = (K_\Psi/K_\Theta) = 1.0$) according to [5]**

included only aerodynamic terms, and the other terms, such as the moments of inertia, remained the same.

Provided the dimensionless propeller hub distance is increased over the value of 2.0 ($(a/R) > 2.0$), the value of the coefficient b_0 in Eqn. 5.12 becomes negative, and therefore the forward whirl mode may be reached. Nevertheless, this condition is outside of the practical applications because it occurs at very high values of the dimensionless velocity ($V_\infty/R\omega_\Theta$).

The influence of the stiffness asymmetry, i.e., $(K_\Psi/K_\Theta) \neq 1.0$, was also discussed in Section 2.2. At first approximation, it can be assessed using the root-mean-square stiffness criterion, which is defined as

$$K_{RMS} = \sqrt{\frac{K_\Theta^2 + K_\Psi^2}{2}} \qquad [5.13]$$

The asymmetric cases are assessed via the symmetric one with the same K_{RMS}. Figure 5.4 shows the family of stability boundary curves dependence on the K_{RMS} for the symmetric stiffness case and various asymmetric cases. As is apparent from this figure, the variance due to asymmetry is low for low K_{RMS}. For high K_{RMS}, the variance becomes high; however, we can consider such an assessment to be conservative because the symmetric case is the worst case in terms of stability.

The effect of the asymmetric damping, i.e. $(\gamma_\Psi/\gamma_\Theta) \neq 1.0$, can be assessed using the average damping criterion, which is defined as

$$\gamma_{AVG} = \frac{1}{2}(\gamma_\Theta + \gamma_\Psi) \qquad [5.14]$$

Figure 5.5 shows the influence of the damping asymmetry on the stability boundary. The average damping γ_{AVG} and the root-mean-square stiffness K_{RMS} are considered to be constant. It is apparent from figure that increasing the damping in the direction with the lower stiffness has a stabilizing effect and vice versa.

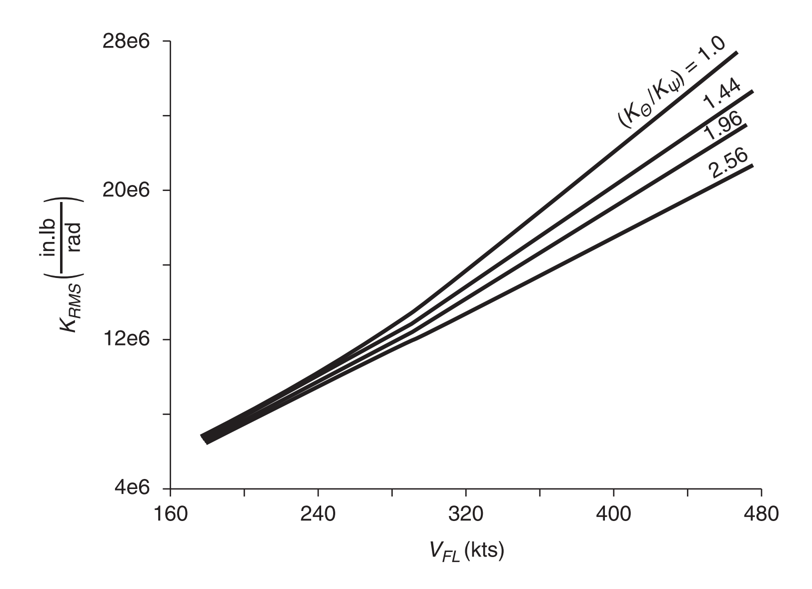


Figure 5.4 **Stability boundaries – assessment of the stiffness asymmetry via K_K ($\gamma_\Psi = \gamma_\Theta = 0.03$; $\Omega = 1020$ rpm) according to [5]**

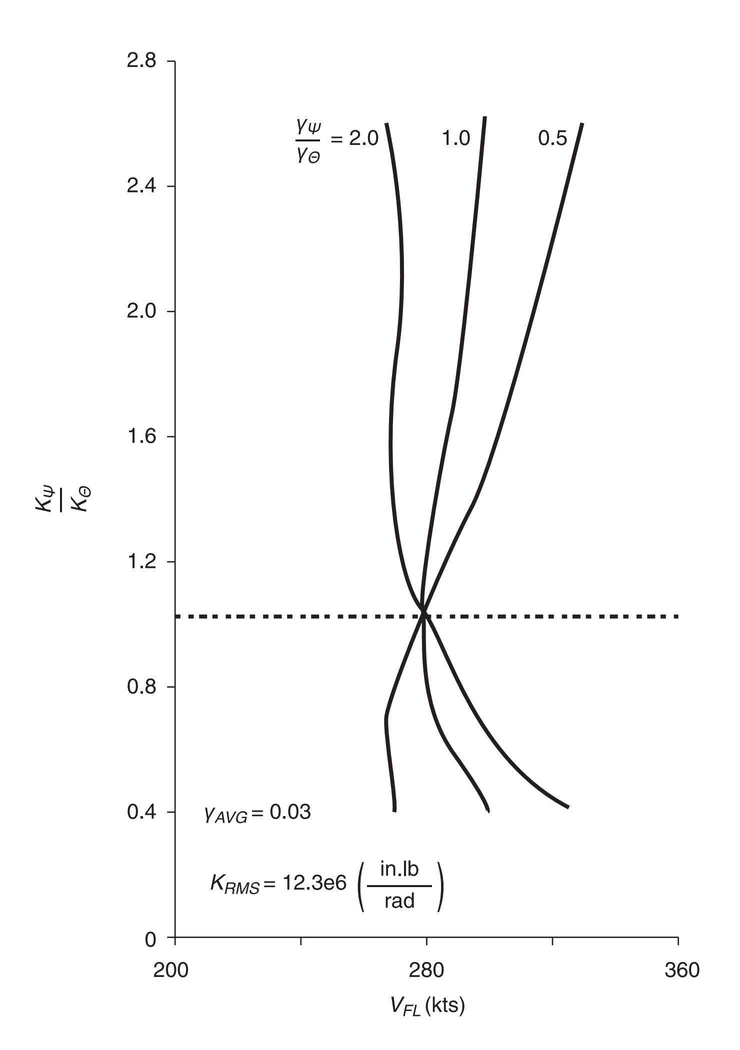


Figure 5.5 **Stability boundaries – assessment of the damping asymmetry ($\gamma_{AVG} = 0.03$; $K_{RMS} = 12.3e+6$ [in-lb/rad]) according to [5]**

5.4 Propeller aerodynamic forces by Strip Theory

As was already mentioned, the power plant pitching and yawing oscillations give rise to aerodynamic forces on the propeller. The fundamental methods for the solution of aerodynamic derivatives are based on the quasi-steady theory and the assumption of 'small angles'.

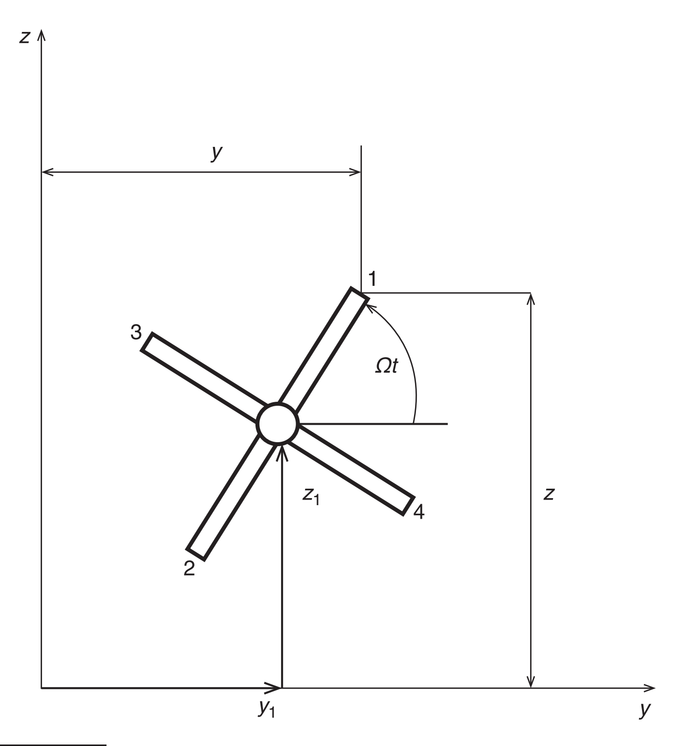


Figure 5.6 Arbitrary position of propeller disc [4]

The analytical methods are based on Ribner's analyses [2], and later Houbolt's analyses [4] become available. Both methods are comparable.

Houbolt's method [4] is based on the Strip Theory first order approximation. Three perturbation quantities are considered, which are: (1) the local section angle of attack (α_1), (2) the perturbation velocity in the propeller plane ($\dot{s}$) and (3) the perturbation velocity out of the propeller plane ($\dot{w}$). An arbitrary position of the propeller disc is shown in Figure 5.6.

In addition to the displacement in the *z*–*y* plane, the propeller disc is pitching and yawing at small angles of Θ and Ψ, respectively, as shown in Figure 2.8.

For blade no. 1 in Figure 5.6, the change in the geometric angle of attack along the blade due to yaw and pitch is

$$\alpha_1 = \Psi \sin \Omega t - \Theta \cos \Omega t \qquad [5.15]$$

Both ($\dot{s}$) and ($\dot{w}$) perturbation velocities are given from the arbitrary position of the blade no. 1 point described by the following equations:

$$y = y_1 + r\cos\Omega t$$
$$z = z_1 + r\sin\Omega t \qquad [5.16]$$
$$w_1 = -\Psi r\cos\Omega t - \Theta r\sin\Omega t$$

with

$$\dot{s} = -\dot{y}_1 \sin\Omega t + \dot{z}_1 \cos\Omega t$$
$$\dot{w} = -\dot{\Psi} r\cos\Omega t + \Psi r\,\Omega\sin\Omega t - \dot{\Theta} r\sin\Omega t - \Theta\, r\,\Omega\cos\Omega t \qquad [5.17]$$

The unsteady lift force on a section of blade no. 1 comes from the quantities α_1, $\dot{s}$ and $\dot{w}$, as shown in Figure 5.7, where β represents the steady state angle of attack of the blade.

Both velocities $\dot{s}$ and $\dot{w}$ lead to velocity components that are normal to the resultant velocity U with a magnitude of

$$-\dot{w}\left(\frac{\Omega r}{U}\right) + \dot{s}\left(\frac{V_\infty}{U}\right) \qquad [5.18]$$

By considering this velocity and the α_1 angle, angle of attack of the effective blade section becomes

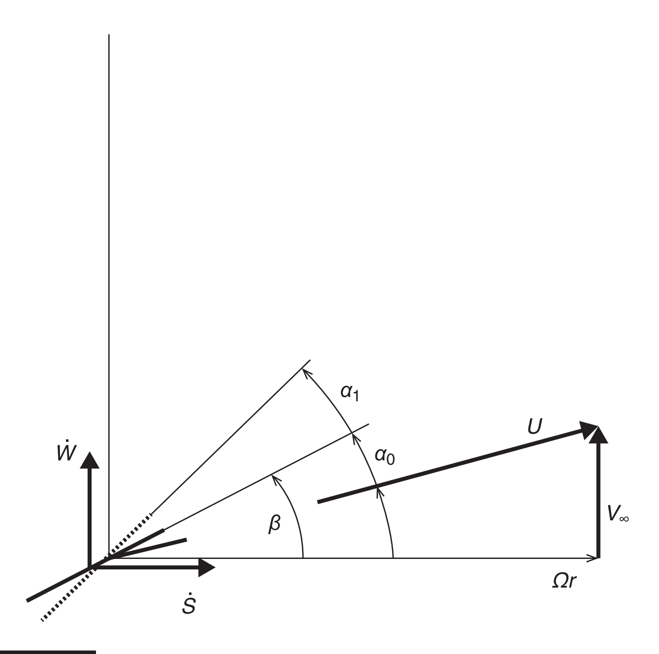


Figure 5.7 **Blade section (angles and velocities) [4]**

$$\alpha_{eff} = \alpha_0 + \alpha_1 - \dot{w}\left(\frac{\Omega r}{U^2}\right) + \dot{s}\left(\frac{V_\infty}{U^2}\right) \qquad [5.19]$$

Both velocities $\dot{s}$ and $\dot{w}$ lead to velocity components in the direction of U, and the effective resultant velocity becomes:

$$U_{eff} = U + \dot{w}\left(\frac{V_\infty}{U}\right) + \dot{s}\left(\frac{\Omega r}{U}\right) \qquad [5.20]$$

The lift force from the blade section is

$$L = \frac{1}{2} a_0 \ \rho \ c_0 \ U_{eff}^2 \alpha_{eff} \qquad [5.21]$$

where a_0 is section lift curve slope, and c_0 is the section chord. After substitution, the equation becomes

$$L = \frac{1}{2} a_0 \ \rho \ c_0 \ U^2 \left[\alpha_0 + \alpha_1 - \frac{\Omega r}{U^2}\left(1 - \frac{2V_\infty}{\Omega r}\alpha_0\right)\dot{w} + \frac{V}{U^2}\left(1 + \frac{2\Omega r}{V_\infty}\alpha_0\right)\dot{s}\right] \qquad [5.22]$$

The first term represents the steady state lift whereas the other terms represent the unsteady lift effects. Note that the unsteady terms that involve the velocities $\dot{s}$ and $\dot{w}$ are influenced by the steady state angle of attack. Both the $(2V_\infty/\Omega\ r).\alpha_0$ and $(2\Omega\ r/V_\infty).\alpha_0$ terms have negligible effects on the blade section lift. Even for the windmilling propellers with the $\alpha_0 = 0.0$, all of the terms associated with α_0 become zero.

Now considering the windmilling propeller, i.e., $\alpha_0 = 0.0$, the blade section lift becomes

$$L = \frac{1}{2} a_0 \ \rho \ c_0 \ U^2 \left(\alpha_1 - \frac{\Omega r}{U^2}\dot{w} + \frac{V}{U^2}\dot{s}\right) \qquad [5.23]$$

We substitute for α_1 from Eqn. 5.15 and for $\dot{s}$ and $\dot{w}$ from Eqn. 5.17. We also express the velocity U as

$$U^2 = r^2\Omega^2 + V_\infty^2 \qquad [5.24]$$

and the section lift of the blade no. 1 becomes

$$L = \frac{1}{2} a_0 \ \rho \ c_0 \Big[\left(-V_\infty^2\Theta + V_\infty \dot{z}_1 + \Omega r^2 \dot{\Psi}\right)\cos\ \Omega t + $$
$$+ \left(V_\infty^2\Psi - V_\infty \dot{y}_1 + \Omega r^2 \dot{\Theta}\right)\sin\ \Omega t\Big] \qquad [5.25]$$

which we rearrange to the form

$$L = -\frac{1}{2} a_0\ \rho\ c_0 \left(V_\infty^2 \Theta - V_\infty \dot{z}_1 - \Omega r^2 \dot{\Psi}\right)\cos\ \Omega t + \\ + \frac{1}{2} a_0\ \rho\ c_0 \left(V_\infty^2 \Psi - V_\infty \dot{y}_1 + \Omega r^2 \dot{\Theta}\right)\sin\ \Omega t \qquad [5.26]$$

and substitute as

$$L_1 = -f_1 \cos\ \Omega t + f_2 \sin\ \Omega t \qquad [5.27]$$

The section lift on the remaining blades can be extracted from Eqn. [5.27] using the substitutions

$\Omega t \to (\Omega t + \pi)$ for blade no. 2

$\Omega t \to (\Omega t + \pi/2)$ for blade no. 3

$\Omega t \to (\Omega t + 3\pi/2)$ for blade no. 4

with respect to the properties and relations of the *sin* and *cos* functions, the blade section lift forces become

$$L_2 = f_1 \cos\ \Omega t - f_2 \sin\ \Omega t = -L_1 \\ L_3 = f_1 \sin\ \Omega t + f_2 \cos\ \Omega t \qquad [5.28] \\ L_4 = -f_1 \sin\ \Omega t - f_2 \cos\ \Omega t = -L_3$$

To determine the unsteady forces and moments of the propeller, we express the blade lift force using the following components: (1) in the x-direction (thrusting component) and (2) perpendicular to the blade in the y–z plane (torque component). The former causes moments ΔM_y and ΔM_z, and the latter causes forces ΔL_y and ΔL_z. According to Figure 5.7 the thrusting component of the blade section lift can be expressed as $(L\ (\Omega r/U))$ and torque component as $(L\ (V_\infty/U))$. Both components are shown in Figure 5.8.

The ΔL_y, ΔL_z, ΔM_y and ΔM_z forces and moments summarised from all four blades are:

$$\Delta L_y = \frac{V_\infty}{U}\left(L_1 \sin \Omega t + L_3 \cos \Omega t - L_2 \sin \Omega t - L_4 \cos \Omega t\right) \\ \Delta L_z = \frac{V_\infty}{U}\left(-L_1 \cos \Omega t + L_3 \sin \Omega t + L_2 \cos \Omega t - L_4 \sin \Omega t\right) \\ \Delta M_y = \frac{\Omega r}{U} r\left(-L_1 \sin \Omega t - L_3 \cos \Omega t + L_2 \sin \Omega t + L_4 \cos \Omega t\right) \\ \Delta M_z = \frac{\Omega r}{U} r\left(-L_1 \cos\ \Omega t + L_3 \sin \Omega t + L_2 \cos \Omega t - L_4 \sin \Omega t\right) \qquad [5.29]$$

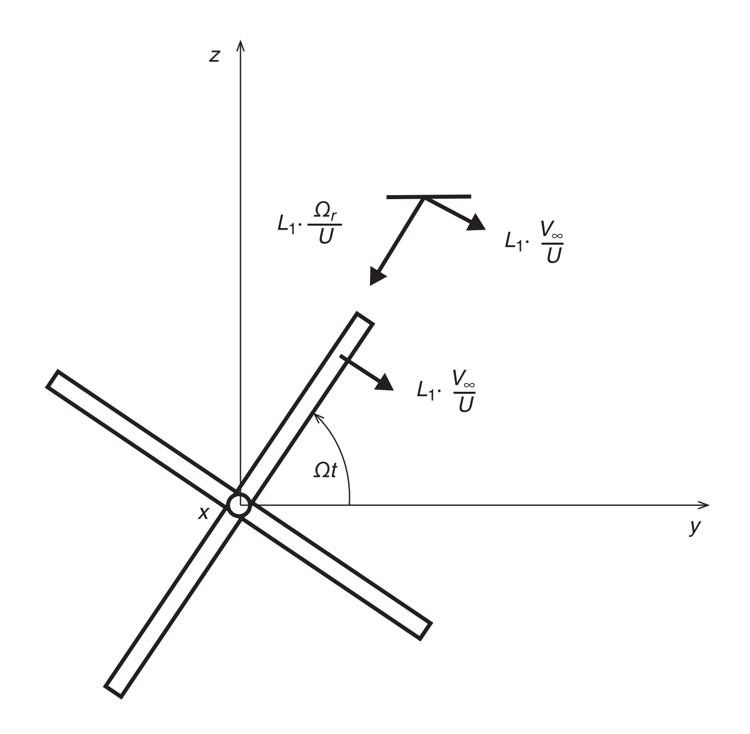


Figure 5.8 Blade section lift force components [4]

Substituting from Eqn. 5.28, we obtain

$$\begin{aligned}
\Delta L_y &= 2\frac{V_\infty}{U}\left(L_1 \sin\ \Omega t + L_3 \cos\ \Omega t\right)\\
\Delta L_z &= 2\frac{V_\infty}{U}\left(-L_1\ \cos\ \Omega t + L_3\ \sin\ \Omega t\right)\\
\Delta M_y &= -2\frac{\Omega r^2}{U}\left(L_1 \sin\ \Omega t + L_3 \cos\ \Omega t\right) = -\frac{\Omega r^2}{V_\infty}\Delta L_y\\
\Delta M_z &= 2\frac{\Omega r^2}{U}\left(-L_1\ \cos\ \Omega t + L_3\ \sin\ \Omega t\right) = \frac{\Omega r^2}{V_\infty}\Delta L_z
\end{aligned} \qquad [5.30]$$

and further substituting from Eqn. 5.27 and Eqn. 5.28 we obtain

$$\begin{aligned}
\Delta L_y = 2\frac{V_\infty}{U}\Big(&-f_1 \cos\ \Omega t\ \sin\ \Omega t + f_2 \sin^2 \Omega t +\\
&+ f_1 \sin\ \Omega t\ \cos\ \Omega t + f_2 \cos^2 \Omega t\Big) = 2\frac{V_\infty}{U} f_2
\end{aligned}$$

$$\Delta L_z = 2\frac{V_\infty}{U}\left(f_1 \cos^2 \Omega t \; - f_2 \;\sin\, \Omega t \;\cos\, \Omega t + \right.$$
$$\left. + f_1 \sin^2 \Omega t + f_2 \cos\; \Omega t \;\sin\; \Omega t\right) = 2\frac{V_\infty}{U} f_1$$
$$\Delta M_y = -2\frac{\Omega r^2}{U} f_2$$
$$\Delta M_z = 2\frac{\Omega r^2}{U} f_1 \qquad [5.31]$$

Using another method and substituting from Eqn. 5.26, we obtain

$$\Delta L_y = a_0 \rho \; c_0 \frac{V_\infty}{U}\left(V_\infty^2 \Psi - V_\infty \dot{y}_1 + \Omega r^2 \dot{\Theta}\right)$$
$$\Delta L_z = a_0 \rho \; c_0 \frac{V_\infty}{U}\left(V_\infty^2 \Theta - V_\infty \dot{z}_1 - \Omega r^2 \dot{\Psi}\right)$$
$$\Delta M_y = -a_0 \rho \; c_0 \frac{\Omega r^2}{U}\left(V_\infty^2 \Psi - V_\infty \dot{y}_1 + \Omega r^2 \dot{\Theta}\right) \qquad [5.32]$$
$$\Delta M_z = a_0 \rho \; c_0 \frac{\Omega r^2}{U}\left(V_\infty^2 \Theta - V_\infty \dot{z}_1 - \Omega r^2 \dot{\Psi}\right)$$

To reach the total aerodynamic forces and moments of the propeller hub, the local section forces and moments of Eqn. 5.32 must be integrated from the hub to the blade tip radius. For this purpose, the blade integrals are defined. The fundamental formulations of these integrals according to [4] are

$$A_1 = \int_0^1 \frac{c_0}{c_r} \; \frac{\mu^2}{\sqrt{\mu^2 + \eta^2}} \; d\eta$$
$$A_2 = \int_0^1 \frac{c_0}{c_r} \; \frac{\mu \; \eta^2}{\sqrt{\mu^2 + \eta^2}} \; d\eta \qquad [5.33]$$
$$A_3 = \int_0^1 \frac{c_0}{c_r} \; \frac{\eta^4}{\sqrt{\mu^2 + \eta^2}} \; d\eta$$

where c_r is blade reference chord, μ is propeller advance ratio defined as $\mu = (V_\infty / \Omega R) = (J_0 / \pi)$ and η is blade dimensionless radius defined as $\eta = (r/R)$. Note that the blade integrals of Eqn. 5.33 use the lift curve slope of $a_0 = 2\pi$. Integrals are dependent on the propeller geometry (chord) and the advance ratio only. The values of integrals for the constant-chord blades are shown in Figure 5.9.

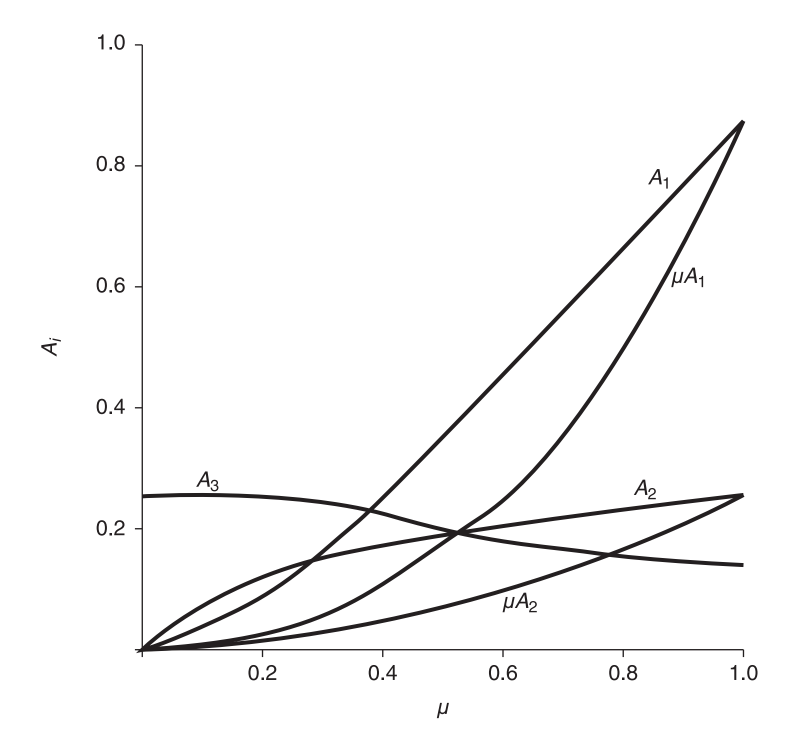


Figure 5.9 **Blade integrals (fundamental formulation of [4])**

The integration of Eqn. 5.32 leads to the total aerodynamic forces and moments of the propeller hub:

$$\begin{aligned}
P_Y &= q_\infty F_p \left(\frac{4\Omega^2 R c_r}{V_\infty^2} \mu A_1 \Psi - \frac{4\Omega c_r}{V_\infty} A_1 \frac{\dot{y}_1}{V_\infty} + \frac{4\Omega R}{V_\infty} A_2 \frac{\dot{\Theta} c_r}{V_\infty} \right) \\
P_Z &= q_\infty F_p \left(\frac{4\Omega^2 R c_r}{V_\infty^2} \mu A_1 \Theta - \frac{4\Omega c_r}{V_\infty} A_1 \frac{\dot{z}_1}{V_\infty} - \frac{4\Omega R}{V_\infty} A_2 \frac{\dot{\Psi} c_r}{V_\infty} \right) \\
M_{Y,P} &= q_\infty F_p D_P \left(-\frac{2\Omega^2 R c_r}{V_\infty^2} \mu A_2 \Psi + \frac{2\Omega c_r}{V_\infty} A_2 \frac{\dot{y}_1}{V_\infty} - \frac{2\Omega R}{V_\infty} A_3 \frac{\dot{\Theta} c_r}{V_\infty} \right) \\
M_{Z,P} &= q_\infty F_p D_P \left(\frac{2\Omega^2 R c_r}{V_\infty^2} \mu A_2 \Theta - \frac{2\Omega c_r}{V_\infty} A_2 \frac{\dot{z}_1}{V_\infty} - \frac{2\Omega R}{V_\infty} A_3 \frac{\dot{\Psi} c_r}{V_\infty} \right)
\end{aligned} \qquad [5.34]$$

These equations can be rearranged using a system of aerodynamic derivatives (e.g., $c_{y\Psi} = (4\Omega c_r/V_\infty).A_1$; $c_{zr} = -(4\Omega c_r/V_\infty).A_2$; $c_{mq} = -(2\Omega c_r/V_\infty).\ A_3$; etc.).

The complete system of equations with 16 derivatives is listed in Eqn. 5.35, although four derivatives are usually neglected, as expressed in Eqn. 2.12:

$$
\begin{aligned}
P_Y &= q_\infty F_p\left(c_{y\Theta}\Theta^* + c_{y\Psi}\Psi^* + c_{yq}\frac{\dot{\Theta}^* R}{V_\infty} + c_{yr}\frac{\dot{\Psi}^* R}{V_\infty}\right)\\
P_Z &= q_\infty F_p\left(c_{z\Theta}\Theta^* + c_{z\Psi}\Psi^* + c_{zq}\frac{\dot{\Theta}^* R}{V_\infty} + c_{zr}\frac{\dot{\Psi}^* R}{V_\infty}\right)\\
M_{Y,P} &= q_\infty F_P D_P\left(c_{m\Theta}\Theta^* + c_{m\Psi}\Psi^* + c_{mq}\frac{\dot{\Theta}^* R}{V_\infty} + c_{mr}\frac{\dot{\Psi}^* R}{V_\infty}\right)\\
M_{Z,P} &= q_\infty F_P D_P\left(c_{n\Theta}\Theta^* + c_{n\Psi}\Psi^* + c_{nq}\frac{\dot{\Theta}^* R}{V_\infty} + c_{nr}\frac{\dot{\Psi}^* R}{V_\infty}\right)
\end{aligned}
\qquad [5.35]
$$

The application of the fundamental formulation of the aerodynamics using the blade integrals from Eqn. (5.33) is limited to the four-blade propellers and blade lift curve slopes of $a_0 = 2\pi$. It also does not account for other important factors.

5.5 Lift lag effect

The blade integrals of Eqn. 5.33 account for the in-phase aerodynamic effects only. However, similar to the oscillating wing, precession movements in the rotating propellers give rise to vortices that cause lift lag with respect to the quasi-steady value. Each blade of the propeller creates a helical wake. These wakes contain two frequency components because the propeller rotation and propeller hub precession frequencies are different in general. The modification of the quasi-steady lift to account for the lag effect is performed using the simplified solution proposed in reference [4]. This solution was verified via experiments and found to be satisfactorily accurate.

Let us consider the components of Eqn. 5.27 in the form of

$$
\begin{aligned}
f_1 &= f_1 e^{j\omega t}\\
f_2 &= f_2 e^{j\omega t}
\end{aligned}
\qquad [5.36]
$$

The blade section lift then becomes

$$
L_1 = -\bar{f}_1 e^{j\omega t}\ \frac{e^{j\Omega t} + e^{-j\Omega t}}{2} + \bar{f}_2 e^{j\omega t}\ \frac{e^{j\Omega t} - e^{-j\Omega t}}{2j} \qquad [5.37]
$$

Equation 5.37 shows that the two mentioned frequencies are $(\Omega+\omega)$ and $(\Omega-\omega)$ where ω is frequency of precession. To account for such a wake, all of the wake effects are represented by separate complex wakes with circulation functions, as are ordinarily used for the oscillating wing (Theodorsen function). The modified lift including lag effect becomes

$$L_1' = -\left[\frac{(F_1 + jG_1)}{2}\right]\left(\bar{f}_1 + j\,\bar{f}_2\right)e^{j(\Omega+\omega)t} - \left[\frac{(F_2 + jG_2)}{2}\right]\left(\bar{f}_1 - j\,\bar{f}_2\right)e^{-j(\Omega-\omega)t} \quad [5.38]$$

where the F and G terms are the real and imaginary parts of the Theodorsen function $F(k)+j.G(k)$, and the reduced frequencies of the blade section for the first and second terms are

$$\begin{aligned} k_1 &= \frac{(\Omega+\omega)c_0}{2\sqrt{V_\infty^2 + \Omega^2 r^2}} \\ k_2 &= \frac{(\Omega-\omega)c_0}{2\sqrt{V_\infty^2 + \Omega^2 r^2}} \end{aligned} \quad [5.39]$$

For the backward mode, Eqn. 5.38 becomes

$$\begin{aligned} L_1' = {} & \frac{F_1+F_2}{2}(-f_1\cos\Omega t + f_2\sin\Omega t) + \frac{G_1+G_2}{2}(f_1\sin\Omega t + f_2\cos\Omega t) + \\ & + \frac{G_1-G_2}{2\omega}(-\dot{f}_1\cos\Omega t + \dot{f}_2\sin\Omega t) - \frac{F_1-F_2}{2\omega}(\dot{f}_1\sin\Omega t + \dot{f}_2\cos\Omega t) \end{aligned} \quad [5.40]$$

and similarly

$$\begin{aligned} L_3' = {} & \frac{F_1+F_2}{2}(f_1\sin\Omega t + f_2\cos\Omega t) - \frac{G_1+G_2}{2}(-f_1\cos\Omega t + f_2\sin\Omega t) + \\ & + \frac{G_1-G_2}{2\omega}(\dot{f}_1\sin\Omega t + \dot{f}_2\cos\Omega t) + \frac{F_1-F_2}{2\omega}(-\dot{f}_1\cos\Omega t + \dot{f}_2\sin\Omega t) \end{aligned} \quad [5.41]$$

Now, we substitute for L_1 and L_3 into Eqn. 5.30 and obtain the propeller section forces including the lag effect as

$$\begin{aligned} \Delta L_y' &= \frac{F_1+F_2}{2}\Delta L_y + \frac{G_1+G_2}{2}\Delta L_z + \frac{G_1-G_2}{2\omega}\Delta\dot{L}_y - \frac{F_1-F_2}{2\omega}\Delta\dot{L}_z \\ \Delta L_z' &= \frac{F_1+F_2}{2}\Delta L_z - \frac{G_1+G_2}{2}\Delta L_y + \frac{G_1-G_2}{2\omega}\Delta\dot{L}_z + \frac{F_1-F_2}{2\omega}\Delta\dot{L}_y \end{aligned} \quad [5.42]$$

The lag effect reduces the quasi-steady lift magnitude and turns it in the direction of rotation by the angle $\tan^{-1}(|G_1+G_2|/(F_1+F_2))$. The practical applications commonly use the first two terms only because the last ones involve the differences (F_1-F_2) and (G_1-G_2) and, therefore, have smaller effects that are unimportant in practical applications.

By considering the fact that the ω is small with respect to Ω and that these terms use the average values $(F_1+F_2)/2$ and $(G_1+G_2)/2$, respectively, we can use common values for F and G based on the reduced frequency involving Ω only:

$$k=\frac{\Omega c_0}{2\sqrt{V_\infty^2+\Omega^2 r^2}} \qquad [5.43]$$

In practical applications, the lift-lag effect is included in the aerodynamic derivatives by means of the Theodorsen function. According to the components of $F(k)+j.G(k)$, we can separate the derivatives as 'in-phase' and 'out-of-phase' contributions. The local blade section reduced frequency used for the $F(k)+j.G(k)$ is defined as

$$k_P=\frac{c_0}{2R\sqrt{\mu^2+\eta^2}} \qquad [5.44]$$

The components of the Theodorsen function that include the lift lag effect are calculated using Bessel functions of the first and second kind, zero and first order as

$$F(k)=\frac{Bj_1(Bj_1+By_0)+By_1(By_1-Bj_0)}{(Bj_1+By_0)^2+(By_1-Bj_0)^2}$$
$$G(k)=-\frac{By_1By_0+Bj_1Bj_0}{(Bj_1+By_0)^2+(By_1-Bj_0)^2} \qquad [5.45]$$

The theodorsen function is good approximation of the lift lag effect for high propeller advance ratios; however, for smaller advance ratios the circulation function is altered due to the helical pattern of the wake. The modified function for a propeller with a helical wake is derived in reference [20]. The results indicate that the lift lag effect for the small advance ratios may be much larger than is predicted by the Theodorsen function. The experimental investigations of Bland and Bennett [21] found a lag of 24° for the lowest advance ratios compared to the theoretical value of 13° based on the Theodorsen function.

5.6 Blade lift curve slope and mach number effects

The integration of the propeller hub aerodynamic forces using the blade integrals of Eqn. 5.33 assumes a theoretical blade lift curve with $a_0 = 2\pi$ and also incompressible flow. Accounting for the compressibility and finite blade length effects is possible using a correction of the lift curve slope a_0.

The compressibility may be taken into account, as suggested in reference [4], through two factors. The first factor is the Prantl-Glauert correction for the compressibility that considers the local blade section Mach number M_r resulting from the velocity $\sqrt{V_\infty^2 + \Omega^2 r^2}$. The correction factor can be expressed as

$$\frac{1}{\sqrt{1-M_r^2}} \quad [5.46]$$

As is apparent from Eqn. 5.46 this correction factor increases the propeller blade integrals and, thus, has a destabilising effect.

The second correction factor is the compressible flow aspect-ratio correction, which can be expressed as

$$\frac{A_r\sqrt{1-M_r^2}}{2+A_r\sqrt{1-M_r^2}} \quad [5.47]$$

where A_r is blade aspect ratio defined as

$$A_r = \frac{R}{c_r \int_0^1 \left(\frac{c}{c_r}\right) d\eta} \quad [5.48]$$

The resulting correction to the compressibility then becomes

$$\frac{1}{\sqrt{1-M_r^2}} \frac{A_r\sqrt{1-M_r^2}}{2+A_r\sqrt{1-M_r^2}} = \frac{A_r}{2+A_r\sqrt{1-M_r^2}} \quad [5.49]$$

which may be rewritten into the more appropriate form, which uses the forward flight Mach number, as

$$\frac{A_r}{2+A_r\sqrt{1-M^2\left(1+\frac{\eta^2}{\mu^2}\right)}} \quad [5.50]$$

Both corrections for the lift lag and compressibility are incorporated into the blade integrals in Eqn. 5.33. Due to the Theodorsen function components, the number of integrals is doubled. $I_{(1-3)}$ are the 'in-phase' integrals and include the $F(k)$ component, whereas $J_{(1-3)}$ are the 'out-of-phase' integrals and include the $G(k)$ component. The blade integrals are expressed as

$$
\begin{aligned}
I_1 &= \frac{\mu^2 A_r}{c_r} \int_0^1 \frac{c_0(\eta)\, F(k_P)}{\sqrt{\mu^2+\eta^2}\left[2 + A_r \sqrt{1 - M^2\left(1+\frac{\eta^2}{\mu^2}\right)}\right]} d\eta \\
J_1 &= \frac{\mu^2 A_r}{c_r} \int_0^1 \frac{c_0(\eta)\, G(k_P)}{\sqrt{\mu^2+\eta^2}\left[2 + A_r \sqrt{1 - M^2\left(1+\frac{\eta^2}{\mu^2}\right)}\right]} d\eta \\
I_2 &= \frac{\mu A_r}{c_r} \int_0^1 \frac{\eta^2 c_0(\eta)\, F(k_P)}{\sqrt{\mu^2+\eta^2}\left[2 + A_r \sqrt{1 - M^2\left(1+\frac{\eta^2}{\mu^2}\right)}\right]} d\eta \\
J_2 &= \frac{\mu A_r}{c_r} \int_0^1 \frac{\eta^2 c_0(\eta)\, G(k_P)}{\sqrt{\mu^2+\eta^2}\left[2 + A_r \sqrt{1 - M^2\left(1+\frac{\eta^2}{\mu^2}\right)}\right]} d\eta \\
I_3 &= \frac{A_r}{c_r} \int_0^1 \frac{\eta^4 c_0(\eta)\, F(k_P)}{\sqrt{\mu^2+\eta^2}\left[2 + A_r \sqrt{1 - M^2\left(1+\frac{\eta^2}{\mu^2}\right)}\right]} d\eta \\
J_3 &= \frac{A_r}{c_r} \int_0^1 \frac{\eta^4 c_0(\eta)\, G(k_P)}{\sqrt{\mu^2+\eta^2}\left[2 + A_r \sqrt{1 - M^2\left(1+\frac{\eta^2}{\mu^2}\right)}\right]} d\eta
\end{aligned}
\qquad [5.51]
$$

where the local blade reduced frequency k_p is given by Eqn. 5.43 and blade aspect ratio A_r is given by Eqn. 5.48. The aerodynamic derivatives calculated using these integrals then become

$$
\begin{aligned}
c_{z\Theta} &= -\left(\frac{4\Omega c_r}{V_\infty}\right) I_1 \qquad & c_{zq} &= \left(\frac{4\Omega c_r}{V_\infty}\right) J_2 \\
c_{m\Theta} &= -\left(\frac{2\Omega c_r}{V_\infty}\right) J_2 \qquad & c_{mq} &= -\left(\frac{2\Omega c_r}{V_\infty}\right) I_3
\end{aligned}
$$

$$c_{y\Theta} = -\left(\frac{4\Omega c_r}{V_\infty}\right) J_1 \qquad c_{yq} = -\left(\frac{4\Omega c_r}{V_\infty}\right) I_2$$
$$c_{n\Theta} = -\left(\frac{2\Omega c_r}{V_\infty}\right) I_2 \qquad c_{nq} = -\left(\frac{2\Omega c_r}{V_\infty}\right) J_3 \qquad [5.52]$$

Other derivatives are apparent from the symmetric or antisymmetric conditions according to Eqn. 2.11.

Practical applications ordinarily require further corrections of the blade integrals. First, real propellers generate lift within the thrusting part of the blade only and not from the hub, as expected in Eqn. 5.51. Therefore, the lower limit of the integrals is shifted toward the value of η_0 which is the dimensionless radius of the propeller boss:

$$\eta_0 = \frac{r_0}{R} \qquad [5.53]$$

In this case, the propeller aspect ratio must be adjusted accordingly:

$$A_r = \frac{R}{c_r} \frac{(1-\eta_0)^2}{\int_{\eta_0}^{1} \left(\frac{c}{c_r}\right) d\eta} \qquad [5.54]$$

Further correction accounts for the finite blade length effect, which is possible via correction of the lift curve slope a_0. The theoretical value of 2π may be corrected either by the effective value a_{0eff} given for the blade or by the real blade lift curve slope distribution $a_0(\eta)$. It is obvious that the latter approach is more accurate because it can account for the cross-section of the blade from the boss to the tip, the reduction of the lift due to the induced effect at the tip region, etc. Optionally, the lift curve slope may be set also using some typical blade lift distribution profiles. Figure 5.10 shows the lift curve slope distribution of two real propellers:

1. Avia AV-844 (4-blades, blade radius R = 1.041 m, $c_{L\,eff}^{\alpha} = 6.2478$)
2. Avia AV-725 (5-blades, blade radius R = 1.150 m, $c_{L\,eff}^{\alpha} = 7.7278$)

As apparent from Figure 5.10, the lift slopes are rather different. In some cases, such as the AV-844 propeller, the use of the effective value may be reasonable. In this case, the default value of 2π would be reasonable as well. However, for the other propellers, such as the AV-725 the use of the effective value may be insufficient, let alone the default value. To demonstrate the influence of the blade lift spanwise distribution,

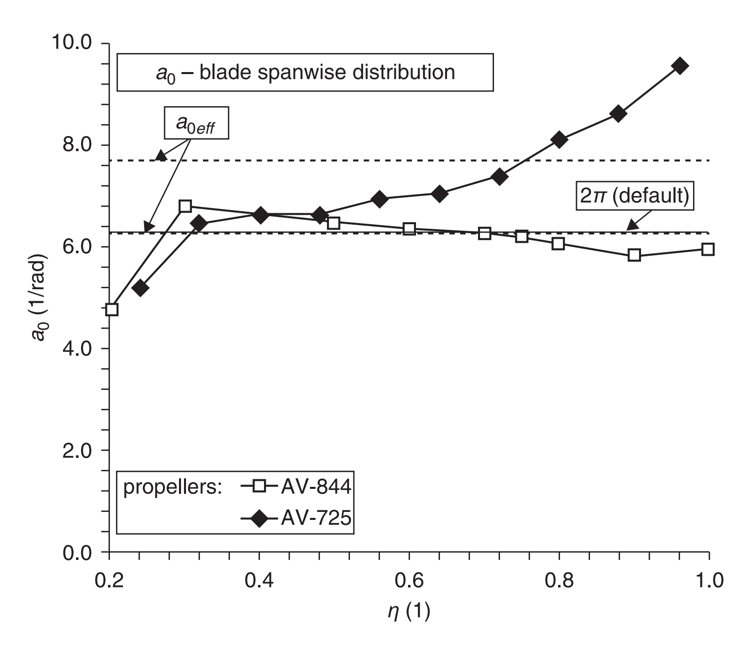


Figure 5.10 **Lift curve slope distribution of AV-844 and AV-725 propellers**

the aerodynamic derivatives of both propellers calculated using Eqn. 5.55 are presented in Figure 5.11 and the following figures. The figures include constant spanwise values of $a_0 = 2\pi$; $a_0 = a_{0eff}$ and the real spanwise variable distribution $a_0 = a_0(\eta)$.

From the aerodynamic derivatives presented in Figures 5.11–5.16 we can see that the effective value a_{0eff} may either decrease (e.g., AV-844 propeller) or increase (e.g., AV-725 propeller) compare to the profile theoretical (2π) value. As is also apparent from Figure 5.10, the difference may be either small (AV-844 propeller) or large (AV-725 propeller). In the former example, the default value should be applicable; however, in the latter example, the default value should not be used. The real lift slope distribution $a_0(\eta)$ gives smaller values for all derivatives than both the (2π) and a_{0eff} values. Thus, the usage of a_{0eff} is applicable because it gives conservative results. Obviously, the real distribution $a_0(\eta)$ gives more accurate and reliable results.

The influence of the a_0 spanwise blade distribution on the whirl flutter critical speed is demonstrated in Figure 5.17, which shows the whirl flutter analysis via the V-g-f diagram of the EV-55M twin turboprop aircraft (see Chapter 7) with PT6A-21 engines and AV-844 propellers.

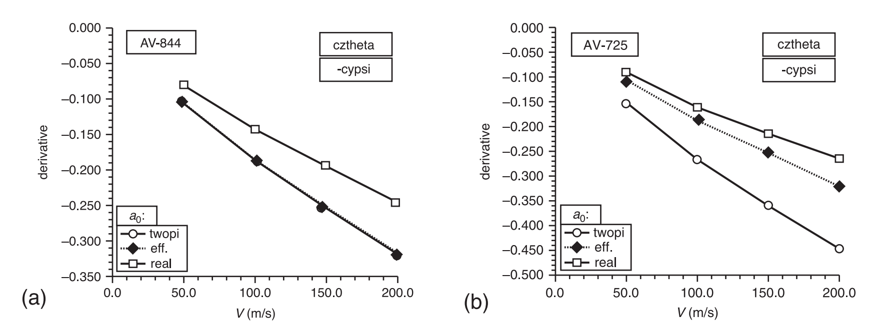


Figure 5.11 Aerodynamic derivatives of the (a) AV-844 and (b) AV-725 propellers

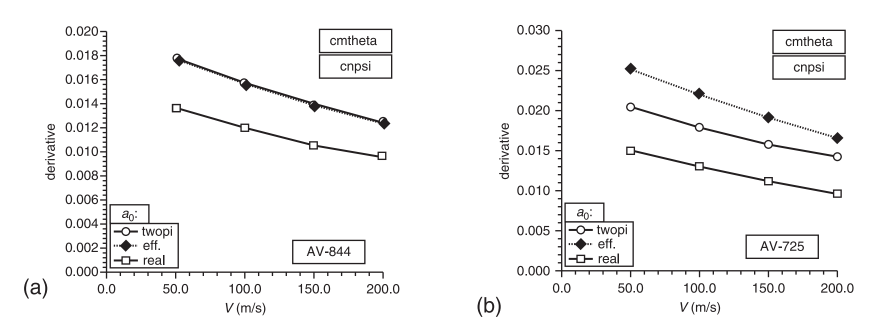


Figure 5.12 Aerodynamic derivatives of the (a) AV-844 and (b) AV-725 propellers

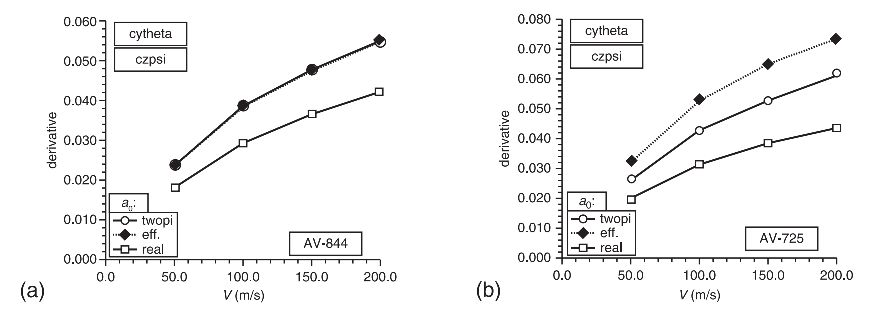


Figure 5.13 Aerodynamic derivatives of the (a) AV-844 and (b) AV-725 propellers

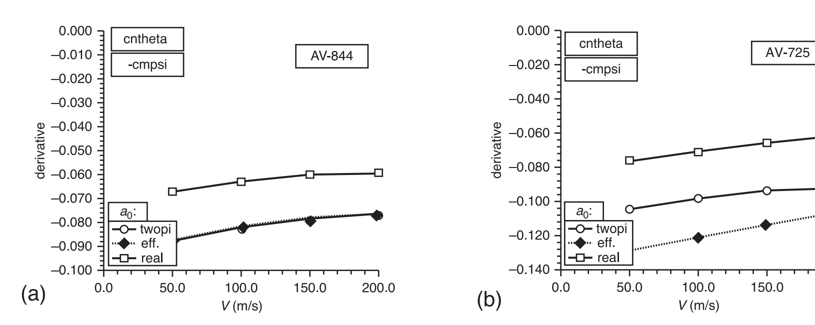


Figure 5.14 Aerodynamic derivatives of the (a) AV-844 and (b) AV-725 propellers

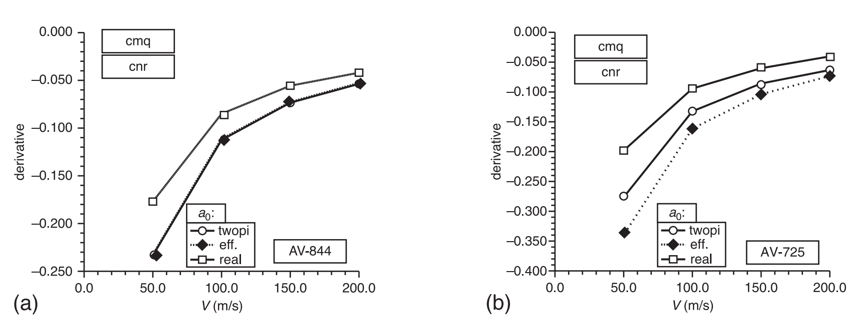


Figure 5.15 Aerodynamic derivatives of the (a) AV-844 and (b) AV-725 propellers

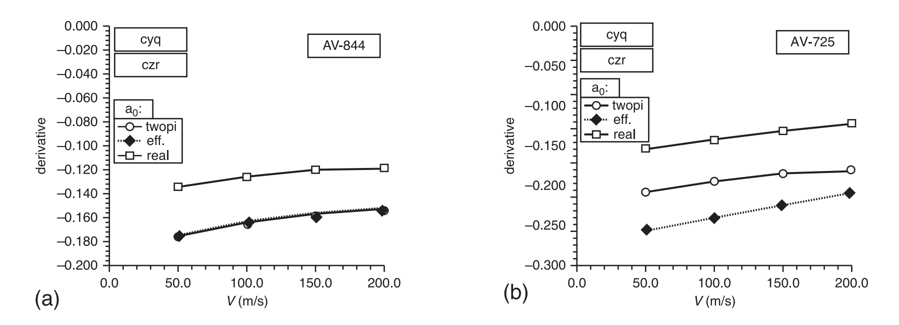


Figure 5.16 Aerodynamic derivatives of the (a) AV-844 and (b) AV-725 propellers

The example represents the case of 50% fuel loading, fuselage loaded by two pilots and two passengers in the third row and statically balanced control surfaces. The engine attachment stiffnesses were reduced by 50% with respect to the nominal for both the vertical and lateral vibrations to reach the flutter speed. In the V-g diagram of Figure 5.17 there is the flutter indicated on the mode #2 which is the engine vertical vibrations mode. The solid lines with markers show the analysis using the effective value of the propeller lift curve slope, while the dotted lines show the analysis using the real distribution of the lift curve slope. There is a visible difference of the modes #2 and #4 in the V-g diagram, which are the engine vertical and lateral vibration modes. Otherwise, the differences are very small. When considering the effective value of the lift curve slope, the flutter speed is $V_{FL} = 166.6$ [m.s^{-1}], and when considering the real lift curve slope distribution the flutter speed becomes $V_{FL} = 182.0$ [m.s^{-1}], which represents an increase in the flutter speed of 9.2%. The flutter frequency is $f_{FL} = 5.8$ [Hz] and the difference between both cases is barely noticeable.

Further explanations of the influence of the a_0 blade spanwise distribution on the whirl flutter characteristics are provided in Figure 5.18. It shows the stability margins for specific flutter velocity. These margins were calculated using the optimisation approach of the whirl flutter analysis (see Chapter 6). The margins define the values of the vertical and lateral engine vibration mode frequencies required to reach the required

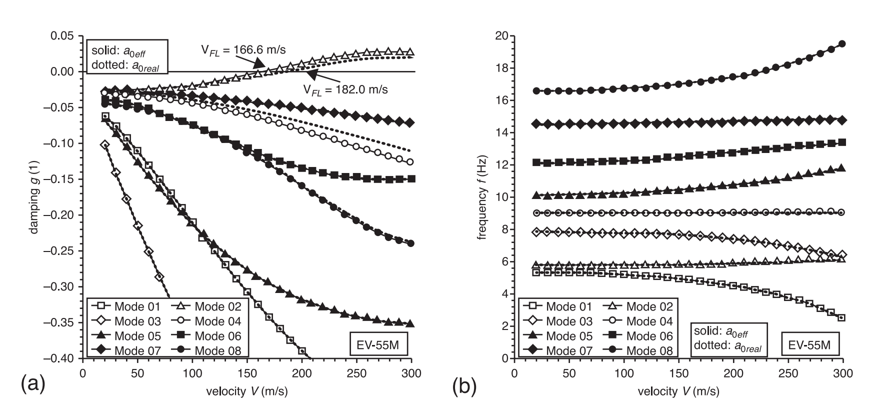


Figure 5.17 Example of the influence of the blade lift curve slope distribution to the whirl flutter speed: (a) *V-g* diagram, (b) *V-f* diagram

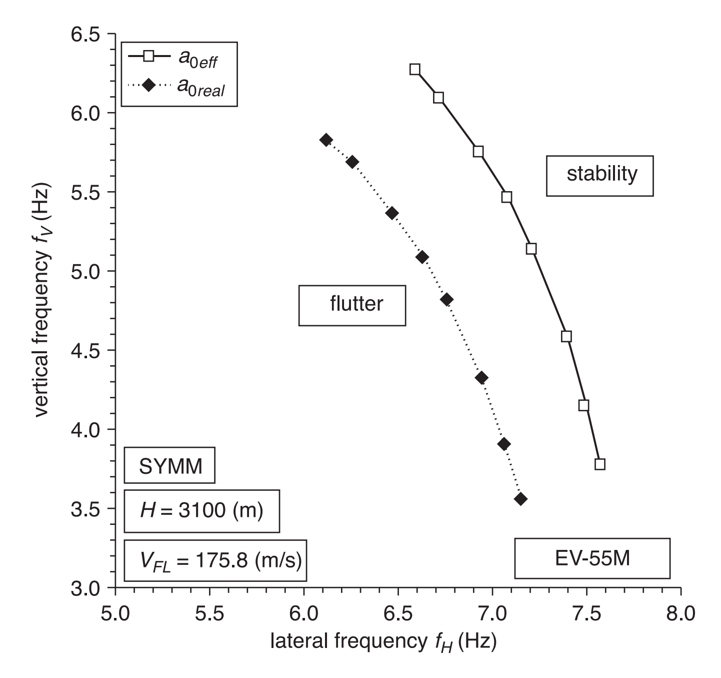


Figure 5.18 **Example of the influence of the blade lift curve slope distributions on the whirl flutter stability margins**

flutter speed. Again, the real spanwise distribution of the lift curve slope gives lower margin frequencies and, thus, higher reserves in terms of stability. Conversely, the effective value of the lift curve slope represents a conservative estimate. The differences between the margin frequencies calculated from the RMS values of the both vertical and lateral contributions range from 5.5% to 7.1%.

5.7 Correction to number of propeller blades

The final correction to the blade integrals of Eqn. 5.33 is provided to account for the number of propeller blades. The integrals in Eqn. 5.33 were derived for four blades. If the number of blades is different, the integrals must be corrected by a factor of (N_b/4). The final formulations of the blade integrals, including all of the described corrections, now become

$$I_1 = \left(\frac{N_b}{4}\right)\left(\frac{1}{2\pi}\right)\frac{\mu^2 A_r}{c_r}\int_{\eta_0}^{1}\frac{a_0(\eta)c_0(\eta)F(k_P)}{\sqrt{\mu^2+\eta^2}\left[2+A_r\sqrt{1-M^2\left(1+\frac{\eta^2}{\mu^2}\right)}\right]}d\eta$$

$$J_1 = \left(\frac{N_b}{4}\right)\left(\frac{1}{2\pi}\right)\frac{\mu^2 A_r}{c_r}\int_{\eta_0}^{1}\frac{a_0(\eta)c_0(\eta)G(k_P)}{\sqrt{\mu^2+\eta^2}\left[2+A_r\sqrt{1-M^2\left(1+\frac{\eta^2}{\mu^2}\right)}\right]}d\eta$$

$$I_2 = \left(\frac{N_b}{4}\right)\left(\frac{1}{2\pi}\right)\frac{\mu A_r}{c_r}\int_{\eta_0}^{1}\frac{\eta^2 a_0(\eta)c_0(\eta)F(k_P)}{\sqrt{\mu^2+\eta^2}\left[2+A_r\sqrt{1-M^2\left(1+\frac{\eta^2}{\mu^2}\right)}\right]}d\eta$$

$$J_2 = \left(\frac{N_b}{4}\right)\left(\frac{1}{2\pi}\right)\frac{\mu A_r}{c_r}\int_{\eta_0}^{1}\frac{\eta^2 a_0(\eta)c_0(\eta)G(k_P)}{\sqrt{\mu^2+\eta^2}\left[2+A_r\sqrt{1-M^2\left(1+\frac{\eta^2}{\mu^2}\right)}\right]}d\eta$$

$$I_3 = \left(\frac{N_b}{4}\right)\left(\frac{1}{2\pi}\right)\frac{A_r}{c_r}\int_{\eta_0}^{1}\frac{\eta^4 a_0(\eta)c_0(\eta)F(k_P)}{\sqrt{\mu^2+\eta^2}\left[2+A_r\sqrt{1-M^2\left(1+\frac{\eta^2}{\mu^2}\right)}\right]}d\eta$$

$$J_3 = \left(\frac{N_b}{4}\right)\left(\frac{1}{2\pi}\right)\frac{A_r}{c_r}\int_{\eta_0}^{1}\frac{\eta^4 a_0(\eta)c_0(\eta)G(k_P)}{\sqrt{\mu^2+\eta^2}\left[2+A_r\sqrt{1-M^2\left(1+\frac{\eta^2}{\mu^2}\right)}\right]}d\eta \qquad [5.55]$$

To avoid the problems with the Mach number correction for the blade tip at supersonic speed (e.g., propeller overspeed) the cut-off value of the compressible lift curve slope is suggested in reference [19]. For the condition of

$$M^2\left(1+\frac{\eta^2}{\mu^2}\right) > 1-\left(\frac{a_0}{a_M}\right)^2 \qquad [5.56]$$

the following correction is applied

$$M^2\left(1+\frac{\eta^2}{\mu^2}\right) = 1-\left(\frac{a_0}{a_M}\right)^2 \qquad [5.57]$$

where a_M is the maximum blade airfoil transonic lift curve slope.

5.8 Influence of wing flexibility

The propeller and nacelle system that was considered in the previous sections assumed flexible mounted engines on rigid wings or other parts of the aircraft. This assumption is useful when describing the influences of the particular parameters on the whirl flutter. However, in general, the flexibility of the wing or other supporting structures influences the dynamic characteristics of the entire system, which consequently influences whirl flutter characteristics. These effects were studied by Zwaan and Bergh [22]. In general, the influences of wing flexibility were found (with some exceptions) to be stabilizing. These effects are summarised in Figure 5.20. This figure shows the flutter margins with respect to the required pitch and yaw stiffnesses for stability at specific flight conditions. It includes three cases, as shown in Figure 5.19: (a) rigid wing with no additional degrees of freedom, (b) the influence of wing bending with additional translational degree of freedom, and (c) the influence of both wing bending and torsion with additional translational and rotational degrees of freedom. In the two latter cases, the aerodynamic forces on both the propellers and wings are considered.

The first case of the rigid wing in Figure 5.19(a) gives a similar stability margin as Figure 2.9, etc. The stability margin is terminated on both sides by the condition of static divergence, and the most critical point is the one on the diagonal (point A) representing the state of $K_\Psi = K_\Theta$ or $(\omega_\Psi/\omega_\Theta) = 1.0$. The second case, including wing bending (Figure 5.19(b)), always gives a greater stability margin compared to the first case. This increased margin is caused by damping forces acting on the wing. The greatest stabilisation effect is given at points B_1 and B_2 when the whirl frequency coincides with the bending frequency $(\omega_\Psi = \omega_h)$ or $(\omega_\Theta = \omega_h)$. At

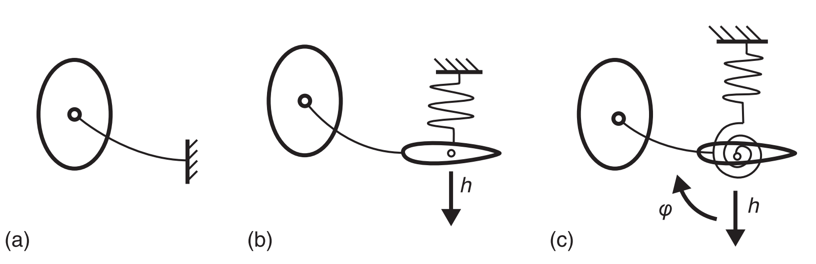


Figure 5.19 **Consideration of the wing flexibility: (a) rigid wing, (b) wing bending flexibility, (c) wing bending and torsional flexibility [23]**

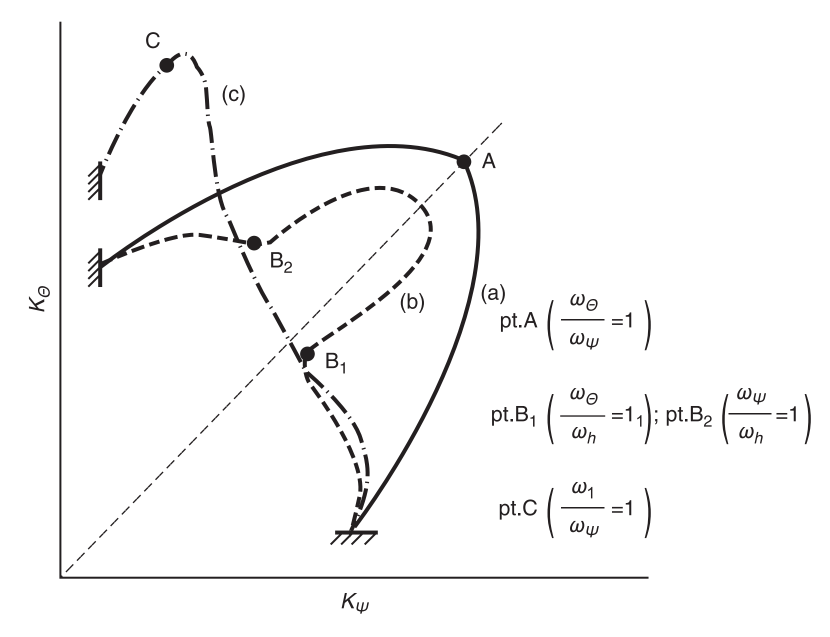


Figure 5.20 **Influence of the wing flexibility on the whirl flutter [23]: (a) rigid wing, (b) wing bending flexibility, (c) wing bending and torsional flexibility**

these points, the whirl motion of the propeller and nacelle drives the wing at the resonant amplitude, and thus it absorbs most of the energy because the system frequency is close to the damper frequency.

The third case (Figure 5.19(c)) includes both wing bending and torsion. In this case, we consider two coupled bending/torsional modes at the frequencies ω_1 and ω_2. The frequency of the first coupled mode ω_1 is considered approximately the same as the bending frequency of the former case ($\omega_1 = \omega_h$). The stability boundary of this case shows the exception to the claim that wing flexibility is stabilizing. This exception is marked in the figure as point C. In fact, the wing torsional or coupled bending torsional mode may substitute the propeller/nacelle pitch mode because it involves the propeller and nacelle pitching motion. The state when the frequency of the wing mode is close to the propeller/nacelle yawing frequency is similar to the state of $(\omega_\Psi/\omega_\Theta) = 1.0$ of the rigid wing case. The most destabilising effect is when the wing frequency and propeller/nacelle yawing frequency coincide ($\omega_1 = \omega_\Psi$).

The analytical solution of whirl flutter, including wing bending and torsional flexibility, is given in reference [24], which considers a system

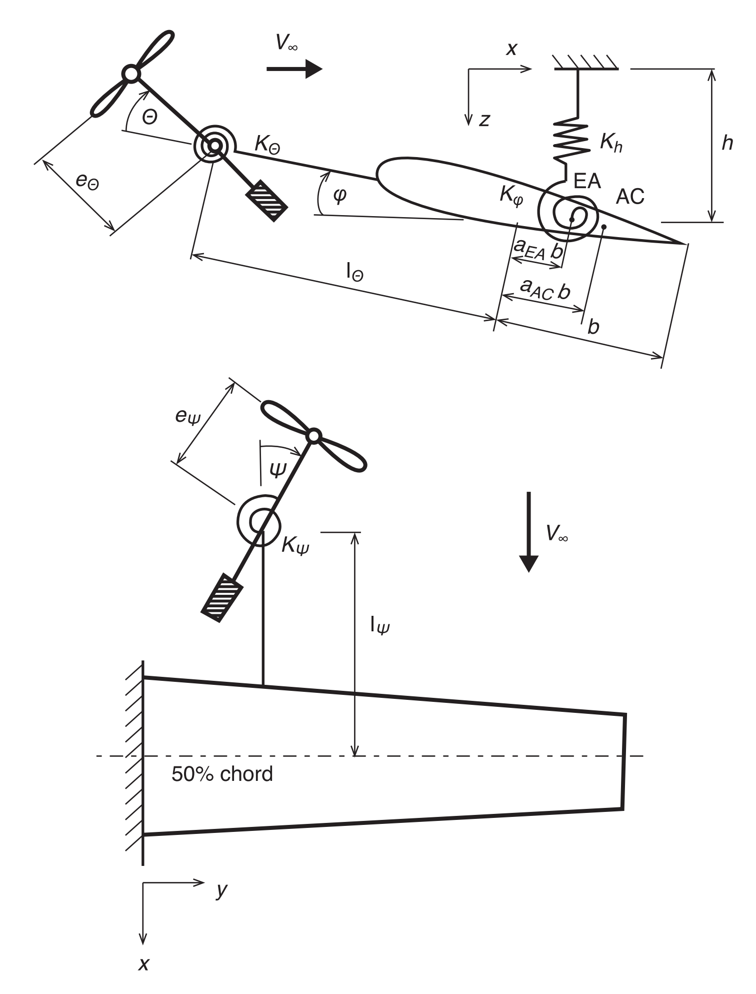


Figure 5.21 **Analytical model with four DOFs including wing bending and torsional flexibility [24]**

with four DOFs, including the pitching and yawing of the propeller and nacelle and the unswept wing bending and torsion, as shown in Figure 5.21. The solution includes both the propeller and wing aerodynamic forces; however, the aerodynamic interference effects between the wing and nacelle are neglected.

The total kinetic energy of the system is

$$E_K = E_{KW} + E_{KP} + E_{K\Omega} \quad [5.58]$$

where the energy components are the contributions of the wing and rigid engine, non-rotating propeller and engine system and finally the contribution of the rotating propeller, including the gyroscopic precession. The kinetic energy of the wing is

$$E_{KW} = \frac{1}{2}\int_{-b}^{b}\int_{0}^{L} m_W(x,y)\dot{z}_W^2\, dx\, dy \qquad [5.59]$$

where deflection in the z-direction from bending and torsion is given as

$$z(x, y, t) = h + (x - a_{EA}b)\varphi \qquad [5.60]$$

Using the mode shapes and modal generalised coordinates, the bending and torsional deflections are

$$\begin{aligned} h(y, t) &= u_h(y)q_h(t) \\ \varphi(y, t) &= u_\varphi(y)q_\varphi(t) \end{aligned} \qquad [5.61]$$

Now, by substituting Eqn. 5.60 and Eqn. 5.61 into Eqn. 5.59, the wing kinetic energy becomes

$$E_{KW} = \frac{1}{2}M_W\dot{q}_h^2 + S_{\varphi W}\dot{q}_h\dot{q}_\varphi + \frac{1}{2}J_{\varphi W}\dot{q}_\varphi^2 \qquad [5.62]$$

where the wing inertia parameters are

$$\begin{aligned} M_W &= L\int_0^1 m_W(y)u_h^2 dy \\ S_{\varphi W} &= L\int_0^1 s_{\varphi W}(y)u_h u_\varphi dy \\ J_{\varphi W} &= L\int_0^1 j_{\varphi W}(y)u_\varphi^2 dy \end{aligned} \qquad [5.63]$$

and the wing sectional inertia parameters are

$$\begin{aligned} m_W &= \int_{-b}^{b} m_W(x,y)dx \\ s_{\varphi W} &= \int_{-b}^{b} m_W(x,y)(x\text{-}a_{AC}b)dx \\ j_{\varphi W} &= \int_{-b}^{b} m_W(x,y)(x\text{-}a_{AC}b)^2 dx \end{aligned} \qquad [5.64]$$

The kinetic energy of the non-rotating propeller and engine becomes

$$E_{KP} = \frac{1}{2}\int m_P(x)(\dot{z}_P^2 + \dot{y}_P^2)dx \qquad [5.65]$$

assuming the mass is concentrated on the propeller axis. The integration is taken over the appropriate x-coordinates of the propeller and engine pivoting system. The deflections are given as

$$\begin{aligned} z_P(x,t) &= h_P + (x - a_{EA}b)\varphi_P + (x - l_\Theta)\Theta \\ y_P(x,t) &= -(x - l_\Psi)\Psi \end{aligned} \qquad [5.66]$$

where pitch and yaw deflections given by the generalised coordinates are

$$\begin{aligned} \Theta(t) &= u_\Theta q_\Theta(t) \\ \Psi(t) &= u_\Psi q_\Psi(t) \end{aligned} \qquad [5.67]$$

Now, by substituting Eqn. 5.67 and Eqn. 5.66 into Eqn. 5.65, the non-rotating propeller and engine kinetic energy becomes

$$\begin{aligned} E_{KP} = &\frac{1}{2}M_P\dot{q}_h^2 + S_{\varphi P}\dot{q}_h\dot{q}_\varphi + \frac{1}{2}J_{\varphi P}\dot{q}_\varphi^2 + S_{\Theta P}\dot{q}_\Theta\dot{q}_h + J_{\Theta\varphi P}\dot{q}_\Theta\dot{q}_\varphi + \\ &+\frac{1}{2}J_{\Theta P}\dot{q}_\Theta^2 + \frac{1}{2}J_{\Psi P}\dot{q}_\Psi^2 \end{aligned} \qquad [5.68]$$

where the generalised inertia parameters are

$$\begin{aligned} M_P &= m_P\, u^2_{hP} \\ S_{\varphi P} &= (s_\Theta + [l_\Theta - (a_{EA}b)_P]m_P)u_{hP}\, u_{\varphi P} \\ J_{\varphi P} &= (j_\Theta + 2[l_\Theta - (a_{EA}b)_P]s_\Theta + [l_\Theta - (a_{EA}b)_P]^2 m_P)u^2_{\varphi P} \\ S_{\Theta P} &= s_\Theta u_\Theta u_{hP} \\ J_{\Theta\varphi P} &= (j_\Theta + [l_\Theta - (a_{EA}b)_P]s_\Theta)u_\Theta u_{hP} \\ J_{\Theta P} &= j_\Theta u^2_\Theta \\ J_{\Psi P} &= j_\Psi u^2_\Psi \end{aligned} \qquad [5.69]$$

The engine and propeller inertia parameters integrated over the appropriate *x*-coordinates of the propeller and engine pivoting system become

$$\begin{aligned} m_P &= \int m_P(x)dx \\ s_\Theta &= \int m_P(x)(x - l_\Theta)dx \\ j_\Theta &= \int m_P(x)(x - l_\Theta)^2\, dx \\ j_\Psi &= \int m_P(x)(x - l_\Psi)^2\, dx \end{aligned} \qquad [5.70]$$

Finally, the kinetic energy of the rotating propeller, including the gyroscopic precession, is given as an extension of Eqn. 2.3, where the pitch angle Θ is substituted by the total angle, including the torsional deformation of the wing, expressed as $(\Theta + \varphi_P)$, and the equation becomes

$$E_{K\Omega} = \frac{1}{2} J_X \Omega^2 + J_X \Omega \Psi (\dot{\Theta} + \dot{\varphi}_P) \qquad [5.71]$$

where J_X is the propeller mass moment of inertia about the axis of rotation.

The generalised parameters of the propeller and engine system are

$$J_{\Theta\Psi} = J_X u_\Theta u_\Psi$$
$$J_{\Psi\varphi} = J_X u_\Psi u_{\varphi P} \qquad [5.72]$$

Using the generalised coordinates of Eqn. 5.61 and Eqn. 5.67 and the generalised parameters of Eqn. 5.72, the kinetic energy of the rotating propeller, including the gyroscopic precession, can be expressed as

$$E_{K\Omega} = \frac{1}{2} J_X \Omega^2 + J_{\Theta\Psi} \Omega \dot{q}_\Theta q_\Psi + J_{\Psi\varphi} \Omega q_\Psi \dot{q}_\varphi \qquad [5.73]$$

Now, the total kinetic energy can be written as

$$E_K = \frac{1}{2} J_{\Theta P}\, \dot{q}_\Theta^2 + J_{\Theta\Psi} \Omega \dot{q}_\Theta q_\Psi + S_{\Theta P}\, \dot{q}_\Theta \dot{q}_h + J_{\Theta\varphi P}\, \dot{q}_\Theta \dot{q}_\varphi + \frac{1}{2} J_{\Psi P}\, \dot{q}_\Psi^2 + $$
$$+ J_{\Psi\varphi} \Omega\, q_\Psi \dot{q}_\varphi + \frac{1}{2} M_{WP}\, \dot{q}_h^2 + S_{\varphi WP}\, \dot{q}_h \dot{q}_\varphi + \frac{1}{2} J_{\varphi WP}\, \dot{q}_\varphi^2 + \frac{1}{2} J_X \Omega^2 \qquad [5.74]$$

where the inertial parameters, including the wing, engine and propeller systems, are defined as

$$M_{WP} = M_W + M_P$$
$$S_{\varphi WP} = S_{\varphi W} + S_{\varphi P}$$
$$J_{\varphi WP} = J_{\varphi W} + J_{\varphi P} \qquad [5.75]$$

The potential energy of the system with four DOFs is expressed as an extension of Eqn. 2.4 in the form

$$E_P = \frac{1}{2} K_\Theta\, q_\Theta^2 + \frac{1}{2} K_\Psi\, q_\Psi^2 + \frac{1}{2} K_h\, q_h^2 + \frac{1}{2} K_\varphi\, q_\varphi^2 \qquad [5.76]$$

By considering the uncoupled modes (frequencies and modal masses), the potential energy can be rewritten as

$$E_P = \frac{1}{2} J_{\Theta P}\, \omega_\Theta^2\, q_\Theta^2 + \frac{1}{2} J_{\Psi P}\, \omega_\Psi^2\, q_\Psi^2 + \frac{1}{2} M_{WP}\, \omega_h^2\, q_h^2 + \frac{1}{2} J_{\varphi WP}\, \omega_\varphi^2\, q_\varphi^2 \qquad [5.77]$$

The structural damping is estimated similarly as in Eqn. 2.5:

$$D = \frac{1}{2} J_{\Theta P}\, \gamma_\Theta \frac{\omega_\Theta^2}{\omega} \dot{q}_\Theta^2 + \frac{1}{2} J_{\Psi P}\, \gamma_\Psi \frac{\omega_\Psi^2}{\omega} \dot{q}_\Psi^2 + \frac{1}{2} M_{WP}\, \gamma_h \frac{\omega_h^2}{\omega} \dot{q}_h^2 + \\ + \frac{1}{2} J_{\varphi WP}\, \gamma_\varphi \frac{\omega_\varphi^2}{\omega} \dot{q}_\varphi^2 \qquad [5.78]$$

where ω is the vibration frequency of the system and the γ-s are the damping coefficients.

Now, we can write the equations of motion using the Lagrange's equation (Eqn. 5.1), where i will become Θ, Ψ, h, φ. We obtain four equations of motion:

$$J_{\Theta P}\left(\ddot{q}_\Theta + \gamma_\Theta \frac{\omega_\Theta^2}{\omega}\, \dot{q}_\Theta + \omega_\Theta^2\, q_\Theta\right) + J_{\Theta\Psi}\Omega\, \dot{q}_\Psi + S_{\Theta P}\, \ddot{q}_h + J_{\Theta\varphi P}\, \ddot{q}_\varphi = Q_\Theta$$

$$-J_{\Theta\Psi}\Omega\, \dot{q}_\Theta + J_{\Psi P}\left(\ddot{q}_\Psi + \gamma_\Psi \frac{\omega_\Psi^2}{\omega}\, \dot{q}_\Theta + \omega_\Psi^2\, q_\Psi\right) - J_{\Psi\varphi}\Omega\, \dot{q}_\varphi = Q_\Psi$$

$$S_{\Theta P}\, \ddot{q}_\Theta + M_{WP}\left(\ddot{q}_h + \gamma_h \frac{\omega_h^2}{\omega}\, \dot{q}_h + \omega_h^2\, q_h\right) + S_{\varphi WP}\, \ddot{q}_\varphi = Q_h$$

$$J_{\Theta\varphi P}\, \ddot{q}_\Theta + J_{\Psi\varphi}\Omega\, \dot{q}_\Psi + S_{\varphi WP}\, \ddot{q}_h + J_{\varphi WP}\left(\ddot{q}_\varphi + \gamma_\varphi \frac{\omega_\varphi^2}{\omega} \dot{q}_\varphi + \omega_\varphi^2\, q_\varphi\right) = Q_\varphi \qquad [5.79]$$

We assume the harmonic motion

$$q_i = \bar{q}_i\, e^{j\omega t} \qquad [5.80]$$

where i will become Θ, Ψ, h, φ and $\bar{q}_i$ are the complex amplitudes of motions. We establish the dimensionless frequency parameters, which are

Wing reduced frequency defined as $k_r = (\omega\, b_r / V_\infty)$;

Frequency ratio defined as $\lambda = (\omega_\Theta / \omega)$;

Propeller advance ratio defined as $J_0 = (\pi V_\infty / \Omega R)$.

where b_r is the wing reference semichord.

By making these substitutions and dividing the equations by $-J_{\Theta P}\, \omega^2\, e^{j\omega t}$ or $-(1/R)\, J_{\Theta P}\, \omega^2\, e^{j\omega t}$, we obtain the dimensionless form of the equations of motion:

$$\left[1-\lambda^2(1+j\gamma_\Theta)\right]\bar{q}_\Theta - jM_{\Theta\Psi}\frac{\pi}{Jk_r}\bar{q}_\Psi + M_{\Theta h}\frac{\bar{q}_h}{R} + M_{\Theta\varphi}\bar{q}_\varphi = -\frac{Q_\Theta}{J_{\Theta P}\,\omega^2}e^{-j\omega t}$$

$$jM_{\Theta\Psi}\frac{\pi}{Jk_r}\bar{q}_\Theta + M_{\Psi\Psi}\left[1-\lambda^2\left(\frac{\omega_\Psi}{\omega_\Theta}\right)^2(1+j\gamma_\Psi)\right]\bar{q}_\Psi + jM_{\Psi\varphi}\frac{\pi}{Jk_r}\bar{q}_\varphi = -\frac{Q_\Psi}{J_{\Theta P}\,\omega^2}e^{-j\omega t}$$

$$M_{\Theta h}\bar{q}_\Theta + M_{hh}\left[1-\lambda^2\left(\frac{\omega_h}{\omega_\Theta}\right)^2(1+j\gamma_h)\right]\frac{\bar{q}_h}{R} + M_{h\varphi}\bar{q}_\varphi = -\frac{R\,Q_h}{J_{\Theta P}\,\omega^2}e^{-j\omega t}$$

$$M_{\Theta\varphi}\bar{q}_\Theta - jM_{\Psi\varphi}\frac{\pi}{Jk_r}\bar{q}_\Psi + M_{h\varphi}\frac{\bar{q}_h}{R} + M_{\varphi\varphi}\left[1-\lambda^2\left(\frac{\omega_\varphi}{\omega_\Theta}\right)^2\left(1+j\gamma_\varphi\right)\right]\bar{q}_\varphi = -\frac{Q_\varphi}{J_{\Theta P}\,\omega^2}e^{-j\omega t}$$

[5.81]

where the dimensionless generalised mass parameters are

$$M_{\Theta\Psi} = \left(\frac{J_{\Theta\Psi}}{J_{\Theta P}}\right)\left(\frac{b_r}{R}\right)$$

$$M_{\Theta h} = \left(\frac{S_{\Theta P}\,R}{J_{\Theta P}}\right)$$

$$M_{\Theta\varphi} = \left(\frac{J_{\Theta\varphi P}}{J_{\Theta P}}\right)$$

$$M_{\Psi\Psi} = \left(\frac{J_{\Psi P}}{J_{\Theta P}}\right)$$

$$M_{\Psi\varphi} = \left(\frac{J_{\Psi\varphi}}{J_{\Theta P}}\right)\left(\frac{b_r}{R}\right)$$

$$M_{hh} = \left(\frac{M_{WP}\,R^2}{J_{\Theta P}}\right)$$

$$M_{h\varphi} = \left(\frac{S_{\varphi WP}\,R}{J_{\Theta P}}\right)$$

$$M_{\varphi\varphi} = \left(\frac{J_{\varphi WP}}{J_{\Theta P}}\right)$$

[5.82]

Now, we will form the equations for the generalised aerodynamic forces. The aerodynamic forces and moments acting on the system with four DOFs are summarised in Figure 5.22.

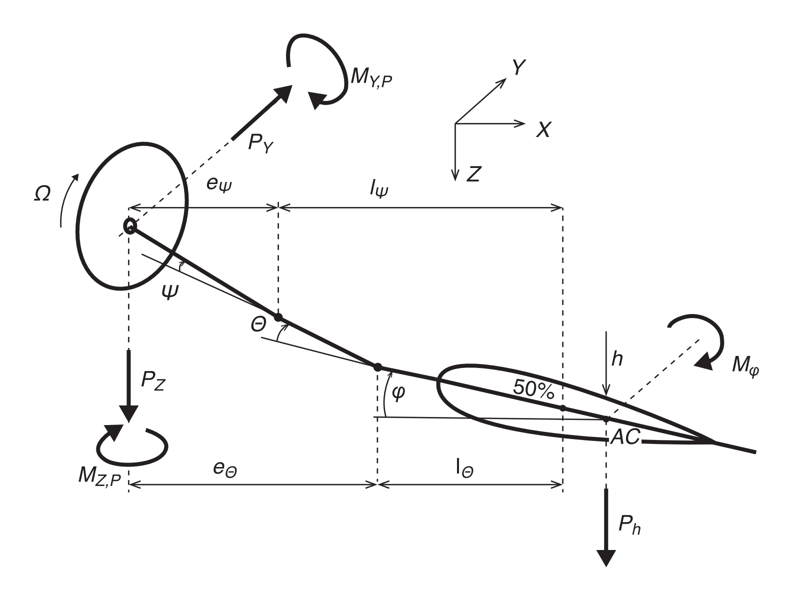


Figure 5.22 **Aerodynamic forces and moments [24]**

The generalised aerodynamic forces have the following representations in terms of the wing and propeller:

$$
\begin{aligned}
Q_\Theta &= Q_{\Theta P}\\
Q_\Psi &= Q_{\Psi P}\\
Q_h &= Q_{hP} + Q_{hW}\\
Q_\varphi &= Q_{\varphi P} + Q_{\varphi W}
\end{aligned}
\qquad [5.83]
$$

The aerodynamic forces acting on the propeller are

$$
\begin{aligned}
Q_{\Theta P} &= (M_{YP} + e_\Theta P_Z)u_\Theta\\
Q_{\Psi P} &= (M_{ZP} - e_\Psi P_Y)u_\Psi\\
Q_{hP} &= P_Z\, u_{hP}\\
Q_{\varphi P} &= [M_{YP} + e_\varphi\, P_Z]u_{\varphi P}
\end{aligned}
\qquad [5.84]
$$

where the distance from the wing elastic axis to the propeller plane is

$$e_\varphi = (e_\Theta + l_\Theta + (a_{AC}b)_P) \qquad [5.85]$$

The aerodynamic forces and moments acting on the propeller P_Y, P_Z, M_{YP} and M_{ZP} are expressed as the means of the aerodynamic derivatives using Eqn. 5.35. The aerodynamic derivatives are given by Eqn. 5.52. By neglecting the aerodynamic interference between the propeller and the wing, we can use simplifications of Eqn. 2.11 and Eqn. 2.12. The effective angles considering the system with four DOFs now become

$$\Theta^* = \Theta + \varphi_P + \frac{e_\Theta}{V_\infty} + \frac{e_\varphi}{V_\infty}\dot{\varphi}_P + \frac{1}{V_\infty}\dot{h}_P$$
$$\Psi^* = \Psi + \frac{e_\Psi}{V_\infty}\dot{\Psi} \qquad [5.86]$$

Equation 5.35, using the generalised coordinates of Eqn. 5.61 and Eqn. 5.67, and the assumption of the harmonic motion using Eqn. 5.80 are now rewritten in the dimensionless form

$$\begin{aligned}
\frac{Q_{\Theta P}}{J_{\Theta P}\,\omega^2} e^{-j\omega t} &= \frac{\kappa_P}{k_r^2}\left(Q_{\Theta\Theta P}\,\bar{q}_\Theta + Q_{\Theta\Psi P}\,\bar{q}_\Psi + Q_{\Theta h P}\frac{\bar{q}_h}{R} + Q_{\Theta\varphi P}\,\bar{q}_\varphi\right)\\
\frac{Q_{\Psi P}}{J_{\Theta P}\,\omega^2} e^{-j\omega t} &= \frac{\kappa_P}{k_r^2}\left(Q_{\Psi\Theta P}\,\bar{q}_\Theta + Q_{\Psi\Psi P}\,\bar{q}_\Psi + Q_{\Psi h P}\frac{\bar{q}_h}{R} + Q_{\Psi\varphi P}\,\bar{q}_\varphi\right)\\
\frac{R\,Q_{h P}}{J_{\Theta P}\,\omega^2} e^{-j\omega t} &= \frac{\kappa_P}{k_r^2}\left(Q_{h\Theta P}\,\bar{q}_\Theta + Q_{h\Psi P}\,\bar{q}_\Psi + Q_{hh P}\frac{\bar{q}_h}{R} + Q_{h\varphi P}\,\bar{q}_\varphi\right)\\
\frac{Q_{\varphi P}}{J_{\Theta P}\,\omega^2} e^{-j\omega t} &= \frac{\kappa_P}{k_r^2}\left(Q_{\varphi\Theta P}\,\bar{q}_\Theta + Q_{\varphi\Psi P}\,\bar{q}_\Psi + Q_{\varphi h P}\frac{\bar{q}_h}{R} + Q_{\varphi\varphi P}\,\bar{q}_\varphi\right)
\end{aligned} \qquad [5.87]$$

where the ratio of mass moment of inertia of the air to moment of inertia parameter is defined here as

$$\kappa_P = \frac{\pi\,\rho\,R^3\,b_r^2}{J_{\Theta P}} \qquad [5.88]$$

The dimensionless generalised propeller aerodynamic forces used in Eqn. 5.87 are:

$$\begin{aligned}
Q_{\Theta\Theta P} &= \left[\left(1 + jk_r\frac{e_\Theta}{b_r}\right)\left(c_{m\Theta} + \frac{e_\Theta}{2R}c_{z\Theta}\right) + \left(jk_r\frac{R}{b_r} - k_r^2\frac{e_\Theta R}{b_r^2}\right)\left(c_{mq} + \frac{e_\Theta}{2R}c_{zq}\right)\right]u_\Theta^2\\
Q_{\Theta\Psi P} &= \left[\left(1 + jk_r\frac{e_\Psi}{b_r}\right)\left(c_{m\Psi} + \frac{e_\Theta}{2R}c_{z\Psi}\right) + \left(jk_r\frac{R}{b_r} - k_r^2\frac{e_\Psi R}{b_r^2}\right)\left(c_{mr} + \frac{e_\Theta}{2R}c_{zr}\right)\right]u_\Theta u_\Psi\\
Q_{\Theta h P} &= \left[jk_r\frac{R}{b_r}\left(c_{m\Theta} + \frac{e_\Theta}{2R}c_{z\Theta}\right) - k_r^2\frac{R^2}{b_r^2}\left(c_{mq} + \frac{e_\Theta}{2R}c_{zq}\right)\right]u_\Theta u_{hP}\\
Q_{\Theta\varphi P} &= \left[\left(1 + jk_r\frac{e_\varphi}{b_r}\right)\left(c_{m\Theta} + \frac{e_\Theta}{2R}c_{z\Theta}\right) + \left(jk_r\frac{R}{b_r} - k_r^2\frac{e_\varphi R}{b_r^2}\right)\left(c_{mq} + \frac{e_\Theta}{2R}c_{zq}\right)\right]u_\Theta u_{\varphi P}
\end{aligned}$$

$$Q_{\Psi\Theta P}=\left[\left(1+jk_r\frac{e_\Theta}{b_r}\right)\left(c_{n\Theta}-\frac{e_\Psi}{2R}c_{y\Theta}\right)+\left(jk_r\frac{R}{b_r}-k_r^2\frac{e_\Theta R}{b_r^2}\right)\left(c_{nq}-\frac{e_\Psi}{2R}c_{yq}\right)\right]u_\Psi u_\Theta$$

$$Q_{\Psi\Psi P}=\left[\left(1+jk_r\frac{e_\Psi}{b_r}\right)\left(c_{n\Psi}-\frac{e_\Psi}{2R}c_{y\Psi}\right)+\left(jk_r\frac{R}{b_r}-k_r^2\frac{e_\Psi R}{b_r^2}\right)\left(c_{nr}-\frac{e_\Psi}{2R}c_{yr}\right)\right]u_\Psi^2$$

$$Q_{\Psi hP}=\left[jk_r\frac{R}{b_r}\left(c_{n\Theta}-\frac{e_\Psi}{2R}c_{y\Theta}\right)-k_r^2\frac{R^2}{b_r^2}\left(c_{nq}-\frac{e_\Psi}{2R}c_{yq}\right)\right]u_\Psi u_{hP}$$

$$Q_{\Psi\varphi P}=\left[\left(1+jk_r\frac{e_\varphi}{b_r}\right)\left(c_{n\Theta}-\frac{e_\Psi}{2R}c_{y\Theta}\right)+\left(jk_r\frac{R}{b_r}-k_r^2\frac{e_\varphi R}{b_r^2}\right)\left(c_{nq}-\frac{e_\Psi}{2R}c_{yq}\right)\right]u_\Psi u_{\varphi P}$$

$$Q_{h\Theta P}=\frac{1}{2}\left[\left(1+jk_r\frac{e_\Theta}{b_r}\right)c_{z\Theta}+\left(jk_r\frac{R}{b_r}-k_r^2\frac{e_\Theta R}{b_r^2}\right)c_{zq}\right]u_{hP}u_\Theta$$

$$Q_{h\Psi P}=\frac{1}{2}\left[\left(1+jk_r\frac{e_\Psi}{b_r}\right)c_{z\Psi}+\left(jk_r\frac{R}{b_r}-k_r^2\frac{e_\Psi R}{b_r^2}\right)c_{zr}\right]u_{hP}u_\Psi$$

$$Q_{hhP}=\frac{1}{2}\left(jk_r\frac{R}{b_r}c_{z\Theta}-k_r^2\frac{R^2}{b_r^2}c_{zq}\right)u_{hP}^2$$

$$Q_{h\varphi P}=\frac{1}{2}\left[\left(1+jk_r\frac{e_\varphi}{b_r}\right)c_{z\Theta}+\left(jk_r\frac{R}{b_r}-k_r^2\frac{e_\varphi R}{b_r^2}\right)c_{zq}\right]u_{hP}u_{\varphi P}$$

$$Q_{\varphi\Theta P}=\left[\left(1+jk_r\frac{e_\Theta}{b_r}\right)\left(c_{m\Theta}+\frac{e_\varphi}{2R}c_{z\Theta}\right)+\left(jk_r\frac{R}{b_r}-k_r^2\frac{e_\Theta R}{b_r^2}\right)\left(c_{mq}+\frac{e_\varphi}{2R}c_{zq}\right)\right]u_{\varphi P}u_\Theta$$

$$Q_{\varphi\Theta P}=\left[\left(1+jk_r\frac{e_\Psi}{b_r}\right)\left(c_{m\Psi}+\frac{e_\varphi}{2R}c_{z\Psi}\right)+\left(jk_r\frac{R}{b_r}-k_r^2\frac{e_\Psi R}{b_r^2}\right)\left(c_{mr}+\frac{e_\varphi}{2R}c_{zr}\right)\right]u_{\varphi P}u_\Psi$$

$$Q_{\varphi hP}=\left[jk_r\frac{R}{b_r}\left(c_{m\Theta}+\frac{e_\varphi}{2R}c_{z\Theta}\right)-k_r^2\frac{R^2}{b_r^2}\left(c_{mq}+\frac{e_\varphi}{2R}c_{zq}\right)\right]u_{\varphi P}u_{hP}$$

$$Q_{\varphi\varphi P}=\left[\left(1+jk_r\frac{e_\varphi}{b_r}\right)\left(c_{m\Theta}+\frac{e_\varphi}{2R}c_{z\Theta}\right)+\left(jk_r\frac{R}{b_r}-k_r^2\frac{e_\varphi R}{b_r^2}\right)\left(c_{mq}+\frac{e_\varphi}{2R}c_{zq}\right)\right]u_{\varphi P}^2$$

[5.89]

The aerodynamic forces and moments acting on the wing P_h and M_φ are rewritten here using the generalised coordinates. In general, they become

$$Q_{hW}=L\int_0^1 P_h(\eta)u_h\,d\eta$$
$$Q_{\varphi W}=L\int_0^1 M_\varphi(\eta)u_\varphi\,d\eta$$

[5.90]

where P_h and M_φ are the wing section lift force and pitching moment respectively. For the demonstration of the solution, we use the simple 'Strip Theory', which was formulated by Theodorsen [6] and Smilg and Wassermann [7] in the modified version as formulated by Yates [25]. Equation 5.90, using the generalised coordinates of Eqn. 5.61 and Eqn. 5.67, and the assumption of the harmonic motion of Eqn. 5.80 in the dimensionless form become

$$\begin{aligned} \frac{R\,Q_{hW}}{J_{\Theta P}\,\omega^2} e^{-j\omega t} &= \frac{\kappa_P}{k_r^2}\left(Q_{hhW}\frac{\bar{q}_h}{R} + Q_{h\varphi W}\,\bar{q}_\varphi \right) \\ \frac{Q_{\varphi W}}{J_{\Theta P}\,\omega^2} e^{-j\omega t} &= \frac{\kappa_P}{k_r^2}\left(Q_{\varphi hW}\frac{\bar{q}_h}{R} + Q_{\varphi\varphi W}\,\bar{q}_\varphi \right) \end{aligned} \qquad [5.91]$$

When considering the unswept wing (unswept EA), the wing dimensionless aerodynamic forces become

$$\begin{aligned} Q_{hhW} &= \left[\left(N_2 + \frac{G}{\pi k_r}N_3\right) - j\frac{F}{\pi k_r}N_3\right]\frac{L}{R}k_r^2 \\ Q_{h\varphi W} &= \left[\left(-N_{13} - \frac{F}{\pi k_r^2}N_{11} + \frac{G}{\pi k_r}N_{12}\right) - j\left(\frac{1}{k_r}N_{14} + \frac{G}{\pi k_r^2}N_{11} + \frac{F}{\pi k_r}N_{12}\right)\right]\frac{L b_r}{R^2}k_r^2 \\ Q_{\varphi hW} &= \left[\left(-N_{13} - \frac{G}{\pi k_r}N_{17}\right) + j\frac{F}{\pi k_r}N_{17}\right]\frac{L b_r}{R^2}k_r^2 \\ Q_{\varphi\varphi W} &= \left[\left(N_{22} + \frac{F}{\pi k_r^2}N_{21} - \frac{G}{\pi k_r}N_{23}\right) - j\left(\frac{1}{k_r}N_{24} - \frac{G}{\pi k_r^2}N_{21} - \frac{F}{\pi k_r}N_{23}\right)\right]\frac{L b_r^2}{R^3}k_r^2 \end{aligned} \qquad [5.92]$$

The circulation functions of the unsteady flow are represented using the Theodorsen function $(F+j\,G)$, which is dependent on the reduced frequency (k_r) and Mach number. The wing aerodynamic spanwise integrals (N_i) are

$$\begin{aligned} N_2 &= \int_0^1 \left(\frac{b}{b_r}\right)^2 u_h^2\, d\eta \\ N_3 &= \int_0^1 c_{L\alpha}\left(\frac{b}{b_r}\right) u_h^2\, d\eta \\ N_{11} &= \int_0^1 c_{L\alpha}\left(\frac{b}{b_r}\right) u_h u_\varphi\, d\eta \end{aligned}$$

$$N_{12} = \int_0^1 c_{L\alpha} \left(\frac{b}{b_r}\right)^2 \left(\frac{c_{L\alpha}}{2\pi} + a_{AC} - a_{EA}\right) u_h u_\varphi \, d\eta$$

$$N_{13} = \int_0^1 \left(\frac{b}{b_r}\right)^3 a_{EA} \, u_h u_\varphi \, d\eta$$

$$N_{14} = \int_0^1 \left(\frac{b}{b_r}\right)^2 u_h u_\varphi \, d\eta$$

$$N_{17} = \int_0^1 c_{L\alpha} \left(\frac{b}{b_r}\right)^2 (a_{EA} - a_{AC}) u_h u_\varphi \, d\eta$$

$$N_{21} = \int_0^1 c_{L\alpha} \left(\frac{b}{b_r}\right)^2 (a_{EA} - a_{AC}) u_\varphi^2 \, d\eta$$

$$N_{22} = \int_0^1 \left(\frac{b}{b_r}\right)^4 \left(\frac{1}{8} + a_{EA}^2\right) u_\varphi^2 \, d\eta$$

$$N_{23} = \int_0^1 c_{L\alpha} \left(\frac{b}{b_r}\right)^3 \left(\frac{c_{L\alpha}}{2\pi} + a_{AC} - a_{EA}\right) (a_{EA} - a_{AC}) u_\varphi^2 \, d\eta$$

$$N_{24} = \int_0^1 \left(\frac{b}{b_r}\right)^3 \left(\frac{c_{L\alpha}}{2\pi} + a_{AC} - a_{EA}\right) u_\varphi^2 \, d\eta \qquad [5.93]$$

Now, we substitute for the generalised aerodynamic forces of the propeller from Eqn. 5.87 and the wing from Eqn. 5.91 into the equations of motion of Eqn. 5.81 and we obtain the flutter equation in the matrix formulation:

$$\begin{bmatrix} A_{\Theta\Theta} & A_{\Theta\Psi} & A_{\Theta h} & A_{\Theta\varphi} \\ A_{\Psi\Theta} & A_{\Psi\Psi} & A_{\Psi h} & A_{\Psi\varphi} \\ A_{h\Theta} & A_{h\Psi} & A_{hh} & A_{h\varphi} \\ A_{\varphi\Theta} & A_{\varphi\Psi} & A_{\varphi h} & A_{\varphi\varphi} \end{bmatrix} \begin{Bmatrix} \bar{q}_\Theta \\ \bar{q}_\Psi \\ \bar{q}_h / R \\ \bar{q}_\varphi \end{Bmatrix} = 0 \qquad [5.94]$$

where the coefficients of the flutter matrix are

$$A_{\Theta\Theta} = 1 - \lambda^2 (1 + j\gamma_\Theta) + \frac{\kappa_P}{k_r^2} Q_{\Theta\Theta P}$$

$$A_{\Theta\Psi} = -jM_{\Theta\Psi} \frac{\pi}{J_0 k_r} + \frac{\kappa_P}{k_r^2} Q_{\Theta\Psi P}$$

$$A_{\Theta h} = M_{\Theta h} + \frac{\kappa_P}{k^2} Q_{\Theta hP}$$

$$A_{\Theta\varphi} = M_{\Theta\varphi} + \frac{\kappa_P}{k_r^2} Q_{\Theta\varphi P}$$

$$A_{\Psi\Theta} = jM_{\Theta\Psi} \frac{\pi}{J_0 k_r} + \frac{\kappa_P}{k_r^2} Q_{\Psi\Theta P}$$

$$A_{\Psi\Psi} = M_{\Psi\Psi} \left[1 - \lambda^2 \left(\frac{\omega_\Psi}{\omega_\Theta}\right)^2 (1 + j\gamma_\Psi)\right] + \frac{\kappa_P}{k_r^2} Q_{\Psi\Psi P}$$

$$A_{\Psi h} = \frac{\kappa_P}{k_r^2} Q_{\Psi h P}$$

$$A_{\Psi\varphi} = jM_{\Psi\varphi} \frac{\pi}{J_0 k_r} + \frac{\kappa_P}{k_r^2} Q_{\Psi\varphi P}$$

$$A_{h\Theta} = M_{\Theta h} + \frac{\kappa_P}{k_r^2} Q_{h\Theta P}$$

$$A_{hh} = M_{hh} \left[1 - \lambda^2 \left(\frac{\omega_h}{\omega_\Theta}\right)^2 (1 + j\gamma_h)\right] + \frac{\kappa_P}{k_r^2} (Q_{hhP} + Q_{hhW})$$

$$A_{h\varphi} = M_{h\varphi} + \frac{\kappa_P}{k_r^2} (Q_{h\varphi P} + Q_{h\varphi W})$$

$$A_{\varphi\Theta} = M_{\Theta\varphi} + \frac{\kappa_P}{k_r^2} Q_{\varphi\Theta P}$$

$$A_{\varphi\Psi} = -jM_{\Psi\varphi} \frac{\pi}{J_0 k_r} + \frac{\kappa_P}{k_r^2} Q_{\varphi\Psi P}$$

$$A_{\varphi h} = M_{h\varphi} + \frac{\kappa_P}{k_r^2} (Q_{\varphi h P} + Q_{\varphi h W})$$

$$A_{\varphi\varphi} = M_{\varphi\varphi} \left[1 - \lambda^2 \left(\frac{\omega_\varphi}{\omega_\Theta}\right)^2 (1 + j\gamma_\varphi)\right] + \frac{\kappa_P}{k_r^2} (Q_{\varphi\varphi P} + Q_{\varphi\varphi W}) \quad [5.95]$$

Now, the solution is similar to the standard flutter. To obtain the non-trivial solution of the flutter equation of Eqn. 5.94, the determinant of the coefficients must become zero:

$$\begin{vmatrix} A_{\Theta\Theta} & A_{\Theta\Psi} & A_{\Theta h} & A_{\Theta\varphi} \\ A_{\Psi\Theta} & A_{\Psi\Psi} & A_{\Psi h} & A_{\Psi\varphi} \\ A_{h\Theta} & A_{h\Psi} & A_{hh} & A_{h\varphi} \\ A_{\varphi\Theta} & A_{\varphi\Psi} & A_{\varphi h} & A_{\varphi\varphi} \end{vmatrix} = 0 \quad [5.96]$$

The determinant is solved for the sequence of values of k_r and γ_Θ, while the other quantities are fixed. The flutter determinant is expanded to give the characteristics polynomial in λ^2. The states of the neutral stability (flutter) are obtained for the combinations of k_r and γ_Θ that make one of the roots of the characteristic polynomial a real, positive quantity. Then, the values of k_{rFL}, $\gamma_{\Theta FL}$ and λ_{FL} given for this state of the neutral stability are used to calculate the flutter frequency as

$$\omega_{FL} = \frac{\omega_\Theta}{\lambda_{FL}} \qquad [5.97]$$

the flutter velocity as

$$V_{FL} = \frac{\omega_\Theta\, b_r}{\lambda_{FL}\, k_{rFL}} = \frac{\omega_{FL}\, b_r}{k_{rFL}} \qquad [5.98]$$

and finally the structural damping required for the neutral stability

$$\gamma_{\Theta FL} = \gamma_\Theta\, \lambda_{FL} \qquad [5.99]$$

By substituting for the flutter state parameters and setting one of the generalised coordinates (e.g., $\bar{q}_\varphi$) arbitrarily, we can now solve the set of equations (Eqn. 5.94) for the ratios of other generalised coordinates. The relative magnitudes and phase relations of these complex ratios give us an indication of the flutter mode.

5.9 Influence of hinged blade flexibility

The above-mentioned analytical solutions consider the propeller blades to be rigid. This assumption is reasonable for conventional propellers; however, when considering large propellers, prop-fans, prop-rotors, etc. with longer flexible blades, the whirl flutter characteristics might also be influenced by the flexibility of the propeller or rotor blades. Another issue is also the mechanical instability caused by the energy of the rotating rotor, which may also be influenced by the propeller whirl aerodynamic forces (see Section 5.11).

The basic model that accounts for the blade flexibility is the hinged blades model, which was examined both experimentally [9], [26], [27] and analytically [9], [27], [28], [29]. The experimental models and results are described in Chapter 4. The fundamental analytical work of reference [28] considered four degrees of freedom: propeller disc pitch, propeller

disc yaw and cyclic flapping of blades in the pitch and yaw directions normal to the propeller. The results of the solution of the characteristic equation with these four degrees of freedom are shown in Figure 5.23, which includes hinge offsets that were evaluated experimentally (see Figure 4.7). Because the propeller was windmilling (Ω is proportional to the airstream), the V-g-f diagram is plotted using the frequency and damping ratio parameters.

The theoretical results [28] are in agreement with the experiments [26] for the backward whirl instabilities, which were found experimentally for large hinge offset $((r_e/R)=0.13$ – see Figure 4.9). However, the theory did not predict the forward whirl instability, which was experimentally found for the low hinge offset $((r_e/R)=0.08$ – see Figure 4.9). The theory was modified to introduce arbitrary phase lag in the propeller aerodynamic forces. Phase lags as high as 45 degrees were considered, and the predicted instability was always in the backward whirl mode. Therefore, it appears that the model used in [28] is not able to predict the forward whirl instabilities of the flapping blade system.

Further studies (both experimental and analytical) were performed in [27]. The analytical model includes the system of N_b blades. The blades are rigid and elastically restrained by flapping hinges at a specific distance from the rotor shaft. The hinges are aligned parallel to the plane of rotation. The motion of the nacelle is considered to be same as the hinges in pitch and yaw. The system scheme is shown in Figure 5.24.

The system uses two coordinate systems: (1) space fixed with X, Y and Z axes fixed with the origin at the centre of nacelle hinges, and (2) body fixed with X_b, Y_b and Z_b axes fixed to the arbitrary blade (identified by suffix 'n'), where the blade axis coincides with Z_b (see Figure 5.24). The Euler angles of both system relations are pitch angle Θ, yaw angle Ψ, blade azimuth angle Φ_n and finally blade flapping angle β_n. The transformation expression between displacements in both coordinate systems becomes

$$\bar{X}_s = \begin{Bmatrix} X \\ Y \\ Z \end{Bmatrix} = [T_\Theta][T_\Psi]\left[[T_\Phi][T_\beta]\begin{Bmatrix} X_b \\ Y_b \\ Z_b \end{Bmatrix} + [T_\Phi]\begin{Bmatrix} x_e \\ y_e \\ z_e \end{Bmatrix} + \begin{Bmatrix} x_C \\ y_C \\ z_C \end{Bmatrix}\right] \quad [5.100]$$

where the transformation matrices are

$$\left[T_{\Theta}\right]=\begin{bmatrix}\cos\Theta & 0 & \sin\Theta\\ 0 & 1 & 0\\ -\sin\Theta & 0 & \cos\Theta\end{bmatrix} \qquad [5.101]$$

$$\left[T_{\Psi}\right]=\begin{bmatrix}\cos\Psi & -\sin\Psi & 0\\ \sin\Psi & \cos\Psi & 0\\ 0 & 0 & 1\end{bmatrix} \qquad [5.102]$$

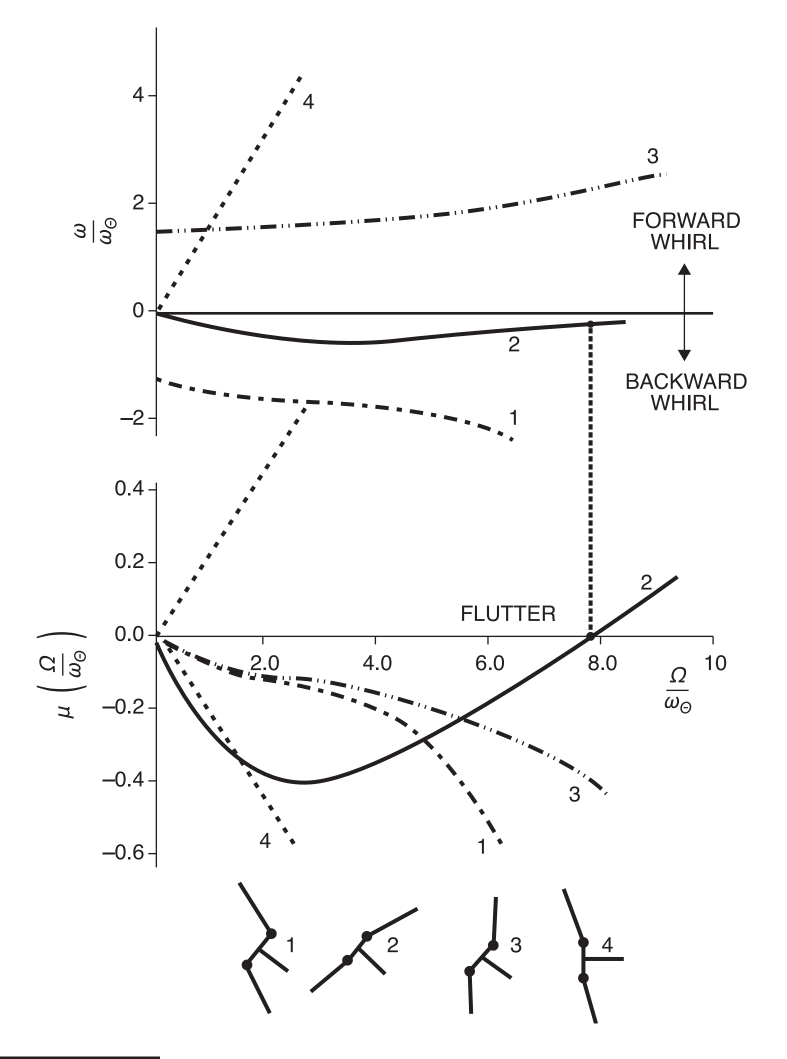


Figure 5.23 Flapping blade whirl modes $((r_e/R)=0.13)$ [28], [30]

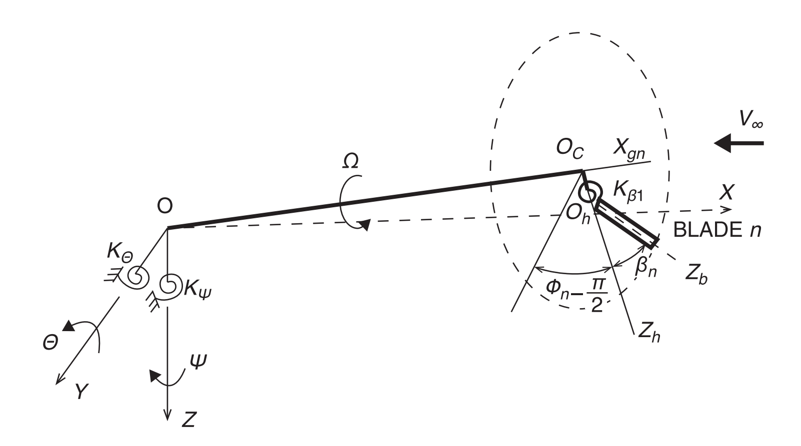


Figure 5.24 **Scheme of the flapping blade dynamic system [27]**

$$\left[T_{\Phi}\right]=\begin{bmatrix} 1 & 0 & 0 \\ 0 & \cos\Phi_n & -\sin\Phi_n \\ 0 & \sin\Phi_n & \cos\Phi_n \end{bmatrix} \qquad [5.103]$$

$$\left[T_{\beta}\right]=\begin{bmatrix} \cos\beta_n & 0 & \sin\beta_n \\ 0 & 1 & 0 \\ -\sin\beta_n & 0 & \cos\beta_n \end{bmatrix} \qquad [5.104]$$

The position vector of the point on the axis of *N*th blade with respect to the axes system of Eqn. 5.100 becomes

$$\bar{X}_S=\begin{Bmatrix} X \\ Y \\ Z \end{Bmatrix}_S=\left[T_{\Theta}\right]\left[T_{\Psi}\right]\left[\left[T_{\Phi}\right]\left[T_{\beta}\right]\begin{Bmatrix} 0 \\ 0 \\ r \end{Bmatrix}+\left[T_{\Phi}\right]\begin{Bmatrix} 0 \\ 0 \\ r_e \end{Bmatrix}+\begin{Bmatrix} a \\ 0 \\ 0 \end{Bmatrix}\right] \qquad [5.105]$$

where r is a local blade radius, r_e is a blade flapping pivot radius and a is the distance between the nacelle pivot point and the propeller hub. Similarly, the position vector of a point on the axis of nacelle becomes

$$\bar{X}_{gn}=\begin{Bmatrix} X \\ Y \\ Z \end{Bmatrix}_{gn}=\left[T_{\Theta}\right]\left[T_{\Psi}\right]\begin{Bmatrix} s \\ 0 \\ 0 \end{Bmatrix} \qquad [5.106]$$

where s is a local coordinate of the nacelle.

5.9.1 Inertial forces

The expression of the kinetic energy of the system is

$$E_k = \frac{1}{2}\sum_{n=1}^{N_b}\int_0^R \left\{\dot{\bar{X}}_S\right\}^T \left\{\dot{\bar{X}}_S\right\} dm_b + \frac{1}{2}\int_0^a \left\{\dot{\bar{X}}_{gn}\right\}^T \left\{\dot{\bar{X}}_{gn}\right\} dm_n \qquad [5.107]$$

After substituting from Eqn. 5.105 and Eqn. 5.106, differentiating and algebraic manipulation, the expression becomes

$$\begin{aligned}
E_k = \sum_{n=1}^{N_b}\int_0^R \frac{1}{2}\, dm_b \Big[& (r\text{-}r_e)^2 \dot{\beta}_n^2 + (r\text{-}r_e)^2 \dot{\Theta}^2 (\cos^2\beta_n \sin^2\Phi_n \sin^2\Psi + \\
& + \cos^2\beta_n \cos^2\Phi_n + \sin^2\beta_n \cos^2\Psi + 2\cos\beta_n \sin\Phi_n \sin\Psi \cos\Psi) + \\
& + (r\text{-}r_e)^2 \Psi^2 (\sin^2\beta_n + \cos^2\beta_n \sin^2\Phi_n) + (r\text{-}r_e)^2 \dot{\Phi}_n^2 \ \cos^2\beta_n + \\
& + 2(r\text{-}r_e)^2 \beta_n \Theta \cos\Phi_n \cos\beta_n + 2(r\text{-}r_e)^2 \dot{\beta}_n \dot{\Psi} \sin\Phi_n + \\
& + 2(r\text{-}r_e)^2 \Theta\Psi (\sin\beta_n \cos\beta_n \cos\Phi_n \sin\Psi + \cos^2\beta_n \sin\Phi_n \cos\Phi_n \cos\Psi) + \\
& + 2(r\text{-}r_e)^2 \Theta\dot{\Phi}_n (\cos^2\beta_n \sin\Psi + \sin\beta_n \cos\beta_n \sin\Phi_n \cos\Psi) + \\
& + 2(r\text{-}r_e)^2 \dot{\Psi}\Phi_n (-\sin\beta_n \cos\beta_n \cos\Phi_n) + r_e^2 \dot{\Theta}^2 (\sin^2\Psi \cos^2\beta_n + \\
& + \cos^2\Phi_n) + r_e^2 \dot{\Psi}^2 \sin^2\Phi_n + r_e^2 \dot{\Phi}_n^2 + 2\, r_e^2 \Theta\Psi (\cos\Phi_n + \\
& + \sin\Phi_n \cos\Psi) + 2\, r_e^2 \Theta\dot{\Phi}_n \sin\Psi + 2(r\text{-}r_e)\, r_e \beta_n \Theta \cos\beta_n \cos\Phi_n \cos\Psi + \\
& + 2(r\text{-}r_e)\, r_e \dot{\beta}_n \dot{\Psi} \cos\beta_n \sin\Phi_n + 2(r\text{-}r_e)\, r_e \Theta\Psi (\sin\beta_n \cos\Phi_n \sin\Psi + \\
& + 2\ \cos\beta_n \cos\Phi_n \cos\Psi \sin\Phi_n) + 2(r\text{-}r_e)\, r_e \Theta\Phi_n\ (2\cos\beta_n \sin\Psi + \\
& + \sin\beta_n \sin\Phi_n \cos\Psi) + 2(r\text{-}r_e)\, r_e \dot{\Psi}\dot{\Phi}_n (-\sin\beta_n \cos\Phi_n) + \\
& + 2(r\text{-}r_e)\, r_e \Theta^2 (\cos^2\beta_n \sin^2\Phi_n \sin^2\Psi + \cos\beta_n \cos^2\Phi_n + \\
& + \sin\beta_n \sin\Phi_n \sin\Psi \cos\Psi) + 2(r\text{-}r_e)\, r_e \dot{\Psi}^2 (\cos^2\beta_n \sin^2\Phi_n) + \\
& + 2(r\text{-}r_e)\, r_e \dot{\Phi}^2 \cos^2\beta_n + a^2\Theta^2 \cos^2\Psi + \\
& + a^2\dot{\Psi}^2 - 2(r\text{-}r_e)\, a\beta_n \Theta \sin\beta_n \cos\Psi \sin\Phi_n + \\
& + 2(r\text{-}r_e)\, a\beta_n \dot{\Psi} (\sin\beta_n \sin\Phi_n) + 2(r\text{-}r_e) a\ \Theta\dot{\Psi} (-\cos\beta_n \cos\Phi_n \sin\Psi) + \\
& + 2(r\text{-}r_e)\, a\ \Theta\dot{\Phi}_n (\cos\beta_n \sin\Phi_n \cos\Psi) + 2(r\text{-}r_e)\, a\ \dot{\Psi}\dot{\Phi}_n (-\cos\beta_n \cos\Phi_n) + \\
& + 2(r\text{-}r_e)\, a\ \Theta^2\ (\sin\beta_n \cos^2\Psi + \cos\beta_n \sin\Phi_n \sin\Psi \cos\Psi) + \\
& + 2(r\text{-}r_e)\, a\dot{\Psi}^2 \sin\beta_n + 2\ r_e\ a\ \Theta^2 \sin\Phi_n \sin\Psi \cos\Psi + \\
& + 2\ r_e\ a\ \Theta\ \dot{\Psi}\ (-\cos\Phi_n \sin\Psi) + 2\ r_e\ a\ \Theta\dot{\Phi}_n (\sin\Phi_n \cos\Psi) + \\
& + 2\ r_e\ a\ \dot{\Psi}\dot{\Phi}_n (-\cos\Phi_n) \Big] + \frac{1}{2}\int_0^a dm_n x^2 (\Theta^2 \cos\Psi + \dot{\Psi}^2)
\end{aligned} \qquad [5.108]$$

Now we express the blade flapping angle β_n, which is a function of the azimuth angle Φ_n as a sum of harmonic motions around two orthogonal axes in the propeller disc plane. The flapping angle then becomes

$$\beta_n = \beta_0 + \beta_{\Theta 1}\cos\Phi_n + \beta_{\Psi 1}\sin\Phi_n + \beta_{\Theta 2}\cos 2\Phi_n + \\ + \beta_{\Psi 2}\sin 2\Phi_n + \ldots\ldots. \quad [5.109]$$

Equation 5.109 covers all possible flapping motions of the *N*th blade. However, only the first harmonic terms have structural and aerodynamic coupling with other modes; therefore, both the coning angle β_0 and the higher harmonic terms may be neglected. The expression, after simplification, becomes

$$\beta_n = \beta_\Theta \cos\Phi_n + \beta_\Psi \sin\Phi_n \quad [5.110]$$

where β_Θ and β_Ψ are $\beta_{\Theta 1}$ and $\beta_{\Psi 1}$ of Eqn. 5.109. The azimuth angle Φ_n of the *n*th blade becomes

$$\Phi_n = \Omega t + \frac{2\,\pi}{N_b}(n-1) \quad [5.111]$$

The trigonometric functions of β_n and Φ_n in Eqn. 5.108 are expanded into a power series. Because the angles β_n, Θ and Ψ are small, all of the terms greater then second order may be neglected. Then, the β_n and Φ_n are substituted from Eqn. 5.110 and Eqn. 5.111, respectively. From the resulting expression of the kinetic energy, the generalised forces may be obtained using Lagrange's equation:

$$P_i = \frac{d}{dt}\left(\frac{\partial E_k}{\partial q_i}\right) - \frac{\partial E_k}{\partial q_i} \quad [5.112]$$

The expressions are linearised with respect to the initial steady state values β_n, Θ and Ψ, and finally, the generalised forces become

$$\begin{aligned} P_\Theta &= \Omega^2(I_\Theta\,\Theta'' + I_{\beta 2}\,\beta''_\Theta + 2\,I_{\beta 2}\,\beta'_\Psi + 2\,I_{\beta 1}\,\Psi') \\ P_\Psi &= \Omega^2(I_\Psi\,\Psi'' + I_{\beta 2}\,\beta''_\Psi - 2\,I_{\beta 2}\,\beta'_\Theta - 2\,I_{\beta 1}\,\Theta') \\ P_{\beta\Theta} &= \Omega^2(I_\beta\,\beta''_\Theta + I_{\beta 2}\,\Theta'' + 2\,I_{\beta 2}\,\Psi' + 2\,I_\beta\,\beta'_\Psi + I_{\beta 0}\,\beta_\Theta \\ P_{\beta\Psi} &= \Omega^2(I_\beta\,\beta''_\Psi + I_{\beta 2}\,\Psi'' - 2\,I_{\beta 2}\,\Theta' - 2\,I_\beta\,\beta'_\Theta + I_{\beta 0}\,\beta_\Psi) \end{aligned} \quad [5.113]$$

where the blade moments of inertia are defined as

$$I_{\beta} = \frac{N_b}{2}\int_{r_e}^{R} m_b \left(r - r_e\right)^2 dr$$
$$I_{\beta 0} = \frac{N_b}{2}\int_{r_e}^{R} m_b\ r_e \left(r - r_e\right)\ dr$$
$$I_{\beta 1} = \frac{N_b}{2}\int_{0}^{R} m_b\ r^2\ dr \qquad [5.114]$$
$$I_{\beta 2} = \frac{N_b}{2}\int_{r_e}^{R} m_b\ r \left(r - r_e\right)\ dr$$

and the complete system moments of inertia are defined as

$$I_{\Theta} = I_{\beta 1} + N_b\ a^2 \int_0^R m_b\ dr + \frac{1}{2}\int_0^a m_n x^2 dx$$
$$I_{\Psi} = I_{\beta 1} + N_b\ a^2 \int_0^R m_b\ dr + \frac{1}{2}\int_0^a m_n x^2 dx \qquad [5.115]$$

Note that the meanings of the notations are

$$\left(f\right)' = \frac{1}{\Omega}\ \left(\dot{f}\right)$$
$$\left(f\right)'' = \frac{1}{\Omega^2}\ \left(\ddot{f}\right) \qquad [5.116]$$

and we consider

$$\sum_{n=1}^{N_b} \sin^2\Phi_n = \frac{N_b}{2} \quad for\ \ N_b \geq 3$$
$$\sum_{n=1}^{N_b} \cos^2\Phi_n = \frac{N_b}{2} \quad for\ \ N_b \geq 3 \qquad [5.117]$$
$$\sum_{n=1}^{N_b} \sin\ \Phi_n\ \cos\ \Phi_n = 0$$

5.9.2 Elastic forces

The potential energy of the system in Figure 5.24 becomes

$$E_P = \frac{1}{2}K_{\Theta}\Theta^2 + \frac{1}{2}K_{\Psi}\Psi^2 + \frac{1}{2}K_{\beta 1}\sum_{n=1}^{N_b}\beta_n^2 \qquad [5.118]$$

We substitute for β_n from Eqn. 5.110, and Eqn. 5.118 becomes

$$E_P = \frac{1}{2}K_\Theta \Theta^2 + \frac{1}{2}K_\Psi \Psi^2 + \frac{1}{2}K_{\beta 1}\sum_{n=1}^{N_b}\left(\beta_\Theta \cos\Phi_n + \beta_\Psi \sin\Phi_n\right)^2 \qquad [5.119]$$

which is

$$E_P = \frac{1}{2}K_\Theta \Theta^2 + \frac{1}{2}K_\Psi \Psi^2 + \frac{1}{2}K_{\beta 1}\left(\sum_{n=1}^{N_b}\beta_\Theta^2 \cos^2\Phi_n + \sum_{n=1}^{N_b} 2\,\beta_\Theta\beta_\Psi \cos\Phi_n \sin\Phi_n + \sum_{n=1}^{N_b}\beta_\Psi^2 \sin^2\Phi_n\right) \qquad [5.120]$$

We make a simplifications of Eqn. 5.117, and the expression for potential energy becomes

$$E_P = \frac{1}{2}K_\Theta \Theta^2 + \frac{1}{2}K_\Psi \Psi^2 + \frac{N_b}{4}K_{\beta 1}\left(\beta_\Theta^2 + \beta_\Psi^2\right) \qquad [5.121]$$

The generalised elastic forces from Eqn. 5.121 can be expressed as

$$\begin{aligned} S_\Theta &= K_\Theta \Theta \\ S_\Psi &= K_\Psi \Psi \\ S_{\beta\,\Theta} &= \frac{N_b}{2}K_{\beta 1}\beta_\Theta = K_\beta \beta_\Theta \\ S_{\beta\,\Psi} &= \frac{N_b}{2}K_{\beta 1}\beta_\Psi = K_\beta \beta_\Psi \end{aligned} \qquad [5.122]$$

We substitute for the stiffnesses K_Θ, K_Ψ and K_β as

$$\begin{aligned} K_\Theta &= \omega_\Theta^2\, I_\Theta \\ K_\Psi &= \omega_\Psi^2\, I_\Psi \\ K_\beta &= \omega_\beta^2\, I_\beta \end{aligned} \qquad [5.123]$$

We define the frequency ratios as

$$\begin{aligned} \chi_\Theta &= \frac{\omega_\Theta}{\Omega} \\ \chi_\Psi &= \frac{\omega_\Psi}{\Omega} \\ \chi_\beta &= \frac{\omega_\beta}{\Omega} \end{aligned} \qquad [5.124]$$

and the generalised elastic forces from Eqn. 5.122 become

$$S_\Theta = \chi_\Theta^2\ \Omega^2\ I_\Theta\ \Theta$$
$$S_\Psi = \chi_\Psi^2\ \Omega^2\ I_\Psi\ \Psi \qquad [5.125]$$
$$S_{\beta\Theta} = \chi_\beta^2\ \Omega^2\ I_\beta\ \beta_\Theta$$
$$S_{\beta\Psi} = \chi_\beta^2\ \Omega^2\ I_\beta\ \beta_\Psi$$

5.9.3 Damping forces

Considering the model of the damping forces in Eqn. 5.126

$$D = \frac{1}{2}\frac{K_\Theta\gamma_\Theta}{\omega_\Theta}\dot{\Theta}^2 + \frac{1}{2}\frac{K_\Psi\gamma_\Psi}{\omega_\Psi}\dot{\Psi}^2 \qquad [5.126]$$

the generalised damping forces become

$$D_\Theta = \frac{K_\Theta\gamma_\Theta}{\omega_\Theta}\dot{\Theta}$$
$$D_\Psi = \frac{K_\Psi\gamma_\Psi}{\omega_\Psi}\dot{\Psi} \qquad [5.127]$$

We substitute for the stiffnesses K_Θ and K_Ψ from Eqn. 5.123 and for both $\dot{\Theta}$ and $\dot{\Psi}$ from Eqn. 5.116. We introduce the frequency ratios of Eqn. 5.124, and the generalised forces take the final form

$$D_\Theta = \Omega^2\ \gamma_\Theta\ I_\Theta\ \chi_\Theta\ \Theta'$$
$$D_\Psi = \Omega^2\ \gamma_\Psi\ I_\Psi\ \chi_\Psi\ \Psi' \qquad [5.128]$$

5.9.4 Aerodynamic forces

The aerodynamic forces are derived using the quasi-steady theory. Similar to Figure 5.6, the forces acting on the blade element are illustrated in Figure 5.25.

The blade section lift and drag forces are expressed as

$$dL = C_L\ \frac{1}{2}\rho\ U^2 dr$$
$$dD = C_D\ \frac{1}{2}\rho\ U^2 dr \qquad [5.129]$$

where lift and drag coefficients are defined as

$$C_L = a_0\ \alpha$$
$$C_D = C_{d0} + C_{d1}\ \alpha + C_{d2}\ \alpha^2 \qquad [5.130]$$

Now, we can express the blade element thrust dT_n and in-plane force dH_n as

$$dT_n = \frac{1}{2}\rho\ dr\left\{a_0\ U\ U_T\left(\nu - \tan^{-1}\left(\frac{U_P}{U_T}\right)\right) - U\ U_P\left[C_{d0} + C_{d1}\left(\nu - \tan^{-1}\left(\frac{U_P}{U_T}\right)\right) + \right.\right.$$
$$\left.\left. + C_{d2}\left(\nu - \tan^{-1}\left(\frac{U_P}{U_T}\right)\right)^2\right]\right\}$$
$$dH_n = \frac{1}{2}\rho\ dr\left\{a_0\ U\ U_P\left(\nu - \tan^{-1}\left(\frac{U_P}{U_T}\right)\right) + U\ U_T\left[C_{d0} + C_{d1}\left(\nu - \tan^{-1}\left(\frac{U_P}{U_T}\right)\right) + \right.\right.$$
$$\left.\left. + C_{d2}\left(\nu - \tan^{-1}\left(\frac{U_P}{U_T}\right)\right)^2\right]\right\} \qquad [5.131]$$

where U_P and U_T are the perpendicular and in-plane components of the velocity, respectively, in the fixed blade coordinates. The velocity vector with respect to the inertia coordinates is given by

$$\bar{V}_s = \begin{pmatrix} -V_\infty & -\dot{X} \\ & -\dot{Y} \\ & -\dot{Z} \end{pmatrix} \qquad [5.132]$$

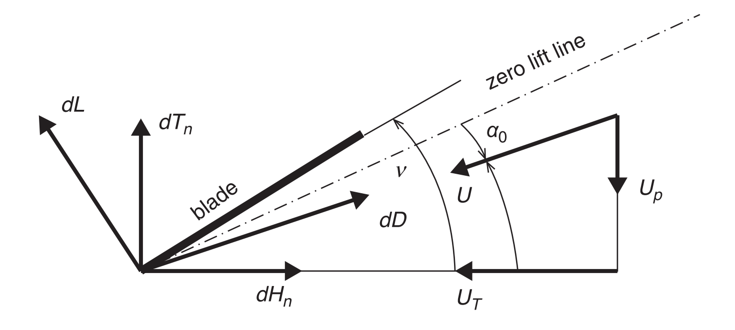


Figure 5.25 Forces on blade section [27]

From the transformation expressions Eqn. 5.100 and Eqn. 5.132, the velocity components on the blade element can be rewritten as

$$\begin{Bmatrix} \dot{X}_b \\ \dot{Y}_b \\ \dot{Z}_b \end{Bmatrix} = \begin{Bmatrix} -U_P \\ U_T \\ U_P \end{Bmatrix} = \left[\left[T_\beta\right]^t \left[T_\Phi\right]^t \left[T_\Psi\right]^t \left[T_\Theta\right]^t \right] \left\{ \bar{V}_s \right\} \qquad [5.133]$$

We make the expansion according to the transformation matrices Eqns. 5.101–5.104, and we obtain

$$\begin{aligned} U_P &= V_\infty\,(\cos\Theta\cos\Psi\cos\beta_n - \cos\Theta\sin\Psi\sin\Phi_n\sin\beta_n - \\ &\quad - \sin\Theta\cos\Phi_n\sin\beta_n) + \Theta\cos\Psi\cos\Phi_n\,(r + a\sin\beta_n) + \\ &\quad + \dot{\Psi}\sin\Phi_n\,(r + a\sin\beta_n) + (r - r_e)\beta_n \\ U_T &= V_\infty\,(\cos\Theta\sin\Psi\cos\Phi_n - \sin\Theta\sin\Phi_n) + r\,\dot{\Theta}(\sin\Psi\cos\beta_n + \\ &\quad + \cos\Psi\sin\Phi_n\sin\beta_n) + a\,\dot{\Theta}\sin\Phi_n\cos\Psi - \\ &\quad - r\dot{\Psi}^2\cos\Phi_n\sin\beta_n + a\Psi\cos\Phi_n + (r - r_e)\Omega\cos\beta_n \end{aligned} \qquad [5.134]$$

The elemental force dF in the inertia coordinate system according Eqn. 5.105 and Eqn. 5.131 is expressed as

$$\left\{d\vec{F}\right\} = \left[\left[T_\Theta\right]\ \left[T_\Psi\right]\ \left[T_\Phi\right]\ \left[T_\beta\right]\right] \begin{Bmatrix} dT_n \\ dH_n \\ 0 \end{Bmatrix} \qquad [5.135]$$

Now, by applying the principle of virtual work, the generalised aerodynamic forces become

$$Q_i = \int_0^R \left\{d\vec{F}\right\}^T \frac{\partial \bar{X}_s}{\partial q_i} \qquad [5.136]$$

The aerodynamic forces are non-linear. Therefore, we make the expansion in Taylor's series around the steady values of Θ, Ψ and β_n and truncate the series at the first order derivatives. The linearised aerodynamic forces after the mathematical manipulations become

$$\begin{aligned} Q_\Theta &= \frac{N_b}{4}\rho\, a_0\, c_0\, R^4\, \Omega^2 \Big[N_{\beta 1}\eta_a \mu\, \Theta + \left(N_{\beta 2} - N_{\beta 1}\eta_a^2\right)\Theta' + \\ &\quad + \mu\, N_{\beta 4}\Psi - \eta_a\left(N_{\beta 4} + N_{\beta 3}\right)\Psi' + \left(N_{\beta 5} - N_{\beta 8}\right)\beta_\Psi - \\ &\quad - \eta_a N_{\beta 6}\beta'_\Psi + \eta_a\left(N_{\beta 6} + N_{\beta 7}\right)\beta_\Theta + N_{\beta 5}\beta'_\Theta \Big] \end{aligned}$$

$$Q_{\Psi} = \frac{N_b}{4}\rho\, a_0\, c_0\, R^4\, \Omega^2 \Big[N_{\beta 1}\, \eta_a \mu\, \Psi + \left(N_{\beta 2} - N_{\beta 1}\eta_a^2\right) \Psi' - \\ -\mu\, N_{\beta 4}\Theta + \eta_a \left(N_{\beta 3} + N_{\beta 4}\right) \Theta' - \left(N_{\beta 5} - N_{\beta 8}\right)\beta_{\Theta} + \eta_a N_{\beta 6}\beta'_{\Theta} + \\ +\eta_a \left(N_{\beta 6} + N_{\beta 7}\right) \beta_{\Psi} + N_{\beta 5}\beta'_{\Psi} \Big] \qquad [5.137]$$

$$Q_{\beta_\Theta} = \frac{N_b}{4}\rho\, a_0\, c_0\, R^4\, \Omega^2 \left[M_{\beta 1}\beta_{\Theta} - M_{\beta 1}\beta'_{\Psi} + \mu\, M_{\beta 3}\Theta - \eta_a M_{\beta 3}\Theta' - M_{\beta 2}\Psi' \right]$$

$$Q_{\beta_\Psi} = \frac{N_b}{4}\rho\, a_0\, c_0\, R^4\, \Omega^2 \left[M_{\beta 1}\beta_{\Psi} + M_{\beta 1}\beta'_{\Theta} + \mu\, M_{\beta 3}\Psi - \eta_a M_{\beta 3}\Psi' + M_{\beta 2}\Theta' \right]$$

where the dimensionless propeller radius η is defined as $\eta = (r/R)$, and the dimensionless propeller hub distance η_a is defined as $\eta_a = (a/R)$. Further auxiliary aerodynamic terms are defined as

$$M_{\beta 1} = -2\, \eta_e^2 \mu^2 \frac{C_{D0}}{\alpha}\, R_{\beta 0} + \left[4\, \eta_e \mu^2 \frac{C_{D0}}{\alpha} + \mu\, \eta_e^2 \left(\alpha_0 + \frac{C_{d1} + 2\, C_{d2}\alpha_0}{\alpha} \right) \right] R_{\beta 1} - \\ -\left[2\mu^2 \frac{C_{D0}}{\alpha} + 2\, \eta_e \mu \left(\alpha_0 + \frac{C_{d1} + 2\, C_{d2}\alpha_0}{\alpha} \right) + \eta_e^2 \left(1 + \frac{C_{D0}}{\alpha} \right) \right] R_{\beta 2} + \\ + \left[\mu \left(\alpha_0 + \frac{C_{d1} + 2\, C_{d2}\alpha_0}{\alpha} \right) + 2\, \eta_e \left(1 + \frac{C_{D0}}{\alpha} \right) \right] R_{\beta 3} - \left(1 + \frac{C_{D0}}{\alpha} \right) R_{\beta 4} \qquad [5.138]$$

$$M_{\beta 2} = 2\, \eta_e \mu^2 \frac{C_{D0}}{\alpha}\, R_{\beta 1} - \left[2\mu^2 \frac{C_{D0}}{\alpha} + \mu\, \eta_e \left(\alpha_0 + \frac{C_{d1} + 2\, C_{d2}\alpha_0}{\alpha} \right) \right] R_{\beta 2} + \\ + \left[\mu \left(\alpha_0 + \frac{C_{d1} + 2\, C_{d2}\alpha_0}{\alpha} \right) + \eta_e \left(1 + \frac{C_{D0}}{\alpha} \right) \right] R_{\beta 3} - \left(1 + \frac{C_{D0}}{\alpha} \right) R_{\beta 4} \qquad [5.139]$$

$$M_{\beta 3} = \eta_e \mu^2 \left(-\alpha_0 + \frac{C_{d1} + 2\, C_{d2}\alpha_0}{\alpha} \right) R_{\beta 0} + \\ + \left[\mu^2 \left(\alpha_0 - \frac{C_{d1} + 2\, C_{d2}\alpha_0}{\alpha} \right) - \mu\, \eta_e \left(1 - \frac{C_{D0}}{\alpha} \right) \right] R_{\beta 1} + \\ + \left[-2\, \eta_e \alpha_0 + \mu \left(1 - \frac{C_{D0}}{\alpha} \right) \right] R_{\beta 2} + 2\, \alpha_0 R_{\beta 3} \qquad [5.140]$$

$$N_{\beta 1} = \mu^2 \left(1 + \frac{C_{D0}}{\alpha} \right) R_{\beta 0} + \mu \left(\alpha_0 + \frac{C_{d1} + 2\, C_{d2}\alpha_0}{\alpha} \right) R_{\beta 1} + 2 \frac{C_{D0}}{\alpha} R_{\beta 2} \qquad [5.141]$$

$$N_{\beta 2} = -2\ \mu^2 \frac{C_{D0}}{\alpha} R_{\beta 2} + \mu \left(\alpha_0 + \frac{C_{d1} + 2\ C_{d2}\alpha_0}{\alpha}\right) R_{\beta 3} - \left(1 + \frac{C_{D0}}{\alpha}\right) R_{\beta 4} \quad [5.142]$$

$$N_{\beta 3} = 2\ \mu^2 \alpha_0 R_{\beta 1} - \mu \left(1 - \frac{C_{D0}}{\alpha}\right) R_{\beta 2} + \left(\alpha_0 - \frac{C_{d1} + 2\ C_{d2}\alpha_0}{\alpha}\right) R_{\beta 3} \quad [5.143]$$

$$N_{\beta 4} = \mu^2 \left(\alpha_0 - \frac{C_{d1} + 2\ C_{d2}\alpha_0}{\alpha}\right) R_{\beta 1} + \mu \left(1 - \frac{C_{D0}}{\alpha}\right) R_{\beta 2} + 2\ \alpha_0 R_{\beta 3} \quad [5.144]$$

$$\begin{aligned} N_{\beta 5} = {} & 2\ \eta_e \eta \frac{C_{D0}}{\alpha} R_{\beta 1} + \left[-2\mu^2 \frac{C_{D0}}{\alpha} - \eta_e \eta \left(\frac{C_{d1} + 2\ C_{d2}\alpha_0}{\alpha} - \eta\alpha_0\right)\right] R_{\beta 2} + \\ & + \eta \left(\alpha_0 + \frac{C_{d1} + 2\ C_{d2}\alpha_0}{\alpha}\right) + \eta_e \left(1 + \frac{C_{D0}}{\alpha}\right) R_{\beta 3} - \left(1 + \frac{C_{D0}}{\alpha}\right) R_{\beta 4} \end{aligned} \quad [5.145]$$

$$\begin{aligned} N_{\beta 6} = {} & -2\ \mu^2 \eta_e \eta R_{\beta 0} + \left[2\ \mu^2 \alpha_0 + \eta_e \eta \left(1 - \frac{C_{D0}}{\alpha}\right)\right] R_{\beta 1} + \\ & + \left[-\eta \left(1 - \frac{C_{D0}}{\alpha}\right) - \eta_e \left(\alpha_0 - \frac{C_{d1} + 2\ C_{d2}\alpha_0}{\alpha}\right)\right] R_{\beta 2} + \\ & + \left(\alpha_0 - \frac{C_{d1} + 2\ C_{d2}\alpha_0}{\alpha}\right) R_{\beta 3} \end{aligned} \quad [5.146]$$

$$N_{\beta 7} = \alpha_0 R_{\beta 11} - \mu \frac{C_{D0}}{\alpha} R_{\beta 10} \quad [5.147]$$

$$N_{\beta 8} = \mu\ R_{\beta 11} \alpha_0 + \frac{C_{D0}}{\alpha} R_{\beta 12} \quad [5.148]$$

where the dimensionless propeller blade flapping hinge radius η_e is defined as $\eta_e = (r_e/R)$, and the propeller advance ratio μ is defined as $\mu = (V_\infty/\Omega R)$. The aerodynamic drag coefficient for the zero-lift angle of attack ($\alpha = \alpha_0$) is expressed similarly to Eqn. 5.130 as

$$C_{D0} = C_{d0} + C_{d1}\ \alpha_0 + C_{d2}\ \alpha_0^2 \quad [5.149]$$

The zero-lift angle of attack can be expressed as

$$\alpha_0 = \nu - \tan^{-1}\left(\frac{\mu}{\eta}\right) \quad [5.150]$$

The auxiliary aerodynamic integrals are defined as

$$R_{\beta 0} = \int_{\eta_e}^{1} \frac{1}{\sqrt{\mu^2 + \eta^2}} d\eta$$
$$R_{\beta 1} = \int_{\eta_e}^{1} \frac{\eta}{\sqrt{\mu^2 + \eta^2}} d\eta$$
$$R_{\beta 2} = \int_{\eta_e}^{1} \frac{\eta^2}{\sqrt{\mu^2 + \eta^2}} d\eta$$
$$R_{\beta 3} = \int_{\eta_e}^{1} \frac{\eta^3}{\sqrt{\mu^2 + \eta^2}} d\eta \qquad [5.151]$$
$$R_{\beta 4} = \int_{\eta_e}^{1} \frac{\eta^4}{\sqrt{\mu^2 + \eta^2}} d\eta$$
$$R_{\beta 10} = \int_{\eta_e}^{1} \sqrt{\mu^2 + \eta^2}\, d\eta$$
$$R_{\beta 11} = \int_{\eta_e}^{1} \eta \sqrt{\mu^2 + \eta^2}\, d\eta$$
$$R_{\beta 12} = \int_{\eta_e}^{1} \eta^2 \sqrt{\mu^2 + \eta^2}\, d\eta$$

The final equations of motion are given by combining all of the forces acting on the system from Eqn. 5.113, Eqn. 5.125, Eqn. 5.128 and Eqn. 5.137 as follows

$$\begin{aligned} & I_\Theta \Theta'' + I_{\beta 2}\, \beta''_\Theta + \left[\gamma_\Theta I_\Theta \chi_\Theta + \frac{N_b}{4}\rho a_0 c_0 R^4 \left(N_{\beta 1}\eta_a^2 - N_{\beta 2}\right)\right]\Theta' + \\ & + \left[2I_{\beta 1} + \frac{N_b}{4}\rho a_0 c_0 R^4 \eta_a \left(N_{\beta 4} + N_{\beta 3}\right)\right]\Psi' - \frac{N_b}{4}\rho a_0 c_0 R^4 N_{\beta 5}\beta'_\Theta + \\ & + \left(2I_{\beta 2} + \frac{N_b}{4}\rho a_0 c_0 R^4 \eta_a N_{\beta 6}\right)\beta'_\Psi + \left(\chi_\Theta^2 I_\Theta - \frac{N_b}{4}\rho a_0 c_0 R^4 N_{\beta 1}\eta_a \mu\right)\Theta - \\ & - \frac{N_b}{4}\rho a_0 c_0 R^4 \mu N_{\beta 4}\Psi - \frac{N_b}{4}\rho a_0 c_0 R^4 \eta_a \left(N_{\beta 6} + N_{\beta 7}\right)\beta_\Theta + \\ & + \frac{N_b}{4}\rho a_0 c_0 R^4 \left(N_{\beta 8} - N_{\beta 5}\right)\beta_\Psi = 0 \end{aligned} \qquad [5.152]$$

$$I_{\Psi}\ \Psi''+I_{\beta 2}\,\beta''_{\Psi}-\left[\frac{N_b}{4}\rho\,a_0\,c_0\,R^4\eta_a\left(N_{\beta 3}+N_{\beta 4}\right)\Theta'+2\,I_{\beta 1}\right]\Theta'+$$
$$+\left[\gamma_{\Psi}\,I_{\Psi}\,\chi_{\Psi}+\frac{N_b}{4}\rho\,a_0\,c_0\,R^4\left(N_{\beta 1}\eta_a^2-N_{\beta 2}\right)\right]\Psi'-$$
$$-\left(\frac{N_b}{4}\rho\,a_0\,c_0\,R^4\eta_a N_{\beta 6}+2I_{\beta 2}\right)\beta'_{\Theta}-$$
$$-\frac{N_b}{4}\rho\,a_0\,c_0\,R^4N_{\beta 5}\beta'_{\Psi}+\frac{N_b}{4}\rho\,a_0\,c_0\,R^4\mu\,N_{\beta 4}\Theta+$$
$$+\left(\chi_{\Psi}^2\,I_{\Psi}-\frac{N_b}{4}\rho\,a_0\,c_0\,R^4N_{\beta 1}\eta_a\mu\right)\Psi+ \qquad [5.153]$$
$$+\frac{N_b}{4}\rho\,a_0\,c_0\,R^4\left(N_{\beta 5}-N_{\beta 8}\right)\beta_{\Theta}-$$
$$-\frac{N_b}{4}\rho\,a_0\,c_0\,R^4\eta_a\left(N_{\beta 6}+N_{\beta 7}\right)\beta_{\Psi}=0$$

$$I_{\beta 2}\,\Theta''+I_{\beta}\,\beta''_{\Theta}-\frac{N_b}{4}\rho\,a_0\,c_0\,R^4M_{\beta 2}\Theta'+$$
$$+\left(2\,I_{\beta 2}+\frac{N_b}{4}\rho\,a_0\,c_0\,R^4\,\eta_a M_{\beta 3}\right)\Psi'-$$
$$-\frac{N_b}{4}\rho\,a_0\,c_0\,R^4M_{\beta 1}\beta'_{\Theta}+2I_{\beta}\,\beta'_{\Psi}-\frac{N_b}{4}\rho\,a_0\,c_0\,R^4\mu\,M_{\beta 3}\Psi+ \qquad [5.154]$$
$$+\left(\chi_{\beta}^2\,I_{\beta}+I_{\beta 0}\right)\beta_{\Theta}-\frac{N_b}{4}\rho\,a_0\,c_0\,R^4M_{\beta 1}\beta_{\Psi}=0$$

$$I_{\beta 2}\,\Psi''+I_{\beta}\,\beta''_{\Psi}-\left(\frac{N_b}{4}\rho\,a_0\,c_0\,R^4\eta_a M_{\beta 3}+2\,I_{\beta 2}\right)\Theta'-$$
$$-\frac{N_b}{4}\rho\,a_0\,c_0\,R^4M_{\beta 2}\Psi'-$$
$$-2\,I_{\beta}\,\beta'_{\Theta}-\frac{N_b}{4}\rho\,a_0\,c_0\,R^4M_{\beta 1}\beta'_{\Psi}+\frac{N_b}{4}\rho\,a_0\,c_0\,R^4\mu\,M_{\beta 3}\,\Theta+ \qquad [5.155]$$
$$+\frac{N_b}{4}\rho\,a_0\,c_0\,R^4M_{\beta 1}\beta_{\Theta}+\left(\chi_{\beta}^2\,I_{\beta}+I_{\beta 0}\right)\beta_{\Psi}=0$$

The equations of motion may be rewritten into the matrix form [28]

$$[A_{\beta}]\{\ddot{q}\}+\Omega\left([B_{\beta}]+[D_{\beta}]\right)\{\dot{q}\}+\left(\Omega^2\left([C_{\beta}]+[E_{\beta}]\right)+[S_{\beta}]\right)\{q\}=\{0\} \qquad [5.156]$$

where the vector of the generalised coordinates is

$$\{q\} = \begin{Bmatrix} \Theta \\ \Psi \\ \beta_{\Theta} \\ \beta_{\Psi} \end{Bmatrix} \quad [5.157]$$

In the following derivation, we will consider the more general case with an unsymmetric mass moment of inertia around the pitch and yaw axes, i.e. $J_Z \neq J_Y$. Additionaly, the non-coincident engine pitch and yaw hinge points, i.e. the distance between the propeller disc plane and the engine pitch and yaw hinges, are defined as a_{Θ} and a_{Ψ}, respectively. Finally, the non-zero structural damping of the blade flapping mode is considered using the structural damping ratio $\gamma_{\beta} \neq 0$. The matrix of the inertial terms of Eqn. 5.156 becomes [9], [28]

$$[A_{\beta}] = \begin{bmatrix} I_{\beta 1} + \eta_{a\Theta}^2 R^2 m_{PROP} + J_{ZN} & 0 & I_{\beta 2} & 0 \\ 0 & I_{\beta 1} + \eta_{a\Psi}^2 R^2 m_{PROP} + J_{YN} & 0 & I_{\beta 2} \\ I_{\beta 2} & 0 & I_{\beta} & 0 \\ 0 & I_{\beta 2} & 0 & I_{\beta} \end{bmatrix} \quad [5.158]$$

where the propeller mass can be expressed as the sum of the hub and blades mass:

$$m_{PROP} = m_{HUB} + N_b \int_0^R m\, dr \quad [5.159]$$

and the dimensionless distances between the propeller disc plane and the engine pitch and yaw hinges are

$$\eta_{a\Theta} = \frac{a_{\Theta}}{R}$$
$$\eta_{a\Psi} = \frac{a_{\Psi}}{R} \quad [5.160]$$

The matrix of the aerodynamic damping terms of Eqn. 5.156 becomes [9], [28]

$$\left[B_{\beta}\right]=\frac{N_b}{4}a_0\ c_0R^4\begin{bmatrix} B_{\beta 11} & B_{\beta 12} & B_{\beta 13} & B_{\beta 14} \\ B_{\beta 21} & B_{\beta 22} & B_{\beta 23} & B_{\beta 24} \\ B_{\beta 31} & B_{\beta 32} & B_{\beta 33} & 0 \\ B_{\beta 41} & B_{\beta 42} & 0 & B_{\beta 44} \end{bmatrix} \quad [5.161]$$

where

$$\begin{aligned}
B_{\beta 11} &= \eta_{a\Theta}^2\,\mu^2\,R_{\beta 0}+R_{\beta 4}\\
B_{\beta 12} &= \mu\,R_{\beta 2}\,(\eta_{a\Theta}-\eta_{a\Psi})\\
B_{\beta 13} &= R_{\beta 4}-\eta_e\,R_{\beta 3}\\
B_{\beta 14} &= B_{\beta 41}=\eta_{a\Theta}\,\mu\,(R_{\beta 2}-\eta_e\,R_{\beta 1})\\
B_{\beta 21} &= \mu\,R_{\beta 2}(\eta_{a\Theta}-\eta_{a\Psi})\\
B_{\beta 22} &= \eta_{a\Psi}^2\,\mu^2\,R_{\beta 0}+R_{\beta 4}\\
B_{\beta 23} &= B_{\beta 32}=-\eta_{a\Psi}\,\mu\,(R_{\beta 2}-\eta_e\,R_{\beta 1})\\
B_{\beta 24} &= B_{\beta 31}=B_{\beta 42}=R_{\beta 4}-\eta_e\,R_{\beta 3}\\
B_{\beta 33} &= B_{\beta 44}=R_{\beta 4}-2\,\eta_e\,R_{\beta 3}+\eta_e^2\,R_{\beta 2}
\end{aligned} \quad [5.162]$$

The matrix of the aerodynamic stiffness terms of Eqn. 5.156 becomes [9], [28]

$$\left[C_{\beta}\right]=\frac{N_b}{4}a_0\ c_0R^4\begin{bmatrix} C_{\beta 11} & C_{\beta 12} & C_{\beta 13} & C_{\beta 14} \\ C_{\beta 21} & C_{\beta 22} & C_{\beta 23} & C_{\beta 24} \\ 0 & C_{\beta 32} & C_{\beta 33} & C_{\beta 34} \\ C_{\beta 41} & 0 & C_{\beta 43} & C_{\beta 44} \end{bmatrix} \quad [5.163]$$

where:

$$\begin{aligned}
C_{\beta 11} &= \eta_{a\Theta}\,\mu^3\,R_{\beta 0}\\
C_{\beta 12} &= -C_{\beta 21}=\mu^2\,R_{\beta 2}\\
C_{\beta 13} &= \eta_{a\Theta}\,\mu\,(R_{\beta 2}-\eta_e\,R_{\beta 1})+R_{\beta 12}\tan\delta_3\\
C_{\beta 14} &= -(R_{\beta 2}-\eta_e\,R_{\beta 1})+\eta_{a\Theta}\,\mu\,R_{\beta 10}\tan\delta_3\\
C_{\beta 22} &= -\eta_{a\Psi}\,\mu^3\,R_{\beta 0}
\end{aligned} \quad [5.164]$$

$$C_{\beta 23} = (R_{\beta 4} - \eta_e R_{\beta 3}) - \eta_{a\Psi} \mu R_{\beta 10} \tan \delta_3$$

$$C_{\beta 24} = \eta_{a\Psi} \mu (R_{\beta 2} - \eta_e R_{\beta 1}) + R_{\beta 12} \tan \delta_3$$

$$C_{\beta 32} = -C_{\beta 41} = \mu^2 (R_{\beta 2} - \eta_e R_{\beta 1})$$

$$C_{\beta 33} = C_{\beta 44} = (R_{\beta 12} - \eta_e R_{\beta 11}) \tan \delta_3$$

$$C_{\beta 34} = -C_{\beta 43} = -(R_{\beta 4} - 2\eta_e R_{\beta 3} + \eta_e^2 R_{\beta 2})$$

where δ_3 is the kinematic pitch-flap coupling angle. The matrix of the structural damping terms of Eqn. 5.156 becomes [9], [28]

$$\left[D_\beta\right] = \begin{bmatrix} \gamma_\Theta \chi_\Theta J_Y & -2 I_{\beta 1} & 0 & -2 I_{\beta 2} \\ 2 I_{\beta 1} & \gamma_\Psi \chi_\Psi J_Z & 2 I_{\beta 2} & 0 \\ 0 & -2 I_{\beta 2} & I_\beta \gamma_\beta \sqrt{1 + \frac{I_{\beta 0}}{I_\beta}} & -2 I_\beta \\ 2 I_{\beta 2} & 0 & 2 I_\beta & I_\beta \gamma_\beta \sqrt{1 + \frac{I_{\beta 0}}{I_\beta}} \end{bmatrix} \quad [5.165]$$

The remaining matrices of Eqn. 5.156 become [9], [28]

$$\left[E_\beta\right] = \begin{bmatrix} 0 & 0 & 0 & 0 \\ 0 & 0 & 0 & 0 \\ 0 & 0 & I_\beta & 0 \\ 0 & 0 & 0 & I_\beta \end{bmatrix} \quad [5.166]$$

$$\left[S_\beta\right] = \Omega^2 \begin{bmatrix} \chi_\Theta^2 \left(I_{\beta 1} + \eta_{a\Theta}^2 R^2 m_{PROP} + J_Z\right) & 0 & 0 & 0 \\ 0 & \chi_\Psi^2 \left(I_{\beta 1} + \eta_{a\Psi}^2 R^2 m_{PROP} + J_Y\right) & 0 & 0 \\ 0 & 0 & \chi_\beta^2 I_\beta & -I_\beta \gamma_\beta \sqrt{1 + \frac{I_{\beta 0}}{I_\beta}} \\ 0 & 0 & I_\beta \gamma_\beta \sqrt{1 + \frac{I_{\beta 0}}{I_\beta}} & \chi_\beta^2 I_\beta \end{bmatrix}$$

[5.167]

Now, we introduce into Eqn. 5.156 the dimensionless time defined as

$$\tau = \Omega t \qquad [5.168]$$

and multiply by $(1/\Omega^2)$. Then, Eqn. 5.156 takes the form

$$\left[A_\beta\right]\{q\}'' + \left(\left[B_\beta\right]+\left[D_\beta\right]\right)\{q\}' + \left(\left(\left[C_\beta\right]+\left[E_\beta\right]\right)+\frac{1}{\Omega^2}\left[S_\beta\right]\right)\{q\} = \{0\} \qquad [5.169]$$

where the derivatives with respect to the dimensionless time are

$$q' = \left(\frac{\partial q}{\partial \tau}\right) = \Omega \dot{q}$$
$$q'' = \left(\frac{\partial^2 q}{\partial \tau^2}\right) = \Omega \ddot{q} \qquad [5.170]$$

The matrices of Eqn. 5.169 are now rewritten into the general form of the equation

$$[M]\{q\}'' + [D]\{q\}' + [K]\{q\} = \{0\} \qquad [5.171]$$

where

$$[M] = \left[A_\beta\right]$$
$$[D] = \left[B_\beta\right]+\left[D_\beta\right] \qquad [5.172]$$
$$[K] = \left[C_\beta\right]+\left[E_\beta\right]+\frac{1}{\Omega^2}\left[S_\beta\right]$$

Equation 5.171 is then rewritten into the eigenvalue form of

$$[K]^{-1}[M]\{q\}'' + [K]^{-1}[D]\{q\}' + [I]\{q\} = \{0\} \qquad [5.173]$$

We introduce the auxiliary vector of the generalised velocities $\{q\}'$ as the identity equation:

$$\{q\}' = \{q\}' \qquad [5.174]$$

and expand Eqn. 5.173 with Eqn. 5.174, and both can be rewritten in the matrix form as

$$\begin{Bmatrix} \{q\}' \\ \{q\} \end{Bmatrix} = \begin{bmatrix} 0 & [I] \\ -[K]^{-1}[M] & -[K]^{-1}[D] \end{bmatrix} \begin{Bmatrix} \{q\}'' \\ \{q\}' \end{Bmatrix} \qquad [5.175]$$

We define the extended vector of the generalised coordinates as

$$\{Q\} = \begin{Bmatrix} \{q\}' \\ \{q\} \end{Bmatrix} \quad [5.176]$$

and Eqn. 5.175 can be rewritten into the compact form of

$$\{Q\} = [A]\{Q\}' \quad [5.177]$$

where $[A]$ is the flutter matrix, definition of which is obvious from Eqn. 5.175. By considering the state of the neutral stability, we can substitute the assumed solution

$$\{Q\} = \{Q_0\}\, e^{\lambda\tau} \quad [5.178]$$

into Eqn. 5.177:

$$\{Q_0\} = \lambda[A]\{Q_0\} \quad [5.179]$$

which can be rewritten into the standard eigenvalue form as

$$[A]\{Q_0\} = \frac{1}{\lambda}\{Q_0\} \quad [5.180]$$

The solution of Eqn. 5.180 is the system of four complex conjugate pairs of eigenvalues λ and eigenvectors $\{Q_0\}$. The resulting complex eigenvalue can be interpreted as

$$\lambda_{(p)} = -\frac{\omega_{(p)}\gamma_{(p)}}{\Omega} + j\,\frac{\omega_{(p)}\sqrt{1-\gamma_{(p)}^2}}{\Omega} \quad [5.181]$$

where $\omega_{(p)}$ is the coupled frequency and $\gamma_{(p)}$ is the damping ratio. The associated complex vector has the form

$$\{Q_0\}_{(p)} = \begin{Bmatrix} \lambda_{FL}\{q\}_{(p)} \\ \{q\}_{(p)} \end{Bmatrix} \quad [5.182]$$

where the lower four elements $\{q\}_{(p)}$ in the modal vector of eight elements define the complex mode shape. The relative amplitude and phase relations between the engine pitch and yaw motions can be given by converting the complex vector to the polar form.

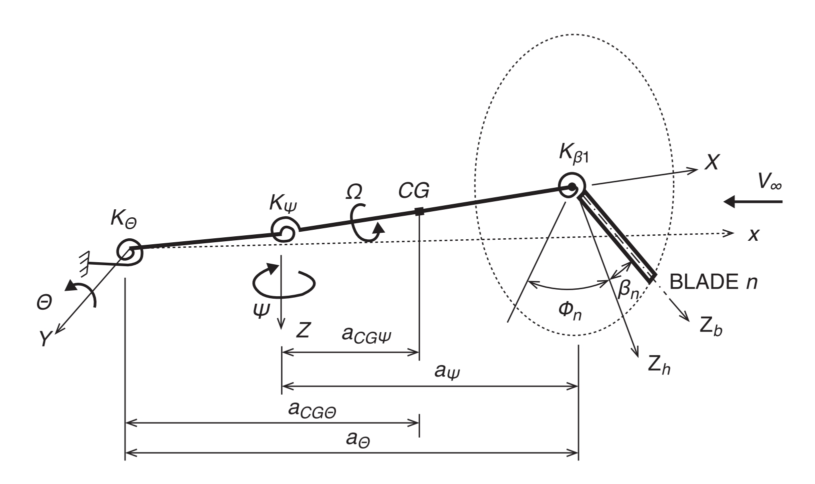


Figure 5.26 Scheme of the gimballed propeller dynamic system

5.10 Influence of gimballed propeller flexibility

The gimballed propeller is characterised by blades rigidly attached to the hub, which is connected to the shaft by the gimbal joint. This model is commonly used for prop-rotor applications. Here, we will consider it to be a special case of the hinged-blade propeller that has zero blade hinge offset ($r_e = 0$), as shown in Figure 5.26.

The equations of motion for the whirl flutter analysis of a gimballed rotor were derived by Kvaternik in [9] and [32] in the general form

$$[M_b]\{\ddot{q}\} + [G_b]\{\dot{q}\} + [D_b]\{\dot{q}\} + [K_b]\{q\} = [D_b^A]\{\dot{q}\} + [K_b^A]\{q\} \qquad [5.183]$$

where the vector of the generalised coordinates is here defined as

$$\{q\} = \begin{Bmatrix} \beta_\Theta \\ \beta_\Psi \\ \Theta \\ \Psi \end{Bmatrix} \qquad [5.184]$$

The matrix of the inertial terms of Eqn. 5.183 becomes [9], [32]:

$$
[M_b]=\begin{bmatrix}
I_b & 0 & I_b+\frac{1}{2}S_b\ \beta_0\ a_\Theta & 0 \\
0 & I_b & 0 & I_b+\frac{1}{2}S_b\ \beta_0\ a_\Psi \\
I_b+\frac{1}{2}S_b\ \beta_0\ a_\Theta & 0 & \begin{matrix} m_{N\Theta}\ a_{CG\Theta}^2+m_{PROP}\ a_\Theta^2+ \\ +I_b+2\ S_b\beta_0\ a_\Theta+J_{ZNCG}\end{matrix} & 0 \\
0 & I_b+\frac{1}{2}S_b\ \beta_0\ a_\Psi & 0 & \begin{matrix} m_{N\Psi}\ a_{CG\Theta}^2+m_{PROP}\ a_\Psi^2+ \\ +I_b+2\ S_b\beta_0\ a_\Psi+J_{YNCG}\end{matrix}
\end{bmatrix}
$$
[5.185]

where I_b is the mass moment of inertia of the flapping propeller, analogous to Eqn. 5.114, defined as

$$I_b=\frac{N_b}{2}\int_0^R m_b\ r^2dr$$ [5.186]

S_b is the mass static moment of the flapping propeller defined as

$$S_b=N_b\int_0^R m_b\ r\ dr$$ [5.187]

a_Θ and a_Ψ are the distances between the propeller disc plane and the pitch and yaw axes, respectively, while $a_{CG\Theta}$ and $a_{CG\Psi}$ are the distances between the nacelle centre of gravity and the pitch and yaw axes, respectively. J_{YNCG} and J_{ZNCG} are the mass moments of inertia of the nacelle in pitch and yaw, respectively, with respect to the centre of gravity axes. Finally, the β_0 is the blade precone angle.

The matrix of the gyroscopic terms of Eqn. 5.183 becomes [9], [32]:

$$[G_b]=2\Omega\begin{bmatrix} 0 & I_b & 0 & I_b \\ -I_b & 0 & -I_b & 0 \\ 0 & I_b & 0 & I_b \\ -I_b & 0 & -I_b & 0 \end{bmatrix}$$ [5.188]

The matrix of the damping terms of Eqn. [5.183] becomes [9], [32]:

$$[D_b]=\begin{bmatrix} g_\beta & 0 & 0 & 0 \\ 0 & g_\beta & 0 & 0 \\ 0 & 0 & g_\Theta & 0 \\ 0 & 0 & 0 & g_\Psi \end{bmatrix}$$ [5.189]

where the viscous damping coefficients in pitch and yaw, respectively, are defined as

$$g_\Theta = \gamma_\Theta\, \omega_\Theta\, J_Z$$

$$g_\Psi = \gamma_\Psi\, \omega_\Psi\, J_Y \qquad [5.190]$$

Note that ω_Θ and ω_Ψ represent the uncoupled pitch and yaw frequencies considering a non-rotating propeller and non-flapping blades, and similarly, J_Z and J_Y are the mass moments of inertia of the system in pitch and yaw for non-flapping blades.

The remaining viscous damping coefficient in the propeller flapping is defined as

$$g_\beta = \gamma_\beta\; I_b\; \Omega\; \sqrt{1+\frac{K_{\beta eq}}{I_b\; \Omega^2}} \qquad [5.191]$$

Note that the propeller flapping damping coefficient appears in the matrix of the stiffness terms as well as in the matrix of the damping terms. This presence is because the viscous structural damping of the flapping propeller is regarded in the rotating system, and the equations of motion are written with respect to the fixed or non-rotating system.

The equivalent stiffness of the propeller flapping spring $K_{\beta eq}$ can be determined from the equations of motion by considering the case including only two cyclic-flapping degrees of freedom of the gimballed propeller. By neglecting the structural damping and the precone angle, the equations of motion reduce to

$$\begin{aligned} I_b\ddot{\beta}_\Theta + 2\, I_b\; \Omega\dot{\beta}_\Psi + K_\beta \beta_\Theta &= \frac{\rho\, a_0 c_0 R^4}{N_b}\left(-R_{\beta 12}\;\beta_\Theta \tan\delta_3 - \frac{R_{\beta 4}}{\Omega}\dot{\beta}_\Theta - R_{\beta 4}\beta_\Psi\right) \\ I_b\ddot{\beta}_\Psi - 2\, I_b\; \Omega\dot{\beta}_\Theta + K_\beta \beta_\Psi &= -\frac{\rho\, a_0 c_0 R^4}{N_b}\left(R_{\beta 12}\;\beta_\Psi \tan\delta_3 + \frac{R_{\beta 4}}{\Omega}\dot{\beta}_\Psi - R_{\beta 4}\beta_\Theta\right) \end{aligned} \qquad [5.192]$$

Now, we express the relation of the reference blade flapping angle to the cyclic flapping degrees of freedom similarly to Eqn. 5.110 as

$$\beta_n = \beta_\Theta \sin\, \Phi_n - \beta_\Psi \cos\Phi_n \qquad [5.193]$$

where the azimuth angle of the reference blade is defined similarly to Eqn. 5.111 as

$$\Phi_n = \Omega t \qquad [5.194]$$

We express the derivatives of Eqn. 5.193 as

$$\dot{\beta}_n = \dot{\beta}_\Theta \sin \Phi_n - \dot{\beta}_\Psi \cos \Phi_n + \Omega \left(\beta_\Theta \cos \Phi_n + \beta_\Psi \sin \Phi_n\right)$$
$$\ddot{\beta}_n = \ddot{\beta}_\Theta \sin \Phi_n - \ddot{\beta}_\Psi \cos \Phi_n + 2\Omega \left(\dot{\beta}_\Theta \cos \Phi_n + \dot{\beta}_\Psi \sin \Phi_n\right) + \Omega^2\left(-\beta_\Theta \sin \Phi_n + \beta_\Psi \cos \Phi_n\right) \quad [5.195]$$

Using the expressions of Eqn. 5.193 and Eqn. 5.194, the equations of motion of Eqn. 5.193 after algebraic manipulations generate the form

$$\ddot{\beta}_n + \frac{\rho\, a_0 c_0 R^4}{N_b}\Omega R_{\beta 4}\dot{\beta}_n + \left(\Omega^2 + \frac{K_\beta}{I_b} + \frac{\rho\, a_0 c_0 R^4}{N_b}\Omega^2 R_{\beta 12}\tan\delta_3\right)\beta_n = 0 \quad [5.196]$$

From Eqn. 5.196, the dimensionless undamped flapping frequency is given as

$$\frac{\omega_\beta}{\Omega} = \sqrt{1 + \frac{K_\beta}{I_b \Omega^2} + \frac{\rho\, a_0 c_0 R^4}{N_b} R_{\beta 12}\tan\delta_3} \quad [5.197]$$

and the aerodynamic damping of the flapping mode

$$\gamma_\beta = \frac{\rho\, a_0 c_0 R^4}{N_b} R_{\beta 4}\frac{\Omega}{\omega_\beta} \quad [5.198]$$

The equivalent stiffness of the propeller flapping spring $K_{\beta eq}$ can now be determined using the requirement that the flapping frequencies for both gimballed blades and hinged blades models are equal. This requirement is expressed by the equation

$$\frac{K_\beta}{I_b\, \Omega^2} + \frac{\rho\, a_0\, c_0 R^4}{N_b} R_{\beta 12}\tan\delta_3 = \frac{I_{\beta 0}}{I_\beta} + \chi_\beta^2 + \frac{\rho\, a_0\, c_0 R^4}{N_b}\eta_e\left(R_{\beta 12} - \eta_e R_{\beta 11}\right)\tan\delta_3 \quad [5.199]$$

Now, we approximate the term $\frac{\rho\, a_0\, c_0 R^4}{N_b}\eta_e$ by $\frac{\rho\, a_0\, c_0 R^4}{N_b}$ and Eqn. 5.199 becomes

$$\frac{K_\beta}{I_b\, \Omega^2} \approx \frac{I_{\beta 0}}{I_\beta} + \chi_\beta^2 - \eta_e \frac{\rho\, a_0\, c_0 R^4}{N_b} R_{\beta 11}\tan\delta_3 \quad [5.200]$$

and finally, the equivalent stiffness of the propeller flapping spring $K_{\beta eq}$ becomes

$$K_{\beta eq} = I_b\, \Omega^2\left(\frac{I_{\beta 0}}{I_\beta} + \chi_\beta^2 - \eta_e \frac{\rho\, a_0\, c_0 R^4}{N_b} R_{\beta 11}\tan\delta_3\right) \quad [5.201]$$

Note that the equivalent stiffness of the propeller flapping spring $K_{\beta eq}$ was given using the flapping frequency ω_β, which includes both the dynamic and aerodynamic terms (see Eqn. 5.197). Because the latter terms are dependent on the flow velocity, the $K_{\beta eq}$ is dependent on both Ω and V_∞.

Now, we can continue describing the matrices of Eqn. 5.183. The matrix of the structural stiffness terms of Eqn. 5.183 becomes [9], [32]:

$$\left[K_b\right]=\begin{bmatrix} K_\beta & \Omega g_\beta & 0 & 0 \\ -\Omega g_\beta & K_\beta & 0 & 0 \\ 0 & 0 & K_\Theta & 0 \\ 0 & 0 & 0 & K_\Psi \end{bmatrix} \qquad [5.202]$$

Note that the viscous damping coefficients appear in both the damping and stiffness matrices because the damping of the flapping motion is considered with respect to the rotating system, whereas the equations of motion are considered with respect to the non-rotating system.

The matrix of the aerodynamic damping terms of Eqn. 5.183 becomes [9], [32]:

$$\left[D_b^A\right]=\frac{\rho a_0 c_0 R^4}{N_b}\Omega^2 \mathrm{I}_\mathrm{b}\begin{bmatrix} D_{11}^A & D_{12}^A & D_{13}^A & D_{14}^A \\ D_{21}^A & D_{22}^A & D_{23}^A & D_{24}^A \\ D_{31}^A & D_{32}^A & D_{33}^A & D_{34}^A \\ D_{41}^A & D_{42}^A & D_{43}^A & D_{44}^A \end{bmatrix} \qquad [5.203]$$

where

$$D_{11}^A = D_{22}^A = D_{31}^A = D_{42}^A = -\frac{R_{\beta 4}}{\Omega}$$

$$D_{12}^A = -\, D_{21}^A = \frac{R_{\beta 3}\mu\beta_0}{\Omega}$$

$$D_{13}^A = -\frac{R_{\beta 4}}{\Omega} - \frac{R_{\beta 1}\mu^2 a_\Theta \beta_0}{\Omega R}$$

$$D_{14}^A = \frac{R_{\beta 3}\mu\beta_0}{\Omega} - \frac{R_{\beta 2}\mu a_\Psi}{\Omega R}$$

$$D_{23}^A = -\frac{R_{\beta 3}\mu\beta_0}{\Omega} + \frac{R_{\beta 2}\mu a_\Theta}{\Omega R}$$

$$D_{24}^A = -\frac{R_{\beta 4}}{\Omega} - \frac{R_{\beta 1}\mu^2 a_\Psi \beta_0}{\Omega R}$$

$$
\begin{aligned}
D_{32}^{A} &= \frac{R_{\beta 3}\mu\beta_0}{\Omega} + \frac{R_{\beta 2}\mu a_{\Theta}}{\Omega R} \\
D_{33}^{A} &= -\frac{R_{\beta 4}}{\Omega} - \frac{R_{\beta 1}\mu^2 a_{\Theta}\beta_0}{\Omega R} - \frac{R_{\beta 0}\mu^2 a_{\Theta}^2}{\Omega R^2} \\
D_{34}^{A} &= \frac{R_{\beta 3}\mu\beta_0}{\Omega} + \frac{R_{\beta 2}\mu\left(a_{\Theta} - a_{\Psi}\right)}{\Omega R} \\
D_{41}^{A} &= -\frac{R_{\beta 3}\mu\beta_0}{\Omega} - \frac{R_{\beta 2}\mu a_{\Psi}}{\Omega R} \\
D_{43}^{A} &= -\frac{R_{\beta 3}\mu\beta_0}{\Omega} + \frac{R_{\beta 2}\mu\left(a_{\Theta} - a_{\Psi}\right)}{\Omega R} \\
D_{44}^{A} &= -\frac{R_{\beta 4}}{\Omega} - \frac{R_{\beta 1}\mu^2 a_{\Psi}\beta_0}{\Omega R} - \frac{R_{\beta 0}\mu^2 a_{\Psi}^2}{\Omega R^2}
\end{aligned}
\qquad [5.204]
$$

Finally, the matrix of the aerodynamic stiffness terms of Eqn. 5.183 becomes [9], [32]:

$$
\left[K_b^A\right] = \frac{\rho\, a_0 c_0 R^4}{N_b}\Omega^2 I_b \begin{bmatrix} K_{11}^A & K_{12}^A & K_{13}^A & K_{14}^A \\ K_{21}^A & K_{22}^A & K_{23}^A & K_{24}^A \\ K_{31}^A & K_{32}^A & K_{33}^A & K_{34}^A \\ K_{41}^A & K_{42}^A & K_{43}^A & K_{44}^A \end{bmatrix} \qquad [5.205]
$$

where

$$
\begin{aligned}
K_{11}^A &= K_{22}^A = -R_{\beta 12}\tan\delta_3 - \mu\,\beta_0\,R_{\beta 3} \\
K_{12}^A &= -K_{21}^A = -R_{\beta 4} + \mu\,\beta_0\,R_{\beta 11}\tan\delta_3 \\
K_{13}^A &= K_{24}^A = \mu^3\beta_0\,R_{\beta 1} \\
K_{14}^A &= -K_{23}^A = K_{34}^A = -K_{43}^A = R_{\beta 2}\,\mu^2 \\
K_{31}^A &= -R_{\beta 12}\tan\delta_3 - \mu\,\beta_0\,R_{\beta 3} - \frac{\mu}{R}a_{\Theta}R_{\beta 2} \\
K_{32}^A &= \mu\,\beta_0\,R_{\beta 11}\tan\delta_3 - R_{\beta 4} + \frac{\mu}{R}a_{\Theta}R_{\beta 10}\tan\delta_3 \\
K_{33}^A &= \mu^3\beta_0\,R_{\beta 1} + \frac{\mu^3}{R}a_{\Theta}R_{\beta 0} \\
K_{41}^A &= R_{\beta 4} - \mu\,\beta_0\,R_{\beta 11}\tan\delta_3 - \frac{\mu}{R}a_{\Psi}R_{\beta 10}\tan\delta \\
K_{42}^A &= -R_{\beta 12}\tan\delta_3 - \mu\,\beta_0\,R_{\beta 3} - \frac{\mu}{R}a_{\Psi}R_{\beta 2} \\
K_{44}^A &= \mu^3\beta_0\,R_{\beta 1} + \frac{\mu^3}{R}a_{\Psi}R_{\beta 0}
\end{aligned}
\qquad [5.206]
$$

The matrices of Eqn. 5.183 are now rewritten into the general form of the equation

$$[M]\{\ddot{q}\} + [D]\{\dot{q}\} + [K]\{q\} = \{0\} \qquad [5.207]$$

where

$$\begin{aligned} [M] &= [M_b] \\ [D] &= [G_b] + [D_b] - [D_b^A] \\ [K] &= [K_b] - [K_b^A] \end{aligned} \qquad [5.208]$$

Equation 5.207 is then rewritten into the eigenvalue form of

$$[I]\{\ddot{q}\} + [M]^{-1}[D]\{q\} + [M]^{-1}[K]\{q\} = \{0\} \qquad [5.209]$$

We introduce the auxiliary vector of the generalised velocities $\{\dot{q}\}$ as the identity equation

$$\{\dot{q}\} = \{\dot{q}\} \qquad [5.210]$$

and expand Eqn. 5.209 with Eqn. 5.210, and both can be rewritten in the matrix form as

$$\begin{Bmatrix} \{\dot{q}\} \\ \{\ddot{q}\} \end{Bmatrix} = \begin{bmatrix} 0 & [I] \\ -[M]^{-1}[K] & -[M]^{-1}[D] \end{bmatrix} \begin{Bmatrix} \{q\} \\ \{\dot{q}\} \end{Bmatrix} \qquad [5.211]$$

We define the extended vector of the generalised coordinates as

$$\{Q\} = \begin{Bmatrix} \{q\} \\ \{\dot{q}\} \end{Bmatrix} \qquad [5.212]$$

and Eqn. 5.175 can be rewritten into the compact form of

$$\{\dot{Q}\} = [A]\{Q\} \qquad [5.213]$$

where $[A]$ is the flutter matrix, the definition of which is obvious from Eqn. 5.211. By considering the state of neutral stability, we can substitute the assumed solution

$$\{Q\} = \{Q_0\}e^{\lambda\tau} \qquad [5.214]$$

into Eqn. 5.213, and we obtain the standard eigenvalue form

$$\lambda\{Q_0\} = [A]\{Q_0\} \qquad [5.215]$$

The solution of Eqn. 5.215 is the system of four complex conjugate pairs of eigenvalues λ and eigenvectors $\{Q_0\}$. Only those roots with positive imaginary parts have a physical interpretation.

The resulting complex eigenvalue can be interpreted as

$$\lambda_{(p)} = -\,\omega_{(p)}\gamma_{(p)} + j\omega_{(p)}\sqrt{1-\gamma_{(p)}^2} \qquad [5.216]$$

where $\omega_{(p)}$ is the pth coupled frequency and $\gamma_{(p)}$ is the critical damping ratio. Provided the real part is positive, the system diverges. The associated complex vector has the form

$$\{Q_0\}_{(p)} = \begin{Bmatrix} \{q\}_{(p)} \\ \lambda_{FL}\ \{q\}_{(p)} \end{Bmatrix} \qquad [5.217]$$

where the upper four elements $\{q\}_{(p)}$ in the modal vector of eight elements define the complex mode shape. The relative amplitude and phase relation between the engine pitch and yaw motions can be given by converting the complex vector to the polar form.

5.11 Influence of twisted blade flexibility

The more complex model that accounts for the blade flexibility is the twisted blade model. Contrary to the previously mentioned flapping blade model that assumed the blade displacement to be normal to the propeller plane, the twisted blade model includes the displacement components normal to the propeller plane as well as in the propeller plane. The characteristics of twisted blade deformation are shown in Figure 5.27.

The contributions from both components to the blade bending vibration modes depend on various parameters (hub diameter, geometric pitch angle, etc.). The in-plane deformations due to the blade flexibility allow an additional self-excited vibrational mechanism, called ground resonance, which is purely mechanical in origin. This phenomenon is very important in rotorcraft. The basic study of ground resonance was examined in reference [31]; further developments can be found in [33]. Ground resonance was also recognised as an important concern in tilt-rotor aircraft [34].

The principle study of whirl flutter, including twisted blades, was examined in reference [35], which includes large parametric variations analysed both analytically and experimentally using a simple, low-speed

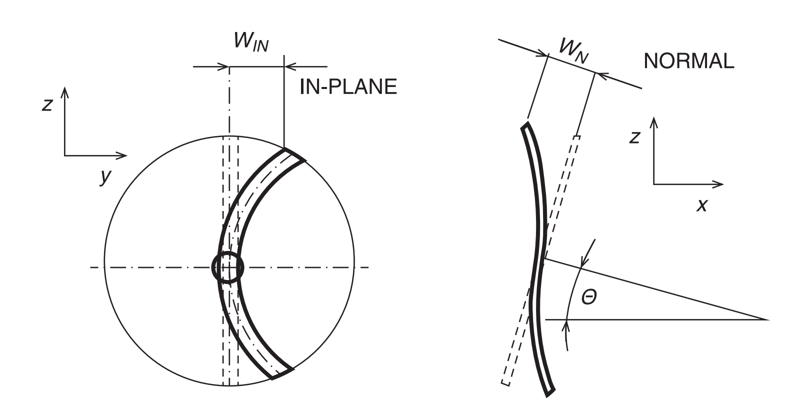


Figure 5.27 **Twisted blade mode and deformation components [30]**

wind tunnel model. The models considered an axisymmetrical nacelle and flexible propeller with constant-chord twisted blades. The blade bending modes that may couple with the whirl flutter are represented by the cyclic pitch and cyclic yaw motions in which the tip path plane is pitched or yawed due to blade bending. These modes are associated with in-plane displacement. An example of the flexible blade mode, represented by the pitch mode with in-plane bending, is illustrated in Figure 5.27. Coning motions of the blades were found to be negligible because they did not couple with the modes involved in the whirl flutter.

The stability characteristics, analysed for the condition of zero damping with no aerodynamic forces (vacuum condition), are shown in Figure 5.28. This plot is similar to the ones presented in reference [31] for the ground resonance mechanism. As the propeller revolutions Ω increase, point (A) is reached where the two frequencies coalesce, resulting in two modes at the same frequency where one is damped and the other is unstable. This point is the beginning of the region of mechanical instability for the forward whirl mode.

The following figures show the influence of the aerodynamic forces on the stability characteristics. The air density parameter is represented by the density ratio. The point (A) in Figure 5.28 is on the zero-density curve. The stability boundaries are presented as plots of the blade frequency and nacelle frequency for both the forward and backward whirl instability. The boundaries for the forward mode originated from the mechanical instability, while the boundaries of the backward mode originated from the whirl flutter instability. Figure 5.29 shows the

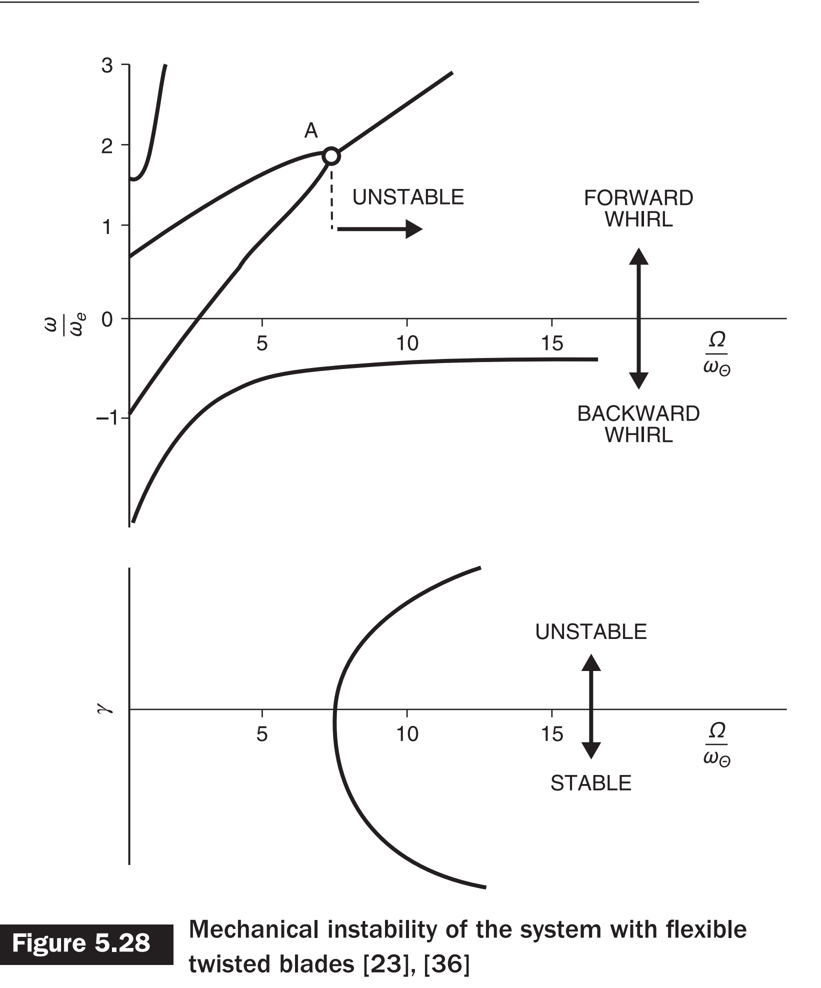


Figure 5.28 **Mechanical instability of the system with flexible twisted blades [23], [36]**

boundaries for the forward whirl instability, which occur in two regions as the density increases. The right hand side region (2) has no practical significance because the rates of growth of the unstable motions were found to be extremely low, and these motions would be eliminated in practice by small structural damping. The other region (1) of the forward whirl instability is worse. Initially the increasing density has a destabilizing effect; however, with further increases in the air density, the unstable region is reduced and possibly eliminated. Mechanical instability appears in the case of $\omega_b < \Omega$, where ω_b is a bending frequency of the blade considering non-rotating propeller.

Figure 5.30 illustrates the boundaries by considering the backward whirl instability, including the asymptotic states for rigid blades. From a

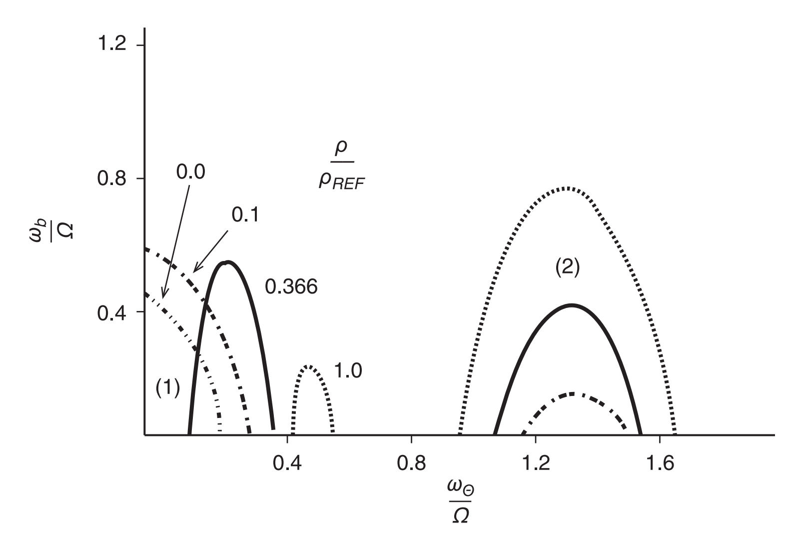


Figure 5.29 Stability boundaries for a system with twisted blades – forward whirl [23], [36]

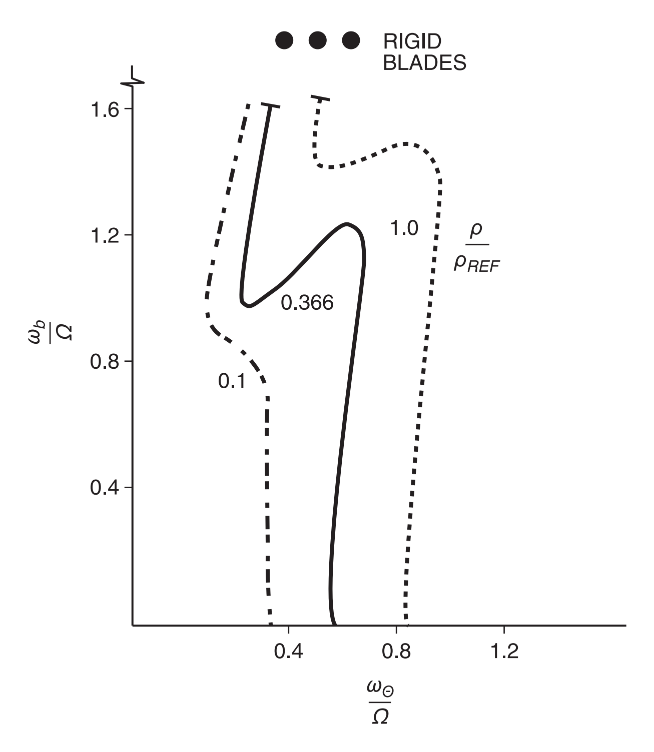


Figure 5.30 Stability boundaries for a system with twisted blades – backward whirl [23], [36]

practical point of view, it can be noted that the influence of the blade flexibility on the propeller backward whirl flutter is small, except for in the region of the frequency ratio ($\omega_b < \Omega$) ≈ 1.0.

5.12 Propeller aerodynamic forces by lifting surface theory

The analytical models that were mentioned above used the fundamental solutions for unsteady aerodynamic forces that were obtained using Strip Theory [2], [4]. Later, the unsteady lifting surface theory was applied to a rotating propeller in a compressible subsonic flow by Hammond, Runyan and Mason [10]. They used the earlier results of Runyan's thesis [11]. The method was was further developed by Williams [37].

The analytical model is based on the linear compressible small disturbance theory. It assumes thin blades and small local angles of attack. The model includes just the helical blade speed, and any further flow distortions are expected to be negligible. Finally, it does not account for the transonic effects that may occur at the blade tips.

The method uses the acceleration potential method to develop the basic downwash integral equation of the fbw. The integral equation is then solved by the Doublett–Lattice method (e.g. [38]). The aerodynamic surface is divided into small trapezoidal lifting elements. The unknown lifting pressures are assumed to be concentrated uniformly across the specified chord location (e.g. 25% chord) of these elements. The downwash condition is satisfied in the one point per element that is located at some other location, typically at the centre spanwise and 75% chordwise.

The derivation of the method [10] is similar to the derivation for the case of a translating wing. First, the relationship between the velocity potential and the acceleration potential is determined. Then, the acceleration potential of the translating and rotating doublet is expressed. This doublet acceleration potential satisfies the differential equation of the flow, and thus can be used for the complete flow solution. Using this method, the integral equation relating the pressure distribution on the propeller blade to the downwash at the surface of the blade is formulated. Finally, the boundary condition is applied to the velocity that is normal to the blade surface. The procedure is outlined here, and a complete derivation can be found in reference [11].

The relation between the velocity potential (ϕ) and the acceleration potential (ψ) is:

$$\psi = \frac{\partial \phi}{\partial t} + \vec{v}\,\nabla\phi \qquad [5.218]$$

Considering a propeller rotating with an angular velocity Ω exposed to a windflow of velocity V_∞, the vector of the velocity $\vec{v}$ as viewed from the blade can be expressed as:

$$\vec{v} = V_\infty \bar{e}_x - r\Omega\,\bar{e}_\theta \qquad [5.219]$$

where the geometry is as shown in Figure 5.31.

In cylindrical coordinates, the velocity potential is:

$$\nabla\phi = \frac{\partial \phi}{\partial r}\bar{e}_r + \frac{l}{r}\frac{\partial \phi}{\partial \theta}\bar{e}_\theta + \frac{\partial \phi}{\partial x}\bar{e}_x \qquad [5.220]$$

and the acceleration potential is therefore:

$$\psi(x,\theta,r,t) = \frac{\partial \phi}{\partial t} + V_\infty \frac{\partial \phi}{\partial \theta} - \Omega \frac{\partial \phi}{\partial \theta} \qquad [5.221]$$

Considering ($\Omega = 0$), the equation reduces to the standard form for a translating wing. The solution for Eqn. 5.221 is obtained using the helical coordinate system that is shown in Figure 5.32.

$$\sigma = \theta + \frac{x}{h}$$
$$\sigma' = \theta - \frac{x}{h} \qquad [5.222]$$

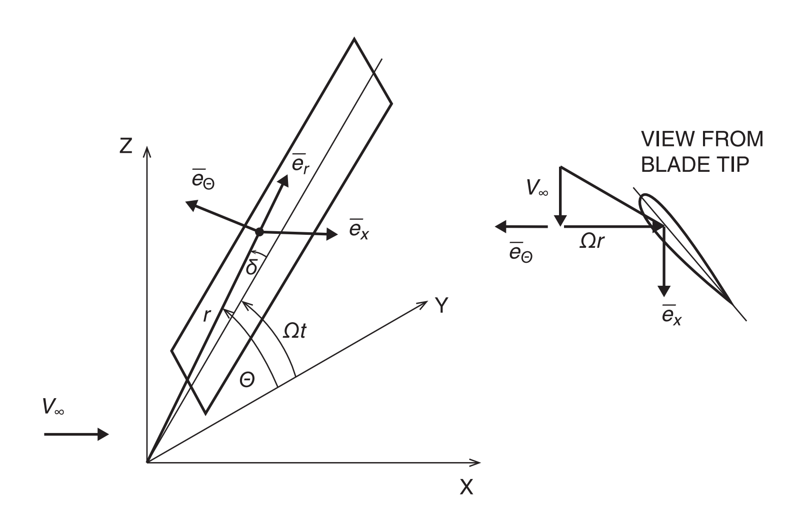


Figure 5.31 **Velocities at the propeller [10]**

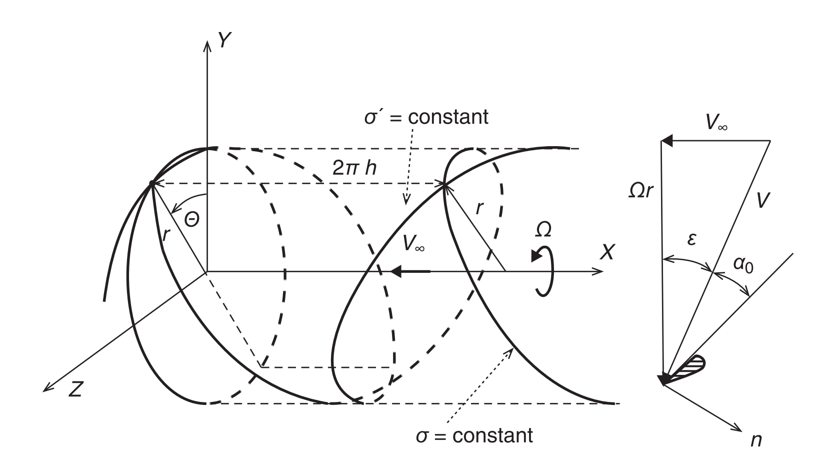


Figure 5.32 **Helical coordinate system at the propeller [10]**

where h is the advance ratio defined here as:

$$h = \frac{V_\infty}{\Omega} \quad [5.223]$$

The transformation of Eqn. 5.223 and the radial distance r determine the position in space. Employing this transformation, Eqn. 5.221 reduces to:

$$\psi(\sigma, \sigma', r, t) = \frac{\partial \phi}{\partial t} - 2\Omega \ \frac{\partial \phi}{\partial \sigma'} \quad [5.224]$$

A similar transformation with coordinates (σ_0; σ_0'; r_0) is used for the location of the doublet:

$$\sigma_0 = \theta_0 + \frac{x_0}{h}$$
$$\sigma_0' = \theta_0 - \frac{x_0}{h} \quad [5.225]$$

Using the helical system, the location of the wake is fixed in a geometric sense as a function of flow velocity and rotational speed. In reality, the wake position is also dependent on the blade loading which would introduce non-linear effects. For the case of static or zero flow velocity, the wake position is a direct function of the blade loading. However, for the case that we are discussing, the position of the wake is described by the helical system with sufficient accuracy.

Assuming harmonic motion of the vibrating blades, expressed as:

$$\begin{aligned}\psi &= \psi_0 \, e^{j\omega t} \\ \phi &= \phi_0 \, e^{j\omega t}\end{aligned} \qquad [5.226]$$

Eqn. 5.224 can be rewritten as:

$$\psi_0(\sigma,\sigma',r,t) = j\omega\phi_0 - 2\Omega \, \frac{\partial \phi_0}{\partial \sigma'} \qquad [5.227]$$

Equation 5.125 is now in the same form as the one for the case of the translating wing. The equation is solved for ϕ_0 resulting in:

$$\varphi_0(\sigma,\sigma',r) = \frac{e^{\frac{j\omega\sigma'}{2\Omega}}}{2\Omega} \int_{\infty}^{\sigma'} e^{\frac{-j\omega\lambda}{2\Omega}} \psi_0(\lambda,\sigma,r) \, d\lambda \qquad [5.228]$$

where λ is the dummy variable of integration. The lower limit of the integration was determined such that there is no disturbance far ahead of the propeller. Equation 5.228 directly relates the velocity potential (ϕ) to the acceleration potential (ψ).

Now, we proceed with the expression for ψ, representing the rotating and translating doublet. The expression may be obtained by several methods (e.g., Green, Küssner). The resulting equation, with a sinusoidally varying doublet strength q, is given as:

$$\psi_D = -\frac{1}{4\pi} q_D \, e^{j\omega t} \, \frac{\partial}{\partial \, \bar{n}_0} \left[\frac{e^{-j\omega(t-\tau)}}{s_D + \frac{1}{a_S}\left[-V_\infty(t-\tau) + V_\infty(x-x_0) - r \, r_0 \Omega \, \sin(\theta-\theta_0)\right]} \right] \qquad [5.229]$$

where:

$$s_D = \sqrt{\left[-V_\infty\left(t-\tau\right)+\left(x-x_0\right)\right]^2 + r^2 + r_0^2 - 2 \, r \, r_0 \cos\left(\theta-\theta_0\right)} \qquad [5.230]$$

As is evident from Eqn. 5.229, ψ_D is a function of (x, r, θ, t, x_0, r_0, θ_0, τ). The partial derivative

$$\frac{\partial}{\partial \bar{n}_0} = -\cos \, \varepsilon_0 \frac{\partial}{\partial x_0} - \frac{\sin \varepsilon_0}{r} \frac{\partial}{\partial \theta_0} \qquad [5.231]$$

where:

$$\varepsilon_0 = \tan^{-1}\left(\frac{V_\infty}{\Omega r_0}\right) \qquad [5.232]$$

represents a derivative that is normal to the resultant velocity vector at time τ. Using derivatives, the acceleration potential for the doublet becomes

$$4\pi\psi_D = \frac{1}{a_S}\frac{\partial q_D}{\partial\tau}\frac{1}{D_D^2}\left\{-\cos\ \varepsilon_0\left[(x-x_0)-V_\infty(t-\tau)\right]-r\sin\varepsilon_0\sin(\theta-\theta_0)\right\}-$$
$$-\frac{q_D}{a_S^2 D_D^3}\left\{\left[a_S^2-V_\infty^2-\Omega^2 r\ r_0\cos(\theta-\theta_0)\right]\left[\cos\varepsilon_0(x-x_0)-\cos\varepsilon_0 V_\infty(t-\tau)+\right.\right.$$
$$\left.\left.+r\sin\varepsilon_0\sin(\theta-\theta_0)\right]\right\}-\frac{q_D}{a_S D_D^2}\left[V_\infty\cos\varepsilon_0-r\ \Omega\ \sin\varepsilon_0\cos(\theta-\theta_0)\right]$$

[5.233]

which is subject to the constraint equation

$$\left(a_S^2-V_\infty^2\right)(t-\tau)^2=(x-x_0)^2-2V_\infty(x-x_0)(t-\tau)+$$
$$+r^2+r_0^2-2r\ r_0\cos(\theta-\theta_0)$$ [5.234]

where the auxiliary quantity D_D is defined as

$$D_D = s_D - \frac{1}{a_S}\left[-V_\infty(x-x_0)+V_\infty^2(t-\tau)+\Omega\ r\ r_0\cos(\theta-\theta_0)\right]$$ [5.235]

Contrary to fixed-surface theory, Eqn. 5.234 cannot be solved explicitly for the time delay $(t-\tau)$ because $(\theta-\theta_0)$ is a function of $(t-\tau)$. Therefore the solution of the doublet acceleration potential is based on numerical determination of $(t-\tau)$.

Similar to the fixed wing analysis, the doublet strength q_D can be related to the pressure differential across the surface as

$$q_D = q_{D0}\ e^{j\omega t} = \frac{\Delta p}{\rho}\ e^{j\omega t} = \frac{\Delta p}{\rho}\ e^{j\omega t}e^{-j\omega(t-\tau)}$$ [5.236]

The reason for deriving Eqn. 5.228 is to determine the downwash conditions at the wing surface. The downwash is determined normal to the resultant velocity vector. The magnitude of the velocity vector at a particular radial location of the blade is

$$V=\sqrt{V_\infty^2+r^2\Omega^2}$$ [5.237]

The velocity vector makes an angle of

$$\varepsilon=\tan^{-1}\left(\frac{V_\infty}{r\Omega}\right)$$ [5.238]

with the *x*-*z* plane. The expression for the normal derivative is the same as the one used for the doublet of Eqn. 5.231, but the derivative is applied at the point (x, r, θ). This becomes

$$\frac{\partial}{\partial \bar{n}} = -\cos\varepsilon\frac{\partial}{\partial x} - \frac{\sin\varepsilon}{r}\frac{\partial}{\partial\theta} \qquad [5.239]$$

Now, we apply the derivative of Eqn. 5.239 to the normal derivative of the velocity potential (ϕ) defined by Eqn. 5.228 resulting in

$$w = \frac{\partial\phi}{\partial\bar{n}} = -\frac{e^{j\omega t}}{2\Omega}\left\{e^{\frac{j\omega\sigma'}{2\Omega}}\left[-\cos\ \varepsilon\frac{\partial\sigma'}{\partial x} - \frac{\sin\ \varepsilon}{r}\frac{\partial\sigma'}{\partial\theta}\right]\right.$$
$$\left[\frac{j\omega}{2\Omega}\int_{+\infty}^{\sigma'} e^{\frac{j\omega\lambda}{2\Omega}}\ \psi_D\ d\lambda + \ \psi_D\left(\sigma'\right)\right] + \qquad [5.240]$$
$$\left. + e^{\frac{j\omega\sigma'}{2\Omega}}\int_{+\infty}^{\sigma'} e^{-\frac{j\omega\lambda}{2\Omega}}\left[-\cos\ \varepsilon\frac{\partial\psi_D}{\partial x} - \frac{\sin\ \varepsilon}{r}\ \frac{\partial\psi_D}{\partial\theta}\right]\ d\lambda\right\}$$

Equation 5.240 represent the downwash at the point (x, r, θ) due to the doublet at point (x_0, r_0, θ_0). To obtain the total downwash at the point (x, r, θ) due to a distribution of doublets over the surface of the blade, Eqn. 5.240 must be integrated over the blade surface (S_B). The downwash integral equation, in dimensionless form, becomes

$$\frac{w}{V_\infty} = \frac{\bar{h}}{2V_\infty^2}e^{jMk\bar{t}}\int_{S_B} e^{j\frac{k\bar{h}}{2}(\sigma'-\sigma_0')}\left\{\int_{+\infty}^{(\sigma'-\sigma_0')} e^{\frac{-jk\bar{h}\lambda}{2}}\left(\cos\ \varepsilon\frac{\partial\psi_D}{\partial\bar{x}} + \frac{\sin\ \varepsilon}{\bar{r}}\frac{\partial\psi_D}{\partial\theta}\right)d\lambda + \right.$$
$$+\left[\frac{M}{\bar{h}}\frac{\partial\left(\bar{t}-\bar{\tau}\right)}{\partial\bar{x}}\cos\ \varepsilon + \frac{M}{\bar{h}\bar{r}}\frac{\partial\left(\bar{t}-\bar{\tau}\right)}{\partial\theta}\sin\ \varepsilon - \frac{\cos\ \varepsilon}{\bar{h}} + \frac{\sin\ \varepsilon}{\bar{r}}\right] \qquad [5.241]$$
$$\left.\left[\frac{jk\bar{h}}{2}e^{\frac{jk\bar{h}}{2}(\sigma'-\sigma_0')}\int_{+\infty}^{(\sigma'-\sigma_0')} e^{\frac{-jk\bar{h}\lambda}{2}}\psi_D\ d\lambda + \psi_D\left(\sigma'-\sigma_0'\right)\right]\right\}dS_B$$

where $\bar{r}$ is the dimensionless radius of the blade, which is defined as

$$\bar{r} = \frac{r}{R} \qquad [5.242]$$

$\bar{x}$ is the dimensionless x-distance, which is defined as

$$\bar{x} = \frac{x}{R} \qquad [5.243]$$

M is the Mach number, which is defined as

$$M = \frac{V_\infty}{a_S} \qquad [5.244]$$

the dimensionless time is defined as

$$(\bar{t}-\bar{\tau})=\frac{a_S}{R}(t-\tau) \qquad [5.245]$$

k is the reduced frequency, which is here defined as

$$k=\frac{\omega R}{V_\infty} \qquad [5.246]$$

and finally, the dimensionless advance ratio h is defined as

$$\bar{h}=\frac{V_\infty}{R\Omega} \qquad [5.247]$$

Then, the equation for the constraint on $(t - \tau)$ becomes (in dimensionless form)

$$\left(1-M^2\right)\left(\bar{t}-\bar{\tau}\right)^2=\frac{\bar{h}^2}{4}\left(\sigma-\sigma_0-\lambda\right)^2-\bar{h}M\left(\sigma-\sigma_0-\lambda\right)+$$
$$+\bar{r}^2+\bar{r}_0^2-2\,\bar{r}\,\bar{r}_0\cos\frac{1}{2}\left(\sigma-\sigma_0-\lambda\right) \qquad [5.248]$$

Both Eqn. 5.241 and Eqn. 5.252 represent the final form that can be used to determine the load on a vibrating propeller blade in a compressible flow. The derivatives used in Eqn. 5.241 are given by Eqn. 5.233, which is rewritten as

$$4\pi\psi_D=\frac{1}{a_S}\frac{\partial\,q_D}{\partial\,\tau}\frac{A_D}{D_D^2}+\frac{q_D}{a_S^2}\frac{B_D}{D_D^3}+\frac{q_D}{a_S}\frac{C_D}{D_D^2} \qquad [5.249]$$

where the auxiliary quantities are expressed from Eqn. 5.241 as

$$A_D=\{-\cos\varepsilon_0[(x-x_0)-V_\infty(t-\tau)]-r\sin\varepsilon_0\sin(\theta-\theta_0)\}$$
$$B_D=-\{[a_S^2-V_\infty^2-\Omega^2 r\,r_0\cos(\theta-\theta_0)][\cos\varepsilon_0(x-x_0)-$$
$$-\cos\varepsilon_0 V_\infty(t-\tau)+r\sin\varepsilon_0\sin(\theta-\theta_0)]\}$$
$$C_D=-[V_\infty\cos\varepsilon_0-r\Omega\sin\varepsilon_0\cos(\theta-\theta_0)] \qquad [5.250]$$

D_D is obtained using Eqn. 5.235, and the doublet strength q_D is obtained using Eqn. 5.236. The derivatives can be obtained using:

$$4\pi\frac{\partial\psi}{\partial x}=\frac{1}{a_S}\left[\frac{\partial}{\partial x}\left(\frac{\partial q_D}{\partial\tau}\right)\frac{A_D}{D_D^2}+\frac{\partial q_D}{\partial\tau}\frac{\partial A_D}{\partial x}\frac{1}{D_D^2}-\frac{2A_D}{D_D^3}\frac{\partial q_D}{\partial\tau}\frac{\partial D_D}{\partial x}\right]+$$
$$+\frac{1}{a_S^2}\left[\frac{\partial q_D}{\partial x}\frac{B_D}{D_D^3}+\frac{q_D}{D_D^3}\frac{\partial B_D}{\partial x}-\frac{3\,q_D B_D}{D_D^4}\frac{\partial D_D}{\partial x}\right]+ \qquad [5.251]$$
$$+\frac{1}{a_S}\left[\frac{\partial q_D}{\partial x}\frac{C_D}{D_D^2}+\frac{q_D}{D_D^2}\frac{\partial C_D}{\partial x}-\frac{2q_D C_D}{D_D^2}\frac{\partial D_D}{\partial x}\right]$$

$$4\pi\frac{\partial\psi}{\partial\theta}=\frac{1}{a_S}\left[\frac{\partial}{\partial\theta}\left(\frac{\partial q_D}{\partial\tau}\right)\frac{A_D}{D_D^2}+\frac{\partial q_D}{\partial\tau}\frac{\partial A_D}{\partial\theta}\frac{1}{D_D^2}-\frac{2A_D}{D_D^3}\frac{\partial q_D}{\partial\tau}\frac{\partial D_D}{\partial\theta}\right]+$$
$$+\frac{1}{a_S^2}\left[\frac{\partial q_D}{\partial\theta}\frac{B_D}{D_D^3}+\frac{q_D}{D_D^3}\frac{\partial B_D}{\partial\theta}-\frac{3\,q_D B_D}{D_D^4}\frac{\partial D_D}{\partial\theta}\right]+ \quad [5.252]$$
$$+\frac{1}{a_S}\left[\frac{\partial q_D}{\partial\theta}\frac{C_D}{D_D^2}+\frac{q_D}{D_D^2}\frac{\partial C_D}{\partial\theta}-\frac{2q_D C_D}{D_D^3}\frac{\partial C_D}{\partial\theta}\right]$$

The derivatives of Eqn. 5.251 and Eqn. 5.252 are expressed in the dimensionless form as

$$\frac{\partial q_D}{\partial\bar{x}}=-j\,q_{D0}M\,k\,e^{j\,M\,k\,\bar{t}}e^{-j\,M\,k(t-\tau)}\frac{\partial\left(\bar{t}-\bar{\tau}\right)}{\partial\bar{x}} \quad [5.253]$$

$$\frac{\partial q_D}{\partial\bar{\tau}}=j\,q_{D0}\;k\,e^{j\,M\,k\,\bar{t}}e^{-j\,M\,k(t-\tau)} \quad [5.254]$$

$$\frac{\partial}{\partial\bar{x}}\frac{\partial q_D}{\partial\tau}=-q_{D0}M\,k^2e^{j\,M\,k\,\bar{t}}e^{-j\,M\,k(\bar{t}-\bar{\tau})}\frac{\partial(\bar{t}-\bar{\tau})}{\partial\bar{x}} \quad [5.255]$$

$$\frac{\partial\left(\bar{t}-\bar{\tau}\right)}{\partial\bar{x}}=\frac{\left[\frac{\bar{h}}{2}\left(\sigma-\sigma_0-\lambda\right)-M\left(\bar{t}-\bar{\tau}\right)+\frac{\bar{r}\,\bar{r}_0}{\bar{h}}\sin\frac{1}{2}\left(\sigma-\sigma_0-\lambda\right)\right]}{\left[\left(2-M^2\right)\left(\bar{t}-\bar{\tau}\right)+\frac{\bar{h}M}{2}\left(\sigma-\sigma_0-\lambda\right)-\frac{M}{\bar{h}}r\,r_0\sin\frac{1}{2}\left(\sigma-\sigma_0-\lambda\right)\right]} \quad [5.256]$$

$$\frac{\partial\bar{A}_D}{\partial\bar{x}}=-\frac{1}{2}\cos\varepsilon_0\left[1-M\frac{\partial(\bar{t}-\bar{\tau})}{\partial\bar{x}}\right]-$$
$$-\frac{\bar{r}}{2\bar{h}}\sin\varepsilon_0\cos\frac{1}{2}\left(\sigma-\sigma_0+\lambda\right)\left[1+M\frac{\partial(\bar{t}-\bar{\tau})}{\partial\bar{x}}\right] \quad [5.257]$$
$$-\frac{1}{a_S^2}\frac{\partial\bar{B}_D}{\partial\bar{x}}=M^2\left\{\frac{\bar{r}\,\bar{r}_0}{2\bar{h}^3}\sin\frac{1}{2}\left(\sigma-\sigma_0-\lambda\right)\left[1+M\frac{\partial(\bar{t}-\bar{\tau})}{\partial\bar{x}}\right]\right\}$$

$$\left\{\cos\varepsilon_0\left[\frac{\bar{h}}{2}(\sigma-\sigma_0-\lambda)-M(\bar{t}-\bar{\tau})\right]+\bar{r}\sin\varepsilon_0\sin\frac{1}{2}(\sigma-\sigma_0-\lambda)\right\}+$$
$$+\left[1-M^2-\frac{M^2}{\bar{h}^2}\bar{r}\;\bar{r}_0\cos\frac{1}{2}(\sigma-\sigma_0-\lambda)\right] \quad [5.258]$$
$$\left\{\frac{1}{2}\cos\varepsilon_0\left[1-M\frac{\partial\;(\bar{t}-\bar{\tau})}{\partial\bar{x}}\right]+\right.$$
$$\left.+\frac{\bar{r}}{2\bar{h}}\sin\varepsilon_0\cos\frac{1}{2}(\sigma-\sigma_0-\lambda)\left[1+M\frac{\partial(\bar{t}-\bar{\tau})}{\partial\bar{x}}\right]\right\}$$

$$-\frac{R}{a_S}\frac{\partial \bar{C}_D}{\partial \bar{x}} = \frac{\bar{r}M}{2\,\bar{h}^2}\sin\varepsilon_0 \sin\frac{1}{2}(\sigma-\sigma_0-\bar{\lambda})\left[1+M\frac{\partial(\bar{t}-\bar{\tau})}{\partial \bar{x}}\right] \quad [5.259]$$

$$\frac{\partial \bar{D}_D}{\partial \bar{x}} = \frac{\partial \bar{s}_D}{\partial \bar{x}_D} + \frac{M}{2} - \frac{M^2}{2}\frac{\partial(\bar{t}-\bar{\tau})}{\partial \bar{x}} - \\ -\frac{M}{2\bar{h}^2}\bar{r}\;\bar{r}_0\cos\frac{1}{2}\left(\sigma-\sigma_0+\bar{\lambda}\right)\left[1+M\frac{\partial(\bar{t}-\bar{\tau})}{\partial \bar{x}}\right] \quad [5.260]$$

where

$$\frac{\partial \bar{s}_D}{\partial \bar{x}} = \frac{1}{2\bar{s}_D}\left\{\frac{\bar{h}}{2}\left(\sigma-\sigma_0-\bar{\lambda}\right) - \frac{1}{2}M\bar{h}\left(\sigma-\sigma_0-\bar{\lambda}\right)\frac{\partial\left(\bar{t}-\bar{\tau}\right)}{\partial \bar{x}} - \\ -M\left(\bar{t}-\bar{\tau}\right) + M^2\left(\bar{t}-\bar{\tau}\right)\frac{\partial\left(\bar{t}-\bar{\tau}\right)}{\partial \bar{x}} + \\ +\frac{\bar{r}\,\bar{r}_0}{\bar{h}}\left[1+M\frac{\partial\left(\bar{t}-\bar{\tau}\right)}{\partial \bar{x}}\right]\sin\frac{1}{2}\left(\sigma-\sigma_0-\bar{\lambda}\right)\right\} \quad [5.261]$$

Further derivatives with respect to θ are obtained as

$$\frac{\partial \psi}{\partial \theta} = \bar{h}\frac{\partial \psi}{\partial \bar{x}} \quad [5.262]$$

To determine the pressure distribution on the blade from Eqn. 5.241, it is necessary to define the left-hand side (w/V_∞) that represents the known velocity in the normal ($\bar{n}$) direction that guarantees that the boundary condition on the airfoil is satisfied.

The velocity of the blade (normal to the resultant vector velocity V) at a distance r from the axis of rotation is

$$w = \frac{\partial u_B}{\partial t} + V\frac{\partial u_B}{\partial l} \quad [5.263]$$

where u_B is the equation for the blade mode shape at r, V is the magnitude of the velocity at r, which is given by Eqn. 5.237, and l is a coordinate in the direction of the V velocity vector. We consider the blade to be operating with a static angle of attack α_0 with a blade vibration mode of frequency ω_B.

Provided that the blade vibration mode is a torsional mode, u_B can be expressed as

$$u_B = (\alpha_0 + \alpha_{B0}e^{j\omega_B t})l \quad [5.264]$$

where α_{B0} is the amplitude of a blade's torsional vibrations. Therefore, Eqn. 5.263 can be rewritten as

$$w = j\omega_B\, l\, e^{j\omega_B t}\alpha_{B0} + V(\alpha_0 + \alpha_{B0}e^{j\omega_B t}) \quad [5.265]$$

Or, in the dimensionless form

$$\frac{w}{V_\infty} = \alpha_{B0}\left[j\,k\,\bar{l} + \frac{V}{V_\infty}\right] e^{j\,M\,k\,\bar{t}} + \frac{V}{V_\infty}\alpha_0 \quad [5.266]$$

where the dimensionless coordinate is defined as

$$\bar{l} = \frac{l}{R} \quad [5.267]$$

The last term in Eqn. 5.266 represents a steady flow, which is usually neglected because the static component does not influence the point of instability. Therefore, we can write

$$\frac{w}{V_\infty} = \alpha_0\left[j\,k\,\bar{l} + \frac{V}{V_\infty}\right] e^{j\,M\,k\,\bar{t}} = w^{Re} + j\,w^{Im} \quad [5.268]$$

where the real and imaginary terms are

$$w^{Re} = \frac{V}{V_\infty}\alpha_{B0}$$
$$w^{Im} = k\,\bar{l}\,\alpha_{B0} \quad [5.269]$$

Provided that the blade vibration mode is bending or flapping, u_B can be expressed as

$$u_B = h_0\, e^{j\omega_B t} \quad [5.270]$$

where h_0 is the magnitude of the bending motion at r. The normal velocity of Eqn. 5.263 can be rewritten as

$$w = j\omega_B h_0\, e^{j\omega_B t} \quad [5.271]$$

Or, in the dimensionless form

$$\frac{w}{V_\infty} = j\,k\,\bar{h}_0\, e^{j\,M\,k\,\bar{t}} \quad [5.272]$$

where the dimensionless amplitude is defined as

$$\bar{h}_0 = \frac{h_0}{R} \quad [5.273]$$

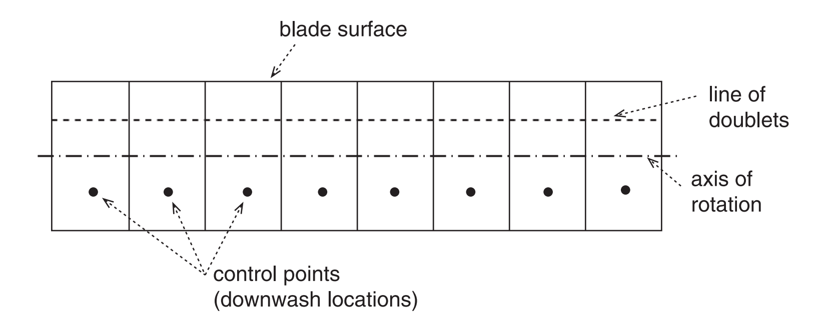


Figure 5.33 **Doublet–Lattice method**

Taking into consideration the complexity of the rotating case in comparison with the case of a translating wing, the resulting downwash integral equations (5.241 and 5.248) are solved using the Doublet–Lattice method [39]. This is one of the simpler methods. This method, which is not described in detail here, divides the surface into panels in both spanwise and chordwise directions. Doublets are distributed over the quarter-line of each panel, and the downwash boundary condition is satisfied at the control point. The control point is centred spanwise at the three-quarter chord, as shown in Figure 5.33.

5.13 Model of coupled bending blades

As has already been mentioned, the rigid blade model is sufficient for the analysis of conventional propellers that are used for commuter aircraft that are certified in accordance with CS/FAR 23 regulations (see Chapter 7). However, the rigid blade model is not sufficient for the large propellers of mid-size or heavy turboprop transport aircraft, such as the C-130, A-400M, An-22, and C-27J. Such aircraft travel with high cruising speeds. However, at the same time, short take-off and landing capabilities (STOL) are required. The aircraft are therefore equipped with large-diameter and large-area propellers (Figure 5.34). The new generation of propellers are characterised by multi-blade configuration and swept tips (Figure 5.35). These features should improve whirl flutter stability. In addition, the concept of twin counter-rotating propellers has been applied (Figure 5.36).

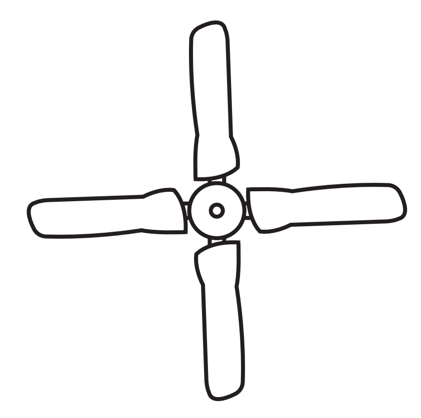


Figure 5.34 Four-blade large area propeller (C-130E)

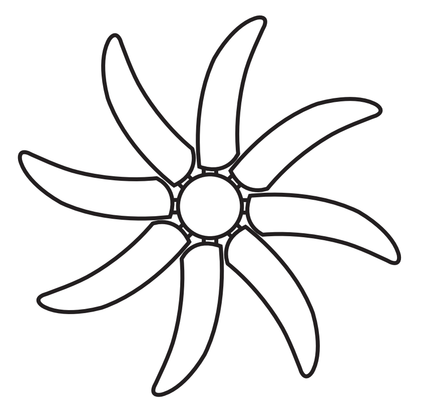


Figure 5.35 Multi-blade swept-tip propeller (A400M)

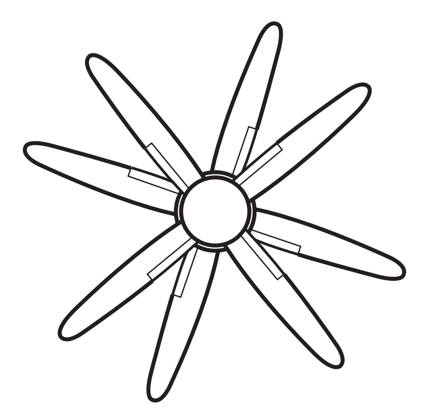


Figure 5.36 Twin counter-rotating propeller (An-22)

Classical whirl flutter models that assume a rigid propeller blade are not sufficient because they predict very low flutter speeds (for some cases) that are not consistent with flight experience. The propeller blade bending dynamic effects are as follows:

1. A forced response of the propeller blade bending due to whirl oscillatory forces that act on the rotating-blade bending mode. This response is structurally and aerodynamically damped. This causes an increase in the propeller shaft moments (due to the whirl aerodynamic moments) with a strong destabilising effect on the whirl flutter.
2. A modal response of the propeller blade bending due to the hub motion. This response is structurally and aerodynamically damped as well. This increases the gyroscopic inertial moments which further decrease the backward whirl flutter frequency but increase the damping of the whirl flutter mode (which arrises from the phase shift of the structurally and aerodynamically damped blade bending dynamic response).

In addition, the engine/nacelle/wing model should include the first engine/nacelle pitch and yaw modes and the fundamental modes of the wing. Donham and Osterholt [40] propose the inclusion of three sets of modes which are: (1) propeller/nacelle/engine vertical and lateral vibration modes characterised as deformation of nacelles vertically and laterally; (2) engine/propeller vertical and lateral pitching with the propeller shaft bending; (3) vertical and lateral bending in the propeller shaft forward of the gearbox. The modes of group (1) have the lowest frequencies and node points that are placed at the farthest aft from the propeller hub. In contrast, the group (3) modes have the highest frequencies and node points that are the closest to the propeller hub.

The effect of propeller bending was elucidated by Donham [41]. The propeller blade flexibility is considered in terms of the coupled flap/in-plane bending mode. The typical blade bending frequencies of the rotating propeller are shown in the Campbell diagram in Figure 5.37.

The first coupled flap/inplane bending frequency is expected to be between 1.5P and 2.7P. Note that 'P' means 'per revolutions'; thus, the

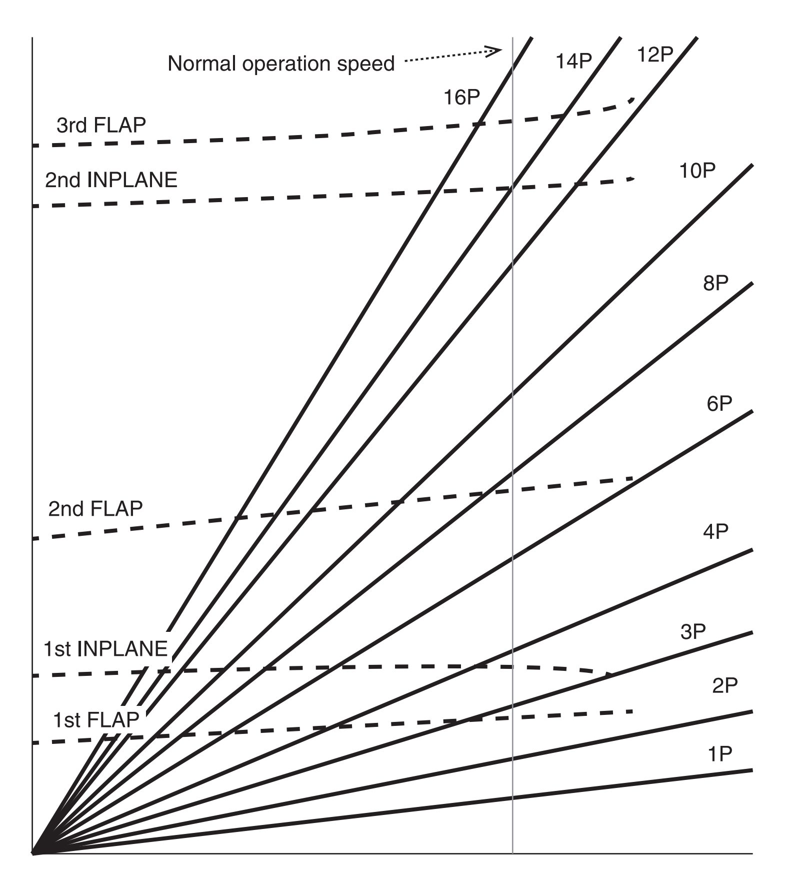


Figure 5.37 **Typical Campbell diagram of the natural frequencies of bending of a rotating propeller [41]**

propeller rotational speed is considered to be '1P'. The typical mode shapes for the first flapping and inplane bending modes are shown in Figure 5.38, and the mode shapes for the second modes are shown in Figure 5.39. The coupled flapping and inplane motions of the rotating blade are expected to occur in these mode shapes.

Considering rotationally symmetric propellers (i.e., three or more blades), the blade harmonics that result in stationary support loads are

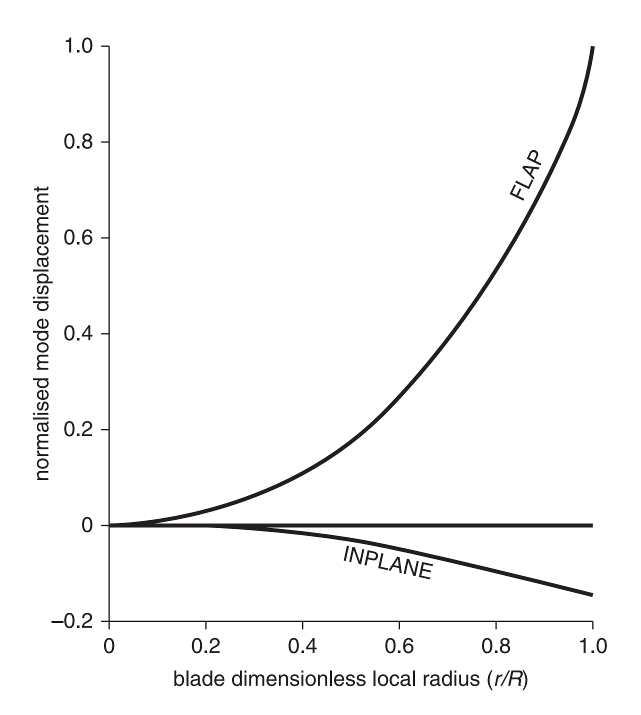


Figure 5.38 Typical blade first bending mode shape [41]

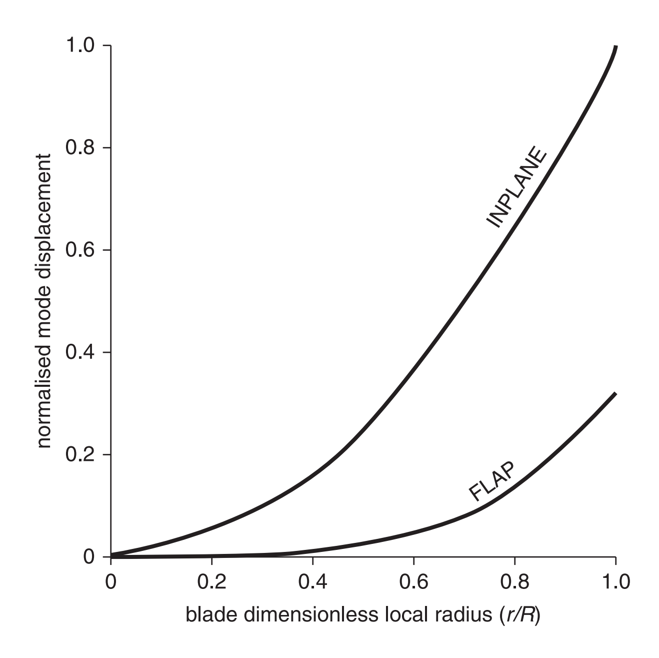


Figure 5.39 Typical blade second bending mode shape [41]

1P (Regressive), (N_b-1)P (Advancing), N_bP (Collective) and (N_b+1)P (Regressive). These patterns for the four-blade propeller are shown in Figure 5.40 for the flapping motion and in Figure 5.41 for inplane motion. The flight loads are at 0P (steady) and N_bP (oscillating).

The differential equations that describe the natural frequency of the cantilevered rotating first bending mode, the mode shape and the

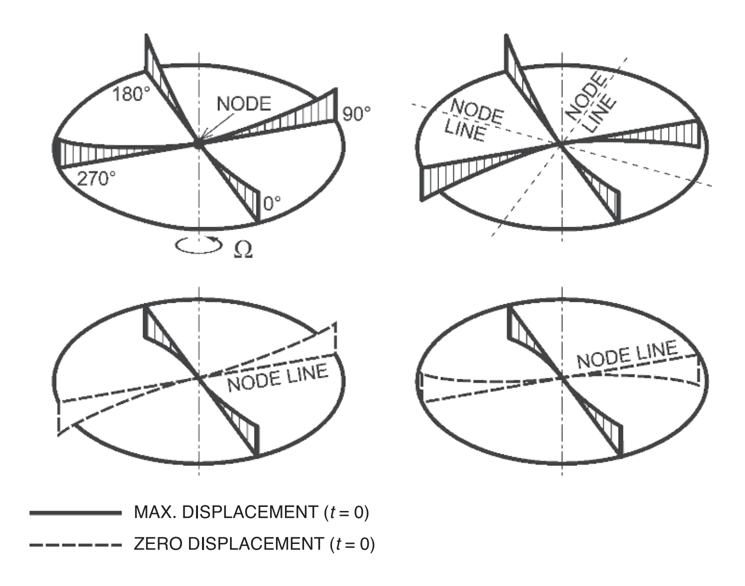


Figure 5.40 Harmonic dynamic response patterns of a rotating four-blade propeller (flapping mode) [41]

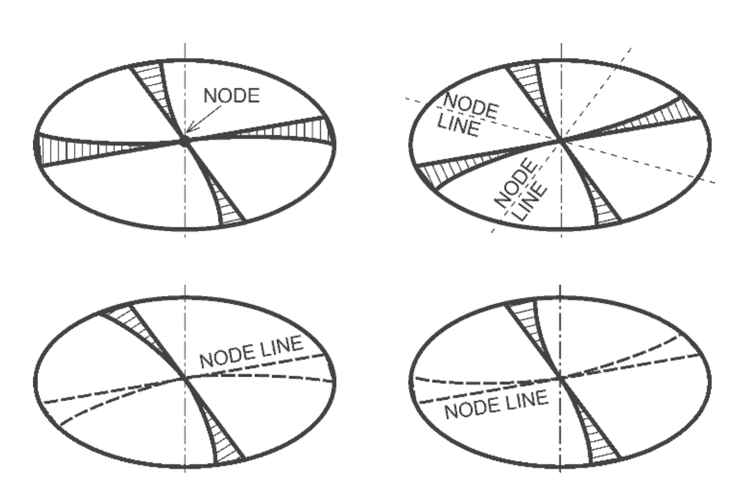


Figure 5.41 Harmonic dynamic response patterns of a rotating four-blade propeller (in-plane mode) [41]

generalised mass are combined with the averaged aerodynamic coefficients to determine the dynamic response of the isolated propeller system to the angle of attack. The dynamic response of the flexible propeller blade is described using rotating natural modes (considering constant shaft revolutions and a fixed pitch angle).

A single degree of freedom (e.g. 1st flap bending mode) over a selected azimuth sector i is described by the equation

$$A_i \frac{d^2\beta}{dt^2} + B_i \frac{d\beta}{dt} + C_i\beta = F_i \qquad [5.274]$$

where A_i, B_i, C_i are coefficients over the azimuth position i and F_i is a constant load acting on the propeller blade over this azimuth. The Laplace transform for each sector, with arbitrary initial conditions at the start of the time period and a constant load acting over the azimuth time period, is

$$\left(A_i s^2 + B_i s + C_i\right)\, \beta(s) = \frac{F_i}{s} + \beta(i)\left(A_i s + B_i\right) + \frac{d\beta_i}{dt} A_i \qquad [5.275]$$

where

$$\beta_i(s) = \frac{F_i}{A_i s\,(s-\alpha_i)(s-\gamma_i)} + \frac{\beta(i)\,A_i s}{A_i(s-\alpha_i)(s-\gamma_i)} + \frac{\beta(i)\,B_i + \frac{d\beta_i}{dt}A_i}{A_i(s-\alpha_i)(s-\gamma_i)} \qquad [5.276]$$

The eigenvalues of the differential equations over sector i are given by α_i and γ_i. $\beta(i)$ and $d\beta(i)/dt$ are the displacement and velocity of these variables at the end of the sector i. The inverse Laplace transform can be determined using partial fractions. Time step integration is not required, and azimuth sector sizes do not have to be equal and stable. Provided that the aerodynamic coefficients are averaged A, B and C become constant over all of the azimuth sectors. The sector step load Laplace transform (F_i/s) may be replaced by the Laplace transform of $F.\sin(\Omega t)$, that is, $F\Omega/(s^2+\Omega^2)$. The initial conditions are set to zero displacement and zero velocity and do not need to be determined for the end of each sector.

The support load for the flexible-support case with gyroscopic moments, is given by Eqn. 5.277 and Eqn. 5.278. The subscript '0' indicates initial conditions, and the subscript 'e' indicates elastic deflections of the support system [*K*].

$$\begin{Bmatrix} M \\ N \\ F_x \\ F_y \end{Bmatrix} = [K]\begin{Bmatrix} \Theta_e \\ \Psi_e \\ X_e \\ Y_e \end{Bmatrix} = [A]\left\{\begin{Bmatrix} \Theta_0 \\ \Psi_0 \\ X_0 \\ Y_0 \end{Bmatrix} + \begin{Bmatrix} \Theta_e \\ \Psi_e \\ X_e \\ Y_e \end{Bmatrix}\right\} + \begin{Bmatrix} M_{gyro} \\ N_{gyro} \\ 0 \\ 0 \end{Bmatrix} \quad [5.277]$$

$$\begin{Bmatrix} \Theta_e \\ \Psi_e \\ X_e \\ Y_e \end{Bmatrix} = \left[[K]-[A]\right]^{-1}\left[[A]\begin{Bmatrix} \Theta_0 \\ \Psi_0 \\ X_0 \\ Y_0 \end{Bmatrix} + \begin{Bmatrix} M_{gyro} \\ N_{gyro} \\ 0 \\ 0 \end{Bmatrix}\right] \quad [5.278]$$

The aerodynamic matrix $[A]$ is defined as:

$$[A] = \begin{bmatrix} M_R & 0 \\ F_R & 0 \end{bmatrix} \quad [5.279]$$

where the M_R values are the rigid propeller aerodynamics, which are dynamically amplified and phase shifted due to the dynamic response of the 1st flap bending mode. The F_R values are the rigid propeller aerodynamics with a time delay.

The load sector should be small enough to adequately determine both the forced dynamic response amplitude and the phase. Donham [41] recommend that a one-degree sector is sufficient, whereas a larger sector may be sufficient for the response amplitude but insufficient for the phase determination.

5.14 Complex models for tilt-rotor applications

The previous sections of Chapter 5 focused on basic and advanced analytical models that used classical analytical approaches that are limited to systems with a reduced number of degrees of freedom. However, advances in computational software tools and hardware in recent years are enabling us now to analyse dynamic systems more or less without limitations. FEM tools are used for structural dynamics, CFD tools for aircraft and propeller aerodynamics, and complex tools for aeroelastic and dynamic simulations. Such complex approaches are also capable of accounting for non-linear effects (e.g., limit cycle oscillations) and their

influence on the dynamic behaviour of the structure. Such complex models are useful for applications with large elastic deflections, helicopters and tilt-rotor aircraft.

Tilt-rotor aircraft are characterised by large rotor pylon systems that are connected to the wing-tips. They combine the hover (helicopter) mode and the high-speed forward flight (airplane) mode. Tilt-rotors are susceptible to whirl flutter, particularly during forward flight, due to the excitation of the wing by the loads that are acting on the rotors. The contributing factors are a high level of rotor blade flapping, bending and control system flexibility. In contrast to an ordinary propeller/wing aircraft, the wing frequencies are much lower due to the large masses that are placed at the wing tips. As mentioned previously, the whirl flutter conditions are the major factors that limit the cruise flight velocity. The whirl flutter of the tilt-rotor aircraft typically involves two modes – a rotor mode and a pylon mode. The pylon mode has the character of a forward whirl, whereas the rotor mode has the character of a backward whirl.

The analytical prediction of a tilt-rotor aircraft whirl flutter instability must be based on detailed modelling of the system components such as the blades, hub, nacelle, wing and control system. Furthermore, the equations of motion are highly coupled and include geometric and aerodynamic nonlinearities. These nonlinearities are important for reliable prediction of the system's coupled dynamics and trim positions, which have a significant influence on the whirl stability. Nonlinear effects that appear in the aircraft mode are caused by high inflow that requires high built-in twist angles. Thus, the nonlinear aerodynamic effects must be considered for the correct evaluation of the effective angles of attack. In addition, during forward flight, significant portions of the blades are exposed to high effective angles of attack and high Mach numbers. Therefore, the compressibility effect must also be considered. Finally, damping effects are also important.

The complexity of tilt-rotor systems prevents the use of simple approximate models. Barkai and colleagues [42] present an analytical model with symbolic exactness that provides insight into the related aeromechanical phenomena. The model includes an elastic wing connected to a rigid fuselage. The nacelle is located at the wing tip. The rotor hub is considered to line up with the nacelle axis. The blades may be connected to the rotor shaft by means of various systems (gimbals, lead-lag, flap and pitch angles or pitch control systems). A general description of the model is shown in Figure 5.42.

The fuselage is considered to be a rigid body with six DOFs – three translations (d_x^F; d_y^F; d_z^F) and three angles (Θ_x^F; Θ_y^F; Θ_z^F). The inertial system

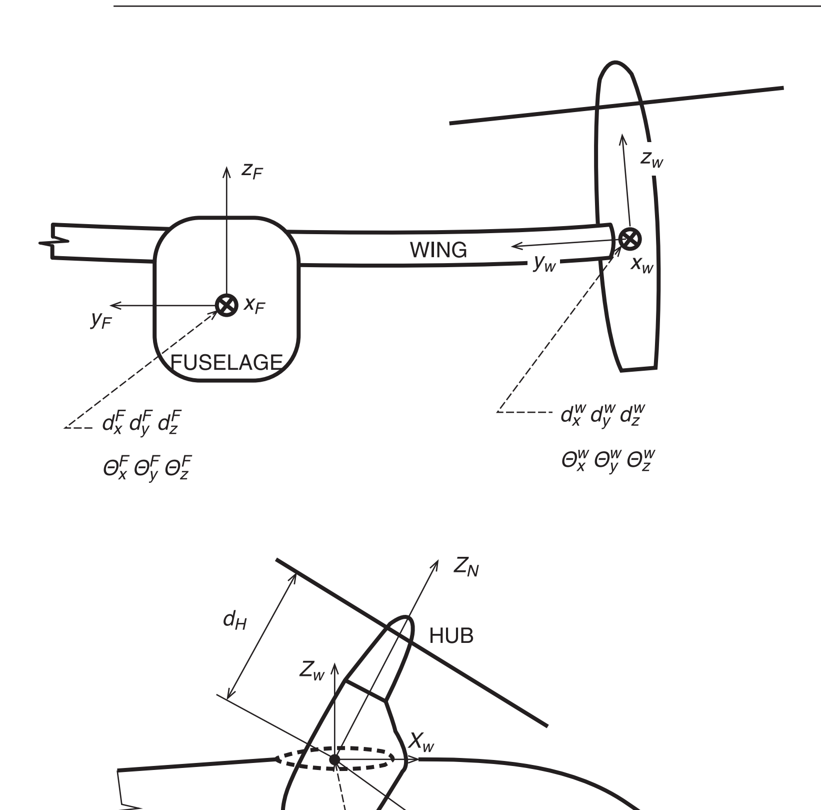


Figure 5.42 **Tilt-rotor aircraft dynamic system outline [42] (used with permission from Elsevier)**

of the fuselage is denoted by x_F; y_F; z_F. The wing is treated as an elastic beam. The wing inertial system x_W; y_W; z_W has its origin at the wing tip. The mode shapes considered in the solution include two vertical bending modes (u_{B1}; u_{B2}), two in-plane bending modes (u_{C1}; u_{C2}), the first torsional mode (u_{T1}) and, finally, the first extension mode (u_{E1}). The wing DOFs are the wing tip displacements (d_x^W; d_y^W; d_z^W) in the x_F; y_F; z_F directions of the fuselage and the three angles (Θ_x^W; Θ_y^W; Θ_z^W) relative to the fuselage system, i.e. in the wing system directions x_W; y_W; z_W. At this stage, a modal transformation is applied, and the modal equations are formulated as the equations of motion for the wing's degrees of freedom (d_x^W; d_y^W; d_z^W; Θ_x^W; Θ_y^W; Θ_z^W). The procedure includes elastic couplings between the wing tip

deflections and rotations. Structural damping is approximated by the viscous model. The wing's aerodynamics include the superposition of steady and unsteady components.

The nacelle coordinate system is denoted by x_N; y_N; z_N. It is connected to the wing tip through three spring and damper constrained hinges. The nacelle angles relative to the wing tip are described by the three Euler angles (Θ_x^N; Θ_y^N; Θ_z^N). The nacelle is assumed to be rigid, and the rotor hub is located at a distance d_H in the z_N direction.

A typical model of the gimbal hub system is shown in Figure 5.43. The hub coordinate system (denoted by x_H; y_H; z_H) rotates about the z_H axis at a constant angular velocity of

$$\vec{\Omega} = \Omega \hat{z}_H = \Omega \hat{z}_N \qquad [5.280]$$

The inner ring is rotating with the shaft and may tilt about the x_H axis by an angle γ_x. The outer ring is connected to the inner ring by an axis

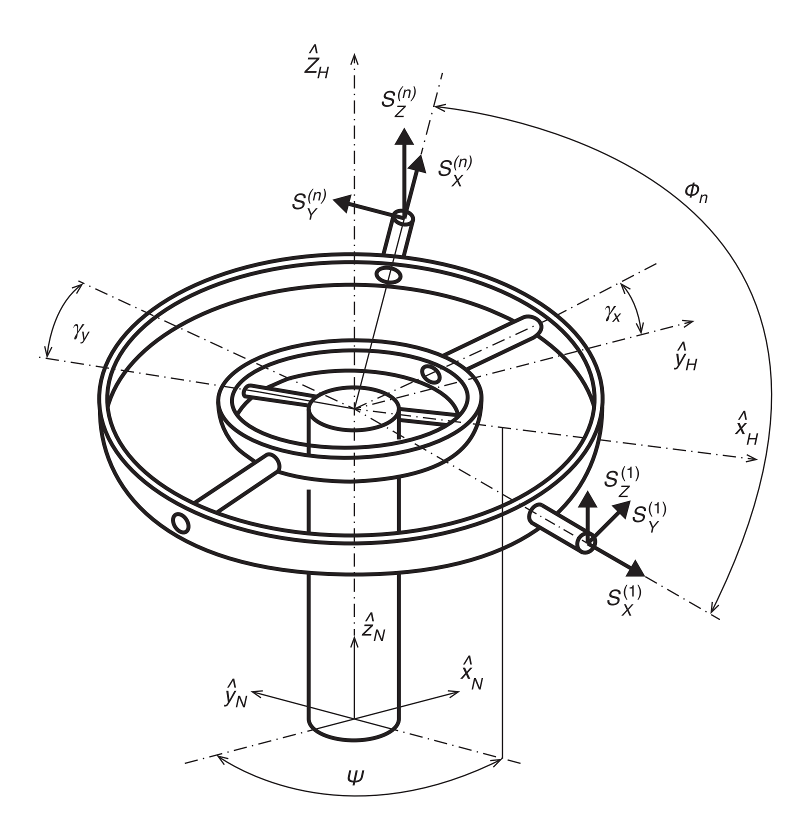


Figure 5.43 Tilt-rotor gimbal geometry [42] (used with permission from Elsevier)

perpendicular to x_H and may tilt by an angle γ_y. The blades are connected to the outer ring. The first blade is connected along the x_H axis. The blade azimuthal spacing is denoted by Φ_n. The azimuthal angle is measured between the $-x_H$ and x_H axes.

The blade root is denoted by $S_x^{(n)}$, $S_y^{(n)}$, $S_z^{(n)}$. Each blade may perform lead-lag (ζ), flapping (β) and pitch (Θ) motions in an arbitrary order as shown in Figure 5.44. The hinges are modelled by means of springs and dampers. The blades are assumed to be rigid and are defined by the mass, static mass moment and mass moment of inertia characteristics that are spanwise variable. These characteristics may also vary among the particular blades.

The control system is modelled as shown in Figure 5.45. It includes the blade pitch-flap coupling angle (δ_3). The control system is connected to the non-rotating swashplate ring that is rigidly connected to the airframe. The pitch links are connected by rod-end bearings to the rotating ring (point A). The blade pitch horn is connected to the pitch link by another rod-end bearing (point C). The stiffness of the pitch link is considered with an equivalent spring stiffness, K_{PL}. The pitch link transfers a force that can be expressed as

$$F_{PL} = -K_{PL} \Delta e_{PL} \qquad [5.281]$$

where Δe_{PL} is the pitch link elastic extension (distance of points A and C). The pitch link force and its moment are accounted for in the pitch motion equilibrium equation.

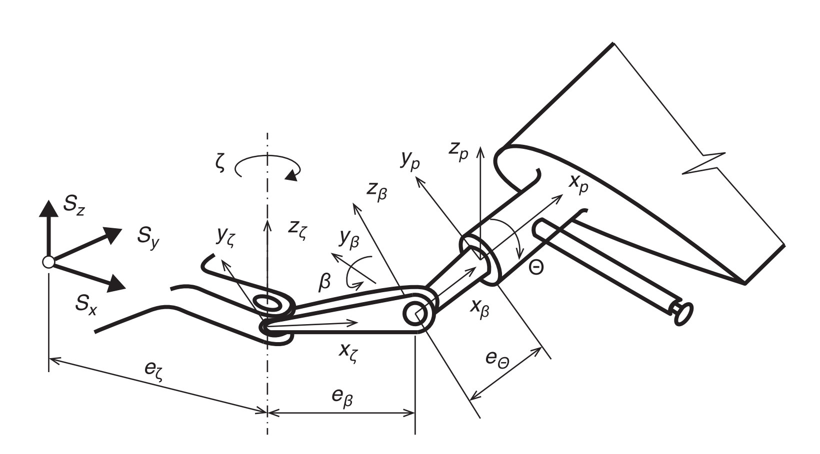


Figure 5.44 Tilt-rotor blade hinge geometry [42] (used with permission from Elsevier)

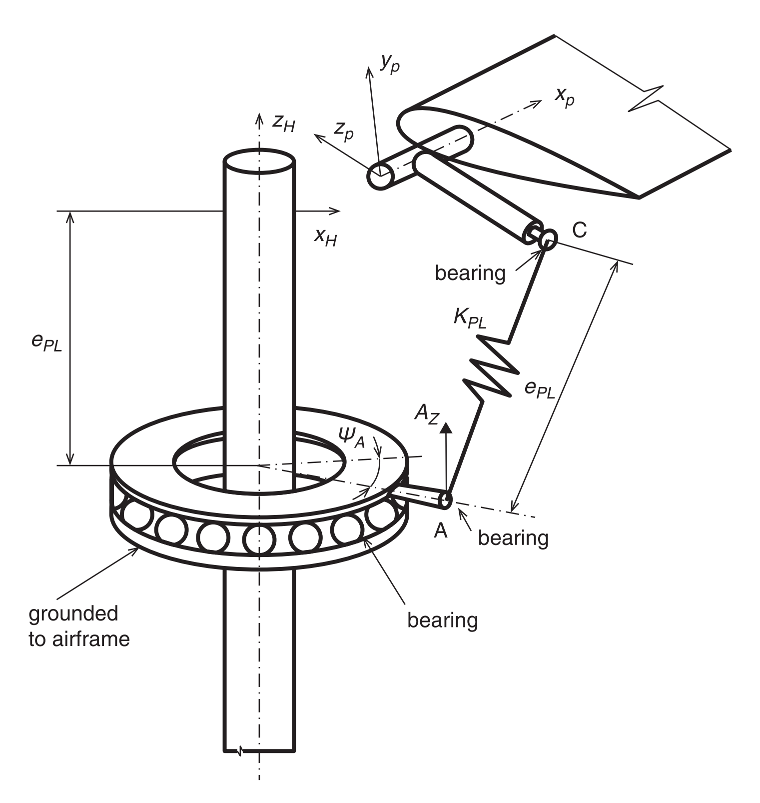


Figure 5.45 Tilt-rotor control system geometry [42] (used with permission from Elsevier)

The solution of the equations of motion of the described model is based on a technique that uses 'objective numbers' (ON). The method is based on the definition of a base vector D_n, where n denotes the ON order. In the solution, we will use the first order which will generate a linear derivation of the equation of motion about the given work point. The base vector includes all quantities that appear in the equation of motion. In general, the first-order base vector is expressed as

$$D_1 = \{d_1, d_2, \ldots, d_N\} \qquad [5.282]$$

The d_i components are the physical unknowns and their derivatives. Considering the three-bladed rotor, the d_i components become

$$
\begin{aligned}
&d_1 = 1\\
&d_2, \ldots, d_{10} = \Theta_x^F, \dot{\Theta}_x^F, \ddot{\Theta}_x^F, \Theta_y^F, \dot{\Theta}_y^F, \ddot{\Theta}_y^F, \Theta_z^F, \dot{\Theta}_z^F, \ddot{\Theta}_z^F\\
&d_{11}, \ldots, d_{19} = d_x^F, \dot{d}_x^F, \ddot{d}_x^F, d_y^F, \dot{d}_y^F, \ddot{d}_y^F, d_z^F, \dot{d}_z^F, \ddot{d}_z^F\\
&d_{20}, \ldots, d_{28} = \Theta_x^W, \dot{\Theta}_x^W, \ddot{\Theta}_x^W, \Theta_y^W, \dot{\Theta}_y^W, \ddot{\Theta}_y^W, \Theta_z^W, \dot{\Theta}_z^W, \ddot{\Theta}_z^W\\
&d_{29}, \ldots, d_{37} = d_x^W, \dot{d}_x^W, \ddot{d}_x^W, d_y^W, \dot{d}_y^W, \ddot{d}_y^W, d_z^W, \dot{d}_z^W, \ddot{d}_z^W\\
&d_{38}, \ldots, d_{46} = \Theta_x^N, \dot{\Theta}_x^N, \ddot{\Theta}_x^N, \Theta_y^N, \dot{\Theta}_y^N, \ddot{\Theta}_y^N, \Theta_z^N, \dot{\Theta}_z^N, \ddot{\Theta}_z^N \qquad [5.283]\\
&d_{47}, \ldots, d_{52} = \gamma_x, \dot{\gamma}_x, \ddot{\gamma}_x, \gamma_y, \dot{\gamma}_y, \ddot{\gamma}_y\\
&d_{53}, \ldots, d_{61} = \beta^1, \dot{\beta}^1, \ddot{\beta}^1, \beta^2, \dot{\beta}^2, \ddot{\beta}^2, \beta^3, \dot{\beta}^3, \ddot{\beta}^3\\
&d_{62}, \ldots, d_{70} = \zeta^1, \dot{\zeta}^1, \ddot{\zeta}^1, \zeta^2, \dot{\zeta}^2, \ddot{\zeta}^2, \zeta^3, \dot{\zeta}^3, \ddot{\zeta}^3\\
&d_{71}, \ldots, d_{79} = \Theta^1, \dot{\Theta}^1, \ddot{\Theta}^1, \Theta^2, \dot{\Theta}^2, \ddot{\Theta}^2, \Theta^3, \dot{\Theta}^3, \ddot{\Theta}^3\\
&d_{80}, \ldots, d_{88} = A_z^1, \dot{A}_z^1, \ddot{A}_z^1, A_z^2, \dot{A}_z^2, \ddot{A}_z^2, A_z^3, \dot{A}_z^3, \ddot{A}_z^3\\
&d_{89}, \ldots, d_{97} = \lambda_0, \dot{\lambda}_0, \ddot{\lambda}_0, \lambda_c, \dot{\lambda}_c, \ddot{\lambda}_c, \lambda_s, \dot{\lambda}_s, \ddot{\lambda}_s,
\end{aligned}
$$

where β^i, ζ^i, Θ^i and A_z^i are values that belong to the *i*th blade. λ_0, λ_c and λ_s are the inflow unknowns.

Now, each time-dependent quantity may be defined as an ON. The quantity that is expressed in general as

$$c(t) = C_1(t)d_1(t) + C_2(t)d_2(t) + \ldots + C_N(t)d_N(t) \qquad [5.284]$$

may be defined as an ON as follows:

$$c(t) = D_1 C \qquad [5.285]$$

where

$$C = \{C_1, C_2, \ldots, C_N\}^T \qquad [5.286]$$

The vector C is handled as a ‘number’. The mathematical operations for this are presented in [43]. Such an approach enables the evaluation of the equations of motion with the symbolic exactness that results from using elementary analytical and numerical operations. When the quantities are defined as ONs, the equations of motion are expressed in the form of generalised loads that include only the inertia contributions. For example, the equation of motion for a single-hinged rigid blade is presented here. The equation of motion may be expressed as

$$M_H = 0 \qquad [5.287]$$

where M_H is the hinge moment. The first-order base vector for this case becomes

$$D_1 = \{1, \beta, \dot{\beta}, \ddot{\beta}\} \qquad [5.288]$$

M_H is then derived as an ON in the form

$$M_H = \{M_{H1}, M_{H2}, M_{H3}, M_{H4}\}^T \qquad [5.289]$$

and the condition of Eqn. 5.287 leads to the following linearised equation for the flapping angle:

$$M_{H1} + M_{H2}\beta + M_{H3}\dot{\beta} + M_{H4}\ddot{\beta} = 0 \qquad [5.290]$$

As mentioned previously, the system includes nonlinearities. For that reason, the system stability characteristics may also be sensitive to the trim or response values of the unknown quantities. Therefore, the detailed high-harmonic-resolution trim and response solution must be obtained prior to the eigenvalue analysis. As shown, the usage of the first-order base vector leads to the linear (first-order) derivation of the equations of motion. The linear derivation depends on a set of assumed values of the quantities appearing in base vector. Again, we show the simple example of the single flapping angle (β). We assume the value of β_R to be the value of β around which the equation of motion should be linearised.

Let us consider an ON defined by Eqn. 5.286. The analytical function of C, expressed generally as $E = f_c(C)$, becomes an ON as well. We can write

$$E = \{E_1, E_2, \ldots, E_N\}^T \qquad [5.291]$$

where

$$E_1 = f_c(C_1)$$

$$E_i = f'_c(C_1)C_i \qquad [5.292]$$

From this result, we can define the component of the base vector (as the correction for β_R) as the quantity $\sin(\beta + \beta_R)$. This can be expressed as an ON, as

$$S_\beta = \{\sin(\beta_R), \cos(\beta_R), 0, 0\}^T \qquad [5.293]$$

Hence, the equations of motion may be linearised using this technique and organised as the standard format for the second-order system based on the set of initial values for the components of the base vector as

$$[M]\{\ddot{D}_1\}^T + [C]\{\dot{D}_1\}^T + [K]\{D_1\}^T = \{f\} \qquad [5.294]$$

The solution of this system yields a correction to the initial values. After this, the equation of motion can be evaluated again using the new

values. This process continues until convergence is reached. This is where the correction to the right-hand side vector is small enough. At this point, Eqn. [5.294] represents a small perturbation system of equations that may be solved by means of the standard eigenvalue analysis.

The blade dynamic characteristics are based on the evaluation of the inertial loads. The acceleration of each blade element is expressed as the function of all of the system DOFs and is therefore defined as an ON. Because the blade is assumed to be rigid, the inertial load is evaluated at three chordwise locations over each cross-section. The acceleration may be expressed as

$$\vec{a} = (a_{x0} + y\vec{a}_{xy} + z\vec{a}_{xz})\hat{x} + (a_{y0} + y\vec{a}_{yy} + z\vec{a}_{yz})\hat{y} + \\ + (a_{z0} + y\vec{a}_{zy} + z\vec{a}_{zz})\hat{z} \qquad [5.295]$$

where the $\hat{x}$, $\hat{y}$, $\hat{z}$ directions are those of the outboard system (see Figure 5.44). The distributed force (p_I) and the moment (q_I) per unit length are given as ONs using the expression

$$(\vec{p}_I, \vec{q}_I) = -\iint_A (\rho\vec{a}, \rho\vec{a} \times \vec{r})dA \qquad [5.296]$$

where $\vec{r}$ is the distance from the coordinates origin to the particular blade mass element. The distributed inertia force components in the $\hat{x}$, $\hat{y}$, $\hat{z}$ directions may be expressed as

$$\begin{aligned} P_x^I &= -a_{x0}m_b - a_{xy}m_b y_{CG} - a_{xz}m_b z_{CG} \\ P_y^I &= -a_{y0}m_b - a_{yy}m_b y_{CG} - a_{yz}m_b z_{CG} \\ P_z^I &= -a_{z0}m_b - a_{zy}m_b y_{CG} - a_{zz}m_b z_{CG} \end{aligned} \qquad [5.297]$$

where m_b is the blade mass per unit length. The distributed moments Q_x^I, Q_y^I and Q_z^I are expressed similarly. Note that all accelerations a_{i0}, a_{ij} ($i, j = x, y, z$) are ONs, and, thus, P_i^I and Q_i^I are ONs as well. The blade unit length inertia loads are then integrated spanwise to yield the root inertia loads.

The blade aerodynamics are based on two-dimensional nonlinear quasi-steady theory. Similar to the inertial load evaluation, the velocity at each blade element must be expressed as a function of all of the system degrees of freedom and will therefore become an ON. Therefore, the cross-sectional free stream velocity is evaluated at the three-quarter chord point as shown in Figure 5.46.

The evaluation of the velocities includes the dynamics of the complete system (fuselage, wing, blades, etc.). It also includes the prescribed inflow distribution, expressed by means of the inflow unknowns λ_0, λ_c and λ_s as:

$$\lambda_t = \lambda_0 + \lambda_c \cos \Psi + \lambda_s \sin \Psi \qquad [5.298]$$

The magnitude of the cross-sectional free stream velocity becomes

$$\vec{U} = U_y \ \hat{y} + U_z \ \hat{z} = \sqrt{U_y^2 + U_z^2} \qquad [5.299]$$

and the effective angle of attack becomes

$$\alpha = \Theta - \tan^{-1}\left(\frac{U_z}{U_y}\right) \qquad [5.300]$$

Using the effective angle of attack and the Mach number corresponding to the free stream velocity, the cross-sectional lift and drag can be determined. Because the U_y and U_z are expressed as ONs, the effective angle of attack and the Mach number become ONs as well. Then, the derivatives $(\partial c_L/\partial \alpha)$; $(\partial c_L/\partial M)$; $(\partial c_D/\partial \alpha)$; $(\partial c_D/\partial M)$; $(\partial c_M/\partial \alpha)$; $(\partial c_M/\partial M)$ and the values of c_L; c_D; c_M may also be evaluated as ONs. Having expressed the aerodynamic coefficients and the free stream velocity as ONs, the aerodynamic loads in the $\hat{y}$ and $\hat{z}$ directions can be evaluated and

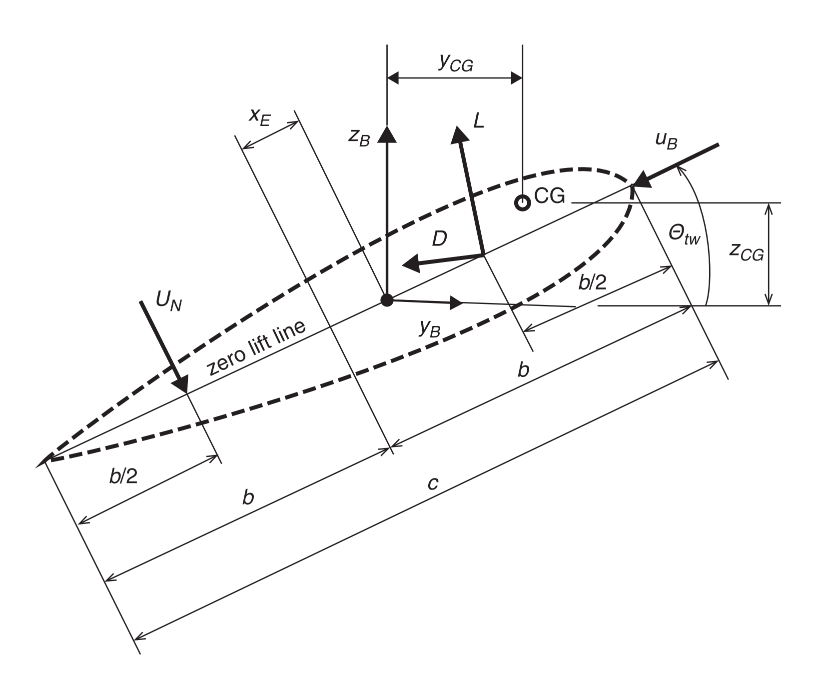


Figure 5.46 **Tilt-rotor blade cross-section [42] (used with permission from Elsevier)**

integrated in the blade spanwise direction. This method was programmed into the code called RAPID (see [42]).

5.14.1 Rotor dynamics comprehensive tools

The standard comprehensive tool that is used for whirl flutter analysis (for the tilt-rotor applications) is the CAMRAD II code [14] [15]. The code couples externally generated wing modes that are provided either analytically (FEM) or experimentally (GVT) with internally generated rotor modes. The model includes complex geometry, inertia and stiffness data. Aerodynamic data of blade airfoils based either on CFD or wind tunnel tests are provided externally as well. The resulting internal aerodynamic solution employs first or second order lifting line theory. As an example, a rotor model [44] is shown in Figure 5.47. The tool is capable of assessing various structural and aerodynamic parameters as demonstrated in the following examples.

The tool was used by Acree et al. [45] [46], who analysed the characteristics of the XV-15 aircraft rotor. The important structural parameter influencing whirl flutter is the wing torsional stiffness. Considering the influence of the wing torsion on the whirl flutter stability, tilt-rotor aircraft usually have wings with high thickness-to-chord ratios. This work analysed the possibility of using of a thinner wing (15% instead of 23%). This type of wing would reduce the aerodynamic drag. However, it would also reduce the whirl flutter speed of the wing-rotor system. To compensate for this negative effect, changes in the rotor blade inertia and aerodynamic characteristics were tested. The blade was divided into several segments, and these were tested with various offsets of the blade's centre of gravity (CG) and offsets of the aerodynamic centre (AC) of the particular blade segment. The AC and CG offset were realised by the shifting of the airfoil and internal masses as shown in Figure 5.48. Note that the CG was offset in the forward direction.

Positive effects were observed for both types of changes. However, the AC changes were found to be much more effective (at least twice as much). An example is shown in Figure 5.49. This figure shows a reduction in the whirl flutter speed when comparing the thick wing and the thin wing. In addition, an increase in the whirl flutter speed is observed when comparing the baseline rotor blades with modified rotor blades. To support the analytical work, the simple whirl flutter model was also tested, as outlined in Section 4.3.1.

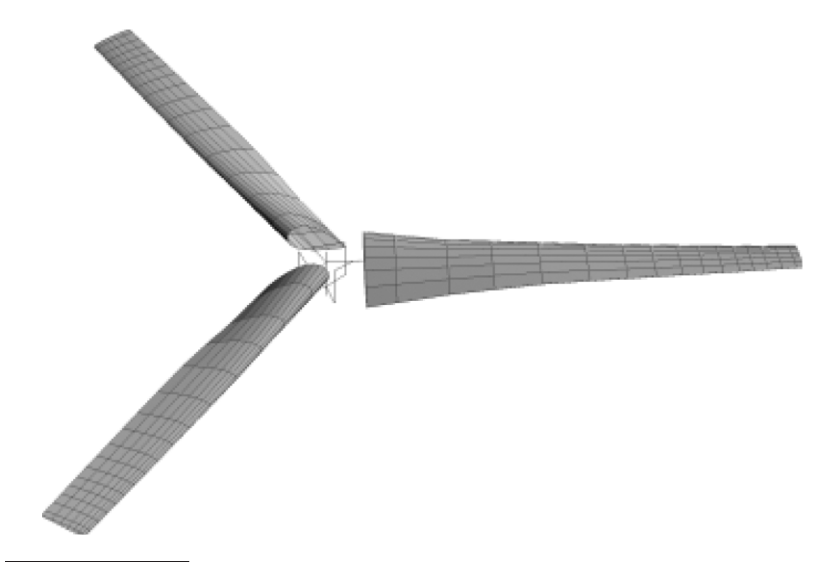


Figure 5.47 CAMRAD II model of tiltrotor aircraft rotor [44]

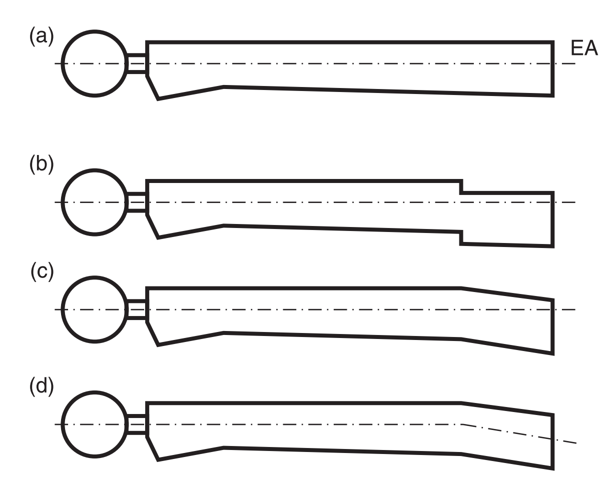


Figure 5.48 Examples of XV-15 rotor blade planforms: (a) baseline; (b) tip segment airfoil shifted; (c) tip segment airfoil sweep, elastic axis (EA) unchanged; (d) tip segment airfoil sweep + EA sweep [45] [46]

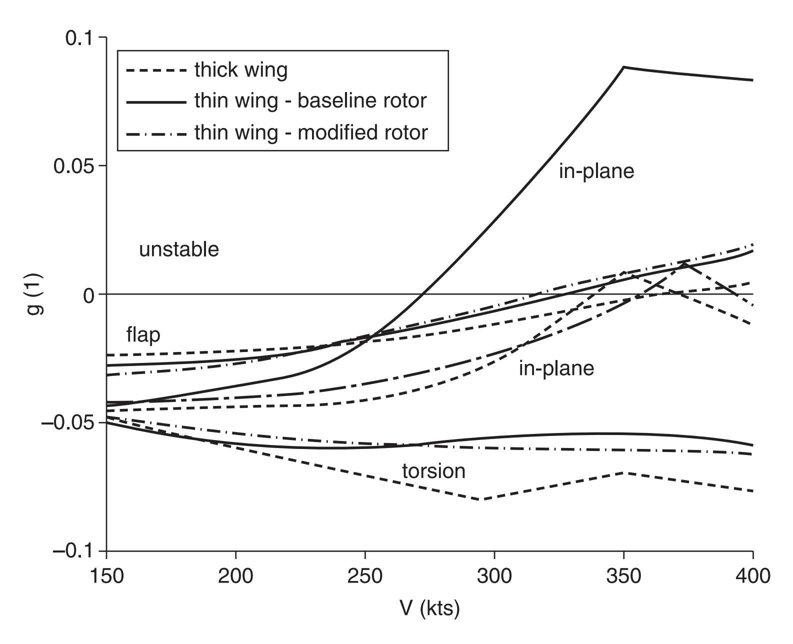


Figure 5.49 **Symmetric whirl mode V-g diagram – comparison of thick wing and thin wing with baseline and modified rotor blades (15% CG offset at tip blade segment) [45] [46]**

An even larger study, that analysed the effects of blade design changes on whirl flutter, was performed by Acree on the V-22 aircraft rotor [44]. For that study, the baseline rotor was artificially destabilised using the pitch/flap coupling (δ_3) parameter. The effects of the changes include swept blades and offset tip masses. Note that the primary purpose of the blade sweep was to improve the whirl flutter stability, not to reduce the effective Mach number. The study also examined the mechanism by which each change affected the stability and loads. The study included various blade sweep and tip mass combinations as shown in Figure 5.50.

For the comparison the blade sweep and tip mass offsets are presented in terms of the equivalent sweep that is expressed as

$$\Lambda = \sin^{-1}\left(\frac{x_m}{R - r_s}\right) \qquad [5.301]$$

where x_m is a tip mass offset, R is a blade radius, and r_s is a sweep starting local radius. A comparison of the effects of the sweep and mass offset, considering the planforms of Figure 5.50, is presented in Figure 5.51.

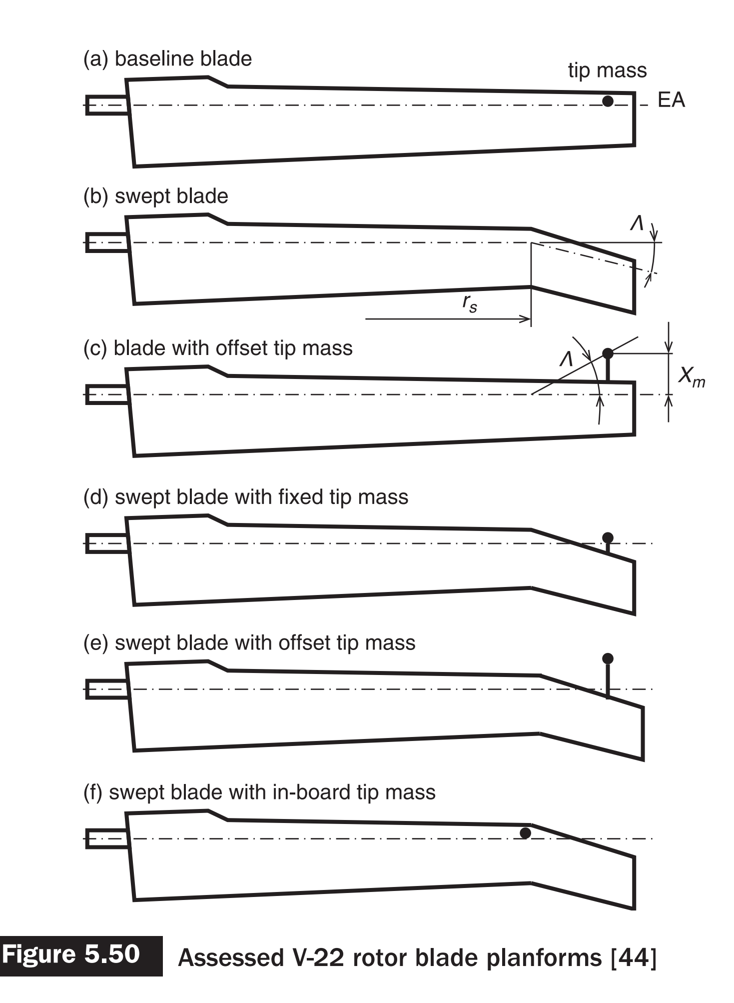


Figure 5.50 **Assessed V-22 rotor blade planforms [44]**

Further parametric studies included the influence of the independent aerodynamic sweep angle and structural mass offset effects, as shown in Figure 5.52.

A comparison of the effects of the independent aerodynamic sweep angle and structural mass offset (as shown in Figure 5.52) are presented in Figure 5.53.

This study also examined the mechanisms and their effects on the whirl stability. Tip-mass offsets increase the inertial coupling about the pitch axis in response to perturbational forces. Tip sweep enhances the torsional components of the blade mode shapes, thereby increasing favourable aerodynamic coupling. Both effects are stabilizing in

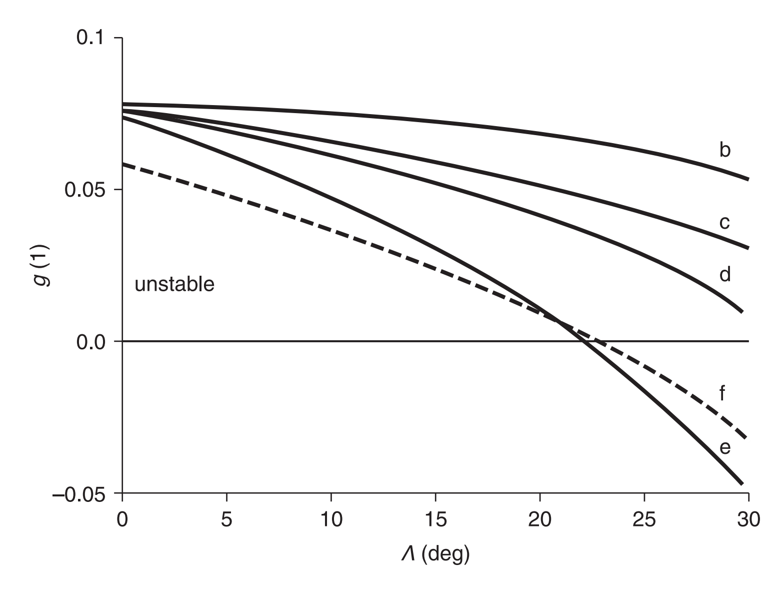


Figure 5.51 **Effects of sweep and mass offset on stability of symmetric bending mode at $V = 300$ kts; $\delta_3 = -30$ deg [44] (legend in accordance with Figure 5.50)**

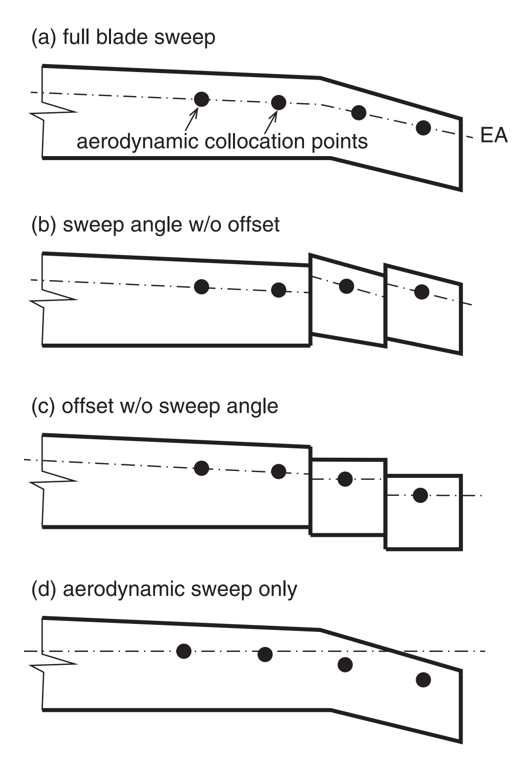


Figure 5.52 **Definition of blade sweep, aerodynamic sweep, panel sweep angle and sweep offset [44]**

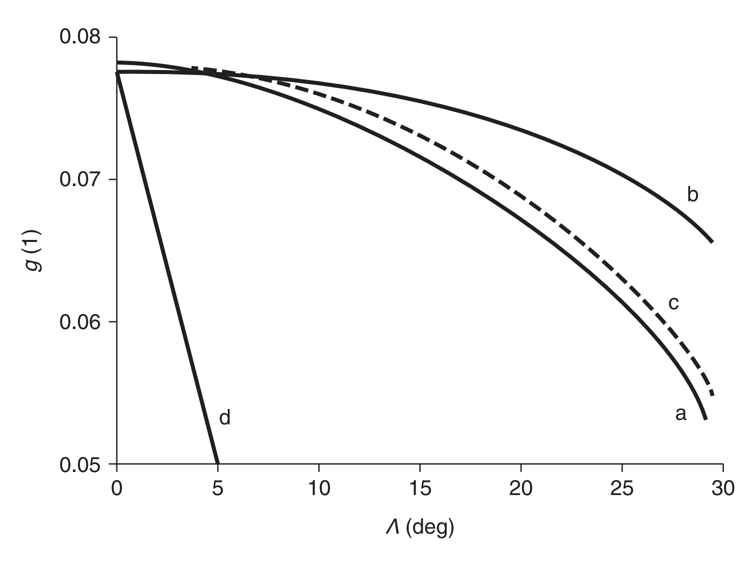


Figure 5.53 **Blade sweep, aerodynamic sweep, panel sweep angle and sweep offset on stability of symmetric bending mode at V = 300 kts; δ_3 = −30 deg [44] (legend in accordance with Figure 5.52)**

nature. Sweep also affects the unsteady loads. However, the effect of stabilisation is lower compared to the other effects. Finally, the reduction of the local lift-curve slope caused by the sweep has only a small effect on the stability.

5.14.2 Multi-body simulation tools

Rezaiean [47] described a solution that is based on FEM code to calculate the system structural dynamics (modal model). Modal data are obtained from a detailed FE model of the wing and nacelle structure. The model was dynamically reduced in order to obtain a reasonable number of degrees of freedom for the final stability calculations. To determine the wing aerodynamic forces, quasi-steady aerodynamics and Strip Theory were employed. The propeller blades were considered to be rigid, and the propeller aerodynamic coefficients related to the airfoil of the blade local sections were calculated using a propeller comprehensive design code. The propeller aerodynamic forces (considering the local section angles of attack) were calculated by the multi-body simulation tool (SIMPACK)

that was used for the final dynamic analysis. The final dynamic stability analysis was performed in the time domain for the selected propeller revolutions and the windflow velocity. Another methodology, which was developed by Rezaiean [48], employs an experimental modal model obtained by ground vibration testing and a comprehensive flutter analysis tool.

A similar methodology that employs a multi-disciplinary multi-body simulation tool was also used by Krueger [16]. The model represented a scaled aeroelastic model of the tilt-rotor aircraft rotor. The model included the rotor and the nacelle attached by means of non-linear springs. The wing structure was represented only structurally by the beam, and the aerodynamic effect of the wing was neglected. The rotor blades were considered to be rigid. Both linear and non-linear analyses were performed in the time domain. The linear analyses showed an instability of the combination of the nacelle forward whirl mode with the wing bending mode. These analyses also examined the influence of the flexibility of the wing. The non-linear analyses included the mechanical non-linearity of both nacelle springs given by the narrow operational range of the springs. The non-linear effect was evaluated at the point of the linear flutter. The unstable motion changed into limit cycle oscillations. The analytical results were also compared with the corresponding wind tunnel test results (see Chapter 4).

A multi-body simulation method was also used by Mueller and colleagues [49], who studied the possibility of augmenting the whirl stability by means of active control. Active control was studied with the objective of expanding the flight envelope, and enhancing the manoeuvrability. However, the possibility of compensating for the negative effect of the thinner wing (that would reduce the aerodynamic drag during cruise flight) to the whirl flutter was also studied. The analytical multi-body model (see Figure 5.54) included a gimballed windmilling prop-rotor that included three wing modes and two rotor flap modes as well as an active control system in the closed loop. Both SISO and MIMO control algorithms were worked out. The aerodynamic coefficients were approximated from airfoil data.

5.14.3 CFD- and CFD/CSM-based tools

Recently, complex CFD methods have been used for the determination of propeller aerodynamics. Such results then can be incorporated into the stability solution. An example of this is the work of Shiravastava and

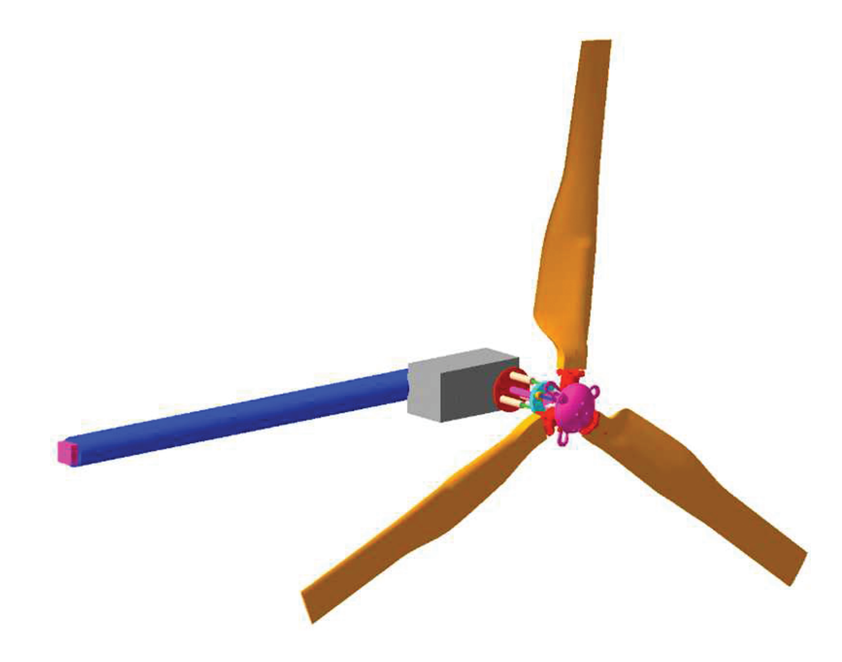


Figure 5.54 Prop-rotor multi-body model [49]

Reddy [17] who developed the CFD code using the three-dimensional unsteady compressible Euler equations.

An even more complex possibility for the solution is CFD/CSM code coupling. The aeroelastic problem may be basically formulated as a coupled structure/fluid problem in which the coupling is only at the boundary interface between the fluid and the structure. Therefore, it is possible to use separate solvers for the flow computation and the structure computation and then to obtain the coupled solution by the exchange data at the common fluid/structure boundary (CFD/CSM coupling). Such an approach allows us to solve aeroelastic problems that include nonlinearities. However, in most cases, the structure may be assumed to be linear. In such a case, it is possible to extract the structural information (e.g., from the FEM solution) as a pre-processing step, and the main solution is then realised directly in the aerodynamic solver.

This approach is adopted by the comprehensive CFD-based tool ELSA that was developed in ONERA [50]. The tool enables aerodynamic computations for compressible viscous or inviscid flow. It is based on the

RANS or URANS (Unsteady Reynolds Averaged Navier-Stokes) equations with a large set of turbulence models. Linearised formulations are also available. The available simulations range from nonlinear or linearised harmonic forced motion simulations to static and dynamic coupling simulations in the time domain with different levels of structural modelling. The solver can account for deformed grids. It implements features such as various time resolution, dual time stepping, implicit phases, multi-grid techniques, parallel computations, etc.

Sicot and Dugeai [18] presented the derivation of a complex deformation model and generalised coordinates for any arbitrary precession movement of an isolated propeller/nacelle configuration that enables the analysis of aerodynamic forces and moments. Later on, the methodology was worked out by Verley and Dugeai [51], who considered a twin counter-rotating multi-blade propeller (front rotor of 11 blades and rear rotor of nine blades). The methodology uses a deformable mesh approach and rotating modes of deformation.

5.15 References

1 Taylor, E.S. and Browne, K.A.: Vibration isolation of aircraft power plants, *Journal of Aerospace Sciences*, Vol. 6, No. 2, December 1938, pp. 43–49.
2 Ribner, H.S.: *Propellers in Yaw*, NACA Report 820, 1945.
3 Ribner, H.S.: *Formulas for Propellers in Yaw and Charts of the Side–Force Derivatives*, NACA Report 819, 1945.
4 Houbolt, J.C. and Reed, W.H.:: Propeller-Nacelle Whirl Flutter, *Journal of Aerospace Sciences*, Vol.29, 1962.
5 Reed, W.H. and Bland, S.R.: *An Analytical Treatment of Aircraft Propeller Precession Instability*, NASA Langley, Technical Note, TN D-659, 1961.
6 Theodorsen, T.: *General Theory of Aerodynamic Instability and the Mechanism of Flutter*, NACA Report 496, 1935.
7 Smilg, B. and Wasserman, L.S.: *Application of Three-Dimensional Flutter Theory to Aircraft Structures*, Army Air Force Technical Report No. 4798, 1942.
8 Sewall, J.L.: *An Analytical Trend Study of Propeller Whirl Instability*, NASA Langley, Technical Note, NASA TN D-996, 1962.
9 Kvaternik, R.G. and Kohn, J.S.: *An Experimental and Analytical Investigation of Proprotor Whirl Flutter*, NASA, Technical Paper, TP 1047,December 1977.
10 Hammond, C.E., Runyan, H.L. and Mason, J.P.: 'Application of Unsteady Lifting Surface Theory to Propellers in forward Flight', AIAA/ASME/SAE 15th Structures, Structural Dynamics and Materials Conference, AIAA Paper No. 74–419, 1974.
11 Runyan, H.L.: 'Unsteady Lifting Surface Theory Applied to a Propeller and Helicopter Rotor', Ph.D. Thesis, Loughborough University of Technology.

12 Runyan, H.L. and Tai, H.: *Compressible Unsteady Lifting Surface Theory for a Helicopter Rotor in Forward Flight*, NASA Technical Paper, TP 2503, 1985.
13 Nitzsche, F.: Insights on the whirl-flutter phenomena of advanced turboprops and propfans, *Journal of Aircraft*, Vol. 28, No. 7, pp. 463–470, 1991.
14 Johnson, W.: CAMRAD II *Comprehensive Analytical Model of Rotorcraft Aerodynamics and Dynamics – Theory Manual*, Johnson Aeronautics, Palo Alto, CA, USA, 1993.
15 Johnson, W.: CAMRAD II *Comprehensive Analytical Model of Rotorcraft Aerodynamics and Dynamics – Rotorcraft Applications*, Johnson Aeronautics, Palo Alto, CA, USA, 1993.
16 Krueger, W.R.: 'Analysis of Whirl Flutter Dynamics on a Tiltrotor Wind Tunnel Model', International Forum of Aeroelasticity and Structural Dynamics, Seattle, WA, USA, 21–25 June 2009.
17 Srivastava, R. and Reddy, T.S.R.: *PROP3D: A Program for 3D Euler Unsteady Aerodynamic and Aeroelastic (Flutter and Forced Response) Analysis of Propellers, Version 1.0*, NASA Contractor Report, CR 198471, 1996
18 Sicot, F. and Dugeai, A.: 'Numerical Investigation of Propellers Whirl Flutter Using elsA', International Forum on Aeroelasticity and Structural Dynamics (IFASD), International Conference, 26–30 June 2011, Paris, France.
19 Rodden, W.P. and Rose, T.L.: 'Propeller/Nacelle Whirl Flutter Addition to MSC/NASTRAN', Paper No. 12, *Proceedings of the 1989 MSC World User's Conference*, Universal City, CA, USA, March 1989.
20 Loewy, R.G.: A two-dimensional approximation to the unsteady aerodynamics of rotary wings, *Journal of Aeronautical Sciences*, Vol. 24, No. 2, February 1957, pp. 81–92.
21 Bland, S.R. and Bennett, R.M.: *Wind-Tunnel Measurement of Propeller Whirl-Flutter Speeds and Static-Stability Derivatives and Comparison with Theory*, NASA, Technical Note, TN D-1807, 1963.
22 Zwaan, R.J. and Bergh, H.: 'Restricted Report, F.228', National Aero-Astronautical Research Institute (NLR), Amsterdam, February 1962.
23 Reed, W.H.: 'Propeller-Rotor Whirl Flutter: A State-of-the-Art Review', Symposium on the Noise and Loading Actions on Helicopter V/STOL Aircraft and Ground Effect Machines, Southampton, UK, September 1965.
24 Bennett, R.M. and Bland, S.R.: *Experimental and Analytical Investigation of Propeller Whirl Flutter of a Power Plant on a Flexible Wing*, NASA, Technical Note, TN D-2399, August 1964.
25 Yates, E.C., Jr.: *Calculation of Flutter Characteristics for Finite-Span Swept or Unswept Wings at Subsonic and Supersonic Speeds by a Modified Strip Analysis*. NACA RM L37L10, 1958.
26 Reed, W.H. and Bennett, R.M.: 'Propeller Whirl Flutter Considerations for V/STOL Aircraft', CAL/TRECOM Symposium, Buffalo, NY, USA, 1963.
27 Krishna Rao, K.V. and Sundararajan, D.: *Whirl Flutter of Flapping Blade Rotor Systems*, NAL Technical Note, TN-18, National Aeronautical Laboratory, Bangalore, India.
28 Richardson, J.R. and Naylor, H.F.W.: *Whirl Flutter of Propellers With Hinged Blades*, Report No. 24, Engineering Research Associates, Toronto, Canada, March 1962.

29 Krishna Rao, K.V.: Effect of steady state coning angle and damping on whirl flutter stability, *Journal of Aircraft*, Vol. 10, No. 11, pp. 664–669, 1973.
30 Reed, W.H.: *Review of Propeller-Rotor Whirl Flutter*, NASA Technical Report, NASA TR R-264, 1967.
31 Coleman, R.P. and Feingold, A.M. (with appendix B by G.W. Brooks): *Theory of Self-Excited Mechanical Oscillations of Helicopter Rotors With Hinged Blades*, NACA Report No. 1351, 1958. (Supersedes NACA TN 3844.)
32 Kvaternik, R.G.: 'Studies in Tilt-Rotor VTOL Aircraft Aeroelasticity', Ph.D. Thesis, Case Western Reserve University, June 1973.
33 Brooks, G.W.: 'The Mechanical Instability and Forced Response of Rotors on Multiple-Degree-of-Freedom Supports', Ph.D. Thesis, Princeton University, 1961.
34 Loewy, R.G. and Yntema, R.T.: Some aeroelastic problems of tilt-wing VTOL aircraft, *Journal of Americal Helicopter Society*, Vol. 3, No. 1, pp. 35–57, January 1958.
35 Richardson, J.R., McKillop, J.A., Naylor, H.F.W. and Bandler, P.A.: *Whirl Flutter of Propellers with Flexible Twisted Blades*. Report No. 43, Engineering Research Associates, Toronto, Canada, 1962.
36 Reed, W.H.: Propeller-rotor whirl flutter: a state-of-the-art review, *Journal of Sound and Vibrations*, Vol. 4, No. 3, November 1966, pp. 526–544.
37 Williams, M.H.: *An Unsteady Lifting Surface Method for Single Rotation Propellers*, NASA Lewis Research Center, Contractor Report, CR-4302, July 1990.
38 Giessing, J.P., Kalman, T.P. and Rodden, W.P.: Subsonic steady and oscillatory aerodynamics for multiple interfering wings and bodies, *Journal of Aircraft*, Vol. 9, pp. 693–702, 1972.
39 Albano, E. and Rodden, W.P.: A Doublet–Lattice method for calculating lift distributions on oscillating surfaces in subsonic flows, *AIAA Journal*, Vol. 7, No. 2, February 1969, pp. 81–91.
40 Donham, R.E. and Osterholt, D.J.: 'Utilizing Test Results to Show Adding Flexibility of Propeller Blades is More Representative than the Classical Rigid Blade Propeller Whirl Flutter Analysis', International Forum on Aeroelasticity and Structural Dynamics, Stockholm, Sweden, 18–20 June 2007.
41 Donham, R.E.: 'Effect of Propeller Blade Bending Dynamics on 1P Loads and Whirl Flutter', International Forum on Aeroelasticity and Structural Dynamics, Munich, Germany 28 June–1 July 2005.
42 Barkai, S.M., Rand, O., Peyran, R.J. and Carlson, R.M.: 'Modeling and Analysis of Tilt-Rotor Aeromechanical Phenomena', American Helicopter Society Aeromechanics Conference, Bridgeport, CT, USA, 11–13 October 1995; also: *Mathematical and Computer Modelling*, Vol. 27, No. 12, pp. 17–43, 1998.
43 Rand. O. and Barkai, S.M.: Numerical evaluation of the equations of motion of helicopter blades with symbolic exactness, *Journal of the American Helicopter Society*, Vol. 40, No. 1, pp. 59–71, January 1995.
44 Acree, C.W., Jr.: *Effects of Swept Tips on V-22 Whirl Flutter and Loads*, NASA, TM-2005–213458, 2005.
45 Acree, C.W., Jr., Peyran, R.J. and Johnson, W.: 'Rotor Design for Whirl Flutter: An Examination of Options for Improving Tiltrotor Aeroelastic

Stability Margins', American Helicopter Society 55th Annual Forum, Montreal, QC, Canada, 25–27 May 1999.
46 Acree, C.W., Jr., Peyran, R.J. and Johnson, W.: *Rotor Design Options for Improving XV-15 Whirl-Flutter Stability Margins*, NASA Technical Paper, TP-2004-212262, AFDD/TR-04-001, 2004.
47 Rezaeian, A.: 'Whirl Flutter Analysis of a Wind Tunnel Model Using Multidisciplinary Simulation and Multibody Dynamics', 37th European Rotorcraft Forum, 2011, Italy.
48 Rezaeian, A.: 'Stability Assessment of a Propeller – Wing Wind Tunnel Model Based on Analysis Using Measured Structural Data', International Forum of Aeroelasticity and Structural Dynamics, Bristol, UK, 24–26 June 2013.
49 Mueller, J.P., Gourinat, Y., Ferrer, R., Krzsinski, T. and Kerdreux, B.: 'A Numerical Study on Active Control for Tiltrotor Whirl Flutter Stability Augmentation', revised version of the paper: 'A Multibody Study on Single- and Multi-Variable Control Algorithms for Tiltrotor Whirl Flutter Stability Augmentation', American Helicopter Society 4th Decennial Specialist's Conference on Aeromechanics, Fisherman's Wharf, San Francisco, CA, USA, 21–23 January 2004.
50 Dugeai, A., Mauffrey, Y. and Sicot, F.: 'Aeroelastic Capabilities of the elsA Solver for Rotating Machines Applications', International Forum on Aeroelasticity and Structural Dynamics, International Conference, 26–30 June 2011, Paris, France.
51 Verley, S. and Dugeai, A.: 'Counter-rotating Open Rotor Whirl Flutter Phenomenon Investigations Using elsA Solver', International Forum of Aeroelasticity and Structural Dynamics, Bristol, UK, 24–26 June 2013.

6

Application to the aircraft certification process

DOI: 10.1533/9781782421863.195

Abstract: This chapter provides the practical information regarding the aircraft certification with respect to the whirl flutter. First, the requirements of the regulation standards (FAR/CS 23 and FAR/CS 25) are summarised, and comments are made. The analytical approaches are then described. The chapter includes a standard approach to computing the flutter states directly and the optimisation-based approach to computing the critical structural parameters and the whirl flutter stability margins. The analysis procedure described is based on the usage of the NASTRAN program system.

Key words: whirl flutter certification, FAR/CS 23, FAR/CS 25, NASTRAN, PROPFM, optimisation, stability margin.

6.1 Requirements of the airworthiness regulations

The airworthiness regulation standards require proving the safety and reliability of the aircraft structure. The parts of these requirements dealing with the aeroelasticity and flutter also include the requirements related to the whirl flutter. Essentially, the whirl flutter requirements are applicable only to the aircraft powered by a turboprop power plant system.

The piston engine aircraft are not required to prove the safety of the whirl flutter, mainly because compared to the turboprops, the piston engines usually have a lower level of performance, and the rotating mass of the piston engine is very small. Furthermore, the piston engines

ordinarily use smaller and lighter propellers. The gyroscopic effect is therefore much lower and the flight performance (velocities, etc.) is also lower compared to the turboprops. However, the absence of the certification requirements related to the whirl flutter for the piston engine-powered aircraft does not mean that the whirl flutter cannot appear on such aircraft. The vibrations induced by the whirl mode become the contributing factor to the structural breakdown, e.g. in the case of the engine mounting damage mentioned in Section 3.3.

The major category of aircraft threatened by the whirl flutter is obviously turboprops due to the large rotating parts of the gas turbine engines and the heavy propellers. Higher operational velocities also contribute. The requirements related to the whirl flutter are therefore incorporated into the regulations of those aircraft categories to which the turboprop power plant systems are applicable. In the following text, the requirements of the particular regulations are evaluated. This evaluation includes the regulations of the European Aviation Safety Agency (EASA) and the Federal Aviation Administration (FAA). Note that both regulation standards correspond to one another, as indicated.

6.1.1 CS-23 – normal, utility, aerobatic and commuter category aeroplanes or FAR-23 – normal, utility, acrobatic and commuter category airplanes

CS-23 Amdt.3 [1] and FAR-23 Amdt.62 [2], [3] represent the simpler category of standards applicable to the smaller turboprop aircraft. The applicability is limited to the aircraft in the normal, utility and aerobatic categories, which have a seating configuration (excluding pilot(s)) of nine or fewer and a maximum certified take-off weight of 5670 kg or less (§1(a)(1)). The standard is also applicable to propeller-driven twin-engine aircraft in the commuter category that have a seating configuration (excluding pilot(s)) of 19 or fewer and a maximum certified take-off weight of 8618 kg or less (§1(a)(2)).

The whirl flutter-related requirements are included in §629 'Flutter'. Expecting the rational analysis to be used for the prediction of the flutter, §629(b) defines the envelope of required aeroelastic stability. The typical envelope for the certification according CS/FAR 23 regulations is shown in Figure 6.1.

The required area of aeroelastic stability is defined by the $1.2 \cdot V_D$ velocity and $1.2 \cdot M_D$ Mach number. For each altitude, the V_{DTAS} velocity

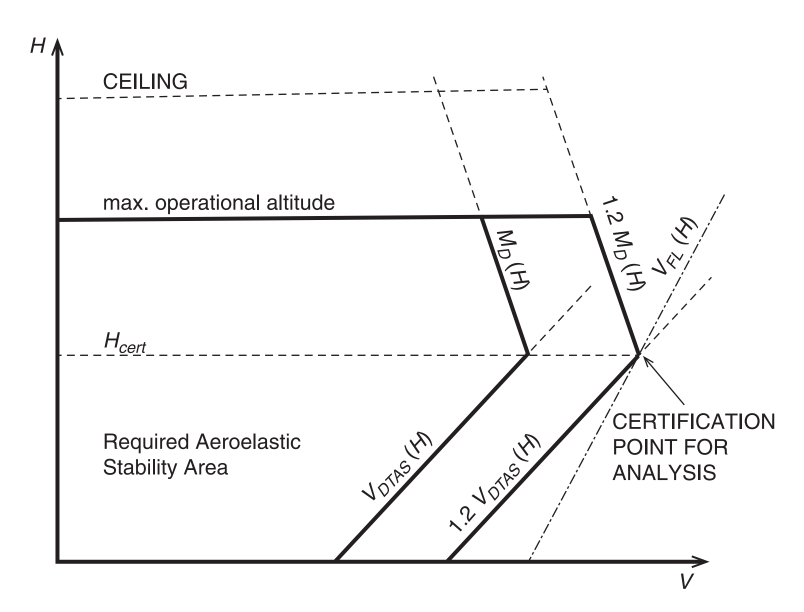


Figure 6.1 **V-H envelope for aeroelastic certification according to the CS/FAR 23 regulations**

is defined by both V_D and M_D. The maximal V_{DTAS} value defines the certification altitude, H_{cert}. For the altitude $H < H_{cert}$, the V_{DTAS} limitation is given by the velocity V_{DEAS}, whereas for the altitude $H > H_{cert}$, the V_{DTAS} limitation is given by the Mach number M_D. The altitude limit of the envelope is given by the maximal operating altitude.

The general dependence of the flutter critical speed on the air density is:

$$V_{FLH} = V_{FL(H=0)} \left(\frac{\rho_{(H=0)}}{\rho_H} \right)^{\varepsilon} \qquad [6.1]$$

where exponent ε for the whirl flutter is considered to be $\varepsilon \approx 0.3$, and for the bending-torsional surface flutter $\varepsilon \approx 0.4$. The EAS and TAS speed conversion is:

$$V_{HTAS} = V_{EAS} \left(\frac{\rho_{(H=0)}}{\rho_H} \right)^{0.5} \qquad [6.2]$$

Because the exponent in Eqn. 6.1 is $\varepsilon < 0.5$, the critical point with regard to the whirl flutter is the point at the altitude of H_{cert} as shown in Figure 6.1.

The requirement to analyse the whirl flutter is included in §629(e). This requirement was introduced to the regulation in the FAR-23 Amdt.7.

However, the requirement was applicable only to the twin-engine configurations because such aircraft are characteristically constructed with the wing-mounted engines that are the category most concerned with the whirl flutter. Aditionally, for the twin-engine pusher configuration, the empennage may be significantly affected by the whirl mode forces. Beginning with FAR-23 Amdt.31, this requirement was also expanded to the single-engine aircraft category. Although the influence of the fuselage structure on the whirl flutter of the single nose-mounted engine configuration is negligible, the potential for the propeller whirl flutter still exists.

The text of §629(e) is reproduced here:

> (e) For turbo-propeller powered aeroplanes, the dynamic evaluation must include – (1) a whirl mode degree of freedom that takes into account the stability of the plane of rotation of the propeller and significant elastic, inertial and aerodynamic forces and (2) propeller, engine, engine mount and aeroplane structure stiffness and damping variations appropriate to the particular configuration.

Section 629(e)(1) includes the main requirement, while §629(e)(2) requires the variation of structural parameters such as the stiffness and damping of the power plant attachment. The whirl flutter analysis must therefore include all significant aircraft configurations with respect to fuel and payload that are applicable to the aircraft operation. The whirl flutter analysis must also include the influence of the variance of the power plant mount structural parameters simulating the possible changes due to the structural damage (e.g., deterioration of engine mount-isolators).

Further requirements that are applicable to the aircraft complying with the fail-safe criteria come from §629(g). The regulation requires analysis of the states after fatigue failure or obvious partial failure of a principal structural element. Similarly, §629(h) is applicable to the aircraft complying with the damage-tolerance criteria. The regulation requires analysis of the states of damage for which the residual strength is demonstrated. Additional aircraft configurations to be analysed may therefore arise from these requirements.

6.1.2 CS-25 – large aeroplanes or FAR-25 – transport category airplanes

CS-25 Amdt.12 [4] and FAR-25 Amdt.135 [5] represent the standard category applicable to larger turboprops. The requirements related to

whirl flutter are included in §629 'Aeroelastic stability requirements'. The compliance with this standard is obviously more complicated in comparison to compliance with the former one. We will therefore go through §629 piece by piece, excluding the texts that are not applicable to the whirl flutter.

(a) General

This introductory section defines the requirement, including the whirl modes associated with any propeller or rotating device that contributes significant dynamic forces to the evaluation of stability, in particular to the flutter analysis.

(b) Aeroelastic stability envelopes

The envelope of required aeroelastic stability for the normal conditions with no failure or malfunction defined by (1) is limited by the velocity of $1.15 \cdot V_D$ and Mach number of $1.15 \cdot M_D$. The range of operational altitudes is here extended to 'negative' altitudes. The envelope applicable to the failure states (d) that is defined by (2) uses $1.15 \cdot V_D$ and $1.15 \cdot M_D$ and the standard range of the operational altitudes only. Note that the regulation includes several definitions of the envelope for the failure states. However, considering the typical velocities of turboprops, the envelope based on the V_D and M_D usually gives the highest velocities at the specific altitudes. Both basic and extended envelopes are shown in Figure 6.2. Because the exponent in Eqn. 6.1 is $\varepsilon < 0.5$, the critical point with regard to the whirl flutter is the one at an altitude of H_{cert}, as shown in Figure 6.2.

(c) Failures, malfunctions and adverse conditions

This section defines the failure, malfunction and adverse condition states to be analysed. The whirl flutter analysis must be included, provided that such state influences the parameters with a significant influence on the whirl flutter.

(d)(1) Critical fuel loading conditions

This section requires the analysis of unsymmetrical conditions of the fuel loading that may come from the mismanagement of the fuel. The whirl flutter analyses should include the combinations of those fuel loading

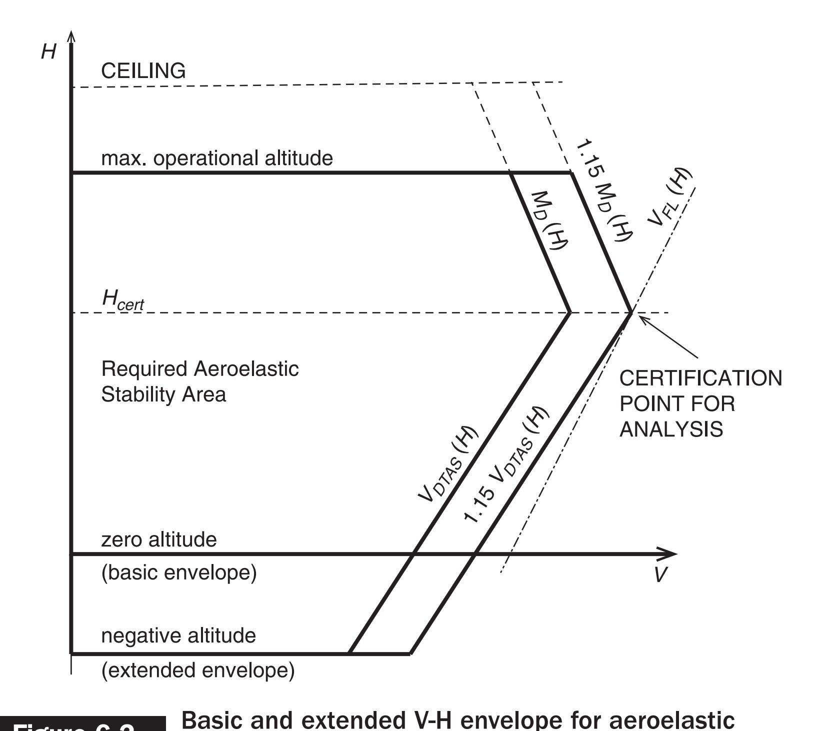


Figure 6.2 **Basic and extended V-H envelope for aeroelastic certification according to CS/FAR 25 regulations**

levels that are representative of the possible influence of the wing structure on the whirl flutter.

(d)(4) Failure of any single element supporting any engine

The failure states required by this section include in particular the failure of any single engine bed truss. The whirl flutter analysis must be included, provided that such a failure has a significant influence on the stiffness or damping characteristics of the power plant mount system. The failure conditions are introduced into a single power plant mount system while other power plant mount systems use a nominal condition. All engines used here use the nominal condition.

Note that this section also includes the failure states that are not usually applicable to turboprops as supporting elements of an independently mounted propeller shaft, a large auxiliary power unit or an externally mounted aerodynamic body.

(d)(5) Failure of any single element of the engine

The failure states required by this section include, in particular, the failure of any single engine mount-isolator. Again, the whirl flutter analysis must be included provided that such a failure has a significant influence on the stiffness or damping characteristics of the power plant mount system. The failure conditions are introduced into a single power plant mount system while other power plant mount systems are subject to nominal conditions. All engine mounts used here were used under nominal conditions.

(d)(6) Absence of aerodynamic and gyroscopic forces due to feathered propellers

The failure states defined in this section represent the states of a nonrotating engine and a nonrotating feathered propeller. The power plant system under such conditions generates no aerodynamic or gyroscopic forces. Such failure states are directly connected with the whirl flutter. Analyses must include the absence of aerodynamic and gyroscopic forces due to any applicable combination of feathered propellers, and the absence of aerodynamic and gyroscopic forces coming from any other significant rotating devices must also be included. These failure states must be analysed for the nominal conditions of the engine and the engine mount systems. In addition, the single feathered propeller or rotating device failure must be coupled with the failures of the engine mount and the engine of sections (d)(4) and (d)(5).

Considering the commonly used twin-engine configuration, a failure state of one feathered propeller and the other propeller under the nominal conditions may occur. The engine mounts and engines are subject to the nominal condition, and those failure conditions analysed in the frame of (d)(4) and (d)(5) have a significant influence on the whirl flutter.

(d)(7) Any single propeller overspeed

The failure states defined in this section represent the states of engine and propeller overspeed. The power plant system under such conditions generates maximal aerodynamic and gyroscopic forces. The overspeed of any other significant rotating device must also be included. The condition of overspeed must include the highest likely overspeed of both engine and propeller. The state of overspeed is applied to any single propeller or rotating device while other propellers or rotating devices are under the nominal conditions.

(d)(8) Failure states required by §571

The failure states selected for investigation by §571 come from the damage-tolerance analysis. The failure states of (d)(4) and (d)(5) may be excluded provided the damage-tolerance analysis does not involve complete failure of the element, and the element cannot fail due to the conditions of the damage-tolerance analysis.

The common practice in the Czech aerospace industry is to assess the specific theoretical recommended failure states that are considered to be more critical with respect to the real damage coming from the damage-tolerance analyses. These failures include brakes of suspension elements that are not backed up and specific fatigue damage to the main load-bearing elements. The whirl flutter analyses must include those factors influencing the structural parameters with a significant influence on the whirl flutter (e.g., engine mount stiffness, wing stiffness, etc.).

(d)(9) Failure states required by §631, §671, §672 and §1309

The failure states selected for investigation by §631 come from bird strike damage, the control systems, the stability augmentation and the power-operated systems and other equipment systems and installations. The whirl flutter analyses must again include those influencing the structural parameters with significant influence on the whirl flutter.

6.2 Analytical approaches

As is apparent from Section 6.1, the requirements of both CS/FAR 23 and 25 regulatory standards may be divided into two main groups: the nominal states and the failure states.

The nominal state analyses include changes in structural parameters that are applicable to the aircraft operation. The most important changes are fuel and payload loading variations. Further parameters may come from the optional aircraft configurations, installation of external stores, fuel tanks, etc.

In practice, we commonly combine the fuel and payload combinations according to the typical flight profiles. The profiles most commonly used are ‘maximal payload’ flight profile and ‘maximal flight distance’ flight profile. Other options include ‘maximal cargo payload’ flight profile, ‘maximal flight distance with extra tanks’, etc. The set of configurations

for analyses is given by the take-off configuration of the specific profile and then by considering the decrease of fuel during the flight ending with the zero fuel.

The whirl flutter calculations for the nominal states must be performed for all such configurations. Analyses of the failure states are performed only on the appropriate selection of configurations that shows the significant influence on the whirl flutter.

The analyses of the failure states represent a much larger group. While the nominal states represent just one analysis per configuration, the failure states may include many analyses per configuration. Although some failure states are considered negligible and are excluded from the analysis, the number of the failure state analyses may become enormous.

We can use two main approaches for the analysis:

1. The standard approach, where the analyses are performed for the known set of structural parameters, and the results are whirl flutter stability characteristics (e.g., whirl flutter speed). The resulting flutter speed is then compared to the certification velocity according to the flight envelope. The analyses are performed sequentially, state by state. Because the number of analyses may become huge (as was mentioned previously) such an approach may become ineffective unless some tool for automated analyses and data handling and processing is used. However, the applicability of such automatic processing systems is always limited.
2. The optimisation approach, where the flutter speed is set equal to the certification speed, and the results are critical values of the structural parameters. The stability margin can then be obtained from these critical structural parameters. The analysed states are then compared only with respect to the structural parameters and the relationship to the stability margin. Such an approach can save large amounts of time because the number of required whirl flutter analyses is dramatically reduced. This approach is called the 'optimisation approach' because the values of parameters are searched by means of the structural optimisation methods (e.g., gradient-based methods) to reach the desired flutter speed.

Both approaches are described in detail in the following sections using the example of the whirl flutter analysis performed by means of the NASTRAN program system. NASTRAN [6] is an FE-based computational system that is used worldwide, in particular in the aerospace and automotive industries. NASTRAN is a standard computational tool for various other types of aeroelastic analyses, so it would be easy to use the

same FE model and incorporate the whirl flutter analysis into the whole aeroelastic certification procedure.

6.2.1 Standard approach

Procedure description

The standard whirl flutter calculation procedure is based on the NASTRAN program system with a DMAP (Direct Matrix Abstraction Program) procedure called propa.alt. The NASTRAN is supplemented by the external preprocessor for calculation of the propeller aerodynamic matrices (program propfm). The calculation of the propeller aerodynamic and gyroscopic forces is based on the Aerodynamic Strip Theory for the rigid propeller in the windmilling mode. For the residual structure, a Wing-Body Interference Theory (Doublet–Lattice and Slender Body Theory) is used [6]. The flutter stability is solved by means of the pk-method [6] using the NASTRAN solver no. 145.

The structural and aerodynamic model is almost the same as the ordinary flutter analysis, but there are specific demands: a node point at the propeller centre of gravity and the propeller coordinate system (see Figure 6.3).

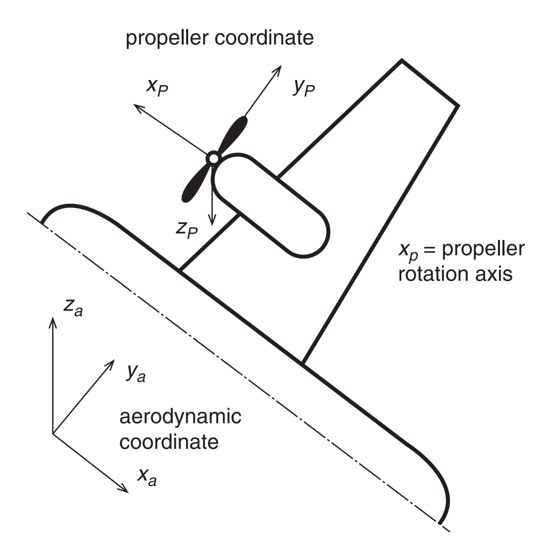


Figure 6.3 **Propeller coordination system used for NASTRAN analysis**

As an option, there is a possibility of including the interference effects between propeller, nacelle and the wing by means of the reduced frequency dependent downwash and sidewash effects. In this case, we input the data via DMI (Direct Matrix Input) cards PARTN1 and PARTN2 to the NASTRAN input file. The first NASTRAN launch calculates downwash and sidewash angles only, and then the calculation is terminated. The output data are stored in the plain output '*.pch' file.

For the next step, we prepare the input data for the external preprocessor to calculate the propeller aerodynamic matrices (propeller, engine inertia, geometry, flow conditions, etc.). The input data may optionally include the '*.pch' file with the downwash and sidewash data. The output from the preprocessor includes the propeller aerodynamic matrices expressed formally as damping and stiffness matrices. The output matrices are written by means of the NASTRAN direct matrix input cards (DMIG) that are to be put on the NASTRAN input file and, if necessary, the DMI PARTN1 and PARTN2 cards are to be removed.

The propeller aerodynamic matrices are set for each flow velocity because there are different global stiffness and damping matrices of the model for the each flow velocity. It is therefore necessary to create a stability solution only for single velocity per subcase. Each subcase is defined by the specific FMETHOD, K2PP and B2PP cards in the case-control deck of the input file. Case-control cards refer to the bulk data section of the specific FLUTTER and FLFACT cards and the DMIG cards from the preprocessor (AEROSxxx and AEROBxxx). This final NASTRAN launch performs a stability analysis. The structure of the output '*.f06' file is different compared to the ordinary flutter calculations. Use of a NASTRAN XYPLOT or other standard NASTRAN postprocessing tools is therefore not possible. For the processing of the whirl flutter output file, the specific software tool named *whout* (unpublished) was created. The program is available at the website of the Aeronautical Research and Test Institute, Prague (*www.vzlu.cz*).

Propeller – nacelle – wing interference

Two options for the calculation of the propeller aerodynamic forces and moments are available. The basic option is to use the quasi-static angles from Eqn. 2.8. This basic option requires just the final NASTRAN launch as described in the previous paragraph.

An alternative option is to include the downwash and sidewash effect of the flow behind the propeller (i.e., the interference effect between the propeller, the nacelle and the wing). Such an effect may be noticeable on

the twin wing-mounted engine aircraft configuration. This advanced option requires an additional NASTRAN launch aimed to calculate downwash and sidewash angles.

The induced downwash angle (in the vertical plane) is subtracted from the effective quasi-static value of Eqn. 2.8 as:

$$\Theta^*_{w1} = \Theta^* - \frac{w_1}{V_\infty} \qquad [6.3]$$

The induced sidewash angle (in the horizontal plane) is added to the quasi-static value as:

$$\Psi^*_{w2} = \Psi^* + \frac{w_2}{V_\infty} \qquad [6.4]$$

where w_1 and w_2 are downwash and sidewash, respectively, induced by the aerodynamic force.

The induced downwash and sidewash angles mentioned above that depend on the reduced frequency can be obtained from the lift solution by partitioning the interference coefficients [7].

$$\left\{\frac{w_1}{V_\infty}, \frac{w_2}{V_\infty}\right\} = Re[A_{Iw} \quad 0 \quad A_{Is}] \begin{Bmatrix} C_w \\ \mu_I \\ \mu_s \end{Bmatrix} \qquad [6.5]$$

where A_{Iw} and A_{Is} are downwash factors for the interference elements from the aerodynamic boxes (wing) and slender body elements (nacelle); and C_w, μ_I and μ_s are strength of doublets on the aerodynamic boxes (wing), interference body elements and slender body elements (nacelle).

Only the real part of the complex downwash is considered to be consistent with other approximations in the quasi-steady theory in Eqn. 6.5. Any damping due to the interference is neglected, and the downwash effect appears in the stiffness matrix only. Downwash effects can be calculated either in the vertical plane (downwash only) or in both the vertical and the horizontal planes (downwash and sidewash). The former choice assumes that the nacelle modelled as body considers vertical forces only (*Z*-body), the latter as a body considering both the vertical and the lateral forces (*ZY*-body).

The solution for a mode $\{\Phi_{ai}\}$ is given by:

$$\begin{Bmatrix} C_w \\ \mu_I \\ \mu_s \end{Bmatrix} = [A]^{-1}[D_{jk}][G_{ka}]\{\Phi_{ai}\} \qquad [6.6]$$

and for all of the modes:

$$\begin{bmatrix} C_w \\ \mu_I \\ \mu_s \end{bmatrix} = [Q_{jh}] \qquad [6.7]$$

where [A] is a downwash factor matrix, $[D_{jk}]$ is a substantial derivative matrix, $[G_{ka}]$ is an aerodynamic-structure interpolation matrix, and $[Q_{jh}]$ is a generalised force matrix for motion.

The solution to obtaining the downwash angles for each mode in the NASTRAN is implemented by means of the DMAP program propa.alt. [7] as:

$$\left\{ \frac{w_1}{V_\infty}, \frac{w_2}{V_\infty} \right\} = Re[P_1][A_{Iw} \quad A_{II} \quad A_{Is}][P_2] \begin{Bmatrix} C_w \\ \mu_I \\ \mu_s \end{Bmatrix} \qquad [6.8]$$

where $[P_1]$ is a partitioning matrix to select the vertical and lateral degrees of freedom of the propeller hub and $[P_2]$ is another partitioning matrix to null the $[A_{II}]$, which is the matrix of the downwash factors on interference elements from interference elements. The downwash and sidewash angles calculated by the NASTRAN first run are then multiplied by the appropriate aerodynamic derivatives and the dimensional factors by means of the preprocessor and then entered into the global stiffness matrix for the final NASTRAN run.

External preprocessor for calculation of propeller forces

The first program for the calculation of propeller aerodynamic forces was created by Rodden in the late 1980s [7], [8]. The program prepared in the DEC/VMS Fortran named *propf* is available at the website of the MSC.Software Corporation.

Another similar program named *propfm* was prepared by Čečrdle (unpublished). Propeller aerodynamic forces and moments are calculated by Eqn. 5.35, effective angles are given from Eqn. 6.3 and Eqn. 6.5. For no downwash, the w_1 become null; for no sidewash, the w_2 become null. The simplifications ($\dot{\Theta}^* \approx \dot{\Theta}$, $\dot{\Psi}^* \approx \dot{\Psi}$) and Eqn. 2.12 are taken into account. The propeller blade integrals with the limits for integration with respect to the thrusting region of the blade include the lift lag effect, the correction for the compressibility, the correction factor for the compressible flow

aspect-ratio, the correction for the number of blades and the spanwise distribution of the lift curve slope as expressed by Eqn. 5.55. Aerodynamic derivatives are then calculated using Eqn. 5.52 employing the simplification given by the symmetry of Eqn. 2.11. The reduced frequency of the blade local section is given by Eqn. 5.44, where the dimensionless radius is defined by Eqn. 5.53 and the propeller advance ratio is defined as $(V_\infty/\Omega R)$. The propeller aspect ratio is calculated using Eqn. 5.54. The lift lag effects may be included by Eqn. 5.45.

The lift curve slope cutoff value for the compressible lift slope in the transonic flow to avoid the problems with the Mach number correction with a supersonic tip (overspeed condition) given by Eqn. 5.54 and Eqn. 5.55 may also be optionally applied. The cutoff value should be applied for calculations of the true states using the true aerodynamics of the particular Mach number. However, the analysis is sometimes aimed to calculate the rate of reserve with respect to the specific velocity. In such a case, the calculation uses the artificial reference states with the aerodynamics valid for the reference Mach number. For such cases, the cutoff value should not be applied.

Gyroscopic moments are given as:

$$M_{Y,P} = J_x \Omega \dot{\Psi}$$
$$M_{Z,P} = -J_x \Omega \dot{\Theta} \qquad [6.9]$$

where the overall mass moment of inertia is given by a sum:

$$J_x = J_p + N_r J_r \qquad [6.10]$$

where J_p is a polar mass moment of inertia of the propeller, and J_r is a polar mass moment of inertia of the rotor (compressor, turbine, shafts, etc.). The direction of rotation must be taken into consideration, making the sum of the engine part contributions (e.g., PT6A engine family). Finally, N_r is a rotor-to-propeller gear ratio.

The aerodynamic derivatives are finally multiplied by the dimensional factors using the preprocessor and then entered into the global stiffness and damping matrices for the final NASTRAN run. The damping matrix terms also include the gyroscopic term.

The program is capable of including the solution for multiple engines and propellers with diverse revolutions and of taking account of the directions of the propeller revolutions. The inverse direction of the propeller revolutions affects the aerodynamic derivatives as:

$$(c_{z\Theta})_{inv} = -c_{z\Theta} \qquad (c_{zq})_{inv} = c_{zq}$$
$$(c_{m\Theta})_{inv} = c_{m\Theta} \qquad (c_{mq})_{inv} = -c_{mq}$$

$$(c_{y\Theta})_{inv} = -c_{y\Theta} \qquad (c_{yq})_{inv} = c_{yq}$$

$$(c_{n\Theta})_{inv} = c_{n\Theta} \qquad (c_{nq})_{inv} = -c_{nq} \qquad [6.11]$$

Other derivatives are apparent from the symmetry or antisymmetry according to Eqn. 2.11. Furthermore the sign of the gyroscopic term must be changed considering the inverse direction of the propeller revolutions.

Considering the typical twin engine wing-mounted configuration with the identical directions of both propeller revolutions as is usual for the smaller aircraft, the derivatives for both propellers are defined as basic values. Provided the directions of both propeller revolutions are inverse as is usual for the large military transport turboprops, the derivatives for the first become basic values, and the derivatives for the second become inverse values. Considering diverse revolutions, the aerodynamic derivatives become diverse for each propeller.

Example

Both standard and optimisation approaches are demonstrated on the example of the Wing–Engine Component Model representing the aeroelastic scaled model of the L-610 turboprop commuter aircraft. Both the aircraft and the aeroelastic model are described in Section 4.4. The analytical FE model is the beam-like structure that includes the stiffness characteristics of the wing, aileron and the engine attachment. The inertia characteristics include the wing, aileron, engine and propeller. The model is fixed at the wing root. The structural model is shown in Figure 6.4.

The nominal values of the engine attachment stiffness are $K_\Theta = 1206.8\,\text{Nm.rad}^{-1}$ (pitch) and $K_\psi = 1298.2\,\text{Nm.rad}^{-1}$ (yaw). The engine and propeller data represents scaled-down characteristics of the Walter M602 engine and Avia V-518 propeller.

Considering the selected mass configuration of 100% of fuel load, we obtain the modes summarised in Table 6.1.

The aerodynamic model includes the wing and splitter surfaces and the nacelle body (Figure 6.5).

The whirl flutter calculation of the nominal state gave us the non-critical state of the whirl flutter up to the velocity of $V_\infty = 100\,\text{m.s}^{-1}$. The wing bending-torsional-aileron flutter state that was found is outside the scope of our interest.

Considering the CS/FAR 23 regulation requirements, the nominal state analysis fulfils the §629(e)(1) requirement whereas the §629(e)(2) requirement needs additional parametric study. We performed the

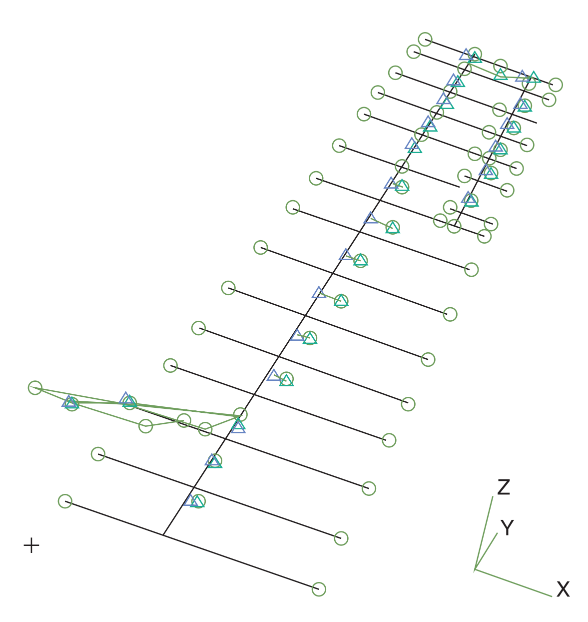


Figure 6.4 Structural FE model of wing/engine component

Table 6.1 Summary of modal characteristics

#	Title	f_0 [Hz]
1	1st wing bending	3.094
2	Engine pitch	3.791
3	Engine yaw	4.628
4	1st wing horizontal bending	8.353
5	2nd wing bending	8.522
6	Aileron flapping	13.567
7	1st wing torsion	16.591
8	3rd wing bending	19.674
9	2nd wing horizontal bending	22.407
10	2nd wing torsion	24.886

bi-parametric study varying both vertical and lateral engine stiffness. The results of such calculations are shown in Figure 6.6 as the flutter speed dependence on both pitch and yaw frequencies.

The stability margin can now be obtained by cutting the flutter speed surface with the plane at the certification speed level as demonstrated in

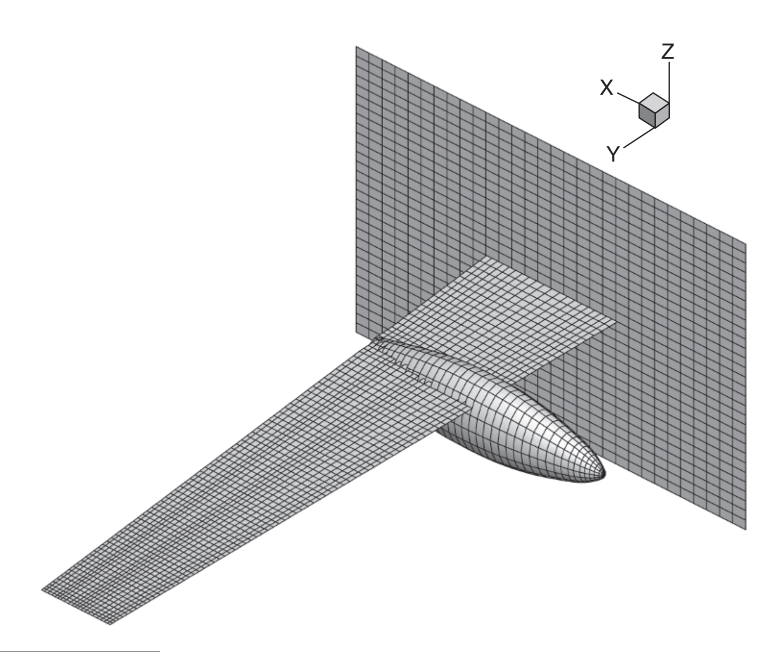


Figure 6.5 Aerodynamic FE model of wing and engine component

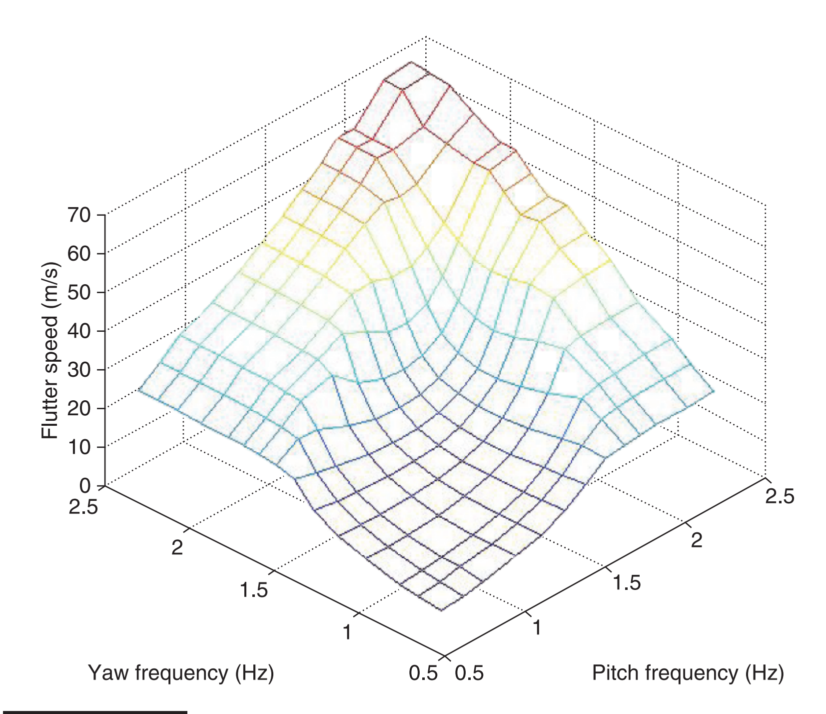


Figure 6.6 Flutter speed dependence on pitch and yaw frequencies

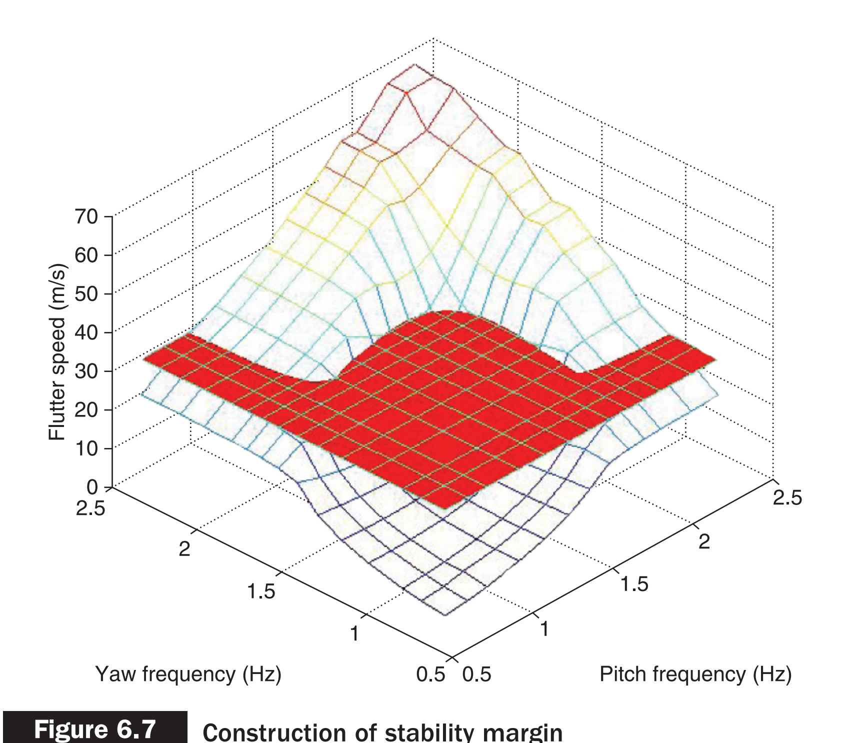


Figure 6.7 Construction of stability margin

Figure 6.7. The certification speed of $V_{cert} = 32\,m.s^{-1}$ applicable for the aeroelastic model was obtained by scaling from the full scale aircraft value.

We can finally draw the stability margin as demonstrated in Figure 6.8 and evaluate the rate of reserve with respect to structural parameters, e.g. pitch and yaw frequencies as demonstrated in Figure 6.9. The Figure shows that the rate of reserve is obviously high enough.

6.2.2 Optimisation-based approach

Fundamentals of design optimisation

The basic optimisation problem can be expressed as seeking the optimal combination of parameters aimed to minimise the specified target function, respecting the constraining functions. The parameters that are changeable are called 'design variables'. The vector of design variables can be expressed as

$$\vec{x} = \{x_1, x_2, \ldots, x_n\} \qquad [6.12]$$

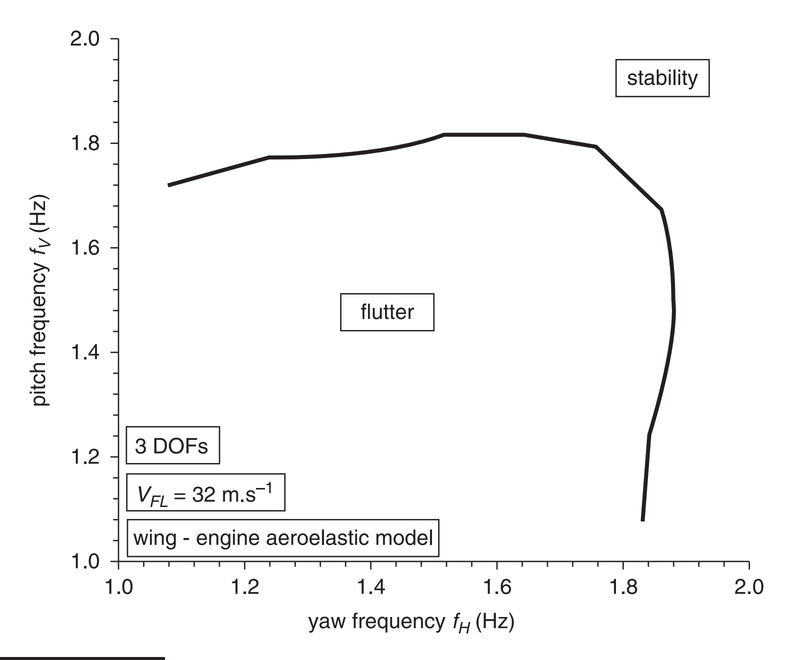


Figure 6.8 Whirl flutter stability margin

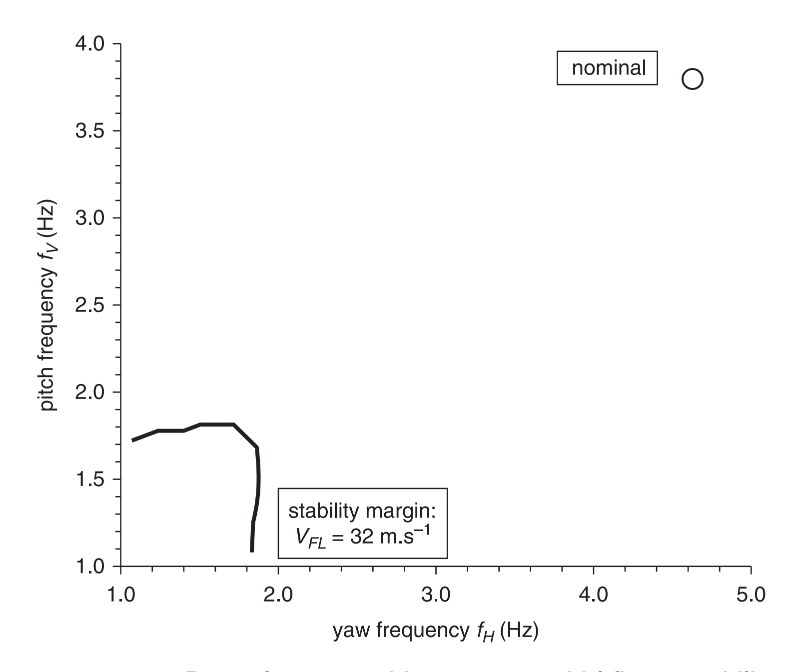


Figure 6.9 Rate of reserve with respect to whirl flutter stability margin

The values of the design variables may be constrained by side constraints:

$$(x^{I}_{i} \le x_i \le x^{U}_{i}) \tag{6.13}$$

The rate of change within the optimisation cycle may also be constrained. The design variables may also be dependent on one another, as

$$x_d = C_0 + \sum_i C_i x_i \tag{6.14}$$

The design variables are related to the properties of the analytical model (design properties). This relationship may become either a linear combination, such as Eqn. 6.14,

$$p_j = C_0 + \sum_i C_i x_i \tag{6.15}$$

or a nonlinear relationship as

$$p_j = h(\{x\},\{C\}) \tag{6.16}$$

The available ranges of the design variables then form the 'design space' for the optimiser.

The optimisation result quantities are called 'design responses'. The design responses may include various types of result quantities such as mass, volume, strain, stress, eigenvalue, dynamic response quantity, aeroelastic stability quantity, etc. These design responses may have the character of either 'design constraints' or 'objective function'. Design constraints constitute the limitations for the optimiser within the design space. Constraints have the basic character of an inequality:

$$R_j \le r_j(\vec{x}) \tag{6.17}$$

Advanced constraints are composed from inequalities, e.g., the equality constraint is composed as

$$R_j \le r_j(\vec{x}) \le R_j \tag{6.18}$$

The objective function is the target scalar function that is minimised by the optimiser. Maximalisation is mathematically provided as the minimisation of the reciprocal value. Design responses may become a combination of other design responses, design variables, design properties, constants and other relationships which may again become either a linear

$$r_d = C_0 + \sum_i C_i x_i + \sum_i C_i p_i + \sum_i C_i r_i \tag{6.19}$$

or nonlinear function

$$r_d = h(\{x\},\{p\},\{r\},\{C\}) \qquad [6.20]$$

The character of the design variables, design responses and the relationships (linear, nonlinear) determine the optimisation algorithm. Optimisation algorithms belong to the family of methods called ‘gradient-based’, because the optimisation algorithms determine the gradients of the objective function and constraints to determine a direction of searching for the optimum in the design space. The optimisation algorithms then proceed in that direction as far as they can go. They then investigate whether we are at the optimum point and if not, the process is repeated until we can make no more improvement of the objective without violating some constraint.

The direction of searching is based on the sensitivity analysis. Sensitivity coefficients Λ are evaluated for a particular design characterised by the vector of the design variables $\vec{x}^0$, giving

$$\Lambda_{ij} = \left(\frac{\partial r_j}{\partial x_i}\right)_{\vec{x}^0} \qquad [6.21]$$

where subscripts are used to indicate the *i*th design variable and the *j*th response. Equation 6.21 is just the slope of the response with respect to the design variable as shown in Figure 6.10.

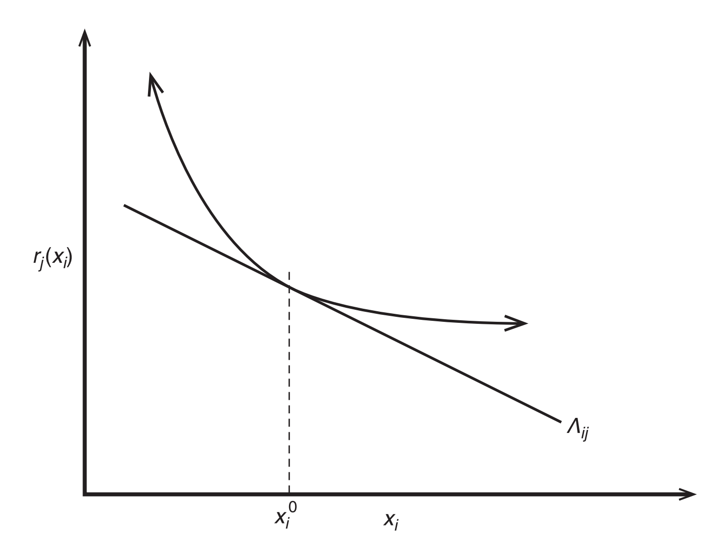


Figure 6.10 Graphical interpretation of sensitivity coefficient

The whirl flutter optimisation employs two types of the design responses (eigenvalue and flutter). The sensitivity coefficients are calculated in the following manner [9].

Eigenvalue response sensitivity

The eigenvalue equation is

$$([K]-\lambda_n[M])\{\phi_n\}=0 \qquad [6.22]$$

where λ_n and ϕ_n are the nth eigenvalue and eigenvector, respectively. *[K]* is the structural stiffness and *[M]* is the structural mass matrix. Equation 6.22 can be differentiated with respect to the ith design variable x_i:

$$([K]-\lambda_n[M])\frac{\partial\{\phi_n\}}{\partial x_i}+\left(\frac{\partial[K]}{\partial x_i}-\lambda_n\frac{\partial[M]}{\partial x_i}\right)\{\phi_n\}=\frac{\partial\lambda_n}{\partial x_i}[M]\{\phi_n\} \qquad [6.23]$$

When Equation 6.23 is premultiplied by ϕ_n^T, the first term becomes zero and Equation 6.23 can then be solved for the eigenvalue derivatives:

$$\frac{\partial\lambda_n}{\partial x_i}=\frac{\{\phi_n\}^T\left(\frac{\partial[K]}{\partial x_i}-\lambda_n\frac{\partial[M]}{\partial x_i}\right)\{\phi_n\}}{\{\phi_n\}^T[M]\{\phi_n\}} \qquad [6.24]$$

In practice, the solution of Equation 6.24 is based on the semi-analytical approach. The derivatives of the mass and stiffness matrices are approximated using the finite differences. The equation is solved for each retained eigenvalue referenced in the design model and for each design variable.

Aeroelastic flutter response sensitivity

The aeroelastic flutter stability equation is given by

$$\left[[M_{hh}]\lambda^2+\left([B_{hh}]-\frac{1}{4}\rho\,\bar{c}\,V_\infty\frac{\left[Q_{hh}^{\mathrm{Im}}\right]}{k}\right)\lambda+\left([K_{hh}]-\frac{1}{2}\rho\,V_\infty^2\left[Q_{hh}^{\mathrm{Re}}\right]\right)\right]\{u_h\}=0 \qquad [6.25]$$

Equation 6.25 represents the p-k method of the flutter solution, which is the only method applicable for the purpose of design sensitivity. $[M_{hh}]$, $[B_{hh}]$ and $[K_{hh}]$ are modal mass, damping and stiffness matrices, respectively, a function of the Mach number (M) and the reduced frequency (k). $[Q_{hh}^{Re}]$ and $[Q_{hh}^{Im}]$ are the real and the imaginary part of a complex aerodynamic matrix, also a function of parameters M and k.

The parameter ρ is the air density, $\bar{c}$ is a reference length, and u_h is a modal amplitude vector. The eigenvalue λ is given as

$$\lambda = \omega\,(\gamma \pm j) \qquad [6.26]$$

and γ is a transient decay rate coefficient. Note that the structural damping coefficient is

$$g = 2.\gamma \qquad [6.27]$$

Flutter sensitivity computes the rates of change of this transient decay rate coefficient γ with respect to changes of the design variables. Equation 6.25 is differentiated with respect to the design variables for the quantity

$$\left(\frac{\partial \gamma}{\partial x_i}\right) \qquad [6.28]$$

The solution is semi-analytical in nature with derivatives approximated using either forward differences or central differences.

Procedure description

Contrary to the standard approach, the optimisation-based approach [10], [11] calculates the stability margin directly. The procedure and means of the analysis are the same procedure and means of analysis used for the standard approach, and therefore are not reproduced here. However, the flutter stability is now solved by means of the NASTRAN solver no. 200, and the DMAP procedure *propa.alt* had to be adapted for this use (*propa_200.alt*).

The important parameters influencing the whirl flutter stability are engine pitch and yaw frequencies. The solution is therefore demonstrated on the example with variation of both frequencies. We consider the inertia characteristics of the engine and propeller system as well as the characteristics of the residual structure to be reliably determined; thus, we will use the engine attachment stiffness as the parameter for the optimisation. We define two design variables: (1) effective stiffness of the engine attachment in pitch, and (2) effective stiffness of the engine attachment in yaw.

The design properties will represent the relationship between these effective values and the properties of the structural model. The simplest option is the rotational spring elements placed at the node points of both pitch and yaw mode shapes. Provided the more complex stiffness model is used (e.g. the system of translational spring elements modelling engine

mount-isolators, beam model, etc.), the relationship to the appropriate model properties must be determined. Design responses come from the structure modal characteristics (requirement of the ratio of the specified engine pitch and yaw frequencies) and from the flutter stability (represented by the requirement of flutter stability at the selected certification speed and below this speed).

The solution that is described is also applicable to the whirl divergence. The basic procedure, including no downwash effect, includes three NASTRAN launches. The solution may optionally continue to account for the downwash and sidewash effects with three further NASTRAN launches. The procedure is described in detail in the following paragraphs.

The first preparatory step is intended to set the initial design variables for the main optimisation. The target frequency ratio (TFR) is set, and both effective stiffnesses (pitch-$K_{\varphi V}$ and yaw-$K_{\varphi H}$) are adjusted to reach this target ratio. This adjustment can be made manually. However, it is much more effective to use the NASTRAN optimisation solution (SOL 200) for normal mode analysis (ANALYSIS = MODES). The design variable is either $K_{\varphi V}$ or $K_{\varphi H}$. The objective function is defined as

$$OBJ = min\left(ABS\left(\frac{f_2}{f_1}\right) - TFR\right) \quad [6.29]$$

where f_1 and f_2 are both pitch and yaw engine frequencies (f_2 is the higher frequency while f_1 is the lower frequency). The order of both pitch and yaw frequencies must be taken under consideration as well because TFR > 1. This preparatory analysis gives the initial values of $K_{\varphi V}$ and $K_{\varphi H}$ for the main optimisation. The ratio of both frequencies (f_V and f_H) is equal to the TFR.

The main optimisation step is the NASTRAN optimisation (SOL 200) composite solution of both normal modes (ANALYSIS = MODES) and aeroelastic flutter solution (ANALYSIS = FLUTTER). The details regarding the optimisation methods and processes are described in reference [9]. The modal SUBCASE includes the design constraint to keep the frequency ratio defined by the equality constraint as:

$$\mathrm{TFR} < \left(\frac{f_2}{f_1}\right) < \mathrm{TFR} \quad [6.30]$$

However, for the practical applications, specification of a softer constraint with the ±2% TFR band is recommended as:

$$0.98 \cdot \mathrm{TFR} < \left(\frac{f_2}{f_1}\right) < 1.02 \cdot \mathrm{TFR} \quad [6.31]$$

The objective function is also defined in the modal subcase simply as:

$$OBJ = min\ (f_1 + f_2) \qquad [6.32]$$

The flutter subcase includes the constraint to keep the flutter stability at the selected certification speed which is $V_{cert} = 1.2 \cdot V_D$ for CS/FAR 23 regulations or $V_{cert} = 1.15 \cdot V_D$ for CS/FAR 25 regulations. This requirement is expressed as:

$$g(V = V_{cert}) < 0) \qquad [6.33]$$

Again, in the practical solution the constraint is modified, for example, as:

$$-\infty < \left(\frac{g(V = V_{cert}) - 0.03}{0.1} \right) < -0.3 \qquad [6.34]$$

The interval shift from the null value is given due to the numerical character of the solution preventing the division by zero. This constraint should also prevent another type of flutter instability below the certification speed that may be caused by the design variable changes. The constraint should therefore be applied to all modes included in the solution. The whirl flutter solution is performed here for the single velocity of V_{cert}, and the solution includes just the single set of DMIG cards of propfm.

Provided the initial values of stiffness $K_{\varphi V}$ and $K_{\varphi H}$ are close to the optimum, the solution performed by SOL 200 is usually faster by comparison with the multiple subcase solution performed by SOL 145 (see Section 6.2.1). The calculations described required the user to have basic knowledge with regard to the flutter behaviour of the structure.

Due to the possibility of switching of the engine pitch or yaw mode frequency with the other modes it is worth using the 'mode tracking' which is capable of re-ordering the modes at the end of the optimisation iteration, provided such mode switch appear. The re-ordering is based on the cross-orthogonality correlation analysis of both sets of modes (before and after the optimisation iteration) using the modal assurance criterion which is expressed as

$$MAC(\psi_1, \psi_2) = \frac{\left| (\{\psi_1\}^t \{\psi_2\}) \right|^2}{(\{\psi_1\}^t \{\psi_1\})(\{\psi_2\}^t \{\psi_2\})} \qquad [6.35]$$

Only engine pitch or yaw modes are switched, if necessary.

The output from this phase is the set of final stiffness parameters ($K_{\varphi V}$ and $K_{\varphi H}$) and the corresponding frequencies f_V and f_H. The frequency

ratio is equal to the TFR. At the same time, the critical flutter speed (or divergence speed) is equal to the certification speed ($V_{FL} = V_{cert}$).

The flutter behaviour of the optimised structure may be then checked by means of the standard whirl flutter analysis (SOL 145) for the range of velocities.

The procedure described above is applicable to the 'no downwash' option (see Section 6.2.1). Provided the downwash effects are to be included, the procedure is enlarged by the extra steps described here. The basic assumption is that the minor change in the engine pitch and yaw frequencies will have negligible effect to the downwash terms. The downwash terms are therefore calculated only for the structure optimised excluding the downwash as described above. These terms are calculated by NASTRAN as described in Section 6.2.1, the resulting *.pch file is processed by the *propfm* program and finally the propeller aerodynamic matrices including the downwash are inserted into the NASTRAN input file. Now the main optimisation step is repeated in the same manner as described above.

The output from this phase is the final stiffness parameters ($K_{\varphi V}$ and $K_{\varphi H}$) and corresponding frequencies f_V and f_H, including the downwash effect. The frequency ratio is kept equal to the TFR and at the same time, the critical flutter speed is equal to the certification speed ($V_{FL} = V_{cert}$).

The flutter behaviour of the optimised structure may be then checked by means of the standard whirl flutter analysis (SOL 145) for the range of velocities.

The procedure described is repeated for several frequency ratios to be able to draw the stability boundary. The target ratios extremely close to the unity value cannot be tuned due to the high coupling of both modes. The downwash angles are to be calculated for each target ratio separately, so it is obvious that the downwash including option makes the calculation much larger. In the practical application, we consider the order of pitch and yaw modes as $f_V < f_H$, which is typical for the commuter aircraft structures, and we thus draw just the one side of the stability boundary (see Chapter 7).

Example

The optimisation-based approach is demonstrated on the same example as the standard approach (see Section 6.2.1). The optimisation analyses were performed for the certification speed of $V_{cert} = 32\,m.s^{-1}$, applicable for the aeroelastic model that was obtained by scaling from the full scale aircraft value. The calculations considered no downwash effect. The

solution includes several frequency ratios considering both options in the mode order ($f_V < f_H$, and $f_H < f_V$) considering the selected mass configuration of 100% of fuel load that gives the modes summarised in Table 6.1. Figure 6.11 shows the stability margin considering two modes (engine pitch, engine yaw) and 10 modes (the modes of Table 6.1). The margin for 10 modes is moved to higher frequencies, thus the effect of the additional modes on the whirl flutter is destabilising. Contrary to this effect, the influence of additional modes on the divergence is barely noticeable. Influences of any other secondary parameters can be evaluated in the same manner.

The example of the V-g-f diagram of the optimised structure is shown in Figure 6.12. Two flutter states can be found: (1) whirl flutter with the critical mode nr. 1 (engine pitch) with TFR = 1.13, $f_V = 1.73$ Hz, $f_H = 1.95$ Hz, $f_{FL} = 1.20$ Hz, $V_{FL} = 32.0$ m.s^{-1}; and (2) wing aileron flutter with the critical mode nr. 7 (wing torsion) with $f_{FL} = 12.2$ Hz and $V_{FL} = 65.1$ m.s^{-1}.

We can also evaluate the rate of reserve with respect to structural parameters, e.g. pitch and yaw frequencies of the nominal state as demonstrated in Figure 6.13. Obviously from the figure, the rate of reserve is sufficiently high.

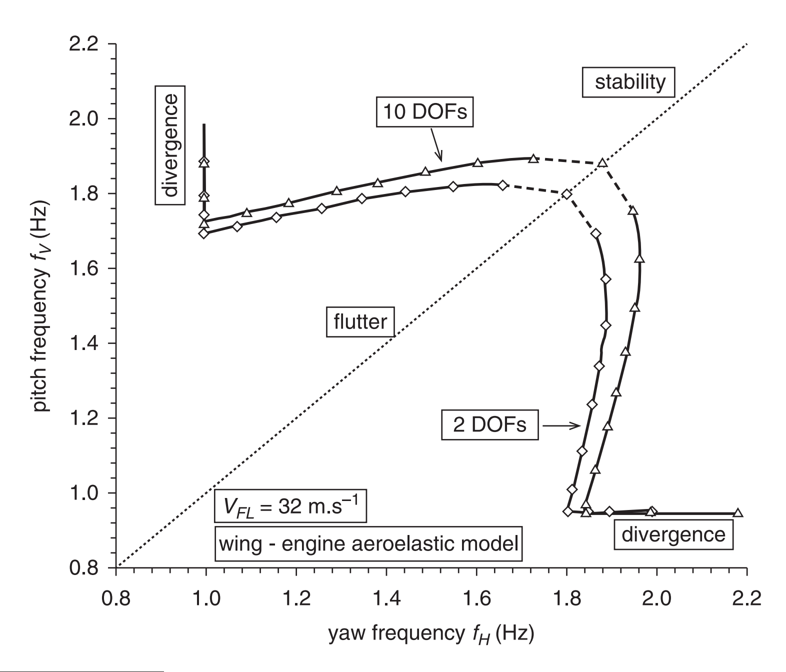


Figure 6.11 **Whirl flutter stability margins**

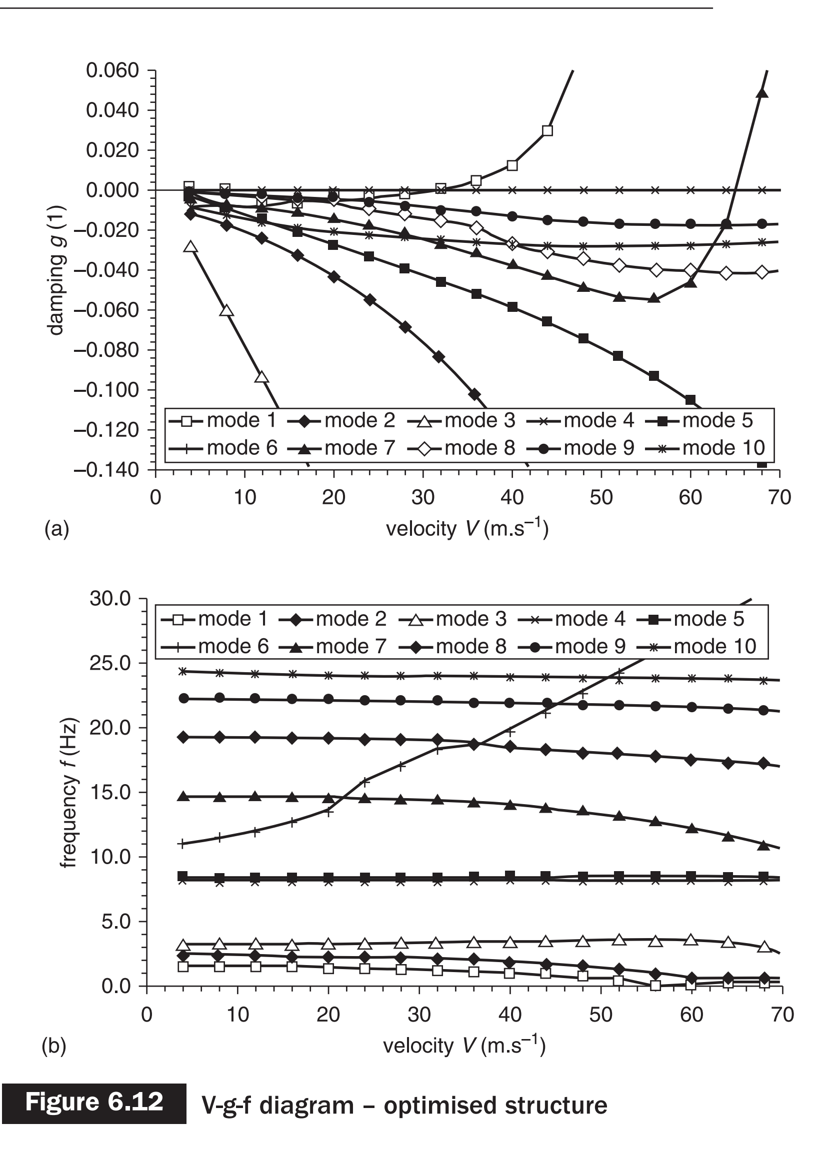


Figure 6.12 **V-g-f diagram – optimised structure**

The final comparison is provided in Figure 6.14, which represents the comparison of stability margins obtained by means of both standard and optimisation approaches. The standard approach includes three modes whereas the optimisation approach includes only two modes. Both curves correspond well with one another. Both approaches lead to the same results, but the optimisation-based approach represents the smart

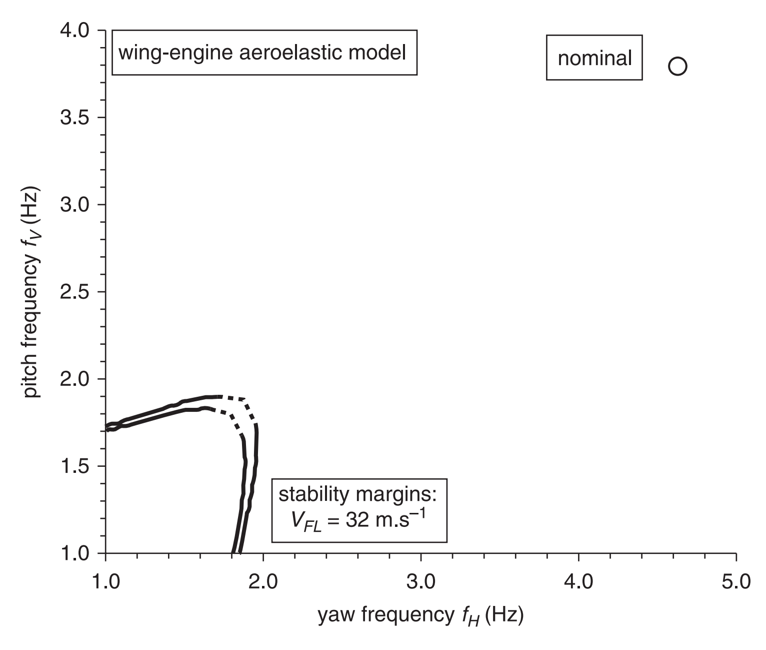


Figure 6.13 **Rate of reserve with respect to whirl flutter stability margins**

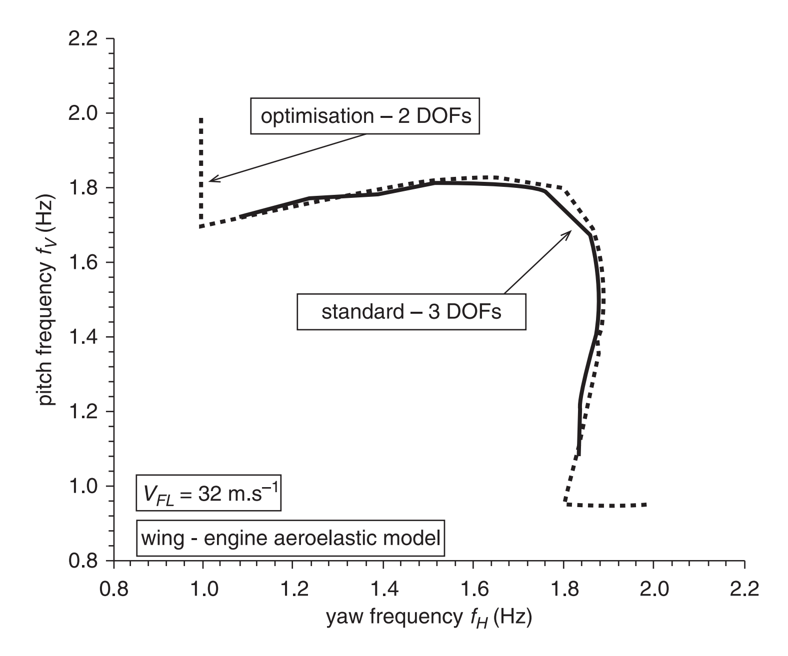


Figure 6.14 **Comparison of stability margins given by standard and optimisation approaches**

solution while the standard approach represents the extensive solution. The optimisation-based approach is also much faster. For these reasons, the optimisation-based approach is commonly used for the practical applications of aircraft certification, as shown in Chapter 7.

6.3 References

1 CS-23, Amdt.3 – Certification Specifications for Normal, Utility, Aerobatic, and Commuter Category Aeroplanes, CS-23, Amendment 3, European Aviation Safety Agency, 20.7.2012.

2 FAR-23, Amdt.62 – Federal Aviation Regulations, Part 23: Airworthiness Standards: Normal, Utility, Acrobatic and Commuter Category Airplanes, FAR-23, Amendment 62, US. Department of Transportation, Federal Aviation Administration, 31.1.2012.

3 AC-23.629-1B, Means of Compliance with Title 14 CFR, Part 23 §23.629, Flutter, Advisory Circular, AC-23.629-1B, US. Department of Transportation, Federal Aviation Administration, 28.9.2004.

4 CS-25, Amdt.12 – Certification Specifications and Acceptable Means of Compliance for Large Aeroplanes CS-25, Amendment 12, European Aviation Safety Agency, 13.7.2012.

5 FAR-25, Amdt.135 – Federal Aviation Regulations, Part 25: Airworthiness Standards: Transport Category Airplanes, FAR-25, Amendment 135, US. Department of Transportation, Federal Aviation Administration, 30.1.2012.

6 Rodden, W.P. and Johnson, E.H.: *MSC/NASTRAN Aeroelastic Analysis User's Guide* v68, Mac Neal Schwendler Corporation, 1994.

7 Rodden, W.P. and Rose, T.L.: 'Propeller/Nacelle Whirl Flutter Addition to MSC/NASTRAN', Paper No.12, *Proceedings of the 1989 MSC World User's Conference*, Universal City, CA, USA, March 1989.

8 Rodden, W.P. and Rose, T.L.: MSC/NASTRAN Addition of Effects of Wing Flow Field on Propeller Aerodynamic Loads, MSC Internal Document, June 1989.

9 Moore, G.J.: *MSC/NASTRAN Design Sensitivity and Optimization User's Guide* v68, Mac Neal Schwendler Corporation, 1994.

10 Čečrdle, J.: 'Exploitation of Optimization Solution for Determination of Whirl Flutter Stability Boundaries,' 26th Congress of the International Council of the Aeronautical Sciences (ICAS 2008), 14–19 September 2008, Anchorage, AK, USA, ICAS2008-P3.2.

11 Čečrdle, J.: 'Utilization of NASTRAN Optimization Solver 200 for Whirl Flutter Analysis,' EMEA MSC.Software Aerospace Summit 2008, Toulouse, France, 7–8 October 2008, http://www.mscsoftware-marketing-eu.com/Newsletter/en/download.

7

Certification examples from aerospace practice

DOI: 10.1533/9781782421863.225

Abstract: This chapter provides examples of the aircraft certification with respect to the whirl flutter, including single nose-mounted engine utility aircraft (Ae 270), twin wing-mounted engine utility aircraft (EV-55) and finally twin wing-mounted engine commuter aircraft with tip-tanks (L-410). The descriptions of aircraft, computational models and analyses results are provided.

Key words: Whirl Flutter Certification, CS/FAR 23, CS/FAR 25, Aero Ae 270, Evektor EV-55, Let L-410.

7.1 Single nose-mounted engine utility aircraft

The first example [1] describes the simplest case of the whirl flutter certification, which is the single fuselage nose-mounted engine aircraft.

7.1.1 Aircraft description

The subject Aero Ae 270 'Ibis' is single nose-mounted engine turboprop pressurised general utility aircraft for eight passengers with a wingspan of 13.82 m, a length of 12.23 m and a maximal take-off weight of 3670 kg (see Figure 7.1) certified according to the CS/FAR 23 regulation standard.

The aircraft was developed by the Czech aircraft company Aero Vodochody. The maiden flight was accomplished in 2000, and six flying



Figure 7.1 Aero Ae 270 'Ibis' aircraft (photo by Petr Kadlec, used with permission)

prototypes in total were manufactured and thouroughly tested before the certification by EASA (2005) and by FAA (2006). Introduction into production was halted by the company owners' decision in 2008. The aircraft was powered by the single Pratt & Whitney Canada PT6A-42A or PT6A-66A turboprop engine of 634 kW and the Hartzell HC-E4N-3P propeller with four blades.

7.1.2 Computational model

The whirl flutter analysis was performed by means of the component model, which included the engine, propeller and the cantilevered engine bed. Such simplification is justified for the single nose-mounted engine aircraft because the engine is attached to the stiff fuselage, and the natural frequencies of fuselage are usually much higher than the natural frequencies of the engine pitch and yaw. The model is shown in Figure 7.2.

The engine and propeller were modelled by means of concentrated masses. The engine attachment (mount isolators) was modelled by means of the rotational springs tuned according to the results of the prototype ground vibration test. The nominal stiffnesses of both springs ($K_{\varphi V}$ and $K_{\varphi H}$) were set to reach both pitch and yaw vibrations frequencies: $f_V = 10.43$ Hz and $f_H = 14.84$ Hz. The positions of both pitch and yaw hinge points were set in accordance with the node points of both measured modes. The aerodynamic model was represented by the dummy aerodynamic surface with which the structural model was combined. The

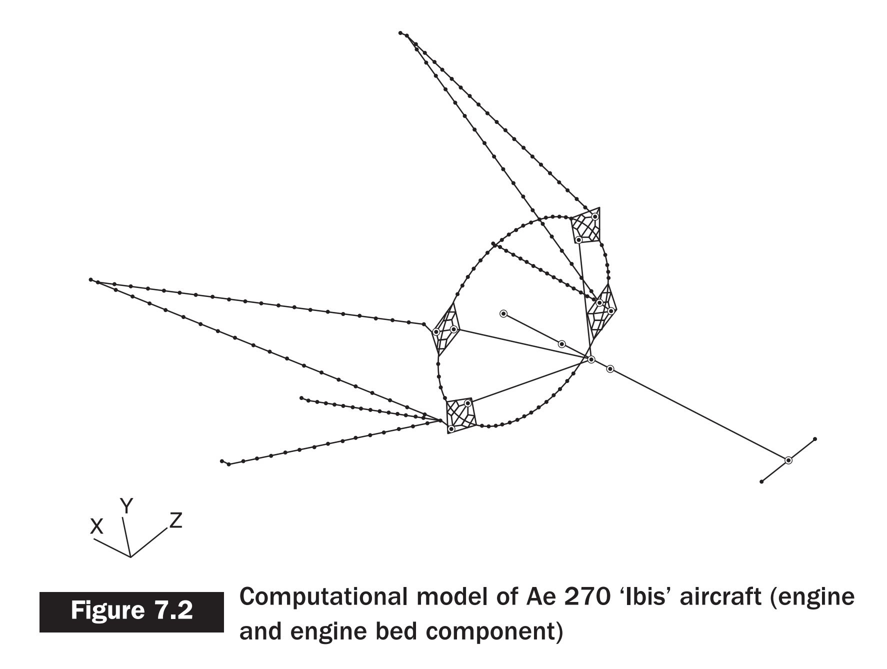


Figure 7.2 Computational model of Ae 270 'Ibis' aircraft (engine and engine bed component)

present whirl flutter analyses included two modes (engine pitch and yaw). The model included additional modes coming from the engine bed vibrations that allowed us to simulate the failure states (engine bed truss brakes) directly with no auxiliary analyses.

7.1.3 Analyses and results

The analysis of the nominal states with no whirl flutter found was performed first. These analyses included both engine options mentioned above. Then, the optimisation-based analyses followed. Analyses included no downwash effect. The flight parameters were considered according to the V-H envelope, as shown in Figure 7.3.

The certification altitude was $H_{cert} = 2500$ m and the certification flutter speed was $V_{cert} = 169.7\,\mathrm{m.s^{-1}}$. The resulting stability margin is shown in Figure 7.4. The rate of reserve of the nominal states of both engine options with respect to the stability margin was evaluated. The stability margin was calculated for the basic engine only. This calculation is justified by the high rate of reserve and also because we do not expect significant variance of the margin for both engines.

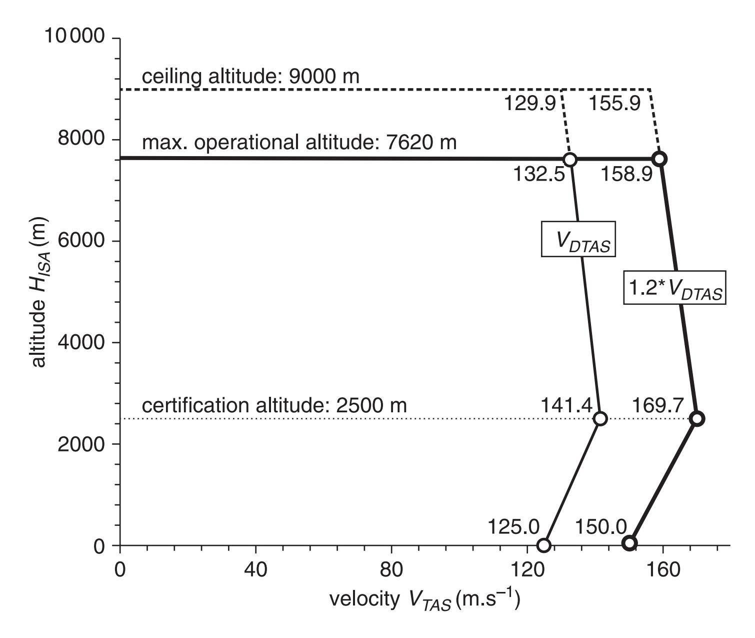


Figure 7.3 V-H envelope according to CS/FAR 23 regulations – Ae 270 'Ibis' aircraft

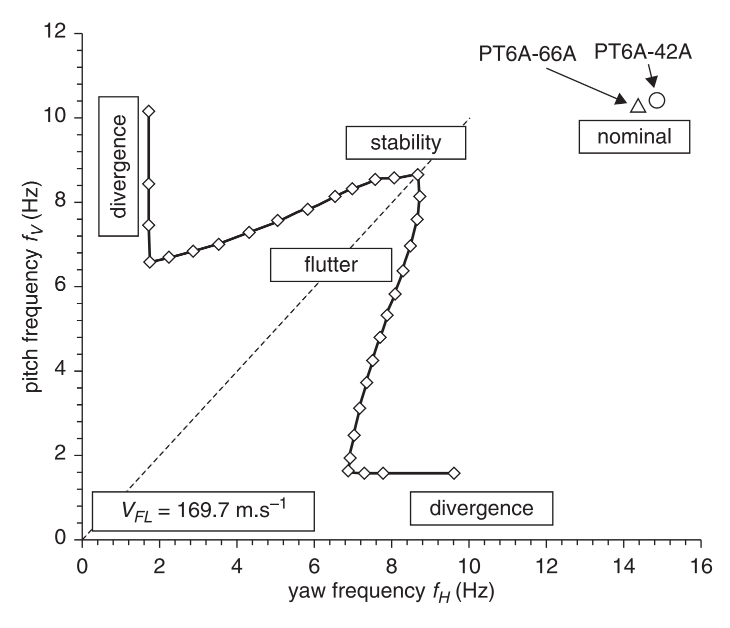


Figure 7.4 Whirl flutter stability margin – Ae 270 'Ibis' aircraft

7.2 Twin wing-mounted engine utility aircraft

The second example [2], [3] describes the most frequent case of the whirl flutter certification that is the twin wing mounted tractor engine aircraft.

7.2.1 Aircraft description

The subject Evektor EV-55 / EV-55M 'Outback' aircraft is a twin wing-mounted tractor engine general utility aircraft for nine passengers with a wingspan of 16.10 m, a length of 14.35 m and a maximal take-off weight of 4600 kg. (see Figure 7.5) certified according to the CS/FAR 23 regulation standard.

The aircraft was developed by the Czech aircraft company Evektor Kunovice. The maiden flight was accomplished in 2011, and the project is presently at the stage of the first prototype flight test. The aircraft is powered by two Pratt & Whitney Canada PT6A-21 turboprop engines of 400 kW each and Avia AV-844 propellers with four blades.



Figure 7.5 Evektor EV-55M 'Outback' aircraft (photo by Petr Štěrba, used with permission)

7.2.2 Computational model

The computational model was prepared as the aircraft half-span dynamic beam model. The simplification used in the former example is not applicable here because the natural frequencies of the wing are comparable to the frequencies of the engine pitch and yaw. Furthermore, the interference effect among propeller, nacelle and the wing must be taken under consideration. The structural model is shown in Figure 7.6.

Stiffness characteristics of the structural parts are modelled by means of the massless beam elements, and inertial characteristics are modelled by concentrated mass elements including appropriate moments of inertia. The body-like parts include moments of inertia around all three axes, while wing-like parts include just moments of inertia around the elastic axis. Flexible engine attachment and control surface actuations are realised by rotational spring elements. The model also includes various conditions and auxiliary elements (controls suspension, visualisation, etc.). Because the model is prepared as the half-span, the half-values of the stiffness and inertial characteristics are applied at the plane of symmetry as well as either symmetric or antisymmetric boundary

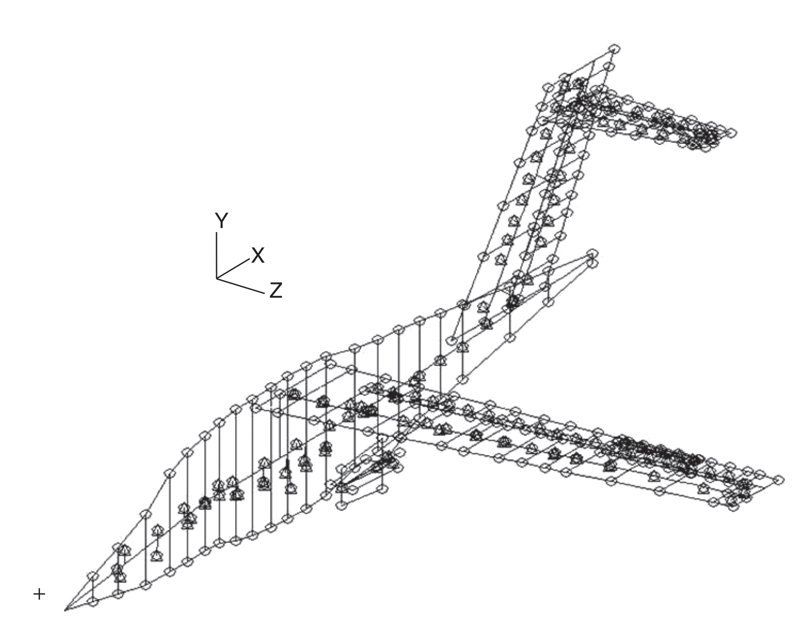


Figure 7.6 Structural half-span model of EV-55M 'Outback' aircraft

conditions. Various options considering the fuel loading, fuselage loading, controls balancing, etc., have been prepared.

The aerodynamic model is based on the Wing Body Interference Theory [4]. The wing and the vertical and horizontal tails are modelled by means of Doublet–Lattice panels, fuselage and nacelle as Slender and Interference bodies. Controls and tabs are modelled separately. The aerodynamic mesh is shown in Figure 7.7. The interpolation of both models is realised by means of beam splines.

Considering the aircraft tractor engine configuration, the aerodynamic model also includes the correction for the propeller slipstream. The nacelle and part of the wing are in the wake of the propeller with the increased velocity. This increased velocity flow increases the aerodynamic lift force and pitching moment causing the increase in the structure deformations. Such an effect is commonly considered as destabilising with respect to the flutter, so this effect should be taken into account in the analysis. Otherwise, the results would become non-conservative.

The simple momentum theory is utilised to determine the slipstream velocity and width in reference [5]. The velocities and geometry of the propeller wake are shown in Figure 7.8.

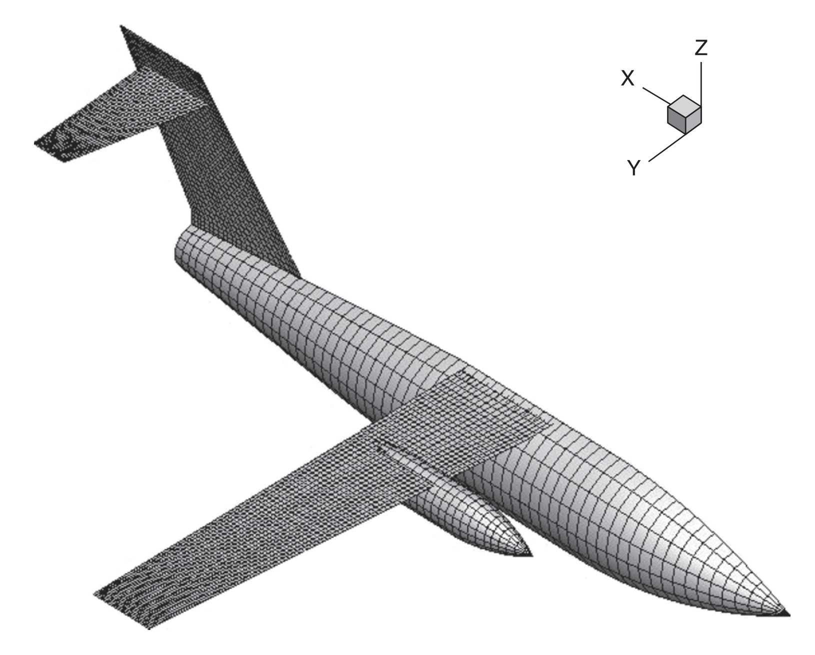


Figure 7.7 **Aerodynamic half-span model of EV-55M 'Outback' aircraft**

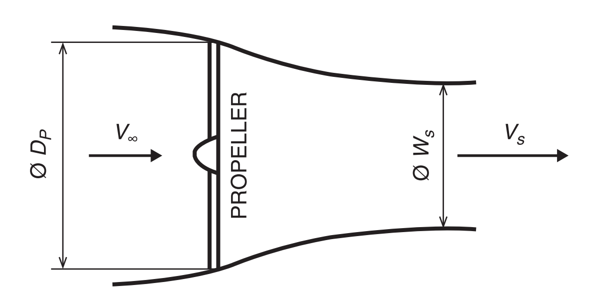


Figure 7.8 Geometry and velocities around propeller [5]

The momentum equation gives us the propeller thrust as:

$$T = S_s \rho V_s (V_s - V_\infty) \tag{7.1}$$

where S_s is the cross-section area of the propeller slipstream wake. The energy equation also gives the thrust as

$$T = \frac{1}{2} S_p \ \rho (V_s^2 - V_\infty^2) \tag{7.2}$$

where S_p is the cross-section area of the propeller. From Equation 7.2, the slipstream velocity is expressed as

$$V_s = V_\infty \sqrt{1 + \frac{2T}{\rho V_\infty^2 S_p}} \tag{7.3}$$

The slipstream-to-propeller area ratio is found by combining both Equation 7.1 and Equation 7.2 as

$$\frac{S_s}{S_p} = \frac{1}{2}\left(1 + \frac{V_\infty}{V_s}\right) \tag{7.4}$$

We substitute for V_s from Equation 7.3 to Equation 7.4 and we obtain the slipstream-to-propeller area ratio expressed as

$$\frac{S_s}{S_p} = \frac{1}{2}\left(1 + \frac{1}{\sqrt{1 + \frac{2T}{\rho V_\infty^2 S_p}}}\right) \tag{7.5}$$

The slipstream-to-propeller area ratio of Equation 7.5 can now be rewritten as a diameter ratio as

$$\frac{S_s}{S_p} = \frac{w_s^2}{D_p^2} \qquad [7.6]$$

From Equation 7.5 and Equation 7.6, the slipstream diameter becomes

$$w_s = \frac{D_p}{\sqrt{2}}\left(1+\frac{1}{\sqrt{1+\frac{2T}{\rho V_\infty^2 S_p}}}\right)^{\frac{1}{2}} \qquad [7.7]$$

The correction factor is now derived with respect to the slipstream velocity and width. The correction is applied to the aerodynamic slender elements of the nacelle and to the aerodynamic boxes of the wing behind the propeller. The geometry is shown in Figure 7.9.

The correction factor is based on the average lift on the wing aerodynamic boxes and nacelle aerodynamic slender elements in the region of the propeller wake. Considering the band on the wing and nacelle behind the propeller with the width of z_p, the correction factor W_{kk} becomes

$$W_{kk} = \frac{z_p + w_s\left(\left(\frac{V_s}{V_\infty}\right)^2 - 1\right)}{z_p} \qquad [7.8]$$

After substitutions the expression becomes

$$W_{kk} = 1+\left(\frac{D_p}{z_p}\right)\left(1+\frac{1}{\sqrt{1+\frac{2T}{\rho V_\infty^2 S_p}}}\right)^{\frac{1}{2}}\left(\frac{T\sqrt{2}}{\rho V_\infty^2 S_p}\right) \qquad [7.9]$$

The correction factor is included in the solution via the diagonal matrix $[W_{kk}]$. The correction applicable for the flutter analysis derived from [4] is expressed as:

$$\{P_k\} = [W_{kk}][S_{kj}]\{f_j\} \qquad [7.10]$$

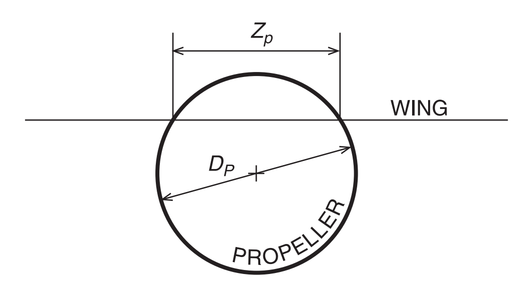


Figure 7.9 Geometry considered for correction for the propeller slipstream

where $\{P_k\}$ is the vector of aerodynamic forces, $[S_{kj}]$ is the aerodynamic integration matrix and $\{f_j\}$ is the vector of aerodynamic pressures. The correction is included in the NASTRAN solution by means of the Direct Matrix Input capability. The appropriate row-column indices of affected degrees of freedom are given according to the aerodynamic element types and numbering.

The appropriate propeller thrust for the calculation of the correction factor is commonly considered as the value applicable for the V_{DTAS} velocity at the given altitude.

7.2.3 Analyses and results

Contrary to the former example, the analyses included multiple mass configurations. These configurations accounted for the fuel loading in the wing that significantly influenced the wing dynamic characteristics. In contrast, the fuselage loading that has negligible influence on the whirl flutter is considered a common value. The fuselage loading was given as the fuselage mass configuration applicable to the maximum distance flight profile that is characterised by maximal fuel loading and fuselage partial loading to reach the maximal take-off weight. Other structural parameters or options (e.g. control balancing, control actuation, etc.) were kept at the nominal values. The analyses of any mass configuration included both symmetric and antisymmetric cases of the half-span model that was used.

Similar to the former example, analyses of the nominal states with no whirl flutter found were performed first. Then the optimisation-based analyses followed. The analyses of the symmetric cases included 15 modes, and the analyses of the antisymmetric cases included 20 modes.

These modes covered the frequency range up to approximately 50 Hz in both cases. These analyses included no downwash effect. The final analysis including the downwash effect was performed for just the mass configuration that was evaluated as the most critical with respect to the whirl flutter. The flight parameters were considered according to the V-H envelope, as shown in Figure 7.10.

The certification altitude was $H_{cert} = 3100$ m and the certification flutter speed was $V_{cert} = 175.8$ m.s^{-1}. As an example of the results, the stability margins of the symmetric cases are shown in Figure 7.11.

Figure 7.11 demonstrates the influence of the wing structure on the whirl flutter. Obviously from the figure, the margins of the fuel loading within 0–75% are rather similar, whereas the margin for the fuel loading of 100% is significantly different. The reason is the influence of the wing 1st symmetric bending mode. Figure 7.12 shows the dependence of the 1st wing symmetric bending frequency on the level of fuel loading. As the fuel is increasing, the bending frequency is decreasing.

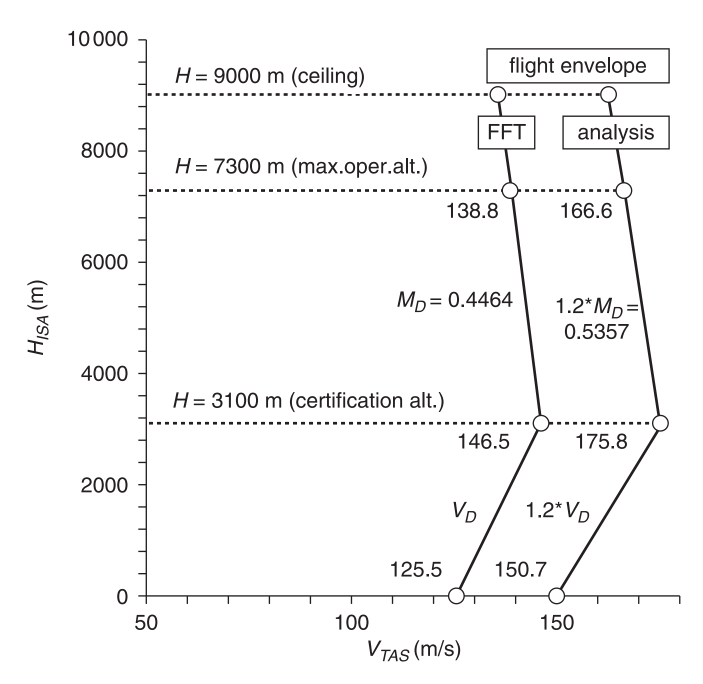


Figure 7.10 V-H envelope according to CS/FAR 23 regulations – EV-55M 'Outback' aircraft

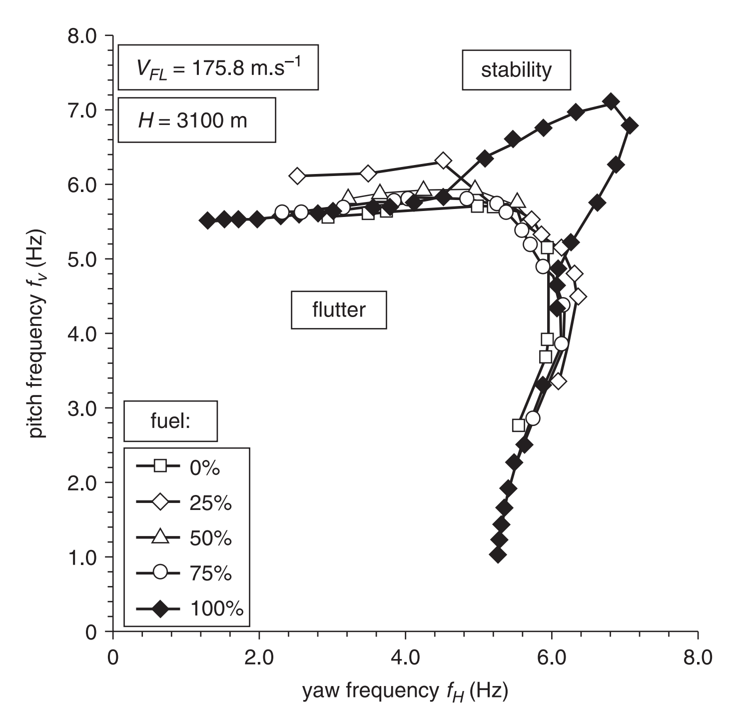


Figure 7.11 EV-55M 'Outback' aircraft – whirl flutter stability margins, no downwash considered, parameter: fuel loading

The natural frequency of this mode is closest to the engine pitch and yaw frequencies of the margin, so this mode has the most significant influence on the whirl flutter. As mentioned in Chapter 5, the wing bending mode has the stabilisation effect, which is maximal provided the wing bending frequency coincides with either engine pitch or yaw frequency. In the practical applications provided, the bending frequency is close to the engine mode frequency, and both modes become coupled with the stabilisation effect on the whirl flutter. Provided the wing bending frequency is far from the engine mode frequency, both modes are uncoupled and the described stabilisation effects do not appear. The latter is the case of the 100% fuel loading margin where provided the engine pitch-to-yaw frequency ratio is close to the unity, both engine frequencies become far from the wing bending with the destabilising outcome.

Figure 7.11 shows that the mass configuration of 100% fuel loading was evaluated as the most critical. Therefore, the mass configuration of

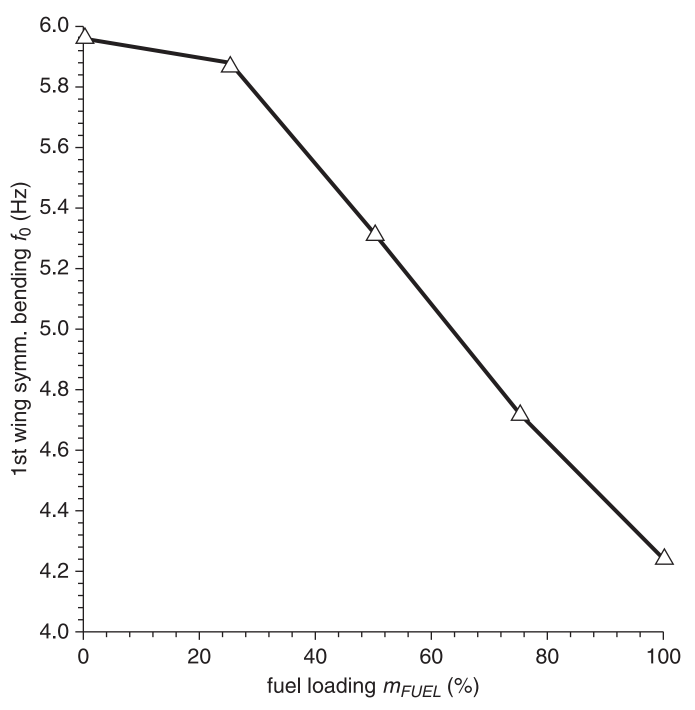


Figure 7.12 **EV-55M 'Outback' aircraft – 1st wing symmetric bending frequency dependence on fuel loading**

100% fuel loading was chosen for the following analysis, including the downwash effect. Figure 7.13 shows the resulting stability margins for both cases excluding and including the downwash.

The effect of the downwash on the margin frequencies may be evaluated as:

$$\Delta dnws = \frac{\sqrt{(f_{Vdnws} - f_V)^2 + (f_{Hdnws} - f_H)^2}}{\sqrt{f_V^2 + f_H^2}} .100 \qquad [7.11]$$

Obviously from the figure, the effect of the downwash is destabilising. This effect may be rather significant. The maximal effect on the margin frequencies found was $\Delta dnws = 8.7\%$ for the case of the uncoupled engine and wing bending modes. Thus the downwash destabilises the worst case. The downwash effect in the case of coupled engine and wing bending modes is negligible, as shown in Figure 7.14.

The evaluation of the rates of reserve towards the stability margins for the symmetric cases is shown in Figure 7.15. The nominal engine pitch

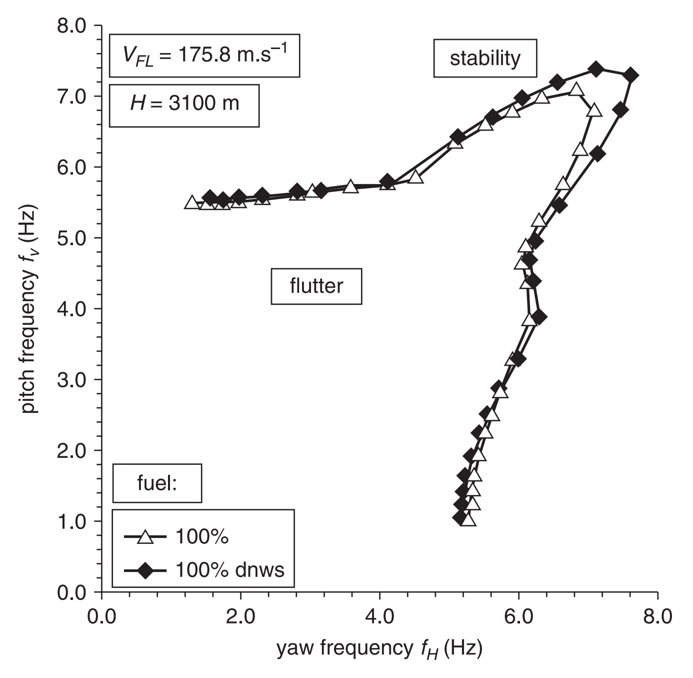


Figure 7.13 EV-55M ‘Outback’ aircraft – whirl flutter stability margins, fuel loading 100%; parameter: downwash effect included/excluded

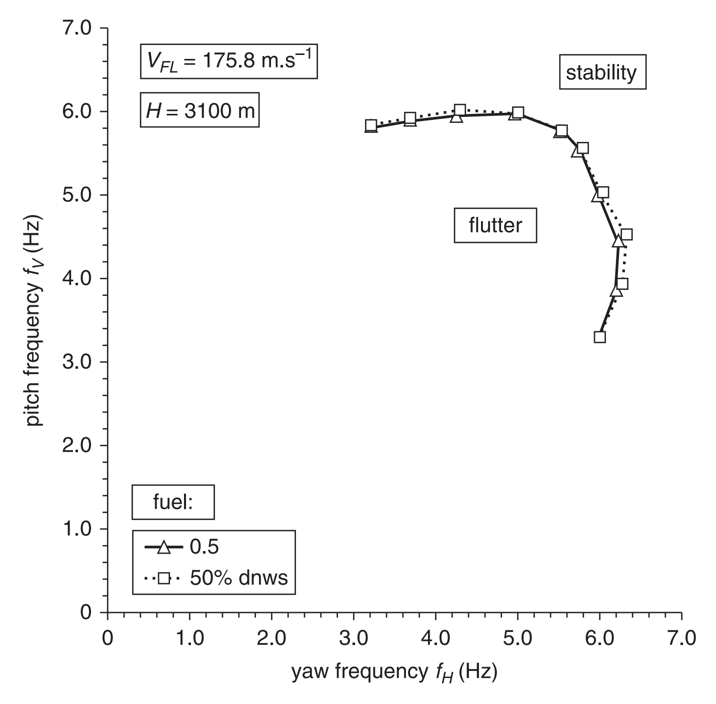


Figure 7.14 EV-55M ‘Outback’ aircraft – whirl flutter stability margins, fuel loading 50%; parameter: downwash effect included/excluded

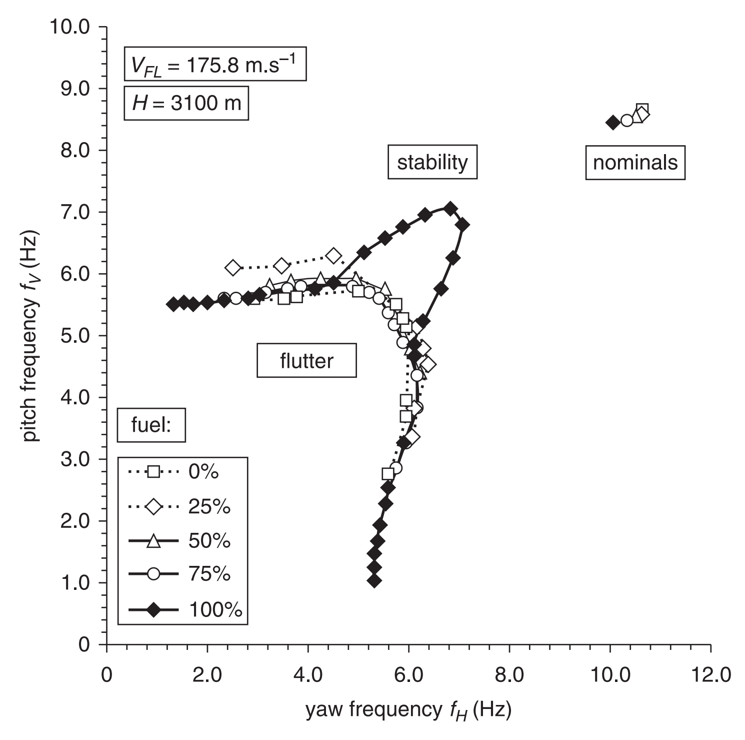


Figure 7.15 **EV-55M 'Outback' aircraft – whirl flutter stability margins, no downwash considered; parameter: fuel loading, comparison with nominal frequencies**

and yaw frequencies are calculated for all mass configurations. The example of additional information is shown for the case of 0% fuel in Figure 7.16 that includes the ±30% stiffness variance margin expressing the influence of the stiffness on both pitch and yaw frequencies. The figure also shows the nominal state obtained by the ground vibration test of the aircraft prototype.

7.2.4 Remark on usage of half-span or full-span model

The analyses described were performed by means of the half-span model. If it is possible the use of the half-span model is advisable because such analyses are simpler and clear compared to the unsymmetrical full-span model. This approach is justified for the aircraft certified

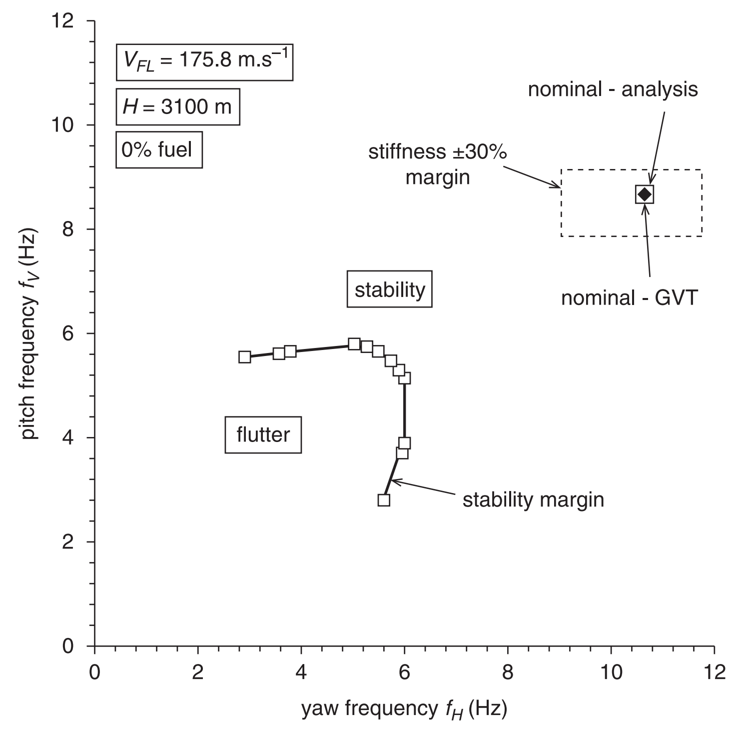


Figure 7.16 **EV-55M 'Outback' aircraft – whirl flutter stability margin, fuel loading 0%, comparison with nominal frequencies and ±30% stiffness variance margin**

according CS/FAR 23 regulation standards. However, provided the CS/FAR 25 regulation standard is applied, the analyses of specific unsymmetrical failure states as described in Section 6.1 (e.g., single propeller overspeed) must be performed using the full-span model. The full-span model may be analysed as unsymmetrical, i.e. both symmetric and antisymmetric modes together. However, linking both sides of the structural model by means of either symmetric or antisymmetric multipoint constrains to filter either symmetric or antisymmetric modes is recommended. Such an approach makes the analysis clearer and allows comparison of the results with those analyses made by the half-span model. Due to the error in the NASTRAN code, the arbitrary selection of modes ordinarily used for the standard flutter analysis is not applicable for the whirl flutter analysis. The full-span structural and aerodynamic model of EV-55M aircraft is shown in Figure 7.17 and Figure 7.18.

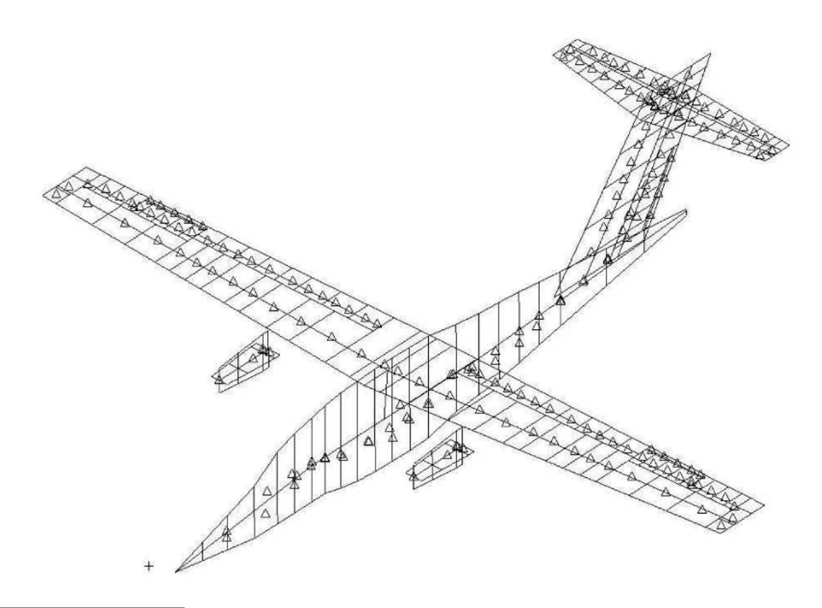


Figure 7.17 Structural full-span model of EV-55M 'Outback' aircraft

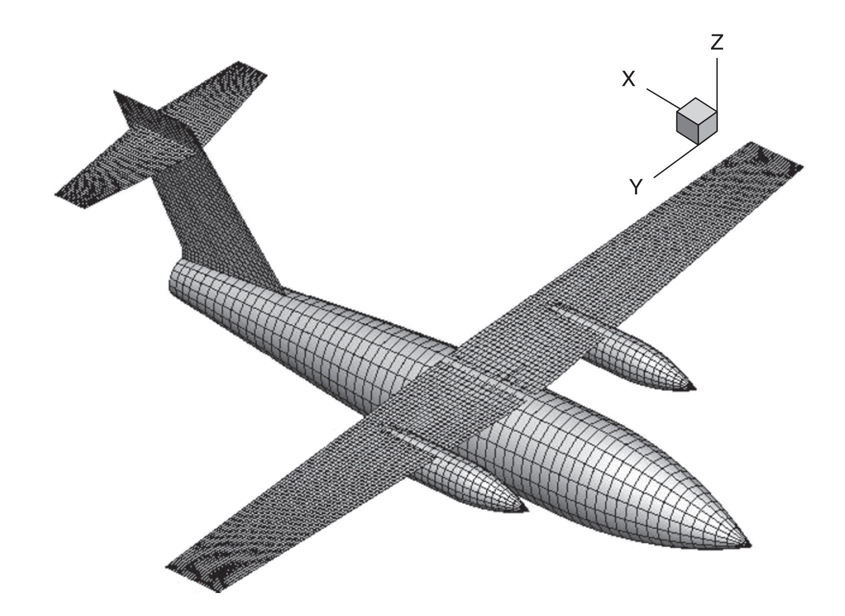


Figure 7.18 Aerodynamic full-span model of EV-55M 'Outback' aircraft

7.3 Twin wing-mounted engine commuter aircraft with tip-tanks

The previous example described the aircraft with the most frequent cases of whirl flutter: the twin wing-mounted tractor engine aircraft. In contrast to the previous case, this example has more complex mass configurations and types of power plant systems.

7.3.1 Aircraft description

The Let L-410 'Turbolet' aircraft is the legendary Czech twin wing-mounted tractor engine commuter aircraft. The actual aircraft specification L-410 UVP-E20 with a wingspan of 19.98 m, a length of 14.42 m and a maximum take-off weight of 6600 kg is assigned for 19 passengers (see Figure 7.19). The aircraft is certified according the CS/FAR 23 regulation standard.

The aircraft was developed by the Czech aircraft company Let Kunovice (currently called Aircraft Industries). The maiden flight was completed in 1969. Since that time, over 1100 aircraft have been delivered, and the aircraft development and production still continues today.

The aircraft development included several specifications, the most important developments of which are the L-410 A, which had Pratt & Whitney Canada PT6A-27 engines of 495 kW each and Hartzell HC-B3TN-3D propellers with three blades; the L-410 M which had



Figure 7.19 Let L-410 UVP-E20 'Turbolet' aircraft (photo copyright Aircraft Industries, a.s., used with permission)

Walter M-601A engines of 545 kW each and Avia V-508 propellers with three blades; the L-410 UVP, which had Walter M-601D engines of 540 kW each and Avia V-508D propellers with three blades; and the L-410 UVP-E, which had Walter M-601E engines of 560 kW each and Avia V-510 propellers with five blades.

The currently produced specification (L-410 UVP-E20) is a minor variation of the last modification. Further developments of the aircraft includes variations in the current specification: L-410 UVP-E20 H-80 with GE Aviation (Walter) GE H80 engines of 597 kW each and Avia AV-725 propellers with five blades; L-410 UVP-E20PT with Pratt & Whitney Canada PT6A-42 engines of 618 kW each and Avia AV-725 propellers with five blades; and the new major specification L-410 NG with GE Aviation (Walter) GE H80 engines of 597 kW each and Avia AV-725 propellers with five blades.

In this section, we will address the major specifications of the L-410 UVP-E, which is characterised by the installation of wing-tip fuel tanks. The wing-tip fuel tanks represent large masses placed on aeroelastically sensitive parts of the aircraft and cause specific aeroelastic problems. Furthermore, we will address three variations of this specification in terms of the power plant. The baseline variant is the L-410 UVP-E20. The second one is the L-410 UVP-E20 H-80, which has different power plants than the baseline model; however, the engine mount system remained unchanged. The last model is the L-410 UVP-E20PT, which changed both the power plants and engine mount system with respect to the baseline model.

7.3.2 Computational model

The computational model was prepared in the same manner as the previous example (using the complete-aircraft half-span dynamic beam model). The structural model is shown in Figure 7.20.

Similar to the previous model, the stiffness characteristics of the structural parts are modelled using massless beam elements. The inertial characteristics are modelled by concentrated mass elements that have the appropriate moments of inertia. Optionally, pairs of concentrated masses are used to model the moments of inertia. The body-like parts included moments of inertia around all three axes, while wing-like parts included just the moments of inertia around the elastic axis. Flexible engine attachment and control surface actuations are realised via rotational spring elements.

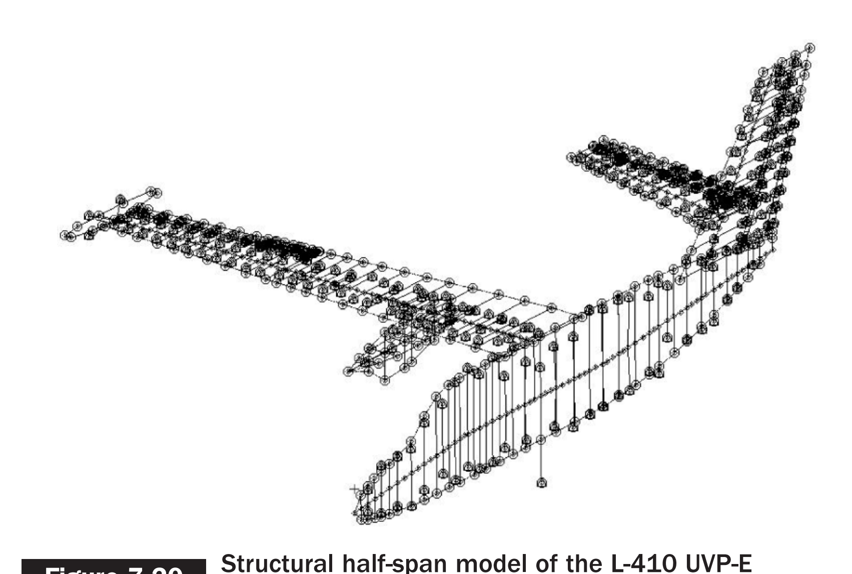


Figure 7.20 Structural half-span model of the L-410 UVP-E 'Turbolet' aircraft

In contrast to the previous model, the control surfaces and tabs do not include the stiffness characteristics and have just one degree of freedom – a flapping mode. The control surfaces or tab mass elements are connected to the main surface via a special system of multipoint constraints. These multipoint constraints ensure that the control and tab deformations follow the deformation of the main surface and, at the same time do not add any stiffness to the system.

Again, the model includes various conditions and auxiliary elements (controls suspension, visualisation, etc.), and the half-values of the stiffness and inertial characteristics are applied at the plane of symmetry as well as either symmetric or antisymmetric boundary conditions. There are various prepared options that consider the fuel loading, fuselage loading, control balance, etc.

The aerodynamic model is based on the Wing Body Interference Theory [4]. The wing, and vertical and horizontal tails are modelled using Doublet–Lattice panels. The fuselage, nacelle and tip-tank are modelled as Slender and Interference bodies. The controls and tabs are modelled separately. The interpolation of both models is realised via beam splines, except the control surfaces and tabs, which are interpolated using surface splines. The aerodynamic mesh is shown in Figure 7.21. Note that this mesh is applicable to the L-410 UVP-E20 and L-410 UVP-E20PT variants, while the L-410 UVP-E20 H-80 variant has elongated vertical tail surface.

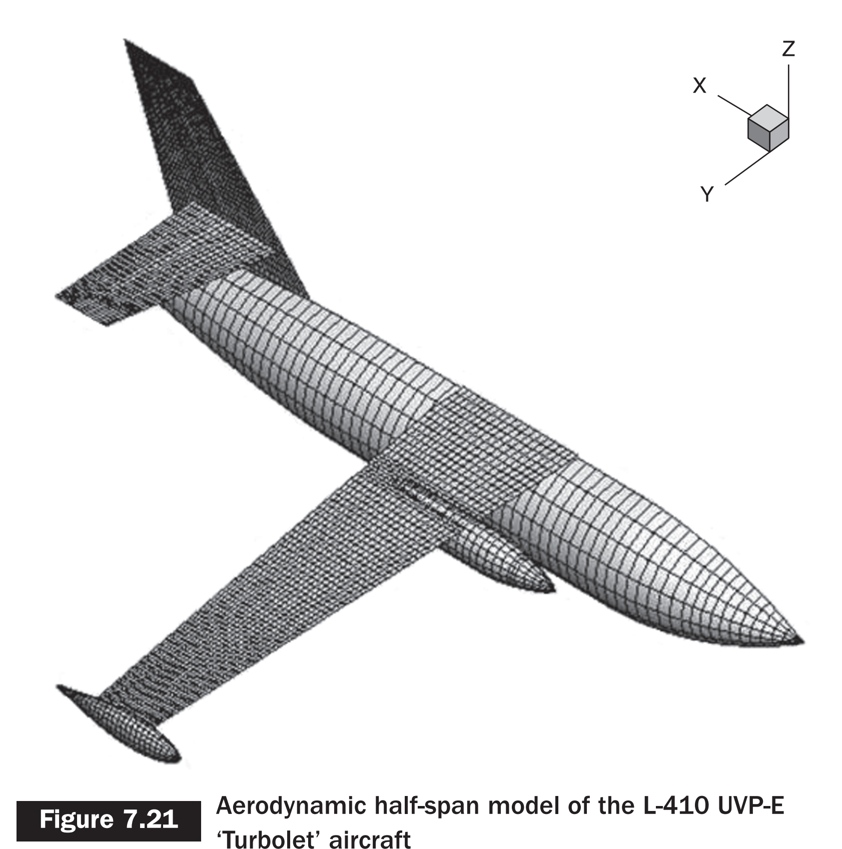


Figure 7.21 **Aerodynamic half-span model of the L-410 UVP-E 'Turbolet' aircraft**

The correction for the propeller slipstream was included in the same manner as described in the previous example.

7.3.3 Analyses and results

Similarly to the previous example, the analyses included multiple mass configurations, accounting for the fuel loading in the wing, which significantly influences the wing dynamic characteristics. In addition to the main wing tank as in the previous example, fuel is included in the tip tank as well. The fuel distribution, i.e., the relationship between the amount of fuel in both the tip and main tanks, must be in accordance with the fuel pumping rules. In fact during flight, the fuel is pumped from the tip to the main tank when enough space becomes available. The amount of fuel in the tip tank decreases while the fuel in the main tank

increases; however, it must also take into account the fuel consumption because the pumping process takes some time during which the aircraft is burning fuel. The fuel rules applicable for the L-410 UVP-E aircraft are shown in Figure 7.22.

Again, the fuselage loading is given as the common value for a fuselage mass configuration that is used for the maximum distance flight profile. The configuration is characterised by maximum fuel loading and the partial loading of the fuselage until the maximum take-off weight is reached. Other structural parameters or options (e.g., control balancing, control actuation, etc.) were kept at the nominal values. The analyses of any mass configuration included both the symmetric and antisymmetric cases of the half-span model.

As usual, the analyses of the nominal states with no whirl flutter were performed first. Next, the optimisation-based analyses followed. The analyses of the symmetric cases included 12 modes; the antisymmetric

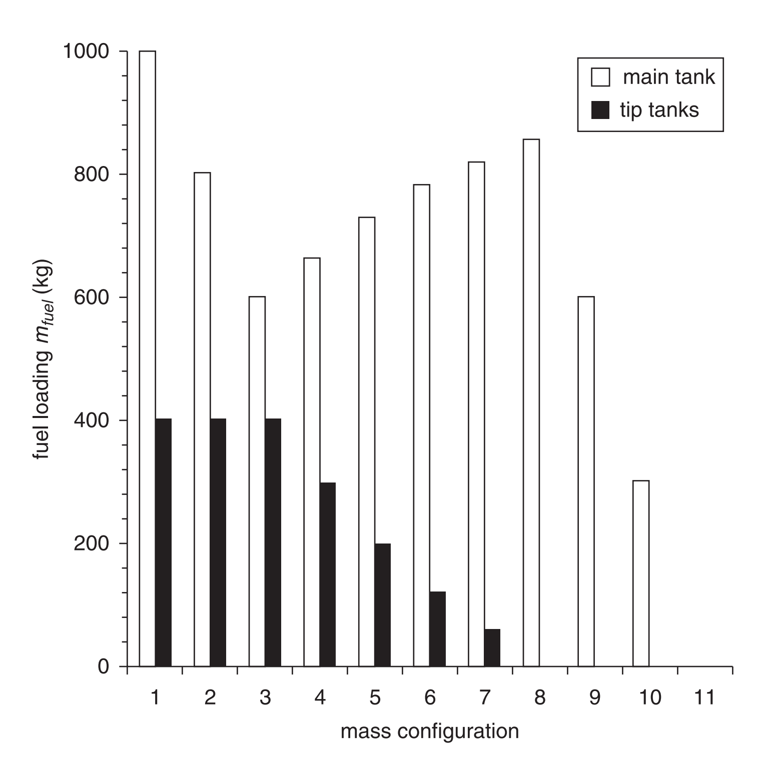


Figure 7.22 **Fuel distribution of the L-410 UVP-E 'Turbolet' aircraft**

cases included 15 modes. These modes covered the frequency range up to approximately 30 Hz in both cases.

The flight parameters were considered according the V-H envelope, as shown in Figure 7.23. The certification altitude was $H_{cert} = 4200$ m and the certification flutter speed was $V_{cert} = 169.7$ m.s^{-1}.

As an example of the stability margins, the symmetric cases excluding the downwash effect are shown in the following figures. The final analyses including the downwash effect were performed as well; however, we will focus here on the influence of the power plant on the whirl flutter characteristics and compare the stability margins.

The stability margins and their comparison with respect to the nominal frequencies are shown for L-410 UVP-E20 in Figure 7.24 and Figure 7.25, for L-410 UVP-E20-H80 in Figure 7.26 and Figure 7.27 and finally for L-410 UVP-E20PT in Figure 7.28 and Figure 7.29.

Stability margins for all aircraft variants have similar characteristics. The mass configuration (wing and tip fuel tanks) slightly influences the stability and the most significant influence can be found for pitch to yaw frequency ratios close to unity. The nominal engine frequencies

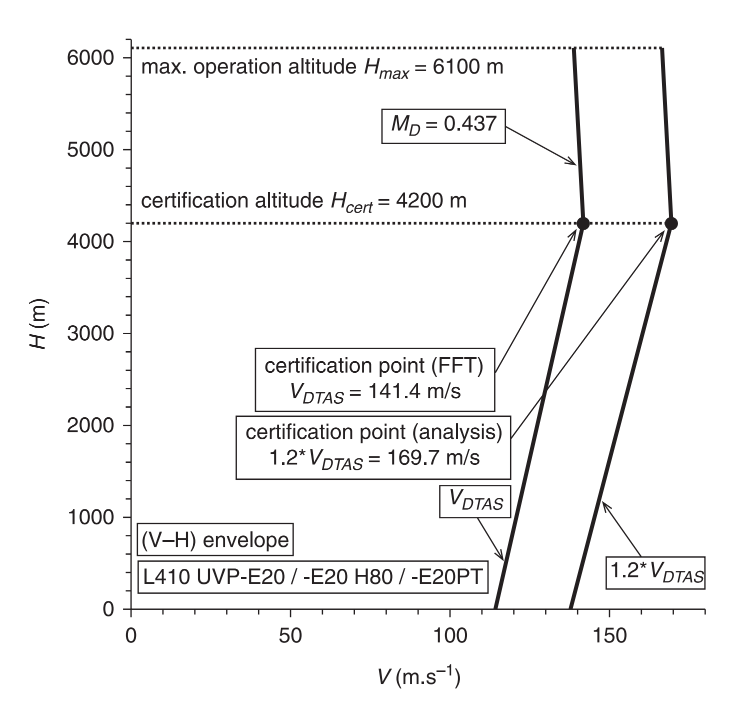


Figure 7.23 **The V-H envelope according to the CS/FAR 23 regulations – L-410 UVP-E 'Turbolet' aircraft**

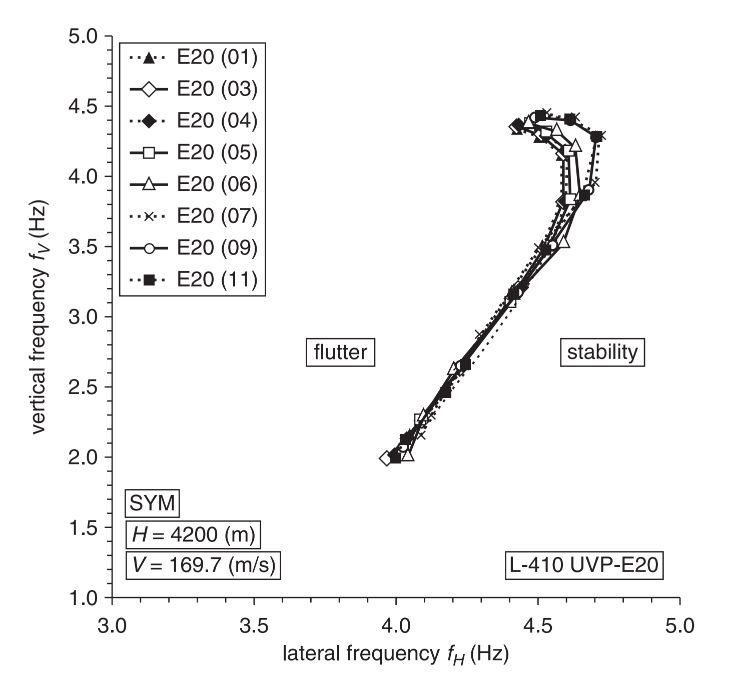


Figure 7.24 L-410 UVP-E20 aircraft – whirl flutter stability margins, no downwash considered; parameter: wing mass configuration (numbered according to Figure 7.22)

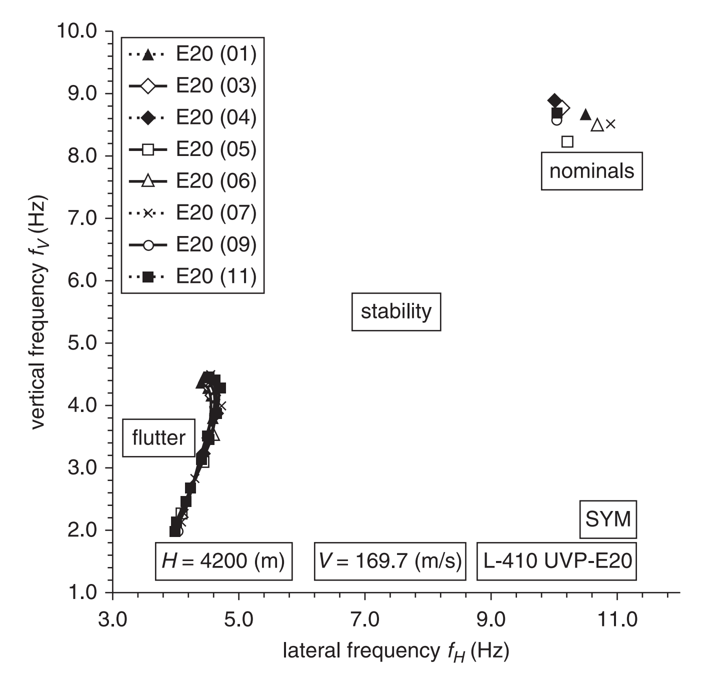


Figure 7.25 L-410 UVP-E20 aircraft – whirl flutter stability margins – comparison with nominal frequencies; parameter: wing mass configuration (numbered according to Figure 7.22)

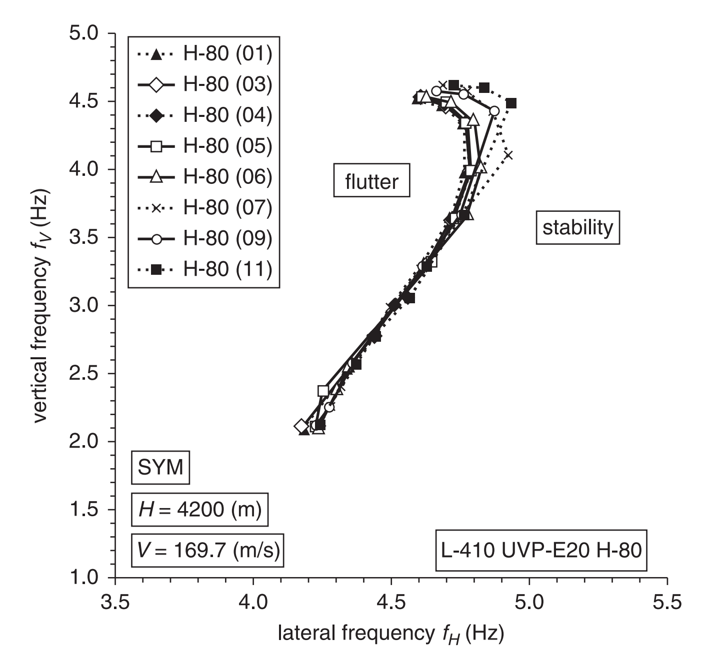


Figure 7.26 L-410 UVP-E20 H-80 aircraft – whirl flutter stability margins, no downwash considered; parameter: wing mass configuration (numbered according to Figure 7.22)

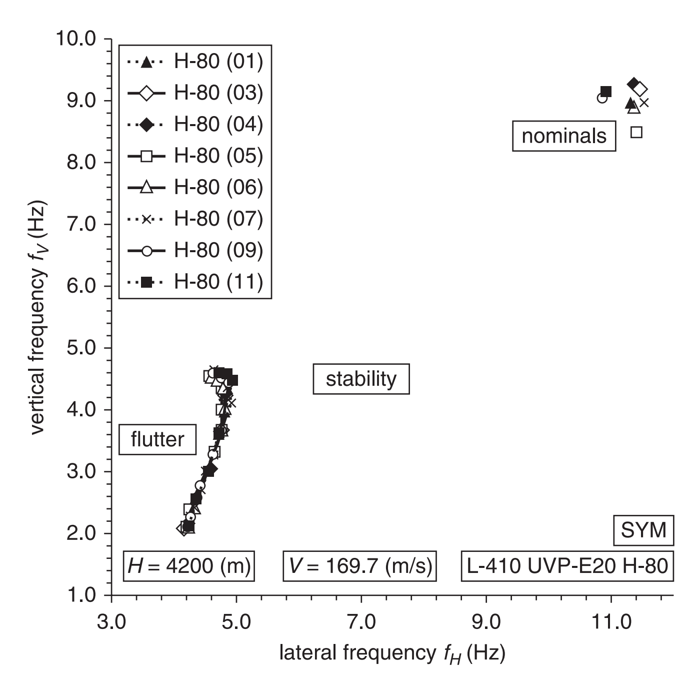


Figure 7.27 L-410 UVP-E20 H-80 aircraft – whirl flutter stability margins – comparison with nominal frequencies; parameter: wing mass configuration (numbered according to Figure 7.22)

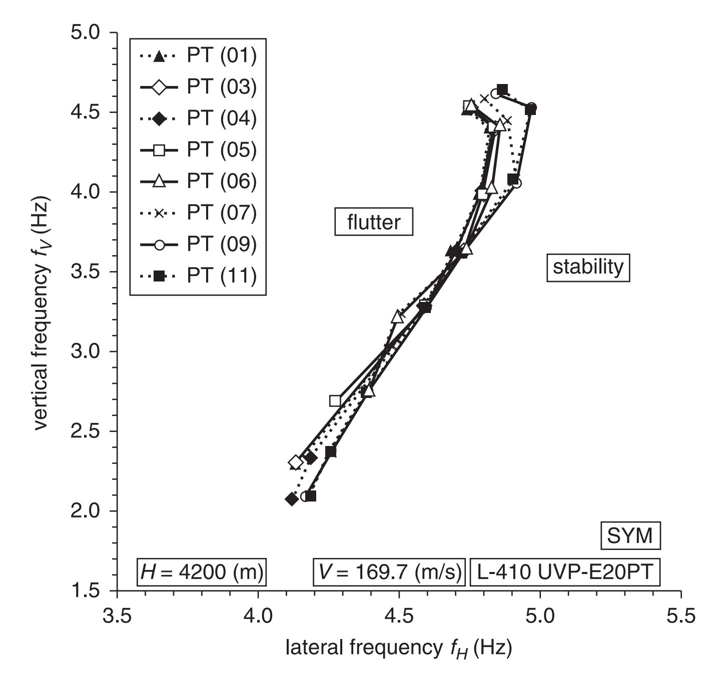


Figure 7.28 L-410 UVP-E20PT aircraft – whirl flutter stability margins, no downwash considered; parameter: wing mass configuration (numbered according to Figure 7.22)

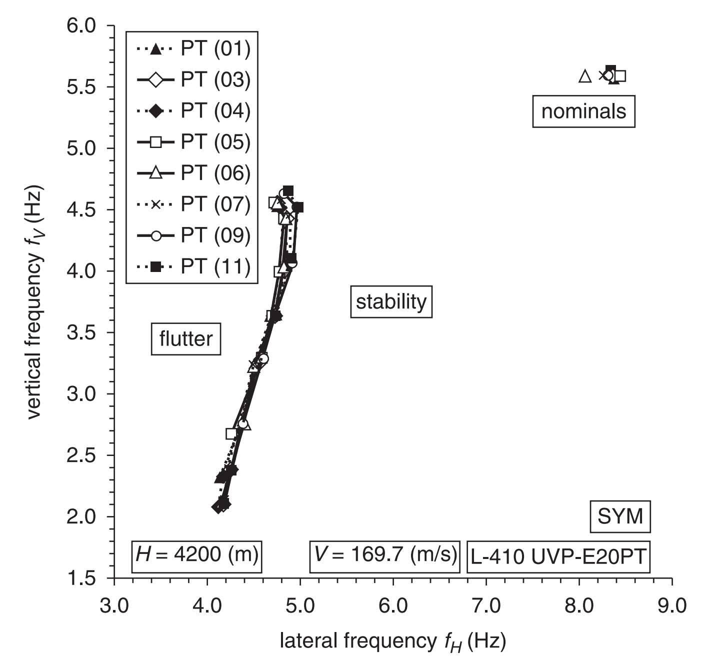


Figure 7.29 L-410 UVP-E20PT aircraft – whirl flutter stability margins – comparison with nominal frequencies; parameter: wing mass configuration (numbered according to Figure 7.22)

for all aircraft variants are in the stable area sufficiently far from margins.

Compared to the nominal frequencies of the baseline aircraft variant (L-410 UVP-E20), the frequencies of L-410 UVP-E20 H-80 are slightly higher. This difference is caused by the lighter AV-725 propeller (by 2.8%), which generates lower mass moments of inertia of the power plant system in pitch and yaw. Note that the engine mount system is kept constant for both variants. The nominal engine vibration frequencies of the L-410 UVP-E20PT variant are fairly low compared to the baseline variant. This difference is caused by the heavier power plant system PT6A-42/AV-725 (by 6.9%) compared to the baseline M-601E/V-510. However, the engine mount system has an even larger effect. The PT6A-42 attachment is realised through two pairs of mount-isolators on both sides, whereas the M-601E attachment is realised by a top-mount-isolator and two side mount-isolators.

The final comparison of the stability margins is shown for the selected mass configurations in Figure 7.30–Figure 7.33.

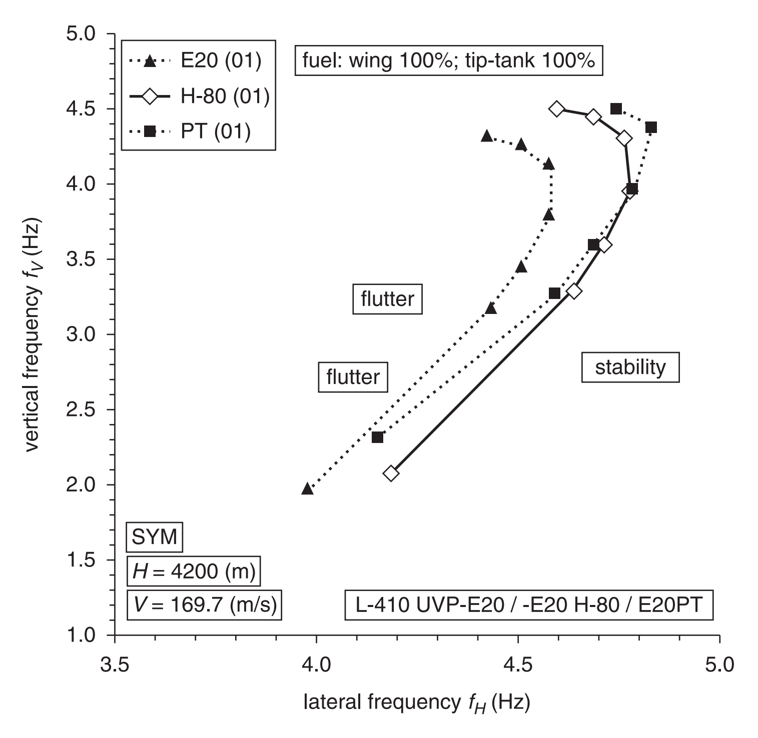


Figure 7.30 **L-410 aircraft whirl flutter stability margins comparison – mass configuration 01**

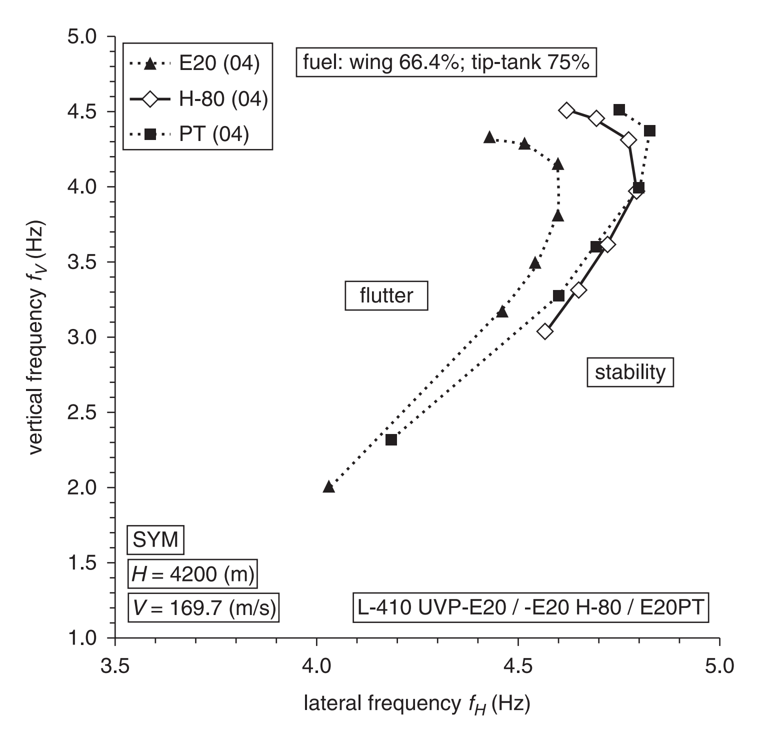


Figure 7.31 L-410 aircraft whirl flutter stability margins comparison – mass configuration 04

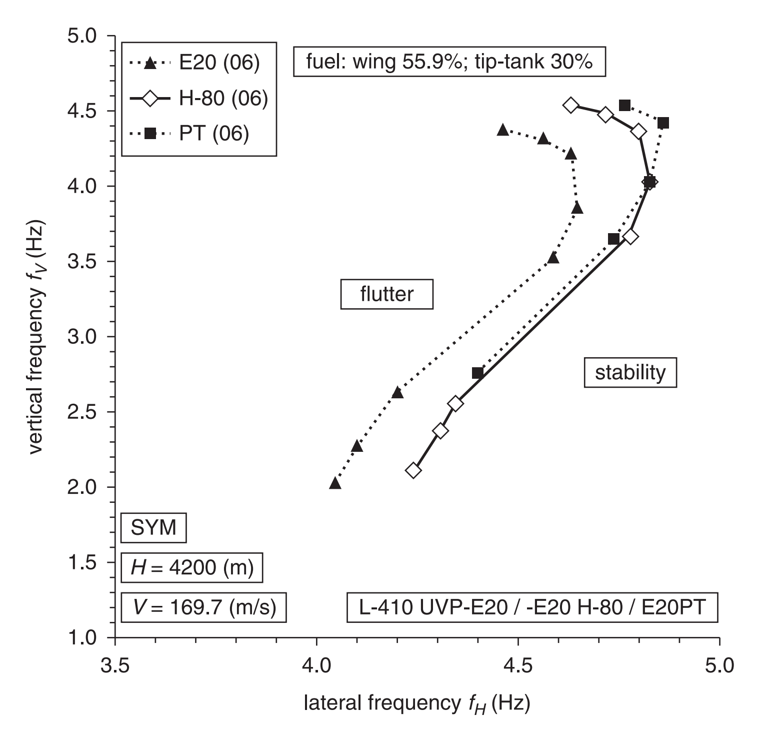


Figure 7.32 L-410 aircraft whirl flutter stability margins comparison – mass configuration 06

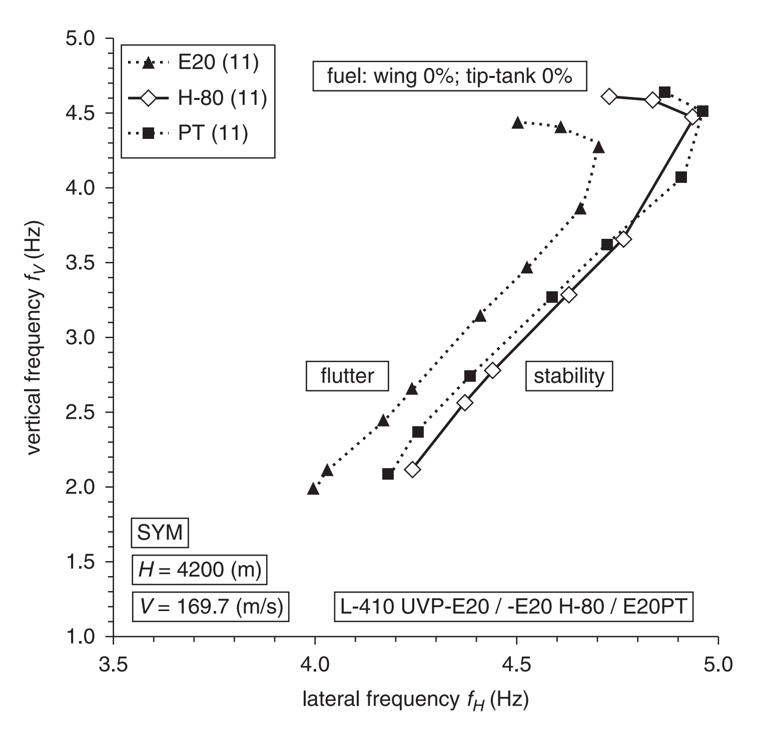


Figure 7.33 L-410 aircraft whirl flutter stability margins comparison – mass configuration 11

The stability margins of all evaluated aircraft variants are similar. The most stable variant is the baseline L-410 UVP-E20. The differences in the L-410 UVP-E20 H-80 variant are caused by the higher effective mass moment of inertia of the rotating parts in the engines and propellers and the different propeller geometries, which have destabilising effects. The differences in the L-410 UVP-E20PT margins are caused by the lower effective mass moment of inertia due to the opposite directions of rotation of the PT6A engines parts, which has a stabilising effect, and also by the node points of the engine vibration modes placed more forward than the baseline variant, which has a destabilising effect.

7.4 References

1 Čečrdle, J.: 'Whirl Flutter Analysis of Small Transport Aircraft', IFASD 07 (International Forum on Aeroelasticity and Structural Dynamics), International Conference, 18–20 June 2007, Stockholm, Sweden, IF-021, CD-ROM.

2 Čečrdle, J.: 'Whirl Flutter Analysis of Twin Turboprop Utility Aircraft', Engineering Mechanics Institute 2010 (EMI 2010), International Conference, 8–11 August 2010, Los Angeles, CA, USA.
3 Čečrdle, J.: Analysis of twin turboprop aircraft whirl-flutter stability boundaries, *Journal of Aircraft*, Vol. 49, No. 6, pp. 1718–1725, Nov–Dec 2012, ISSN 0021-8669, E-ISSN 1533-1013.
4 Rodden, W.P. and Johnson, E.H.: *MSC/NASTRAN Aeroelastic Analysis User's Guide* v68, Mac Neal Schwendler Corporation, 1994.
5 Rodden, W.P. and Rose, T.L.: 'Propeller/Nacelle Whirl Flutter Addition to MSC/NASTRAN', Paper No. 12, Proceedings of the 1989 MSC World User's Conference, Universal City, CA, USA, March 1989.

Nomenclature

α	[rad]	Angle of attack
α_0	[rad]	Blade local section steady state angle of attack
α_0	[rad]	Zero lift angle of attack
α_1	[rad]	Angle the effective blade section
α_1	[rad]	Blade local section angle of attack
α_{B0}	[rad]	Amplitude of blade torsional vibrations
α_{eff}	[rad]	Blade local section effective angle of attack
α_i		Eigenvalue over blade azimuth sector i
α_T	[rad]	Inflow angle of tilt-rotor power plant
α_T	[rad]	Angle of attack of undeformed airfoil
β	[rad]	Aileron flapping deflection
β	[rad]	Propeller blade steady state angle of attack
β	[rad]	Propeller or tiltrotor blade flapping angle
β_R	[rad]	Tiltrotor blade flapping angle baseline value
β_n	[rad]	nth propeller blade flapping angle
β_0	[rad]	Aileron flapping amplitude
β_0	[rad]	Propeller blade precone angle
β_0		Flapping blade angle zero-order term
β_Θ; $\beta_{\Theta 1}$		Flapping blade angle first-order harmonic Θ term
β_Ψ; $\beta_{\Psi 1}$		Flapping blade angle first-order harmonic Ψ term
$\beta_{\Theta 2}$		Flapping blade angle second-order harmonic Θ term
$\beta_{\Psi 2}$		Flapping blade angle second-order harmonic Ψ term
γ	[1]	Transient decay rate coefficient
γ_Ψ	[1]	Structural damping ratio – engine pitch vibrations mode
γ_Θ	[1]	Structural damping ratio – engine yaw vibrations mode

γ_φ	[1]	Structural damping ratio – wing torsion mode
γ_b	[1]	Structural damping ratio – wing bending mode
γ_β	[1]	Structural damping ratio – blade flapping mode
$\gamma_{\Theta FL}$	[1]	Critical (flutter) damping ratio
$\gamma_{\Theta 1FL}$	[1]	Forward whirl mode critical (flutter) damping ratio
$\gamma_{\Theta 2FL}$	[1]	Backward whirl mode critical (flutter) damping ratio
γ^2	[1]	Ratio of yaw stiffness to pitch stiffness
γ_{AVG}	[1]	Average structural damping ratio
γ_i		Eigenvector over blade azimuth sector *i*
γ_x	[rad]	Tiltrotor gimbal hub inner ring tilt angle (about x_H axis)
γ_y	[rad]	Tiltrotor gimbal hub outer ring tilt angle (perpendicular to x_H axis)
δ	[rad]	Aileron deflection
δ_3	[deg]	Kinematic pitch-flap coupling angle of tiltrotor or hinged blade propeller
ε	[1]	Exponent
ε	[rad]	Angle between reference velocity and plane of rotation at field point
ε_0	[rad]	Angle between reference velocity and plane of rotation at source point
ζ	[rad]	Tiltrotor blade lead-lag angle
η	[1]	Propeller dimensionless radius (r/R)
η_0	[1]	Propeller lifting part starting dimensionless radius (propeller boss dimensionless radius)
η_a	[1]	Propeller hub dimensionless distance (a/R)
$\eta_{a\Theta}$	[1]	Propeller hub dimensionless distance (a_Θ/R)
$\eta_{a\Psi}$	[1]	Propeller hub dimensionless distance (a_Ψ/R)
η_e	[m]	Propeller blade flapping hinge dimensionless radius (r_e/R)
Θ	[rad]	Engine angular displacement around horizontal axis (pitching)
Θ	[rad]	Tiltrotor blade pitch angle
Θ^*	[rad]	Engine effective angular displacement around horizontal axis (pitching)
Θ_0	[rad]	Engine pitch angle – initial condition
Θ_e	[rad]	Engine pitch angle – elastic deflection

$\Theta_{w1}{}^{*}$	[rad]	Engine effective angular displacement around horizontal axis (pitching) including downwash effect
Θ_x^F	[rad]	Tiltrotor fuselage *x*-angle
Θ_x^N	[rad]	Tiltrotor nacelle *x*-angle
Θ_x^W	[rad]	Tiltrotor wing-tip *x*-angle
Θ_y^F	[rad]	Tiltrotor fuselage *y*-angle
Θ_y^N	[rad]	Tiltrotor nacelle *y*-angle
Θ_y^W	[rad]	Tiltrotor wing-tip *y*-angle
Θ_z^F	[rad]	Tiltrotor fuselage *z*-angle
Θ_z^N	[rad]	Tiltrotor nacelle *z*-angle
Θ_z^W	[rad]	Tiltrotor wing-tip *z*-angle
θ	[rad]	Angular position of field point at time τ, referred to time $t = 0$ and reference blade radius
θ_0	[rad]	Angular position of source point at time t, referred to time $t = 0$ and reference blade radius
κ	[1]	Ratio of mass moment of inertia of propeller air cylinder to pitching moment of inertia of the power plant
κ_P	[1]	Ratio of mass moment of inertia of air to moment of inertia
Λ	[rad]	Tiltrotor blade equivalent sweep angle
Λ_{ij}		Sensitivity coefficient of *i*th design variable and the *j*th design response (optimisation)
λ		Dummy variable of integration
λ	[1]	Frequency ratio (ω_Θ/ω) or (ω/ω_Θ)
λ	[1]	Eigenvalue (general symbol)
λ^2	[1]	Eigenvalue
λ_n	[1]	*n*th eigenvalue
λ_0		Tiltrotor blade inflow absolute component
λ_s		Tiltrotor blade inflow sine component
λ_c		Tiltrotor blade inflow cosine component
λ_t		Tiltrotor blade inflow distribution function
λ_{FL}	[1]	Frequency ratio for the neutral stability (flutter) state
λ_1	[1]	Forward whirl mode eigenvalue
λ_2	[1]	Backward whirl mode eigenvalue
μ	[1]	Propeller advance ratio $(J_0/\pi) = (V_\infty/\Omega R)$
μ_I		Strength of doublets on interference body elements

μ_s		Strength of doublets on slender body elements
ν	[rad]	Blade helical angle
ρ	[kg.m^{-3}]	Air density
$\rho_{(H=0)}$	[kg.m^{-3}]	Air density at altitude of $H = 0$
ρ_H	[kg.m^{-3}]	Air density at altitude of H
σ_0		Helical coordinate $\left(\theta_0 + \frac{x_0}{h}\right)$
σ_0'		Helical coordinate $\left(\theta_0 - \frac{x_0}{h}\right)$
σ		Helical coordinate $\left(\theta + \frac{x}{h}\right)$
σ'		Helical coordinate $\left(\theta - \frac{x}{h}\right)$
τ	[1]	Dimensionless time
τ	[s]	Time of initiation of source disturbance
ϕ		Velocity potential
ϕ_n		*n*th eigenvector
ϕ_0		Amplitude of velocity potential
Φ_n	[rad]	Tiltrotor blade azimuthal spacing
Φ_n	[rad]	Propeller *n*th blade azimuth angle
φ	[rad]	Wing torsional deformation
φ	[rad]	Propeller turning angle
φ	[rad]	Torsional deformation; twist angle
φ_P	[rad]	Wing torsional displacement at propeller station
φ_0	[rad]	Initial twist angle, amplitude of twist vibrations
χ_Ψ	[1]	Frequency ratio for engine yaw (ω_Ψ/Ω)
χ_Θ	[1]	Frequency ratio for engine pitch (ω_Θ/Ω)
χ_β	[1]	Frequency ratio for blade flapping (ω_β/Ω)
Ψ	[rad]	Engine angular displacement around vertical axis (yawing)
Ψ	[rad]	Tiltrotor hub azimuth angle
Ψ_0	[rad]	Engine yaw angle – initial condition
Ψ_e	[rad]	Engine yaw angle – elastic deflection
Ψ^*	[rad]	Engine effective angular displacement around vertical axis (yawing)
$\Psi_{w2}{}^*$	[rad]	Engine effective angular displacement around vertical axis (yawing) including sidewash effect
ψ		Acceleration potential

ψ_1		Mode shape of 1st correlated mode
ψ_2		Mode shape of 2nd correlated mode
ψ_0		Amplitude of acceleration potential
ψ_D		Acceleration potential of doublet
ω	[rad.s^{-1}]	Angular frequency
ω_1	[rad.s^{-1}]	Angular frequency – first wing bending torsional coupled mode
ω_2	[rad.s^{-1}]	Angular frequency – second wing bending torsional coupled mode
ω_Ψ	[rad.s^{-1}]	Angular frequency – engine horizontal vibrations (yaw)
ω_Θ	[rad.s^{-1}]	Angular frequency – engine vertical vibrations (pitch)
ω_φ	[rad.s^{-1}]	Angular frequency – wing torsional mode
ω_h	[rad.s^{-1}]	Angular frequency – wing bending mode
ω_β	[rad.s^{-1}]	Angular frequency – blade flapping mode
ω_{FL}	[rad.s^{-1}]	Angular frequency for the neutral stability (flutter) state
ω_X	[rad.s^{-1}]	Angular frequency in the deflected *x*-axis of propeller rotation
ω_Y	[rad.s^{-1}]	Angular frequency in the deflected *y*-axis of propeller rotation
ω_Z	[rad.s^{-1}]	Angular frequency in the deflected *z*-axis of propeller rotation
Ω	[rad.s^{-1}]	Propeller angular rotational speed
$\vec{\Omega}$	[rad.s^{-1}]	Tiltrotor hub angular rotational speed
Ω_{nom}	[rad.s^{-1}]	Propeller nominal angular rotational speed
[A]		Downwash factor matrix
[A]		Flutter matrix (general symbol)
[A]		Aerodynamic matrix (general symbol)
$[A_b]$		Matrix of inertia coefficients for system with gimbaled propeller
$[A_\beta]$		Matrix of inertia coefficients for system with flapping blades
A_1		Propeller blade integral
A_2		Propeller blade integral
A_3		Propeller blade integral
A_D		Auxiliary quantity
A_i		Coefficient over blade azimuth position *i*
A_{II}		Downwash factors on interference elements from interference elements

A_{Is}		Downwash factors on interference elements from slender body elements (nacelle)
A_{Iw}		Downwash factors on interference elements from aerodynamic boxes (wing)
A_r	[1]	Propeller blade aspect ratio
A_z	[N]	Tiltrotor blade pitch-flap link force
$A_{\Theta\varphi}$		Flutter determinant coefficient
$A_{\Theta h}$		Flutter determinant coefficient
$A_{\Theta\Theta}$		Flutter determinant coefficient
$A_{\Theta\Psi}$		Flutter determinant coefficient
$A_{\Psi\varphi}$		Flutter determinant coefficient
$A_{\Psi h}$		Flutter determinant coefficient
$A_{\Psi\Theta}$		Flutter determinant coefficient
$A_{\Psi\Psi}$		Flutter determinant coefficient
$A_{\varphi\varphi}$		Flutter determinant coefficient
$A_{\varphi h}$		Flutter determinant coefficient
$A_{\varphi\Theta}$		Flutter determinant coefficient
$A_{\varphi\Psi}$		Flutter determinant coefficient
$A_{h\varphi}$		Flutter determinant coefficient
A_{hh}		Flutter determinant coefficient
$A_{h\Theta}$		Flutter determinant coefficient
$A_{h\Psi}$		Flutter determinant coefficient
$\vec{a}$	[m.s^{-2}]	Tiltrotor blade acceleration vector
a	[m]	Distance from propeller disc to engine attachment
a_0	[1]	Coefficient
a_0	[1]	Propeller blade lift curve slope (incompressible)
a_M	[1]	Propeller blade lift curve slope (maximal transonic)
a_{0eff}	[1]	Propeller blade effective lift curve slope
a_Θ	[m]	Distance from propeller disc to engine pitch hinge
a_Ψ	[m]	Distance from propeller disc to engine yaw hinge
a_1	[1]	Coefficient
a_2	[1]	Coefficient
a_{AC}	[1]	Dimensionless distance from wing midchord to aerodynamic center for steady flow (+ direction rearward, fraction of semichord)
$a_{CG\Theta}$	[m]	Distance from propeller disc to engine pitch hinge

$a_{CG\Psi}$	[m]	Distance from propeller disc to engine yaw hinge
a_{EA}	[1]	Dimensionless distance from wing midchord to elastic axis (+ direction rearward, fraction of semichord)
a_S	$[m.s^{-1}]$	Speed of sound
a_{x0}	$[m.s^{-2}]$	Tiltrotor blade acceleration vector component
a_{xy}	$[m.s^{-2}]$	Tiltrotor blade acceleration vector component
a_{xz}	$[m.s^{-2}]$	Tiltrotor blade acceleration vector component
a_{y0}	$[m.s^{-2}]$	Tiltrotor blade acceleration vector component
a_{yy}	$[m.s^{-2}]$	Tiltrotor blade acceleration vector component
a_{yz}	$[m.s^{-2}]$	Tiltrotor blade acceleration vector component
a_{z0}	$[m.s^{-2}]$	Tiltrotor blade acceleration vector component
a_{zy}	$[m.s^{-2}]$	Tiltrotor blade acceleration vector component
a_{zz}	$[m.s^{-2}]$	Tiltrotor blade acceleration vector component
$[B_{hh}]$		Modal damping matrix
$[B_\beta]$		Matrix of aerodynamic damping coefficients for system with flapping blades
B_D		Auxiliary quantity
B_i		Coefficient over blade azimuth position *i*
$B_{\beta 11}$		Term of matrix of aerodynamic damping coefficients for system with flapping blades
$B_{\beta 12}$		Term of matrix of aerodynamic damping coefficients for system with flapping blades
$B_{\beta 13}$		Term of matrix of aerodynamic damping coefficients for system with flapping blades
$B_{\beta 14}$		Term of matrix of aerodynamic damping coefficients for system with flapping blades
$B_{\beta 21}$		Term of matrix of aerodynamic damping coefficients for system with flapping blades
$B_{\beta 22}$		Term of matrix of aerodynamic damping coefficients for system with flapping blades
$B_{\beta 23}$		Term of matrix of aerodynamic damping coefficients for system with flapping blades
$B_{\beta 24}$		Term of matrix of aerodynamic damping coefficients for system with flapping blades
$B_{\beta 31}$		Term of matrix of aerodynamic damping coefficients for system with flapping blades
$B_{\beta 32}$		Term of matrix of aerodynamic damping coefficients for system with flapping blades

$B_{\beta 33}$		Term of matrix of aerodynamic damping coefficients for system with flapping blades
$B_{\beta 41}$		Term of matrix of aerodynamic damping coefficients for system with flapping blades
$B_{\beta 42}$		Term of matrix of aerodynamic damping coefficients for system with flapping blades
$B_{\beta 43}$		Term of matrix of aerodynamic damping coefficients for system with flapping blades
b	[m]	Wing semichord (perpendicular to EA)
b	[m]	Tiltrotor blade cross-section semi-chord
b_0	[1]	Coefficient
b_1	[1]	Coefficient
b_2	[1]	Coefficient
b_r	[m]	Wing reference semichord (perpendicular to EA)
$[C_\beta]$		Matrix of aerodynamic stiffness coefficients for system with flapping blades
C_0		Constant term of relation (optimisation)
C_D		Auxiliary quantity
C_D	[1]	Aerodynamic drag coefficient
C_{D0}	[1]	Aerodynamic drag coefficient for zero-lift angle of attack
C_{d0}		Aerodynamic drag coefficient – zero order term
C_{d1}		Aerodynamic drag coefficient – first order term
C_{d2}		Aerodynamic drag coefficient – second order term
C_i		i-th multiplication term of relation (optimisation)
C_i		Coefficient over blade azimuth position i
C_L	[1]	Aerodynamic lift coefficient
C_N		Objective number function *N*th coefficient
C_w		Strength of doublets on the aerodynamic boxes (wing)
$C_{\beta 11}$		Term of matrix of aerodynamic stiffness coefficients for system with flapping blades
$C_{\beta 12}$		Term of matrix of aerodynamic stiffness coefficients for system with flapping blades
$C_{\beta 13}$		Term of matrix of aerodynamic stiffness coefficients for system with flapping blades

$C_{\beta 14}$		Term of matrix of aerodynamic stiffness coefficients for system with flapping blades
$C_{\beta 21}$		Term of matrix of aerodynamic stiffness coefficients for system with flapping blades
$C_{\beta 22}$		Term of matrix of aerodynamic stiffness coefficients for system with flapping blades
$C_{\beta 23}$		Term of matrix of aerodynamic stiffness coefficients for system with flapping blades
$C_{\beta 24}$		Term of matrix of aerodynamic stiffness coefficients for system with flapping blades
$C_{\beta 32}$		Term of matrix of aerodynamic stiffness coefficients for system with flapping blades
$C_{\beta 33}$		Term of matrix of aerodynamic stiffness coefficients for system with flapping blades
$C_{\beta 34}$		Term of matrix of aerodynamic stiffness coefficients for system with flapping blades
$C_{\beta 41}$		Term of matrix of aerodynamic stiffness coefficients for system with flapping blades
$C_{\beta 43}$		Term of matrix of aerodynamic stiffness coefficients for system with flapping blades
$C_{\beta 44}$		Term of matrix of aerodynamic stiffness coefficients for system with flapping blades
c	[m]	Propeller or tiltrotor blade chord; characteristic dimension
c		Objective number function
c_0	[m]	Blade local section chord
c_r	[m]	Blade reference chord
c_D	[1]	Tiltrotor blade cross-sectional drag coefficient
c_L	[1]	Tiltrotor blade cross-sectional lift coefficient
$c_{L\alpha}$	[1]	Wing local section lift curve slope of steady flow
c_M	[1]	Tiltrotor blade cross-sectional moment coefficient
c_T	[1]	Thrust coefficient
$c_{m\Theta}$	[1]	Aerodynamic derivative (pitching moment due to pitch angle)
$c_{m\Psi}$	[1]	Aerodynamic derivative (pitching moment due to yaw angle)
c_{mq}	[1]	Aerodynamic derivative (pitching moment due to pitching)

c_{mr}	[1]	Aerodynamic derivative (pitching moment due to yawing)
$c_{n\Theta}$	[1]	Aerodynamic derivative (yawing moment due to pitch angle)
$c_{n\Psi}$	[1]	Aerodynamic derivative (yawing moment due to yaw angle)
c_{nq}	[1]	Aerodynamic derivative (yawing moment due to pitching)
c_{nr}	[1]	Aerodynamic derivative (yawing moment due to yawing)
$c_{y\Theta}$	[1]	Aerodynamic derivative (side force due to pitch angle)
$c_{y\Psi}$	[1]	Aerodynamic derivative (side force due to yaw angle)
c_{yq}	[1]	Aerodynamic derivative (side force due to pitching)
c_{yr}	[1]	Aerodynamic derivative (side force due to yawing)
$c_{z\Theta}$	[1]	Aerodynamic derivative (vertical force due to pitch angle)
$c_{z\Psi}$	[1]	Aerodynamic derivative (vertical force due to yaw angle)
c_{zq}	[1]	Aerodynamic derivative (vertical force due to pitching)
c_{zr}	[1]	Aerodynamic derivative (vertical force due to yawing)
$(c_{m\Theta})_{inv}$	[1]	Aerodynamic derivative (pitching moment due to pitch angle) for inverse rotation
$(c_{mq})_{inv}$	[1]	Aerodynamic derivative (pitching moment due to pitching) for inverse rotation
$(c_{n\Theta})_{inv}$	[1]	Aerodynamic derivative (yawing moment due to pitch angle) for inverse rotation
$(c_{nq})_{inv}$	[1]	Aerodynamic derivative (yawing moment due to pitching) for inverse rotation
$(c_{y\Theta})_{inv}$	[1]	Aerodynamic derivative (side force due to pitch angle) for inverse rotation
$(c_{yq})_{inv}$	[1]	Aerodynamic derivative (side force due to pitching) for inverse rotation
$(c_{z\Theta})_{inv}$	[1]	Aerodynamic derivative (vertical force due to pitch angle) for inverse rotation

$(c_{zq})_{inv}$	[1]	Aerodynamic derivative (vertical force due to pitching) for inverse rotation
$[D]$		Structural damping matrix
$[D]$		Damping matrix (general symbol)
$[D^A]$		Aerodynamic damping matrix
$[D_b]$		Matrix of structural damping coefficients for system with gimbaled propeller
$[D_b^A]$		Matrix of aerodynamic damping coefficients for system with gimbaled propeller
$[D_{jk}]$		Substantial derivative matrix
$[D_\beta]$		Matrix of structural damping coefficients for system with flapping blades
D_{b11}^A		Term of matrix of aerodynamic damping coefficients for system with gimbaled propeller
D_{b12}^A		Term of matrix of aerodynamic damping coefficients for system with gimbaled propeller
D_{b13}^A		Term of matrix of aerodynamic damping coefficients for system with gimbaled propeller
D_{b14}^A		Term of matrix of aerodynamic damping coefficients for system with gimbaled propeller
D_{b21}^A		Term of matrix of aerodynamic damping coefficients for system with gimbaled propeller
D_{b22}^A		Term of matrix of aerodynamic damping coefficients for system with gimbaled propeller
D_{b23}^A		Term of matrix of aerodynamic damping coefficients for system with gimbaled propeller
D_{b24}^A		Term of matrix of aerodynamic damping coefficients for system with gimbaled propeller
D_{b31}^A		Term of matrix of aerodynamic damping coefficients for system with gimbaled propeller
D_{b32}^A		Term of matrix of aerodynamic damping coefficients for system with gimbaled propeller
D_{b33}^A		Term of matrix of aerodynamic damping coefficients for system with gimbaled propeller
D_{b34}^A		Term of matrix of aerodynamic damping coefficients for system with gimbaled propeller
D_{b41}^A		Term of matrix of aerodynamic damping coefficients for system with gimbaled propeller
D_{b42}^A		Term of matrix of aerodynamic damping coefficients for system with gimbaled propeller

D_{b43}^{A}		Term of matrix of aerodynamic damping coefficients for system with gimbaled propeller
D_{b44}^{A}		Term of matrix of aerodynamic damping coefficients for system with gimbaled propeller
D	[N]	Damping force
D	[N]	Aerodynamic drag force
D	[N]	Tiltrotor blade cross-sectional drag force
D_D		Auxiliary quantity
D_n		Base vector nth order (objective number technique)
D_P	[m]	Propeller diameter
D_Θ		Generalised damping force in Θ generalised coordinate
D_Ψ		Generalised damping force in Ψ generalised coordinate
d_N		Objective number vector Nth component
$\Delta dnws$	[%]	Effect of downwash on flutter margin frequencies
d_H	[m]	Distance of rotor hub from wing-tip (in z_N direction)
d_x^F	[m]	Tiltrotor fuselage x-translation
d_y^F	[m]	Tiltrotor fuselage y-translation
d_z^F	[m]	Tiltrotor fuselage z-translation
d_x^W	[m]	Tiltrotor wing-tip x-translation
d_y^W	[m]	Tiltrotor wing-tip y-translation
d_z^W	[m]	Tiltrotor wing-tip z-translation
$[E_\beta]$		Matrix of coefficients for system with flapping blades
Δe_{PL}	[m]	Tiltrotor blade pitch-flap link elastic extension
E	[J]	Energy (general symbol)
E		General function
E_φ	[J]	Energy of torsional motion
E_β	[J]	Energy of flapping motion
E_b	[J]	Energy of bending motion
E_k	[J]	Kinetic energy
$E_{k\Omega}$	[J]	Kinetic energy of rotating propeller including gyroscopic precession
E_{kP}	[J]	Kinetic energy of non-rotating propeller and engine system
E_{kW}	[J]	Kinetic energy of wing

E_P	[J]	Potential energy
e_φ	[m]	Distance from wing elastic axis to propeller disc plane (+ direction rearward)
e_ζ	[m]	Tiltrotor blade lead-lag system offset
e_{PL}	[m]	Tiltrotor blade pitch-flap link offset
$\bar{e}_r$		Cylindrical unit vector (*r*-direction)
$\bar{e}_x$		Cylindrical unit vector (*x*-direction)
e_β	[m]	Tiltrotor blade flapping system offset
e_Θ	[m]	Distance from engine pitch gimbal axis to propeller disc plane (+ direction rearward)
e_Θ	[m]	Tiltrotor blade pitch system offset
$\bar{e}_\theta$		Cylindrical unit vector (θ-direction)
e_Ψ	[m]	Distance from engine yaw gimbal axis to propeller disc plane (+ direction rearward)
$\{f_j\}$		Vector of aerodynamic pressures
$\vec{F}$		Force vector in inertia coordinates
$F(k)$; F		Real component of Theodorsen function (complex circulation function)
F_1		real component of Theodorsen function for first term
F_2		Real component of Theodorsen function for second term
F_i		Constant load on blade over blade azimuth position *i*
F_P	[m^2]	Propeller disc area
F_{PL}	[N]	Tiltrotor blade pitch-flap link force
F_R		Rigid propeller aerodynamics with time delay
F_x	[N]	Force for flexible propeller support
F_y	[N]	Force for flexible propeller support
f		General function
f_Θ	[1]	Dimensionless generalised propeller force in pitch
f_Ψ	[1]	Dimensionless generalised propeller force in yaw
f_0	[Hz]	Natural frequency (general symbol)
f_1		Function
f_2		Function
f_1	[Hz]	Natural frequency of either engine pitch or yaw mode (lower one)
f_2	[Hz]	Natural frequency of either engine pitch or yaw mode (higher one)

f_C		General function
f_{FL}	[Hz]	Flutter frequency
f_H	[Hz]	Natural frequency of engine's lateral vibrations (yaw)
f_V	[Hz]	Natural frequency of engine's vertical vibrations (pitch)
f_{Hdnws}	[Hz]	Natural frequency of engine's lateral vibrations including downwash effect
f_{Vdnws}	[Hz]	Natural frequency of engine's vertical vibrations including downwash effect
$[G]$		Gyroscopic matrix
$[G_b]$		Matrix of gyroscopic coefficients for system with gimbaled propeller
$[G_{ka}]$		Aerodynamic – structure interpolation matrix
G	[1]	Ratio of yaw damping to pitch damping
$G(k)$; G		Imaginary component of Theodorsen function (complex circulation function)
G_1		Imaginary component of Theodorsen function for first term
G_2		Imaginary component of Theodorsen function for second term
g	[1]	Total artificial damping of vibrating system
g_β	[1]	Viscous damping coefficient in blade flapping
g_Θ	[1]	Viscous damping coefficient in pitch
g_Ψ	[1]	Viscous damping coefficient in yaw
H	[m]	Flight altitude
H	[1]	Ratio of polar moment of inertia of propeller to pitching moment of inertia of power plant
ΔH	[N]	Horizontal component force
H_{cert}	[m]	Certification flight altitude
H_{ISA}	[m]	Flight altitude according to the International Standard Atmosphere
H_n	[N]	Propeller blade local section in-plane force
$\bar{h}_0$	[1]	Dimensionless amplitude of blade bending vibrations
h	[m]	Wing bending deformation
h	[m]	Advance ratio (V_∞/Ω)
h	[m]	Dimensionless advance ratio ($V_\infty/R\Omega$)
$h(\{x\},\{C\})$		Non-linear function of relation for design property (optimisation)

$h(\{x\},\{p\},\{r\},\{C\})$		Non-linear function of relation for design property (optimisation)
h_0	[m]	Initial bending deformation, amplitude of bending vibrations
h_0	[m]	Amplitude of blade bending vibrations
h_P	[m]	Wing elastic axis bending deformation at propeller station
I_1		Propeller blade integral (in-phase)
I_2		Propeller blade integral (in-phase)
I_3		Propeller blade integral (in-phase)
I_b	[kg.m^2]	Gimbaled propeller mass moment of inertia
I_β	[kg.m^2]	Hinged blade propeller mass moment of inertia
$I_{\beta 0}$	[kg.m^2]	Hinged blade propeller mass moment of inertia
$I_{\beta 1}$	[kg.m^2]	Hinged blade propeller mass moment of inertia
$I_{\beta 2}$	[kg.m^2]	Hinged blade propeller mass moment of inertia
I_Θ	[kg.m^2]	Nacelle and propeller complete system moment of inertia
I_Ψ	[kg.m^2]	Nacelle and propeller complete system moment of inertia
Im		Imaginary part
i		Blade azimuth position index
J_1		Propeller blade integral (out-of-phase)
J_2		Propeller blade integral (out-of-phase)
J_3		Propeller blade integral (out-of-phase)
J_0	[1]	Propeller advance ratio ($\pi V_\infty / \Omega R$)
J_p	[kg.m^2]	Polar mass moment of inertia of propeller
J_r	[kg.m^2]	Polar mass moment of inertia of engine rotor
J_x	[kg.m^2]	Mass moment of inertia about x-axis
J_Y	[kg.m^2]	Mass moment of inertia about y-axis (propeller + nacelle)
J_{YN}	[kg.m^2]	Nacelle (engine) mass moment of inertia about y-axis
J_{YNCG}	[kg.m^2]	Nacelle (engine) mass moment of inertia about its CG y-axis
J_Z	[kg.m^2]	Mass moment of inertia about z-axis (propeller + nacelle)

J_{ZN}	[kg.m^2]	Nacelle (engine) mass moment of inertia about *z*-axis
J_{ZNCG}	[kg.m^2]	Nacelle (engine) mass moment of inertia about its CG *z*-axis
$J_{\varphi P}$	[kg.m^2]	Generalised mass moment of inertia of engine and propeller about elastic axis
$J_{\varphi W}$	[kg.m^2]	Generalised mass moment of inertia of wing about elastic axis
$J_{\varphi WP}$	[kg.m^2]	Total generalised mass moment of inertia of wing and engine and propeller about elastic axis
$J_{\Theta\varphi P}$	[kg.m^2]	Generalised cross mass moment of inertia of engine and propeller about pitch and elastic axes
$J_{\Theta P}$	[kg.m^2]	Generalised mass moment of inertia of engine and propeller about pitch axis
$J_{\Theta\Psi}$	[kg.m^2]	Generalised mass moment of inertia of propeller about rotation axis
$J_{\Psi\varphi}$	[kg.m^2]	Generalised mass moment of inertia of propeller about rotation axis
$J_{\Psi P}$	[kg.m^2]	Generalised mass moment of inertia of engine and propeller about yaw axis
j		Imaginary unit
j_{Θ}	[kg.m^2]	Engine and propeller unit-length mass moment of inertia about pitch axis
j_{Ψ}	[kg.m^2]	Engine and propeller unit-length mass moment of inertia about yaw axis
$j_{\varphi W}$	[kg.m^2]	Wing unit-length mass moment of inertia about elastic axis
$[K]$		Structural stiffness matrix
$[K]$		Stiffness matrix (general symbol)
$[K^A]$		Aerodynamic stiffness matrix
$[K_b]$		Matrix of structural stiffness coefficients for system with gimbaled propeller
$[K_b^A]$		Matrix of aerodynamic stiffness coefficients for system with gimbaled propeller
$[K_{hh}]$		Modal stiffness matrix
K_{b11}^A		Term of matrix of aerodynamic stiffness coefficients for system with gimbaled propeller
K_{b12}^A		Term of matrix of aerodynamic stiffness coefficients for system with gimbaled propeller

K^{A}_{b13}		Term of matrix of aerodynamic stiffness coefficients for system with gimbaled propeller
K^{A}_{b14}		Term of matrix of aerodynamic stiffness coefficients for system with gimbaled propeller
K^{A}_{b21}		Term of matrix of aerodynamic stiffness coefficients for system with gimbaled propeller
K^{A}_{b22}		Term of matrix of aerodynamic stiffness coefficients for system with gimbaled propeller
K^{A}_{b23}		Term of matrix of aerodynamic stiffness coefficients for system with gimbaled propeller
K^{A}_{b24}		Term of matrix of aerodynamic stiffness coefficients for system with gimbaled propeller
K^{A}_{b31}		Term of matrix of aerodynamic stiffness coefficients for system with gimbaled propeller
K^{A}_{b32}		Term of matrix of aerodynamic stiffness coefficients for system with gimbaled propeller
K^{A}_{b33}		Term of matrix of aerodynamic stiffness coefficients for system with gimbaled propeller
K^{A}_{b34}		Term of matrix of aerodynamic stiffness coefficients for system with gimbaled propeller
K^{A}_{b41}		Term of matrix of aerodynamic stiffness coefficients for system with gimbaled propeller
K^{A}_{b42}		Term of matrix of aerodynamic stiffness coefficients for system with gimbaled propeller
K^{A}_{b43}		Term of matrix of aerodynamic stiffness coefficients for system with gimbaled propeller
K^{A}_{b44}		Term of matrix of aerodynamic stiffness coefficients for system with gimbaled propeller
K_{Θ}	[Nm.rad^{-1}]	Rotational stiffness of engine attachment in pitch
K_{Ψ}	[Nm.rad^{-1}]	Rotational stiffness of engine attachment in yaw
K_{φ}	[Nm.rad^{-1}]	Rotational stiffness for wing torsion
K_{b}	[N.m^{-1}]	Stiffness for wing bending
K_{β}	[Nm.rad^{-1}]	Effective rotational stiffness constant of propeller flapping
$K_{\beta 1}$	[Nm.rad^{-1}]	Rotational stiffness constant of single blade flapping
$K_{\beta eq}$	[Nm.rad^{-1}]	Equivalent rotational stiffness constant of propeller flapping for gimbaled propeller

$K_{\varphi H}$	[Nm.rad^{-1}]	Rotational stiffness of engine attachment in yaw (used for optimisation)
$K_{\varphi V}$	[Nm.rad^{-1}]	Rotational stiffness of engine attachment in pitch (used for optimisation)
K_{PL}	[N.m^{-1}]	Tiltrotor blade pitch-flap link eqquivalent stiffness
K_{RMS}	[Nm.rad^{-1}]	Root mean square value of rotational stiffness of engine attachment
k	[1]	Reduced frequency ($\omega c/2V_\infty$)
k_1	[1]	Reduced frequency for first term
k_2	[1]	Reduced frequency for second term
k_r	[1]	Wing reference reduced frequency ($\omega b_r/V_\infty$)
k_{rFL}	[1]	Wing reference reduced frequency for neutral stability (flutter) state
k_Θ	[1]	Propeller reduced frequency ($\omega_\Theta R/V_\infty$)
L	[m]	Wingspan (half wing)
L	[N]	Propeller blade section lift force
L	[N]	Tiltrotor blade cross-sectional lift force
L_1	[N]	Propeller blade no. 1 section lift force
L_2	[N]	Propeller blade no. 2 section lift force
L_3	[N]	Propeller blade no. 3 section lift force
L_4	[N]	Propeller blade no. 4 section lift force
L'_1	[N]	Propeller blade no. 1 section lift force including lift lag effect
L'_3	[N]	Propeller blade no. 3 section lift force including lift lag effect
ΔL_y	[N]	Propeller section lateral force (4 blades summ)
ΔL_z	[N]	Propeller section vertical force (4 blades summ)
$\Delta L'_y$	[N]	Propeller section lateral force (4 blades summ) including lift lag effect
$\Delta L'_z$	[N]	Propeller section vertical force (4 blades summ) including lift lag effect
l	[m]	Coordinate in direction $\bar{V}_0$
l_Θ	[m]	Distance from wing midchord to engine pitch gimbal axis (+ direction rearward)
l_Ψ	[m]	Distance from wing midchord to engine yaw gimbal axis (+ direction rearward)
$\bar{l}$	[1]	Dimensionless coordinate
$[M]$		Mass matrix (general symbol)
$[M_{hh}]$		Modal mass matrix

M	[1]	Mach number
M	[Nm]	Moment for flexible propeller support
M_{φ}	[Nm]	Oscillatory wing aerodynamic moment around elastic axis
$M_{\varphi\varphi}$	[1]	Dimensionless generalised mass
$M_{h\varphi}$	[1]	Dimensionless generalised mass
M_{hh}	[1]	Dimensionless generalised mass
$M_{\Theta\varphi}$	[1]	Dimensionless generalised mass
$M_{\Theta h}$	[1]	Dimensionless generalised mass
$M_{\Theta\Psi}$	[1]	Dimensionless generalised mass
$M_{\Psi\varphi}$	[1]	Dimensionless generalised mass
$M_{\Psi\Psi}$	[1]	Dimensionless generalised mass
M_P	[kg]	Engine and propeller generalised mass
M_W	[kg]	Wing generalised mass
M_{WP}	[kg]	Total wing and engine and propeller generalised mass
M_Y	[Nm]	Aerodynamic moment around lateral axis (y-axis)
$M_{Y,P}$; M_{YP}	[Nm]	Aerodynamic moment around lateral axis (y-axis) – in propeller disc plane
M_Z	[Nm]	Aerodynamic moment around vertical axis (z-axis)
$M_{Z,P}$; M_{ZP}	[Nm]	Aerodynamic moment around vertical axis (z-axis) – in propeller disc plane
ΔM_y	[N]	Propeller section moment around lateral axis (4 blades summ)
ΔM_z	[N]	Propeller section moment around vertical axis (4 blades summ)
M_D	[1]	Design maximum Mach number
M_{gyro}	[Nm]	Gyroscopic moment
M_H	[N.m]	Tiltrotor blade hinge moment
M_k	[Nm]	Torque
M_r	[1]	Propeller blade local section resultant Mach number
M_R		Rigid propeller aerodynamics dynamically amplified and phase shifted due to dynamic response of the first flap bending mode and aerodynamic forces time delayed
M_{z0}	[Nm]	Pitch moment for $Y = 0$
$M_{\beta 1}$		Auxiliary aerodynamic term for flapping blades model

$M_{\beta 2}$		Auxiliary aerodynamic term for flapping blades model
$M_{\beta 3}$		Auxiliary aerodynamic term for flapping blades model
m_b	[kg.m^{-1}]	Propeller (rotor) blade unit-length mass
m_b	[kg.m^{-1}]	Tiltrotor blade unit-length mass
m_n	[kg.m^{-1}]	Nacelle unit-length mass
$m_{N\Theta}$	[kg]	Nacelle (engine) mass effective in pitch
$m_{N\Psi}$	[kg]	Nacelle (engine) mass effective in yaw
m_W	[kg.m^{-1}]	Wing unit-length mass, mass sectional distribution
m_P	[kg.m^{-1}]	Engine and propeller unit-length mass, mass distribution
m_{PROP}	[kg]	Propeller total mass
m_{HUB}	[kg]	Propeller hub mass
m_{FUEL}	[%]	Relative fuel loading
m_{fuel}	[kg]	Fuel loading
N	[Nm]	Moment for flexible propeller support
N_{11}	[1]	Wing dimensionless aerodynamic integral
N_{12}	[1]	Wing dimensionless aerodynamic integral
N_{13}	[1]	Wing dimensionless aerodynamic integral
N_{14}	[1]	Wing dimensionless aerodynamic integral
N_{17}	[1]	Wing dimensionless aerodynamic integral
N_2	[1]	Wing dimensionless aerodynamic integral
N_{21}	[1]	Wing dimensionless aerodynamic integral
N_{22}	[1]	Wing dimensionless aerodynamic integral
N_{23}	[1]	Wing dimensionless aerodynamic integral
N_{24}	[1]	Wing dimensionless aerodynamic integral
N_3	[1]	Wing dimensionless aerodynamic integral
N_b	[1]	Propeller number of blades
N_{gyro}	[Nm]	Gyroscopic moment
N_r	[1]	Engine rotor/propeller gear ratio
$N_{\beta 1}$		Auxiliary aerodynamic term for flapping blades model
$N_{\beta 2}$		Auxiliary aerodynamic term for flapping blades model
$N_{\beta 3}$		Auxiliary aerodynamic term for flapping blades model
$N_{\beta 4}$		Auxiliary aerodynamic term for flapping blades model

$N_{\beta 5}$		Auxiliary aerodynamic term for flapping blades model
$N_{\beta 6}$		Auxiliary aerodynamic term for flapping blades model
$N_{\beta 7}$		Auxiliary aerodynamic term for flapping blades model
$N_{\beta 8}$		Auxiliary aerodynamic term for flapping blades model
$\bar{n}$		Unit vector normal to reference surface at time t
$\bar{n}_0$		Unit vector normal to reference surface at time τ
$\{P_k\}$		Vector of aerodynamic forces
$[P_1]$		Partitioning matrix to select propeller hub vertical and lateral degrees of freedom
$[P_2]$		Partitioning matrix to null matrix of downwash factors on interference elements from interference elements
P_h	[N]	Oscillatory wing aerodynamic force in vertical direction (z-axis) – lift (+ direction down)
P_i		Generalised inertia force in ith generalised coordinate
P_Y	[N]	Propeller aerodynamic force in lateral direction (y-axis) at propeller disc plane
P_Z	[N]	Propeller aerodynamic force in vertical direction (z-axis) at propeller disc plane
P_x^I	[N]	Tiltrotor blade distributed inertia force x-component
P_y^I	[N]	Tiltrotor blade distributed inertia force y-component
P_z^I	[N]	Tiltrotor blade distributed inertia force z-component
$P_{\beta\Theta}$		Generalised inertia force in β_Θ generalised coordinate
$P_{\beta\Psi}$		Generalised inertia force in β_Ψ generalised coordinate
P_Θ		Generalised inertia force in Θ generalised coordinate
P_Ψ		Generalised inertia force in Ψ generalised coordinate

p_I	[N.m^{-1}]	Tiltrotor blade distributed unit-length force
p_j		*j*th design property (optimisation)
Δp		Pressure differential across blade surface
$\{Q\}$		Vector of generalised coordinates
$\{Q_0\}$		Eigenvector (general symbol)
$[Q_{hh}^{Im}]$		Imaginary part of complex aerodynamic matrix
$[Q_{hh}^{Re}]$		Real part of complex aerodynamic matrix
$[Q_{jh}]$		Generalised force matrix for motion
Q_q	[N]	Generalised aerodynamic force
Q_Θ	[N]	Generalised aerodynamic force in propeller pitch mode
Q_Ψ	[N]	Generalised aerodynamic force in propeller yaw mode
Q_h	[N]	Generalised aerodynamic force in wing bending mode
Q_φ	[N]	Generalised aerodynamic force in wing torsion mode
$Q_{\Theta P}$	[N]	Generalised propeller aerodynamic force in propeller pitch mode
$Q_{\Psi P}$	[N]	Generalised propeller aerodynamic force in propeller yaw mode
$Q_{\varphi W}$	[N]	Generalised wing aerodynamic force in wing torsion mode
Q_{hW}	[N]	Generalised wing aerodynamic force in wing bending mode
$Q_{\varphi P}$	[N]	Generalised propeller aerodynamic force in wing torsion mode
Q_{hP}	[N]	Generalised propeller aerodynamic force in wing bending mode
$Q_{\Psi\Theta P}$	[1]	Dimensionless generalised propeller aerodynamic force
$Q_{\Psi\varphi P}$	[1]	Dimensionless generalised propeller aerodynamic force
$Q_{\Psi h P}$	[1]	Dimensionless generalised propeller aerodynamic force
$Q_{\Psi\Psi P}$	[1]	Dimensionless generalised propeller aerodynamic force
$Q_{\Theta\Theta P}$	[1]	Dimensionless generalised propeller aerodynamic force

$Q_{\varphi\Theta P}$	[1]	Dimensionless generalised propeller aerodynamic force
$Q_{\Theta\varphi P}$	[1]	Dimensionless generalised propeller aerodynamic force
$Q_{\varphi\varphi P}$	[1]	Dimensionless generalised propeller aerodynamic force
$Q_{\varphi\varphi W}$	[1]	Dimensionless generalised propeller aerodynamic force
$Q_{\Theta h P}$	[1]	Dimensionless generalised propeller aerodynamic force
$Q_{\varphi h P}$	[1]	Dimensionless generalised propeller aerodynamic force
$Q_{\varphi h W}$	[1]	Dimensionless generalised propeller aerodynamic force
$Q_{\Theta\Psi P}$	[1]	Dimensionless generalised propeller aerodynamic force
$Q_{\varphi\Psi P}$	[1]	Dimensionless generalised propeller aerodynamic force
$Q_{h\Theta P}$	[1]	Dimensionless generalised propeller aerodynamic force
$Q_{h\varphi P}$	[1]	Dimensionless generalised propeller aerodynamic force
$Q_{h\varphi W}$	[1]	Dimensionless generalised propeller aerodynamic force
Q_{hhP}	[1]	Dimensionless generalised propeller aerodynamic force
Q_{hhW}	[1]	Dimensionless generalised propeller aerodynamic force
$Q_{h\Psi P}$	[1]	Dimensionless generalised propeller aerodynamic force
Q_x^I	[N.m]	Tiltrotor blade distributed inertia moment x-component
Q_y^I	[N.m]	Tiltrotor blade distributed inertia moment y-component
Q_z^I	[N.m]	Tiltrotor blade distributed inertia moment z-component
q_i; q		Generalised coordinate
q_Θ		Generalised coordinate of engine pitching mode
q_Ψ		Generalised coordinate of engine yawing mode

q_{φ}		Generalised coordinate of wing torsion mode
q_{h}		Generalised coordinate of wing bending mode
q	[Pa]	Dynamic pressure ($\rho V^2/2$) – general symbol
$\bar{q}_i$		Complex amplitude of generalised coordinate
$\bar{q}_{\Theta}$		Complex amplitude of generalised coordinate of engine pitching mode
$\bar{q}_{\Psi}$		Complex amplitude of generalised coordinate of engine yawing mode
$\bar{q}_{h}$		Complex amplitude of generalised coordinate of wing bending mode
$\bar{q}_{\varphi}$		Complex amplitude of generalised coordinate of wing torsion mode
q_{∞}	[Pa]	Flow dynamic pressure ($\rho V_{\infty}^2/2$)
q_{D}		Doublet strength
q_{D0}		Doublet strength amplitude
q_{DIV}	[Pa]	Divergence dynamic pressure ($\rho V^2_{DIV}/2$)
q_{I}	[N]	Tiltrotor blade distributed unit-length moment
R	[m]	Propeller radius
Re		Real part
R_j		Boundary value of *j*th design response (optimisation)
$R_{\beta 0}$		Auxiliary aerodynamic integral for flapping blades model
$R_{\beta 1}$		Auxiliary aerodynamic integral for flapping blades model
$R_{\beta 10}$		Auxiliary aerodynamic integral for flapping blades model
$R_{\beta 11}$		Auxiliary aerodynamic integral for flapping blades model
$R_{\beta 12}$		Auxiliary aerodynamic integral for flapping blades model
$R_{\beta 2}$		Auxiliary aerodynamic integral for flapping blades model
$R_{\beta 3}$		Auxiliary aerodynamic integral for flapping blades model
$R_{\beta 4}$		Auxiliary aerodynamic integral for flapping blades model
r	[m]	Radius; propeller blade local radius
$\vec{r}$	[m]	Distance from coordinates origin to blade mass element

$\bar{r}$	[1]	Blade dimensionless radius
r_0	[m]	Doublet position radius
r_d		Dependent design response (optimisation)
r_e	[m]	Propeller blade flapping hinge radius
r_j		jth design response (optimisation)
r_s	[m]	Tiltrotor blade sweep starting local radius
$[S_{kj}]$		Aerodynamic integration matrix
$[S_\beta]$		Matrix of coefficients for system with flapping blades
S_b	[kg.m]	Gimbaled propeller mass static moment
S_p	[m^2]	Propeller disc cross-section area
S_s	[m^2]	Propeller slipstream cross-section area
$S_x^{(n)}$	[N]	Tiltrotor nth blade root force in x-direction
$S_y^{(n)}$	[N]	Tiltrotor nth blade root force in y-direction
$S_z^{(n)}$	[N]	Tiltrotor nth blade root force in z-direction
S_β		Objective number base vector corrected for β_R
$S_{\varphi P}$	[kg.m]	Generalised mass static moment about elastic axis
$S_{\Theta P}$	[kg.m]	Engine and propeller generalised mass static moment about pitch axis
$S_{\varphi W}$	[kg.m]	Wing generalised mass static moment about elastic axis
$S_{\varphi WP}$	[kg.m]	Total wing and engine and propeller generalised mass static moment about elastic axis
$S_{\beta\Theta}$		Generalised elastic force in β_Θ generalised coordinate
$S_{\beta\Psi}$		Generalised elastic force in β_Ψ generalised coordinate
S_Θ		Generalised elastic force in Θ generalised coordinate
S_Ψ		Generalised elastic force in Ψ generalised coordinate
$(\dot{s})$	[m.s^{-1}]	Perturbation velocity in the propeller plane
s	[m]	Nacelle local coordinate
s		Laplace operator
s_D		Distance from source point at time τ to field point at time t
$s_{\varphi W}$	[kg.m]	Wing unit-length mass static moment about elastic axis

s_{Θ}	[kg.m]	Engine and propeller unit-length mass static moment about pitch axis
$[T_{\beta}]$		Transformation matrix for *n*th blade flapping angle
$[T_{\Theta}]$		Transformation matrix for pitch angle
$[T_{\Phi}]$		Transformation matrix for *n*th blade azimuth angle
$[T_{\psi}]$		Transformation matrix for yaw angle
T	[N]	Propeller thrust
T_n	[N]	Propeller blade local section thrust force
ΔT	[N]	Tangential component force
$(\bar{t} - \bar{\tau})$	[1]	Dimensionless time
t	[s]	Time
U	[m.s^{-1}]	Propeller blade local section resultant velocity
U_B	[N]	Tiltrotor blade cross-sectional in-plane free stream velocity
U_N	[m.s^{-1}]	Tiltrotor blade cross-sectional normal free stream velocity
U_P	[m.s^{-1}]	Propeller blade local section perpendicular velocity component
U_T	[m.s^{-1}]	Propeller blade local section tangential velocity component
U_{eff}	[m.s^{-1}]	Propeller blade local section effective resultant velocity
$\vec{U}$	[m.s^{-1}]	Tiltrotor blade cross-sectional free stream velocity
U_y	[N]	Tiltrotor blade cross-sectional free stream velocity *y*-component
U_z	[N]	Tiltrotor blade cross-sectional free stream velocity *z*-component
u_{φ}		Vibration mode shape of wing torsional mode
$u_{\varphi P}$		Vibration mode shape of wing torsional mode at propeller station
u_B		Vibration mode shape of blade
u_{B1}		Tiltrotor wing mode shape – 1st vertical bending
u_{B2}		Tiltrotor wing mode shape – 2nd vertical bending
u_{C1}		Tiltrotor wing mode shape – 1st in-plane bending

u_{C2}		Tiltrotor wing mode shape – 2nd in-plane bending
u_{E1}		Tiltrotor wing mode shape – 1st extension
u_{T1}		Tiltrotor wing mode shape – 1st torsion
u_b		Vibration mode shape of wing bending mode
u_{bP}		Vibration mode shape of wing bending mode at propeller station
u_{Θ}		Vibration mode shape of engine pitching mode
u_{Ψ}		Vibration mode shape of engine yawing mode
$\vec{V}_s$		Velocity vector in inertia coordinates
V_{∞}	[m.s^{-1}]	Air velocity, flight speed
V_{cert}	[m.s^{-1}]	Certification speed according regulation
V_D	[m.s^{-1}]	Design maximum speed
V_{DEAS}	[m.s^{-1}]	Design maximum speed – EAS
V_{DTAS}	[m.s^{-1}]	Design maximum speed – TAS
V_{DIV}	[m.s^{-1}]	Divergence speed
V_{FL}	[m.s^{-1}]	Flutter speed
$V_{FL(H=0)}$	[m.s^{-1}]	Flutter speed at altitude of $H = 0$
V_{FLH}	[m.s^{-1}]	Flutter speed at altitude of H
V_{HTAS}	[m.s^{-1}]	TAS speed at altitude of H
V_{REV}	[m.s^{-1}]	Reversal speed
V_s	[m.s^{-1}]	Propeller slipstream velocity
V_{TAS}	[m.s^{-1}]	Flight speed – TAS
v	[m.s^{-1}]	Velocity (general symbol)
$[W_{kk}]$		Diagonal matrix of correction factors for propeller slipstream
W_{kk}		Correction factor for propeller slipstream
w	[m.s^{-1}]	Downwash velocity normal to reference surface
w_1	[m.s^{-1}]	Downwash in vertical plane induced by aerodynamic forces
w_2	[m.s^{-1}]	Downwash in horizontal plane induced by aerodynamic forces
$(\dot{w})$	[m.s^{-1}]	Perturbation velocity out of the propeller plane
w_s	[m]	Propeller slipstream diameter
X		Deflected x-axis of propeller rotation
X		Space-fixed x-axis with origin at nacelle pitch and yaw hinge

$\vec{X}_s$		Position vector of point of *n*th blade in inertia coordinates
X_0	[m]	Engine support deflection – initial condition
X_e	[m]	Engine support deflection – elastic deformation
X_b		Blade-fixed *x*-axis (both rotating and flapping blade) with origin at blade flapping hinge (point O_b)
X_{gn}		Nacelle-fixed *x*-axis with origin at nacelle pitch and yaw hinge
X_h		Blade-fixed *x*-axis (rotating but not flapping blade) with origin at propeller disc center (point O_C)
$\tilde{x}$	[–]	Intermediate axis
$\vec{x}$		Vector of design variables (optimisation)
x	[m]	Undeflected *x*-axis, *x*-direction distance
x	[m]	Field point *x*-coordinate
$\bar{x}$	[1]	Dimensionless *x*-distance
$\vec{x}^0$		Vector of design variables – zero design cycle (optimisation)
x_ξ		Tiltrotor blade lead-lag inertial system *x*-axis
x_0	[m]	Source point x-coordinate
x_i^0		*i*th design variable – zero design cycle (optimisation)
x_C	[m]	*x*-coordinate of propeller disc centre (point O_C) in nacelle-fixed coordinate system (gn)
x_d		Dependent design variable (optimisation)
x_e	[m]	*x*-coordinate of blade flapping hinge (point O_b) in blade-fixed coordinate system (*h*)
x_E		Tiltrotor blade cross-section system offset
x_F		Tiltrotor fuselage inertial system *x*-axis
x_H		Tiltrotor hub inertial system *x*-axis
x_i		*i*th design variable (optimisation)
x_i^l		Inner bound of *i*th design variable (optimisation)
x_m	[m]	Tiltrotor blade tip-mass offset
x_N		Tiltrotor nacelle inertial system *x*-axis
x_P		Tiltrotor blade outboard inertial system *x*-axis
x_i^U		Upper bound of *i*th design variable (optimisation)

x_W		Tiltrotor wing-tip inertial system *x*-axis
x_β		Tiltrotor blade flapping inertial system *x*-axis
x_Θ		Tiltrotor blade pitch inertial system x-axis
Y	[N]	Lift force
Y		Deflected *y*-axis
Y		Space-fixed *y*-axis with origin at nacelle pitch and yaw hinge
Y_b		Blade-fixed *y*-axis (both rotating and flapping blade) with origin at blade flapping hinge (point O_b)
Y_e	[m]	Engine support deflection – elastic deformation
Y_0	[m]	Engine support deflection – initial condition
Y_{gn}		Nacelle-fixed *y*-axis with origin at nacelle pitch and yaw hinge
Y_h		Blade-fixed *y*-axis (rotating but not flapping blade) with origin at propeller disc center (point O_C)
ΔY_φ	[N]	Force due to twisting deformation
ΔY_δ	[N]	Force due to aileron deflection
y	[m]	Undeflected *y*-axis, *y*-direction distance
y	[m]	Field point *y*-coordinate
y_0	[m]	Source point *y*-coordinate
y_1	[m]	*y*-direction distance of propeller hub arbitrary position
y_B		Tiltrotor blade cross-section system *y*-axis
y_C	[m]	*y*-coordinate of propeller disc center (point O_C) in nacelle-fixed coordinate system (*gn*)
y_{CG}	[m]	*y*-coordinate of tiltrotor blade cross-section center of gravity
y_e	[m]	*y*-coordinate of blade flapping hinge (point O_b) in blade-fixed coordinate system (*h*)
y_ζ		Tiltrotor blade lead-lag inertial system *y*-axis
y_Θ		Tiltrotor blade pitch inertial system *y*-axis
y_β		Tiltrotor blade flapping inertial system *y*-axis
y_F		Tiltrotor fuselage inertial system *y*-axis
y_H		Tiltrotor hub inertial system *y*-axis
y_N		Tiltrotor nacelle inertial system *y*-axis
y_P		Tiltrotor blade outboard inertial system*y*-axis
y_P	[m]	Lateral displacement of engine – propeller mass element (+ direction right)

y_W		Tiltrotor wing-tip inertial system *y*-axis
Z		Deflected *z*-axis
Z		Space-fixed *z*-axis with origin at nacelle pitch and yaw hinge
Z_b		Blade-fixed *z*-axis (both rotating and flapping blade) with origin at blade flapping hinge (point O_b)
Z_{gn}		Nacelle-fixed *z*-axis with origin at nacelle pitch and yaw hinge
Z_h		Blade-fixed *z*-axis (rotating but not flapping blade) with origin at propeller disc center (point O_C)
z	[m]	Undeflected *z*-axis, *z*-direction distance
z	[m]	Field point *z*-coordinate
z_ζ		Tiltrotor blade lead-lag inertial system *z*-axis
z_0	[m]	Source point *z*-coordinate
z_1	[m]	*z*-direction distance of propeller hub arbitrary position
z_B		Tiltrotor blade cross-section system *z*-axis
z_C	[m]	*z*-coordinate of propeller disc centre (point O_C) in nacelle-fixed coordinate system (*gn*)
z_{CG}	[m]	*z*-coordinate of tiltrotor blade cross-section centre of gravity
z_e	[m]	*z*-coordinate of blade flapping hinge (point O_b) in blade-fixed coordinate system (*h*)
z_F		Tiltrotor fuselage inertial system *z*-axis
z_H		Tiltrotor hub inertial system *z*-axis
z_N		Tiltrotor nacelle inertial system *z*-axis
z_P		Tiltrotor blade outboard inertial system *z*-axis
z_P	[m]	Vertical displacement of engine – propeller mass element (+ direction down)
z_p	[m]	Width of wing band behind propeller
z_W		Tiltrotor wing-tip inertial system *z*-axis
z_W	[m]	*y*-displacement of wing mass element (+ direction down)
z_β		Tiltrotor blade flapping inertial system *z*-axis
z_Θ		Tiltrotor blade pitch inertial system *z*-axis
(-)		Amplitude
(˙); (*d*/*dt*)		Time derivative
AC		Aerodynamic Centre

CFD	Computational Fluid Dynamics
CG	Centre of Gravity
DMAP	Direct Matrix Abstraction program
DOF	Degree of Freedom
EA	Elastic Axis
EAS	Equivalent Air Speed
EASA	European Aviation Safety Agency
EC	Elastic Centre
FAA	Federal Aviation Administration
FFT	Flight Flutter Test
ISA	International Standard Atmosphere
MAC	Modal Assurance Criterion
MIMO	Multi Input Multi Output
NTSB	National Transportation Safety Board
OBJ	Objective Function
ON	Objective Number
RANS	Reynolds Averaged Navier-Stokes
SISO	Single Input Single Output
TAS	True Air Speed
TFR	Target Frequency Ratio
TsAGI	Central Aero-hydrodynamic Institute in Zhukovski, Russia
URANS	Unsteady Reynolds Averaged Navier-Stokes
VZLU	Aeronautical Research and Test Institute in Prague, Czech Republic

This page intentionally left blank

Chronological bibliography

1913 Clark, T.W.K.: Effect of Side Wind on a Propeller, R.&M. No.80, British A.C.A., 1913.

1914 Bramwell, F.H., Relf, E.F. and Bryant, L.W.: Experiments on Model Propellers at the National Physical Laboratory. (ii) Experiments to Determine the Lateral Force on a Propeller in a Side Wind, R.&M. No.123, British A.C.A., 1914.

1918 Harris, R.G.: Forces on a Propeller Due to Sideslip, R.&M. No.427, British A.C.A., 1918.

1919 Glauert, H.: The Stability Derivatives of an Airscrew, R.&M. No.642, British A.C.A., 1919.

1926 Durand, W.F. and Lesley E.P.: Comparison of Tests on Air Propellers in Flight with Wind Tunnel Model Tests on Similar Forms, NACA Technical Report No.220, 1926.

1928 Pistolesi, E.: Nuove considerazioni sul problema dell'elica in un vento laterate, *L'Aerotecnica*, Vol.7, No.3, March 1928.

1929 Lesley, E.P. and Reid, E.G.: Tests of Five Metal Model Propellers with Various Pitch Distributions in a Free Wind Stream and in Combination with a Model VE-7 Fuselage, NACA Technical Report No.326, 1929.

1930 Flachsbart, O. and Kröber, G.: Experimental Investigation of Aircraft Propellers Exposed to Oblique Air Currents, NACA, TM No.562, 1931.

1931 Freeman, H.B.: The Effect of Small Angles of Yaw and Pitch on the Characteristics of Airplane Propellers, NACA Technical Report No.389, 1931.

Ower, E. and Hutton, C.T.: On the Interference of a Streamline Nacelle on a Monoplane Wing, R.&M. No.1395, British A.R.C., 1931.

1933 Misztal, F.: The Problem of the Propeller in Yaw with Special Reference to Airplane Stability, NACA, TM No.696, 1933.

1935 Glauert, H.: 'Airplane propellers. Miscellaneous airscrew problems', in W.F. Durand (ed). *Aerodynamic Theory*, Vol. IV, Springer–Verlag, 1935.

Theodorsen, T.: General Theory of Aerodynamic Instability and the Mechanism of Flutter, NACA Report 496, 1935.

1936 Lesley, E.P., Worley, G.F. and Moy, S.: Air Propellers in Yaw, Report No.597, Daniel Guggenheim Aeronautical Laboratory, Stanford University, CA, USA, 1936.

Milikan, C.B., Russell, J.S. and McCoy, H.M.: Wind tunnel tests on a high wing monoplane with running propeller, Parts 1 and 2, *Journal of Aerospace Sciences*, Vol.3, No.3, pp. 73–85, January 1936.

Robinson, R.G. and Herrenstein, W.H., Jr.: Wing–Nacelle–Propeller Interference for Wings of Various Spans Force and Pressure Distribution Tests, Report No.569, NACA, Langley Field, VA, USA, 1936.

1937 Lesley, E.P., Worley, G.F. and Moy, S.: Air Propellers in Yaw, NACA Report No.597, 1937.

1938 Klingermann, G. and Weinig, F.: Die Kräfte und Momente der Luftschraube bei Schräganblasung und Flugyeugdrehung, *Luftfahrtforschung*, Vol.15, No.4, pp. 206–213, April 1938.

Taylor, E.S. and Browne, K.A.: Vibration isolation of aircraft power plants, *Journal of Aerospace Sciences*, Vol.6, No.2, pp. 43–49, December 1938.

1939 Biermann, D. and Hartman, E.P.: Test of Two Full-Scale Propellers with Different Pitch Distributiona at Blade Angles up to 60°, NACA Report No.658, 1939.

1941 Goett, H.J. and Pass, H.R.: Effect of Propeller Operation on the Pitching Moments of Single-engine Monoplane, NACA ACR, May 1941.

1942 Rumph, L.B., White, R.J. and Grummann, H.R.: Propeller forces due to yaw and their effect on airplane stability, *Journal of Aerospace Sciences*, Vol.9, No.2, pp. 465–470, October 1942.

Runckel, J.F.: The Effect of Pitch on Force and Moment Characteristics of Full-Scale Propellers of Five Solidities, NACA ARR, June 1942.

Smilg, B. and Wasserman, L.S.: Application of Three-Dimensional Flutter Theory to Aircraft Structures, Army Air Force Technical Report No.4798, 1942.

1943 Ribner, H.S.: Formulas for Propellers in Yaw and Charts of the Side–Force Derivatives, NACA Report 819, 1943.

Ribner, H.S.: Proposal for a Propeller Side Force Factor, NACA, RB No.3L02, 1943.

Weiss, H.K.: Dynamics of constant–speed propellers, *Journal of Aerospace Sciences*, Vol.10, No.2, p. 58, February 1943.

1945 Ribner, H.S.: Propellers in Yaw, NACA Report 820, 1945.

1950 Scanlan, R.H. and Truman, J.C.: The gyroscopic effect of a rigid rotating propeller on engine and wing vibration modes, *Journal of Aerospace Sciences*, Vol.17, No.10, pp. 653–659, 666, October 1950.

1954 McLemore, H.C. and Cannon, M.D.: Aerodynamic Investigation of a Four-Blade Propeller Operating Through an Angle-of-Attack Range From 0° to 180°, NACA, TIV 3228, 1954.

1957 Loewy, R.G.: A two-dimensional approximation to the unsteady aerodynamics of rotary wings, *Journal of Aeronautical Sciences*, Vol.24, No.2, pp. 81–92, February 1957.

Timman, R. and Van de Vooren, A.I.: Flutter of a helicopter rotor rotating in its own wake, *Journal of Aeronautical Sciences*, Vol.24, No.9, September 1957, pp. 694–702.

1958 Coleman, R.P. and Feingold, A.M. (with appendix B by G.W. Brooks): Theory of Self Excited Mechanical Oscillations of Helicopter Rotors With Hinged Blades, NACA Report 1351, 1958. (Supersedes NACA TN 3844).

Loewy, R.G. and Yntema, R.T.: Some aeroelastic problems of tilt-wing VTOL aircraft, *Journal of American Helicopter Society*, Vol.3, No.1, pp. 35–57, January 1958.

Shenhman, A.M.: Generalized Performance of Conventional Propellers for VTOL-STOL Aircraft, Hamilton Standard, Report No. HS-1829, March 1958.

Yates, E.C., Jr.: Calculation of Flutter Characteristics for Finite-Span Swept or Unswept Wings at Subsonic and Supersonic Speeds by a Modified Strip Analysis, NACA, RM L37L10, 1958.

1960 Yaggi, P.F. and Rogallo, V.L.: A Wind-Tunnel Investigation of Three Propellers Through an Angle-of-Attack Range from 0° to 85°, NASA, Technical Note, TN D-318, 1960.

1961 Brooks, G.W.: 'The Mechanical Instability and Forced Response of Rotors on Multiple-Degree-of-Freedom Supports', Ph.D. Thesis, Princeton University, 1961.

Quickley, H.C. and Koenig, D.G.: A Flight Study of the Dynamic Stability of a Tilting Rotor Convertiplane, NASA Technical Note, TN D-778, 1961.

Reed, W.H., and Bland, S.R.: An Analytical Treatment of Aircraft Propeller Precession Instability, NASA Langley, Technical Note, TN D-659, 1961.

1962 Galardo, V.C. and Flannelly, W.: Propeller Nacelle Whirl Flutter Analysis of K-16B Amphibious VTOL/STOL Aircraft, Kaman Aircraft Corporation, Report No.G-113-41, August 1962.

Gallardo, V., Jr.: Propeller-Nacelle Whirl Flutter Analysis of K-16B Amphibious VTOL/STOL Aircraft, Report No. G-113-41, Kaman Aircraft Corp., August 1962.

Houbolt, J.C. and Reed, W.H.: Propeller–nacelle whirl flutter, *Journal of Aerospace Sciences*, Vol.29, No.3, March 1962, pp. 333–346.

Richardson, J.R. and Naylor, H.F.W.: Whirl Flutter of Propellers With Hinged Blades, Report No.24, Engineering Research Associates, Toronto, Canada, March 1962.

Richardson, J.R., McKillop, J.A., Naylor, H.F.W. and Bandler, P.A.: Whirl Flutter of Propellers with Flexible Twisted Blades, Report No. 43, Engineering Research Associates, Toronto, Canada, 1962.

Sewall, J.L.: An Analytical Trend Study of Propeller Whirl Instability, NASA Langley, Technical Note, NASA TN D-996, 1962.

Zwaan, R. J. and Bergh, H.: Propeller–Nacelle Flutter of the Lockheed Electra Aircraft, Restricted Report, F.228, National Aero-Astronautical Research Institute (NLR), Amsterdam, February 1962.

1963 Abbott, F.T., Jr., Kelly, H.N. and Hampton, K.D.: Investigation of Propeller-Power Plant Autoprecession Boundaries for a Dynamic-Aeroelastic Model of a Four-Engine Turboprop Transport Airplane, NASA Technical Note, TN D-1806, August 1963.

Bennett, R.M., Kelly, H.N. and Gurley, J.R., Jr.: Investigation in the Langley Transonic Dynamics Tunnel of a 1/8–Size Aeroelastic–Dynamic Model of the Lockheed Electra Airplane with Modifications in the Wing–Nacelle Region, NASA TM SX-818, March 1963.

Bland, S.R. and Bennett, R.M.: Wind-Tunnel Measurement of Propeller Whirl-Flutter Speeds and Static-Stability Derivatives and Comparison with Theory, NASA TN D-1807, August 1963.

Dathe, H.M.: Ueber die Verteilung der induzierten Geschwindigkeiten in der Umlaufebene einer schrag angestromten Luft-schraube und ihren Einfluss auf die Luftkraftverteilungen und Blattbeanspruchungen, *Z. Flugwiss.*, Vol.11, No.5, pp. 177–192, 1963.

Head, A.L. and Smith, W.D.: Dynamic model testing of the XC-142A aircraft, *Proceeding of Symposium on Aeroelastic and Dynamic Modeling Technology, RTD-TDR-63-4197*, Part I, pp. 723–762, 1963.

Head, A.L., Jr.: A review of the structural dynamic characteristics of the XC-142A aircraft, *CAL / TRECOM Symposium Proceedings Vol II–Dynamic Load Problems Associated With Helicopters and V/STOL Aircraft*, June 1963.

Ravera, R.J.: Effects of Steady State Blade Angle of Attack on Propeller Whirl Flutter, Grumman Aircraft Engineering Corporation, Report No. ADR 06-01-63.1, July 1963.

Reed, W.H. and Bennett, R.M.: 'Propeller Whirl Flutter Considerations for V/STOL Aircraft,' CAL/TRECOM Symposium, Buffalo, NY, USA, 1963.

Serling, R.J.: *The Electra Story*, Garden City, NY, USA, 1963.

1964 Bennett, R.M. and Bland, S.R.: Experimental and Analytical Investigation of Propeller Whirl Flutter of a Power Plant on a Flexible Wing, NASA, Technical Note, TN D-2399, August 1964.

Fradenburgh, E.A. and Kiely, E.F.: Development of dynamic model rotor blades for high speed helicopter research, *Journal of American Helicopter Society*, Vol. 9, 1964, pp. 3–20.

Head, A.L., Jr. and Smith, W.D.: Dynamic Model Testing of the XC-142A Aircraft, Proceedings of Symposium on Aeroelastic & Dynamic Modeling Technology, RTD-TDR-63-4197, Pt. I, U.S. Air Force, March 1964, pp. 723–762.

Küssner, H.G. and Gollnitz, H.: Theorie und Methode der Flatterrechnung von Flugzeugen unter Benutzung des Standschwingungsversuchs, AVA FB 64–01, 1964.

1965 Baker, K.E., Smith, R. and Toulson, K.W.: Notes on propeller whirl flutter, *Canadian Aeronautical Space Journal*, Vol.11, No.8, October 1965, pp. 305–313.

De Young, J.: Propeller at high incidence, *Journal of Aircraft*, Vol.2, No.3, May–June 1965, pp. 241–249.

Emslie, B. and Kepert, J.L.: Whirl Flutter of an Engine–Propeller System, Dept. of Supply, Australian Defense Scientific Service, Aeronautical Research Laboratories, ARL / SM 304, 1965.

Reed, W.H.: 'Propeller-Rotor Whirl Flutter: A State-of-the-Art Review', Symposium on the Noise and Loading Actions on Helicopter V/STOL Aircraft and Ground Effect Machines, Southampton, UK, 30.9.1965.

1966 Hall, W.E., Jr.: Prop-rotor stability at high advance ratios, *Journal of American Helicopter Society*, Vol.11, No.2, April 1966, pp. 11–26.

Reed, W.H.: Propeller-rotor whirl flutter: a state-of-the-art review, *Journal of Sound and Vibrations*, Vol.4, No.3, November 1966, pp. 526–544

Smith, G.E.: Whirl of an Aircraft Power–Plant Installation and its Interaction with the Flutter Motion of a Flexible Wing, ARC R&M No.3536, 1966.

1967 Reed, W.H.: Review of Propeller–Rotor Whirl Flutter, NASA Technical Report, NASA TR R-264, 1967.

Reed, W.H.: Propeller–Rotor Whirl Flutter, *AGARD Manual of Aeroelasticity*, Part III, Chapter 9, 1967.

Richardson, J.R.: The Effect of Hinged or Flexible Blades on Propeller Whirl Flutter, Engineering Research Associates, Report No.43/2, Toronto, Canada, 1967.

Wernicke, K.G. and Gaffey, T.M.: 'Review and Discussion of the Influence of Blade Flapping Restraint on the Dynamic Stability of Low Disk Loading Propeller-Rotors,' 23rd American Helicopter Society Annual Forum, Washington, DC, May 1967.

Wernicke, K.G. and Gaffey, T.M.: Review and discussion of the influence of blade flapping restraint on the dynamic stability of low disk loading propeller-rotors, *Journal of the American Helicopter Society*, Vol.12, No.4, 1967, pp. 55–60.

Young, M.T. and Lytwyn, R.T.: 'The Influence of Blade Flapping Restraint on the Dynamic Stability of Low Disk Loading Propeller-Rotor', 23th Annual Forum of the American Helicopter Society, Washington, DC, USA, May 1967, pp. 38–54.

Young, M.T. and Lytwyn, R.T.: 'The influence of blade flapping restraint on the dynamic stability of low disk loading propeller-rotors, *Journal of American Helicopter Society*, Vol.12, October 1967, pp. 38–54.

1968 Edenborough, H.K.: Investigation of tilt-rotor VTOL aircraft rotor-pylon stability, *Journal of Aircraft*, Vol.5, No.6, March–April 1968, pp. 97–105.

Sissingh, G.J.: Dynamics of rotors operating at high advance ratios, *Journal of American Helicopter Society*, Vol.13, pp. 56–63, 1968.

1969 Brandt, D.E.: Aeroelastic problems of Flexible V/STOL Rotors, AGARD CP-46, Chapter 8, 1969.

Crimi, P.: A Method for Analyzing the Aeroelastic Stability of a Helicopter Rotor in Forward Flight, NASA CR-1332, 1969.

DeLarm, L.N.: Whirl flutter and divergence aspects of tilt-wing and tilt-rotor aircraft, *Proceedings of the V/STOL Technology and Planning Conference, Las Vegas, NV, USA*, September 1969.

Gaffey, T.M., Yen, J.G. and Kvaternik, R.G.: Analysis and model tests of the proprotor dynamics of a tilt-proprotor VTOL aircraft, *Proceedings of the V/STOL Technology and Planning Conference, Las Vegas, NV, USA*, 23–25 September 1969.

Gaffey, T.M.: The effect of positive pitch-flap coupling (negative δ_3) on rotor blade motion stability and flapping, *Journal of the American Helicopter Society*, Vol.14, No.2, April 1969.

Heinig, K.: Stabilitatschrechnung fur das Rotor–Gondel–Flugel–System von Kipprotorflugzeugen, MBB–Bericht DF 100, 1969.

Heinig, K.: Durch Luftkrafte bedingte Instabilitat des Rotor–Gondel–Flugsystems von Kipprotorflugzeugen, DLR Report, 69–08, 1969.

Krishna Rao, K.V. and Sundararajan, D.: Whirl Flutter of Flapping Blade Rotor Systems, NAL Technical Note, TN-18, National Aeronautical Laboratory, Bangalore, India, 1969.

Kuntz, W.H.,: Wasserman, L.S. and Alexander, H.R.: Dynamically similar model tests of rotary wing and propeller types of VTOL aircraft, *Proceedings of Air Force V/STOL Technology and Planning Conference, Las Vegas, NV, USA*, September 1969.

Loewy, R.G.: Review of Rotary–wing V/STOL dynamics and aeroelastic problems, *Journal of American Helicopter Society*, Vol.14, No.3, 1969, pp. 3–23.

Reed, W.H.: ‘Propeller Rotor Whirl Flutter, A State of the Art review’, Symposium on the Noise and Loading Actions on Helicopters, V/STOL and Ground Effect Machines, The University of Southampton, UK, August–September 1969.

Wernicke, K.G.: Tilt proprotor composite aircraft, design state of the art, *Journal of American Helicopter Society*, Vol.14, No.2, April 1969, pp. 10–25.

Williams, J.: Technical problems in the conception and utilisation of V/STOL transport aircraft, *Z. Flugwiss*, Vol.17, pp. 369–391, 1969.

1970 Detore, J.A. and Gaffey, T.M.: The stopped-rotor variant of the proprotor VTOL aircraft, *Journal of the American Helicopter Society*, Vol.15, No.3, July 1970.

Krause: Strukturuntersuchungen fur Propeller / Rotoren grossen Durchmessers, VFW M-26-70, Bd.2, 1970.

Magee, J.P. and Pruyn, R.R.: ‘Prediction of the Stability Derivatives of Large Flexible Prop / Rotors by a Simplified Analysis’, American Helicopter Society National Forum, 1970.

Piarulli, V.J. and White, R.P.: A Method for Determining the Characteristic Functions Associated with the Aeroelastic Instabilities of Helicopter Rotors in Forward Flight, NASA CR-1577, 1970.

1971 Gmelin, B.: Berechnung der Stabilitat des Systems Rotor–Rotormast, Teil I: Halbstarrer Rotor, IB 027-71/1, DFVLR, Institut fur Drechflugelflugzeuge, 1971.

Peters, D.A. and Hohenemser, K.H.: Application of the floquet transition matrix to problems of lifting rotor stability, *Journal of American Helicopter Society*, Vol.16, pp. 25–33, 1971.

Richardson, D.A.: The application of hingeless rotors to tilting prop / rotor aircraft, *Journal of American Helicopter Society*, July 1971, pp. 34–38.

Yen, J.G., Weber, G.E. and Gaffey, T.M.: A Study of Folding Proprotor VTOL Aircraft Dynamics, AFFDL-TR-71-7, Vol.1, September 1971.

1972 Albrecht, C.O.: ‘Factors in the Design and Fabrication of Powered Dynamically Similar V/STOL Wind Tunnel Models,’ American Helicopter Society Mid-East Region Symposium on the Status of Testing and Modeling Techniques for V/STOL Aircraft, Essington, PA, USA, 26–28 October 1972.

Baird, E.F., Bauer, E.M. and Kohn, J.S.: 'Model Tests and Analysis of Prop-Rotor Dynamics for Tilt-Rotor Aircraft', American Helicopter Society Mid-East Region Symposium on the Status of Testing and Modeling Techniques for V/STOL Aircraft, Essington, PA, USA, 26–28 October 1972.

Edenborough, H.K., Gaffey, T.M. and Weiberg, J.A.: 'Analyses and Tests Confirm Design of Proprotor Aircraft,' AIAA 4th Aircraft Design, Flight Test and Operations Meeting, Los Angeles, CA, USA, 7–9 August 1972.

Hohenemser, K.H. and Yin, S.K.: Some applications of the methods of multiblade coordinates, *Journal of American Helicopter Society*, Vol.17, No.3, pp. 3–12, 1972.

Johnston, R.A.: 'Parametric Studies of Instabilities Associated With Large, Flexible Rotor Propellers', Preprint No. 615, 28th Annual National Forum, American Helicopter Society, May 1972.

Marr, R.L. and Neal, G.T.: 'Assessment of Model Testing of a Tilt–Proprotor VTOL Aircraft', American Helicopter Society Mid-East Region Symposium on the Status of Testing and Modeling Techniques for V/STOL Aircraft, Essington, PA, USA, 26–28 October 1972.

Ormiston, R.A. and Hodges, D.H.: Linear flap-lag dynamics of hingeless helicopter rotor blades in hover, *Journal of the American Helicopter Society*, Vol.17, No.2, 1972.

Scheiman, J.: 'Analytical Investigation of the Tilt Rotor Whirl Instability', Ph.D. Thesis, Virginia Polytechnic Institute & State University, 1972.

1973 Alexander, H.R. and Leone, P.F.: V/STOL Dynamics and Aeroelastic Rotor-Airframe Technology. Volume I. State-of-the-Art Review of V/STOL Rotor Technology. AFFDL-TR-72-40, Volume I, U.S. Air Force, January 1973.

Donham, R.E. and Cardinale, S.V.: Flight Test and analytical Data for Dynamics and Loads in a Hingeless Rotor, Lockheed Report 26215, December 1973, U.S Army Av. Systems Command, St. Louis, MO, USA.

Hammond, C.E. and Pierce, G.A.: A Compressible Unsteady Aerodynamic Theory for Helicopter Rotors, AGARD CR-111, Aerodynamics of Rotary Wings, paper no.13, February 1973.

Helf, S., Broman, E., Gatchel, S. and Charles, B.: Full-scale Hover Test of a 25-foot Tilt Rotor, BHT Report 300-099-010, NASA CR 114626, May 1973.

Krishna Rao, K.V.: Effect of steady state coning angle and damping on whirl flutter stability, *Journal of Aircraft*, Vol.10, No.11, pp. 664–669, November 1973.

Kvaternik, R.G.: 'Studies in Tilt-Rotor VTOL Aircraft Aeroelasticity', Ph.D. Thesis, Case Western University, Cleveland, OH, USA, June 1973.

Magee, J.P., Alexander, H.R., Gillmore, K.B., Richardson, D.A. and Peck, W.B.: Wind Tunnel Tests of a Full Scale Hingeless Prop/Rotor Design for the Boeing Model 222 Tiltrotor Aircraft, Report No. D222-10059-1, Contract NAS2-6505, April, 1973.

Ormiston, R.A.: Helicopter modelling, *Aeronautical Journal*, November 1973, pp. 579–591.

Runyan, H.L.: 'Unsteady Lifting Surface Theory Applied to a Propeller and Helicopter Rotor', Ph.D. Thesis, Loughborough University of Technology.

1974 Alexander, H.R., Hengen, L.M. and Weiberg, J.A.: 'Aeroelastic-Stability Characteristics of a V/STOL Tilt-Rotor Aircraft with Hingeless Blades: Correlation of Analysis and Test', 30th Annual Forum of the American Helicopter Society, Washington, DC, USA, May 1974, pp. 12–22.

Forsching, H.W.: *Grundlagen der Aeroelastik*, published by Springer–Verlag, 1974, ISBN 0387065407, 9780387065403, also: *Osnovy Aerouprugosti* (in Russan), published by Mašinostroenie, Moscow, Russia, 1984.

Frick, J. and Johnson, W.: Optimal Control Theory Investigation of Proprotor / Wing Response to Vertical Gust, NASA-TM-X-62384, September 1974.

Hammond, C.E., Runyan, H.L. and Mason, J.P.: 'Application of Unsteady Lifting Surface Theory to Propellers in forward Flight', AIAA/ASME/SAE 15th Structures, Structural Dynamics and Materials Conference, AIAA Paper No.74–419, 1974.

Johnson, W.: Analytical Modeling for Tilting Proprotor Aircraft Dynamics Including Blade Torsion and Coupled Bending modes, and Conversion Mode Operation, NASA TM X-62, 369, 1974.

Johnson, W.: 'Theory and Comparison With Tests of Two Full-Scale Proprotors', AHS/NASA Ames Specialists' Meeting on Rotorcraft Dynamics, CA, USA, 13–15 February 1974, pp. 1–11.

Johnson, W.: Dynamics of Tilting Proprotor Aircraft in Cruise Flight, NASA Technical Note, TN D-7677, May 1974.

Kiessling, F.: Zur Problematik von Whirl-Flatteruntersuchungen von V/STOL-Flugzeugen, Forschungsbericht 74-11, German Aerospace Research Center (DLR), Institute of Aeroelasticity, Goettingen, Germany, 1974, also: Some Problems in Research on Whirl Flutter in V/STOL Aircraft, ESRO TT-160, 1975.

Kvaternik, R.G.: 'Experimental and Analytical Studies in Tilt-Rotor Aeroelasticity', AHS/NASA Ames Specialists' Meeting on Rotorcraft Dynamics, Moffet Field, CA, USA, 13–15 February 1974.

Sissingh G.J. and Donham R.E.: 'Hingeless Rotor Theory and Experiment on Vibration Reduction by Periodic Variation of Conventional Controls', American Helicopter Society / NASA Ames Specialists Meeting on Rotorcraft Dynamics, 13–15 February 1974.

1975 Johnson, W.: Analytical Modeling Requirements for Tilting Proprotor Aircraft Dynamics, NASA, Technical Note, TN D-8013, July 1975.

1976 Kvaternik, R.G.: A review of some tilt-rotor aeroelastic research at NASA Langley, *Journal of Aircraft*, Vol.13, No.5, pp. 357–363, May 1976.

1977 Johnson, W.: Optimal control alleviation of tilting proprotor gust response, *Journal of Aircraft*, Vol.14, No.3, March 1977, pp. 301–308.

Kvaternik, R.G. and Kohn, J.S.: An Experimental and Analytical Investigation of Proprotor Whirl Flutter, NASA, Technical Paper, TP 1047, December 1977.

Kvaternik, R.G.: Some Remarks on the Use of Scale Models, NASA, Langley Research Center, Hampton, Virginia 23681, NASA/TP-2006-212490/Vol2/PART2, Document ID: 20070008392.

1980 Chang, L.K.: 'The Theoretical Performance of High Efficiency Propellers', Ph.D. Thesis, Purdue University, December 1980.

Johnson, W.: A Comprehensive Analytical Model of Rotorcraft Aerodynamics and Dynamics. Part I: Analysis Development, NASA TM-81182, June 1980.

Johnson, W.: Comparison of Calculated and Measured Blade Loads on a Full–Scale Tilting Proprotor in a Wind Tunnel, NASA TM 81228, September 1980.

Komatsuzaki, T.: 'An Analytical Study of Tilt Proprotor Aircraft Dynamics in Airplane Cruise Configuration Including the Effects of Fuselage Longitudinal Rigid Body Motion', Ph.D. Thesis, Princeton University, January 1980.

Rizk, M.H.: Propeller slipstream/wing interaction in the transonic regime, *Journal of Aircraft*, Vol.18, No.3, 1980, pp. 184–191.

1981 Anderson, S.B.: Historical Overview of V/STOL Aircraft Technology, NASA TM 81280, March 1981.

Bilger, J.M, Marr, R.L. and Zahedi, A.: In-flight Structural Dynamic Characteristics of the XV-15 Tilt-rotor Research Aircraft, AIAA Paper 81-0612, 1981.

Farassat, F.: Linear acoustic formulas for calculation of rotating blade noise, *AIAA Journal*, Vol.119, No.9, September 1981.

1982 Costes, J.J., Nicolas, J. and Petot, D.: Etude de la stabilite d'une maquette de convertible (Stability study of a tilt–rotor aircraft model), *Research Aerospace*, No.1982-6, November–December 1982, pp. 413–440.

Kiessling, F.: Computer aided derivation of equations of motion for rotary–wing aeroelastic problems, *Proceedings of 13th Congress of the ICAS/AIAA Aircraft Systems and Technology Conference, Seattle, WA, USA*, 22–27 August 1982.

Kopřiva, Z. and Maleček, J.: *Aeroelasticita* (in Czech), Military Technical Academy, Brno, Czech Republic, 1982.

Runyan, H.L.: Noise from a vibrating propeller, *Journal of Aircraft*, Vol.19, pp. 419–24, 1982.

Schroers, L.G.: Dynamic Structural Aeroelastic Stability Testing of the XV-15 Tilt Rotor Research Aircraft, NASA TM-84293, December 1982.

Silverthorn, L.J.: Whirl mode stability of the main rotor of the YAH-64 advanced attack helicopter, *Proceedings of the 38th Annual Forum of the American Helicopter Society, Alexandria, VA*, March 1982, pp. 80–89.

1983 Hanson, D.B.: Compressible helicoidal surface theory for propeller aerodynamics and noise, *AIAA Journal*, Vol.21, No.6, June 1983, p. 881.

Janetzke, D.C. and Krishna Rao, K.V.: Whirl flutter analysis of a horizontal-axis wind turbine with a two-bladed teetering rotor, *Solar Energy*, Vol.31, No.2, 1983, pp. 173–182.

1984 Jenks, M.D. and Narramore, J.C.: Final Report for the 2-D Test of Model 901 Rotor and Wing Airfoils (BSWT 592). Bell-Boeing Report No. D901-99065-1, Bell Helicopter Textron, May 1984.

Johnson, W.: An Assessment of the Capability to Calculate Tilting Prop-Rotor Aircraft Performance, Loads, and Stability, NASA TP-2291, March 1984.

Mikkelson, D.C., Mitchell, G.A. and Bober, L.J.: Summary of Recent NASA Propeller Research, NASA TM 83733, 1984.

Popelka, D., Sheffler, M. and Bigler, J.: 'Correlation of Test and Analysis for the 1/5 Scale V-22 Aeroelastic Model', 41st Annual Forum of American Helicopter Society, Fort Worth, TX, USA, 15–17 May 1985 (also:*Journal of American Helicopter Society*, Vol.32, No.2, April 1987, pp. 21–33).

1985 Arrington, W.L., Kumpel, M., Marr, R.L. and McEntire, K.G.: XV-15 Tilt Rotor Research Aircraft Flight Test Data Report, Vol II: Performance and Handling Qualities, NASA CR-NAS2-7600, June 1985.

Arrington, W.L., Kumpel, M., Marr, R.L. and McEntire, K.G.: XV-15 Tilt Rotor Research Aircraft Flight Test Data Report, Vol III: Structural Loads and Dynamics, NASA CR 177406, U.S. Army Aviation Systems Command, TR-86-A-1, June 1985.

Hong, C.H. and Chopra, I.: Aeroelastic stability analysis of a composite rotor blade, *Journal of the American Helicopter Society*, Vol.30, No.2, 1985, pp. 57–67.

Lesieutre, D.J. and Sullivan, J.P.: The Analysis of Counter Rotating Propeller Systems, SAE Technical Paper 850869, April 16, 1985.

Runyan, H.L. and Tai, H.: Compressible Unsteady Lifting Surface Theory for a Helicopter Rotor in Forward Flight, NASA Technical Paper, TP 2503, 1985.

Williams, M.H.: An Unsteady Lifting Surface Theory for Single Rotation Propellers, Purdue University Report, School of Aeronautics and Astronautics, June 1985.

Williams, M.H.: User's Guide to UPROP3S, Purdue University Report, School of Aeronautics and Astronautics, January 1985.

1986 Bartie, K., Alexander, H., McVeigh, M., La Mon, S. and Bishop, H.: Hover Performance Test of Baseline Metal and Advanced Technology Blade (ATB) Rotor System for the XV-15 Tilt Rotor Aircraft, NASA CR 177436, Contract NAS2-11250, October 1986.

Donham, R.E., Dupack, J.D. and Conner, F.: Application of a Panel Method (QUADPAN) to the Prediction of Propeller Blade Loads, SAE 861743, Long Beach CA, USA, 13–18 October 1986.

Johnson W., Lau, B.H. and Bowles, J.V.: 'Calculated Performance, Stability and Maneuverability of High Speed Tilting Proprotor Aircraft', 12th European Rotorcraft Forum, Garmisch–Parkenkirchen, Germany, September 1986.

Johnson, W., Lau, B.H. and Bowles, J.V.: Calculated Performance, Stability and Maneuverability of High-Speed Tilting-Prop-Rotor, NASA TM 88349, September 1986.

Nasu, K.: Tilt-Rotor Flutter Control in Cruise Flight, NASA TM 88315, December 1986.

Sprangers, C.A. and Stevenson, M.K.: 'Results of the V-22 Preliminary Design Test Program', 42nd Annual Forum of the American Helicopter Society, Washington, DC, USA, June 1986, pp. 327–338.

1987 Popelka, D., Sheffler, M. and Bigler, J.: Correlation of test and analysis for the 1/5-scale V-22 aeroelastic model, *Journal of the American Helicopter Society*, Vol.32, No.2, April 1987.

1988 Felker, F.F.: 'A Review of Tilt Rotor Download Research', 14th European Rotorcraft Forum, Milano, Italy, September 1988, pp. 14.1–14.31.

Ormiston, R.A., Warmbrodt, W.G., Hodges, D.H. and Peters, D.A.: Rotorcraft aeroelastic stability, NASA / Army Rotorcraft Technology, Volume 1: *Aerodynamics, Dynamics and Aeroelasticity*, NASA CP-2495, 353–529, 1988.

Wilkerson, J.B. and Taylor, R.S.: 'Civil Tiltrotor Aircraft: A Comparison of Five Candidate Designs', 44th Annual Forum of the American Helicopter Society, Washington, DC, June 1988.

1989 Brunken, J.E., Popelka, D.A. and Bryson, R.J.: 'A Review of the V-22 Dynamics Validation Program', 45th Annual Forum of the American Helicopter Society, Boston, MA, USA, May 1989, pp. 51–63.

Favier, D., Ettaouil, A. and Maresca, C.: Numerical and experimental investigation of isolated propeller wakes in axial flight, *Journal of Aircraft*, Vol.26, No.9, 1989, pp. 837–846.

Parham, T.C. and Chao, D.: 'Tiltrotor Aeroservoelastic Design Methodology at BHTI', 45th Annual Forum of the American Helicopter Society, Boston, MA, USA, May 1989.

Rodden, W.P. and Rose, T.L.: MSC/NASTRAN Addition of Effects of Wing Flow Field on Propeller Aerodynamic Loads, MSC Internal Document, June 1989.

Rodden, W.P. and Rose, T.L.: 'Propeller / Nacelle Whirl Flutter Addition to MSC/NASTRAN', Paper No.12, *Proceedings of the 1989 MSC World User's Conference, Universal City, CA, USA*, March 1989.

Settle, T.B. and Kidd, D.L.: 'Evolution and Test History of the V-22 0.2-Scale Aeroelastic Model', American Helicopter Society National Specialists' Meeting on Rotorcraft Dynamics, Arlington, TX, USA, November 1989.

Witkowski, P., Lee, A.K.H. and Sullivan, J.P.: Aerodynamic interaction between propellers and wings, *Journal of Aircraft*, Vol.26, No.9, 1989, pp. 829–836.

Wolkovitch, J., Wainfan, B., Ben-Harush, Y. and Johnson, W.: Application of the Joined Wing to Tiltrotor Aircraft, NASA CR-177543, November 1989.

1990 Friedmann, P.P. and Robinson, L.H.: Influence of unsteady aerodynamics on rotor blade aeroelastic stability and response, *AIAA Journal*, Vol.28, No.10, 1990, pp. 1806–1812.

Totah, J.J. and Madden, J.F.: 'Rotor and Control System Loads Analysis of the XV-15 with the Advanced Technology Blades', American Helicopter Society Meeting on Innovations in Rotorcraft Test Technologies, October 1990.

Williams, M.H.: An Unsteady Lifting Surface Method for Single Rotation Propellers, NASA Lewis Research Center, Contractor Report, CR-4302, July 1990.

1991 Fradenburgh, E.A.: 'High Speed Challenge for Rotary Wing Aircraft', International Pacific Air and Space Technology Conference and 29th Aircraft Symposium, Gifu, Japan, October 1991, pp. 91–109.

Fratello, G., Favier, D. and Maresca, C.: Experimental and numerical study of the propeller–fixed wing interaction, *Journal of Aircraft*, Vol.28, No.6, 1991, pp. 365–373.

Liu, J. and McVeigh, M.A.: 'Design of Swept Blade Rotors for High-Speed Tiltrotor Application, AIAA 91-3147', AIAA/AHS/ASEE Aircraft Design Systems and Operations Meeting, Baltimore, MD, USA, September 1991.

Nitzsche, F.: Insights on the whirl-flutter phenomena of advanced turboprops and propfans, *Journal of Aircraft*, Vol.28, No.7, pp. 463–470, 1991.

Parham, T, Jr. and Miller, D.G.: 'V-22 Pilot-in-the-loop Aeroelastic Stability Analysis', 47th Annual Forum of the American Helicopter Society, Phoenix, AZ, USA, 6–8 May 1991, pp. 1307–1319.

Senn, E.E.: 'The Effect of Composite Material on the Configuration and Design of the V-22 Wing', American Helicopter Society National Technical Specialists' Meeting on Rotorcraft Structures, Williamsburg, VA, October 1991, pp. 1–6.

Totah, J.J.: 'Description of a Tilt Wing Mathematical Model for Piloted Simulation', 47th Annual Forum of the American Helicopter Society, Phoenix, AZ, USA, May 1991, p. 16 .

Van Aken, J.M.: 'Alleviation of Whirl-Flutter on Tilt-Rotor Aircraft Using Active Controls', 47th Annual Forum of the American Helicopter Society, Phoenix, AZ, USA, May 1991, pp. 1321–1344.

Vorwald, J. and Chopra, I.: 'Stabilizing Pylon Whirl Flutter on a Tilt-Rotor Aircraft', 32nd AIAA/ASME/ASCE/AHS/ASC Structures, Structural Dynamics and Materials Conference, Baltimore, MD, USA, 8–10 April 1991, AIAA-91-1259-CP.

Yeager, W.T., Jr., Mirick, P.H., Hamouda, M.N.H., Wilbur, M.L., Singleton, J.D. and Wilkie, W.K.: 'Rotorcraft Aeroelastic Testing in the Langley Transonic Wind Tunnel', 47th Annual Forum of the American Helicopter Society, Phoenix, AZ, USA, May 1991 (also *Journal of the American Helicopter Society*, July 1993, pp. 73–82).

1992 Airline Pilots Association Report, Beechcraft 1900C N811BE, 1992.

Chappel, D.P. and Peyran, R.J.: 'Methodology for Estimating Wing Weights for Conceptual Tilt-Rotor and Tilt-Wing Aircraft', 51st Annual Conference of the Society of Allied Weight Engineers, Inc. Hartford, CT, USA, 18–20 May 1992, pp. 1–12.

Chattopadhyay, A. and Narayan, J.R.: 'Optimum Design of High Speed Prop-Rotors Using a Multidisciplinary Approach', 48th Annual Forum of the American Helicopter Society, Alexandria, VA, June 1992.

Fradenburgh, E.A. and Matuska, D.G.: 'Advancing Tiltrotor State-of-the-Art with Variable Diameter Rotors', Annual Forum of the American Helicopter Society, Washington, DC, 1992, Vol.2, pp. 1115–1135.

Kunz, D.L.: On the effect of pitch / mast-bending coupling on whirl-mode stability, *Proceedings of the 48th Annual Forum of the American Helicopter Society, Alexandria*, VA, June 1992, pp. 87–93.

Kvaternik, R.G.: A Historical Overview of Tiltrotor Aeroelastic Research at Langley Research Center, NASA TM 107578, April 1992.

Lake, R.C., Nixon, M.W., Wilbur, M.L., Singleton, J.D. and Mirick, P.H.: 'A Demonstration of Passive Blade Twist Control Using Extension-Twist Coupling', AIAA/ASME/ASCE/AHS/ASC Structures, Structural Dynamics and Materials Conference, Dallas, TX, USA, 1992, pp. 774–781.

Lowey, R.G.: Aeroelasticity and the tiltrotor VTOL aircraft, *Vertzflite*, Vol.88, No.3, pp. 53–66, May–June 1992.

Nixon, M.W.: 'Parametric Studies for Tiltrotor Aeroelastic Stability in High-Speed Flight', 33rd AIAA/ASME/ASCE/AHS Structures, Structural Dynamics, and Materials Conference, Dallas, TX, USA, April 1992.

O' Heron, P.J., Kunz, D.L., Nikravesh, P.E. and Arabyan, A.: 'A Multibody Approach to Modeling Tilt-Wing Rotorcraft Dynamics', 30th AIAA Aerospace Sciences Meeting and Exhibit, Reno, NV, January 1992, AIAA Paper No.92-0488.

O' Heron, P.J., Nikravesh, P.E., Arabyan, A. and Kunz, D.L.: 'Tilt-Wing Rotorcraft Dynamic Analysis Using a Multibody Formulation', 18th ASME Design Automotive Conference, Scottsdale, AZ, September 1992.

Settle, T.B. and Kidd, D.L.: Evolution and test history of the V-22 0.2-scale aeroelastic model, *Journal of the American Helicopter Society*, Vol. 37, No.1, January 1992, pp. 31–45.

Stettner, M. and Schrage, D.P.: 'An Approach to Tiltrotor Wing Aeroservoelastic Optimization through Increased Productivity', 4th AIAA/USAF/NASA/OAI Symposium on Multidisciplinary Analysis and Optimization, Cleveland, OH, USA, September 1992, AIAA-92-4781-CP, pp. 749–759.

Wang, J.C.: 'A tilt-rotor aircraft whirl-flutter alleviation using active controls', in J. Clark *et al.*, eds., *Active Control of Noise and Vibration*, Vol.38, pp. 139–148, American Society of Mechanical Engineers, New York, 1992.

1993 Acree, C.W. and Tischler, M.B.: Determining XV-15 Aeroelastic Modes from Flight Data with Frequency Domain Methods, NASA Technical Paper, TP3330, U.S. Army Aviation and Troop Command, TR 93-A-004, May 1993.

Acree, C.W., Jr.: An Improved CAMRAD Model for Aeroelastic Stability Analysis of the XV-15 with Advanced Technology Blades, NASA, TM 4448, March 1993.

Chattopadhyay, A., McCarthy, T.R. and Madden, J.F., Jr.: 'Optimum Design of High Speed Prop Rotors Including the Coupling of Performance, Aeroelastic Stability and Structures', 49th Annual Forum of the American Helicopter Society, St. Louis, MO, USA, May 1993.

Editorial Staff Report: 'Fatal commuter training flight cash blamed on spatial disorientation, poor judgment', *Flight Safety Foundation, Accident Prevention*, Vol.50, No.10, October 1993.

Friehmelt, H.: 'Design of a Tiltrotor Wing for a EUROFAR-type Configuration', M.Sc. Thesis, Braunschweig Technical University / Georgia Institute of Technology, March 1993.

Jessop, D.A.C. and Juggins, P.T.W.: Wind Tunnel Testing of a EUROFAR Tilt Rotor Aeroelastic Stability Model, G1-2 G1-15.

Jessop, D.A.C. *et al.*: 'Wind Tunnel Testing of a EUROFAR Tilt Rotor Aeroelastic Stability Model, 19th European Rotorcraft Forum, 1993.

Johnson, W.: *CAMRAD II Comprehensive Analytical Model of Rotorcraft Aerodynamics and Dynamics – Theory Manual*, Johnson Aeronautics, Palo Alto, CA, USA, 1993.

Johnson, W.: *CAMRAD II Comprehensive Analytical Model of Rotorcraft Aerodynamics and Dynamics – Rotorcraft Applications*, Johnson Aeronautics, Palo Alto, CA, USA, 1993.

Juggins, P.T.W.: Analysis of a 1/6 Scale EUROFAR Semi-Span Wind Tunnel Model for Aeroelastic Stability and Loads, 62-01-62-19.

Lynn, R.R.: The rebirth of the tiltrotor – the 1992 Alexander A. Nikolsky Lecture, *Journal of the American Helicopter Society*, Vol.38, No.1, 1993, pp. 3–16.

Matuska, D.G. and Studebaker, K.: 'Reduced Tip Speed Testing of a Variable Diameter Tiltrotor', European Rotorcraft Forum, Cernobbio, Italy, September 1993.

Moore, M.J., Yablonski, M.J., Mathew, B. and Liu, J.: 'High Speed Tiltrotors: Dynamics Methodology', 49th Annual Forum of the American Helicopter Society, St. Louis, MO, May 1993, pp. 1255–1268.

National Transportation Safety Board, Washington, D.C. 20594, Aircraft Accident / Incident, Summary Report: Loss of Control Business Express, Inc. Beechcraft 1900C N811BE Near Block Island, Rhode Island, December 28, 1991, adopted 27 April 1993.

Nibbelink, B.D. and Peters, D.A.: 'Flutter Calculations for Fixed and Rotating Wings with State-Space Inflow Dynamics', 34th AIAA/ASME/ASCE/AHS/ASC Structures, Structural Dynamics, and Materials Conference, La Jolla, CA, USA, April 1993.

Nixon, M.W.: Parametric studies for tiltrotor aeroelastic stability in high speed flight, *Journal of the American Helicopter Society*, Vol.38, No.4, October 1993, pp. 71–79.

Nixon, M.W.: 'Aeroelastic Response and Stability of Tiltrotors with Elastically Coupled Composite Rotor Blades', Ph.D. Thesis, University of Maryland, 1993.

Schleicher, D.R., Phillips, J.D. and Carbajal, K.B.: Design Optimization of High-Speed Proprotor Aircraft, NASA-TM-103988, April 1993.

Stettner, M. and Schrage, D.P.: 'Tiltrotor Performance Sensitivities for Multidisciplinary Wing Optimization', American Helicopter Society Specialists' Meeting on Rotorcraft Multidisciplinary Design Optimization, Atlanta, GA, USA, 27–28 April 1993.

Studebaker, K. and Matuska, D.: 'Variable Diameter Tiltrotor Wind Tunnel Test Results', 49th Annual Forum of the American Helicopter Society, St. Louis, MO, USA, May 1993.

1994 Lake, R.C., Nixon, M.W. and Wilbur, M.L.: Demonstration of an elastically coupled twist control concept for tilt rotor blade application, *AIAA Journal*, Vol.32, No.7, 1994, pp. 1549–1551.

Nitzsche, F.: Whirl-flutter suppression in advanced turboprops and turbofans by active control techniques, *Journal of Aircraft*, Vol.31, No.3, 1994, pp. 713–719.

Rais-Rohani, M. and Baker, J.D.: 'Wing Design of a Civil Tilt-Rotor Transport Aircraft, a Preliminary Study', 35th AIAA/ASME/ASCE/AHS/ASC Structures, Structural Dynamics and Materials Conference, Hilton Head, SC, USA, 18–20 April 1994.

1995 Barkai, S.M., Rand, O., Peyran, R.J. and Carlson, R.M.: 'Modeling and Analysis of Tilt-Rotor Aeromechanical Phenomena', American Helicopter Society Aeromechanics Conference, Bridgeport, CT, USA, 11–13 October 1995.

Brunson, S.L.: 'Design of a Wing Box Structure for the Civil Tilt-Rotor Transport Aircraft', M.Sc. Thesis, Department of Aerospace Engineering, Mississippi State University, August 1995.

Brunson, S.L.: 'Structural Optimization of a Civil Tilt-Rotor Wing', Regional Student Conference, Atlanta, GA, USA, 13–14 April 1995.

Charles, B.D., JanakiRam, R.D., Hassan, A.A. and Quackenbush, T.R.: 'An Assessment of Current Methodology for Predicting Tiltrotor Blade-Vortex Interaction Aerodynamics', 51st Annual Forum of the American Helicopter Society, Fort Worth, TX, USA, 9–11 May 1995.

McCarthy, T.R., Chattopadhyay, A., and Zhang, S., 'Coupled Rotor/Wing Optimization Procedure for High Speed Tilt-Rotor Aircraft', Annual Forum of the American Helicopter Society, Fort Worth, TX, USA, 1995, Vol.2, pp. 924–936.

Popelka, D., Lindsay, D., Parham, T., Jr., Berry, V. and Baker, D.L.: 'Results of an Aeroelastic Tailoring Study for a Composite Tiltrotor Wing', 51st Annual Forum of the American Helicopter Society, Fort Worth, TX, USA, 9–11 May 1995.

Rand, O. and Barkai, S.M.: Numerical evaluation of the equations of motion of helicopter blades with symbolic exactness, *Journal of the American Helicopter Society*, Vol.40, No.1, pp. 59–71, January 1995.

Rodden, W.P. and Rose, T.L.: Propeller / Nacelle Whirl Flutter Addition to MSC/NASTRAN, MSC/NASTRAN Aeroelastic Analysis, Reference Material Version 68, January 1995.

Shang, X.: 'Aeroelastic Stability of Composite Hingless Rotors with Finite-State Unsteady Aerodynamics', Ph.D. Thesis, Georgia Institute of Technology, Atlanta, GA, USA, 1995.

Srinivas, V., Chopra, I. and Nixon, M.: 'Assessment of Aeroelastic Analyses of Advanced Tiltrotor Aircraft', 36th AIAA/ASME/ASCE/AHS/ASC Structures, Structural Dynamics and Materials Conference and Adaptive Structures Forum, New Orleans, LA, USA, April 1995.

Srinivas, V.: 'Aeroelastic Analysis of Advanced Tiltrotor Aircraft', Ph.D. Thesis, University of Maryland, College Park, MD, USA, 1995.

Stettner, M., Mavris, D.N. and Schrange, D.P.: 'Aeroelastic Tailoring for a Civil Tiltrotor Configuration', American Helicopter Society Vertical Lift Aircraft Design Conference, San Francisco, CA, USA, 18–20 January 1995.

Tadghighi, H., Rajagopalan, G. and Burley, C.: 'Simulation of Tiltrotor Fountain Flow Field Effects Using a Finite Volume Technique – An Aero / Acoustic Study', 51st Annual Forum of the American Helicopter Society, Fort Worth, TX, USA, 9–11 May 1995.

Wang, J.M., Torok, M.S. and Nixon, M.W.: 'Experimental and Theoretical Study of Variable Diameter Tilt Rotor Dynamics', American Helicopter Society Vertical Lift Aircraft Design Conference, San Francisco, CA, USA, 18–20 January 1995.

1996 Brunson, S.L. and Rais-Rohani, M.: 'A Thin Tailored Composite Wing for the Civil Tiltrotor Aircraft', 37th AIAA/ASME/ASCE/AHS/ASC Structures, Structural Dynamics and Materials Conference and Adaptive Structures Forum, Salt Lake City, UT, USA, 15–17 April 1996.

Chiaramonte, Y., Favier, D.C. and Benneceur, S.: Aerodynamic interaction study of the propeller–wing under different flow configurations, *Journal of Aircraft*, Vol.33, No.1, 1996, pp. 46–53.

Clements, T.M. and Rais-Rohami, M.: 'Sensitivity Analysis of a Tilt-Rotor Composite Wing Natural Frequencies with Respect to Structural Parameters', SECTAM XVIII, Tuscaloosa, AL, USA, 14–16 April 1996.

Glusman, S.I., Hyland, R.A. and Marr, R.L.: 'V-22 Technical Chalenges', AGARD FVP Symposium on Advances in Rotorcraft Technology, Ottawa, ON, Canada, 27–30 May 1996.

Kosmatka, J.B. and Lake, R.C.: 'Passive Approach of Controlling Twist in Composite Tilt-Rotor Blades', SPIE Conference on Smart Structures and Integrated Systems, San Diego, CA, USA, 26–29 February 1996, pp. 146–157.

McCarthy, T.R. and Chattopadhyay, A.: A coupled rotor / wing optimization procedure for high speed tilt-rotor aircraft, *Journal of the American Helicopter Society*, Vol.41, No.4, October 1996.

Rand, O., Barkai, S.M., Carlson, R. and Peyran, R.: 'RAPID – Rotorcraft Analysis for Preliminary Design: Methodology and Implementation', 36th Israel Annual Conference on Aerospace Sciences, 21–22 February 1996.

Srinivas, V. and Chopra, I.: 'An Assessment of Aeroelastic Analyses for Tiltrotor Aircraft', 37th AIAA/ASME/ASCE/AHS/ASC Structures, Structural Dynamics and Materials Conference and Adaptive Structures Forum, Salt Lake City, UT, USA, 15–17 April 1996.

Srivastava, R. and Reddy, T.S.R.: PROP3D: A Program for 3D Euler Unsteady Aerodynamic and Aeroelastic (Flutter and Forced Response) Analysis of Propellers, Version 1.0, NASA Contractor Report, CR 198471, 1996.

1997 Clements, T.M.: 'Global–Local Analysis and Design Optimization of Composite Tilt-Rotor Wing Box Structure', M.Sc. Thesis, Department of Aerospace Engineering, Mississippi State University, May 1997.

Corso, L.M., Popelka, D.A. and Nixon, M.W.: 'Design, Analysis, and Test of a Composite Tailored Tiltrotor Wing', American Helicopter Society 53rd Annual Forum, Virginia Beach, VA, USA, 29 April–1 May 1997.

Donham, R.E. and Watts, G.A.: 'Whirl flutter first case', in *The Revolution in Structural Dynamics*, (ed. Dr. Hugh Flomenhoft), ISBN 0-9659773-0-7 MIT memorial book to Dr. Raymond Bisplinghoff, 1997.

Light, J.S., Kitaplioglu, C. and Acree, C.W.: 'XV-15 Aeroacoustic Testing at NASA Ames', 23th European Rotorcraft Forum, Dresden, Germany, September 1997, pp. 109.1–109.10.

Light, J.S.: 'Results from an XV-15 Rotor Test in the National Full-Scale Aerodynamics Complex', 53th Annual Forum of the American Helicopter Society, Virginia Beach, VA, USA, May 1997, pp. 231–239.

Marretta, R.M.A.: Different wings flowfields interaction on the wing–propeller coupling, *Journal of Aircraft*, Vol.34, No.6, 1997, pp. 740–747.

Nixon, M.W., Kvaternik, R.G. and Settle, T.B.: 'Tiltrotor Vibration Reduction Through Higher Harmonic Control', American Helicopter Society 53rd Annual Forum, Virginia Beach, VA, USA, April 1997.

Parham, T. and Froebel, A.: V-22 EMD Intermediate Flutter and Divergence, Report. Bell-Boeing No. 901-910-039, Bell Helicopter Textron, September 1997.

Piatak, D.J., Nixon, M.W. and Kosmatka, J.B.: Stiffness Characteristics of Composite Rotor Blades with Elastic Couplings, NASA Technical Paper, TP 3641, ARL Technical Report 1279, April 1997.

Popelka, D., Lindsay, D., Parham, T., Berry, V. and Baker, D.J.: Results of an aeroelastic tailoring study for a composite tiltrotor wing, *Journal of the American Helicopter Society*, Vol.42, No.2, 1997, pp. 126–136.

Settle, T.B. and Nixon, M.W.: 'MAVSS Control of an Active Flaperon for Tiltrotor Vibration Reduction', American Helicopter Society 53rd Annual Forum, Virginia Beach, VA, USA, April 1997.

Stearman, R.O., Schulze, G.H., Rohre, S.M. and Buschow, M.C.: 'Aircraft Damage Detection from Acoustic Signals Found by a Cockpit Voice Recorder', Acoustical Society of America 133rd Meeting, State College, PA, USA, 17 June 1997.

1998 Barkai, S.M., Rand, O., Peyran, R.J. and Carlson, R.M.: Modeling and analysis of tilt-rotor aeromechanical phenomena, *Mathematical and Computer Modelling*, Oxford, Vol.27, No.12, 1998, p. 17.

Barkai, S.M. and Rand, O.: The influence of composite induced couplings on tiltrotor whirl flutter stability in forward flight, *Journal of the American Helicopter Society*, Vol.43, No.2, April 1998, pp. 133–145.

Boyne, W.J.: *Beyond the Horizons – The Lockheed Story*, St. Martin Press, New York, 1998.

Donham, R.E.: 'Whirl Flutter of Rigid and Flexible Propeller Systems in Tractor and Pusher Configurations', Aerospace Flutter and Dynamics Council, 7–8 May 1998, Phoenix, AZ, USA.

Madden, J.F. and Peyran, R.J.: Aeroelastic Stability Enhancer for Tilt-Rotor Aircraft, Invention Disclosure, NASA, Case No.ARC-14298-1CU, May 1998.

Nixon, M.W., Kvaternik, R.G. and Settle, T.B.: Tiltrotor vibration reduction through higher harmonic control, *Journal of the American Helicopter Society*, Vol.43, No.3, July 1998.

Petersen, J.T. and Madsen, H.E.: Prediction of Dynamic Loads and Induced Vibrations in Stall, RISO National Laboratory Report, Denmark, May 1998, RISO-R-1045(EN).

Singleton, J.D. and Yeager, W.T., Jr.: Important Scaling Parameters for Testing Model – Scale Helicopter Rotors, AIAA-98-2881.

Srinivas, V., Chopra, I. and Nixon, M.W.: Aeroelastic analysis of advanced geometry tiltrotor aircraft, *Journal of the American Helicopter Society*, Vol.43, No.3, July 1998, pp. 212–221.

Srinivas, V. and Chopra, I.: Formulation of a comprehensive aeroelastic analysis for tiltrotor aircraft, *Journal of Aircraft*, Vol.25, No.2, March–April 1998, pp. 280–287.

Srinivas, V. and Chopra, I.: Validation of a comprehensive aeroelastic analysis for tiltrotor aircraft, *Journal of the American Helicopter Society*, Vol. 43, No. 4, 1998, pp. 333–341.

Young, L.A.: 'Tilt Rotor Aeroacoustic Model (TRAM): A New Rotorcraft Research Facility', American Helicopter Society Specialists' Meeting on Advanced Rotorcraft Technology and Disaster Relief, Gifu, Japan, April 1998.

1999 Acree, C.W., Jr., Peyran, R.J. and Johnson, W.: 'Rotor Design for Whirl Flutter: An Examination of Options for Improving Tiltrotor Aeroelastic Stability Margins', American Helicopter Society 55th Annual Forum, Montreal, QC, Canada, 25–27 May 1999.

Booth, E.R., Jr., McCluer, M. and Tadghighi, H.: 'Acoustic Characteristics of a Model Isolated Tiltrotor in the DNW', American Helicopter Society 55th Annual Forum, Montreal, QC, Canada, 25–27 May 1999.

Ghiringhelli, G.L., Massarati, P., Mantegazza, P. and Nixon, M.W.: 'Multi-Body Analysis of the 1/5 Scale Wind Tunnel Model of the V-22 Tiltrotor', American Helicopter Society 55th Annual Forum, Montreal, QC, Canada, 25–27 May 1999.

Ghiringhelli, G.L., Massarati, P., Mantegazza, P. and Nixon, M.W.: 'Multi-Body Analysis of an Active Control for a Tiltrotor', CEAS/AIAA/ICASE/NASA Langley Forum on Aeroelasticity and Structural Dynamics 1999, Williamsburg, VA, USA, 22–25 June 1999, pp. 149–158, NASA CP-1999-209136/PT 1.

Ghiringhelli, G.L., Massarati, P., Mantegazza, P. and Nixon, M.W.: Multi-body analysis of a tiltrotor configuration, *Nonlinear Dynamics*, Vol.19, 1999, pp. 333–357.

Hirschberg, M.: On the vertical horizon – Bell designs are accelerating at full tilt, *Vertiflite*, Vol.45, No.4, 1999, pp. 14–17.

Marretta, R.M.A. and Lombardi, G.: Wing pitching and loading with propeller interference, *Journal of Aircraft*, Vol.36, No.2, 1999, pp. 468–471.

Nixon, M.W., Piatak, D.J., Corso, L.M. and Popelka, D.A.: 'Aeroelastic Tailoring for Stability Augmentation and Performance Enhancements of Tiltrotor Aircraft', American Helicopter Society 55th Annual Forum, Montreal, QC, Canada, 25–27 May 1999.

Nixon, M.W., Piatak, D.J., Corso, L.M. and Popelka, D.A.: 'Aeroelastic Tailoring for Stability Augmentation and Performance Enhancements of Tiltrotor Aircraft', NASA Langley Research Center's International Forum on Aeroelasticity and Structural Dynamics, Williamsburg, VA, 22–25 June 1999, pp. 121–138.

Parham, T., Jr. and Corso, L.M.: 'Aeroelastic and Aeroservoelastic Stability of the BA 609', 25th European Rotorcraft Forum, Rome, Italy, 14–16 September 1999.

Peyran, R. and Rand, O.: 'The Effect of Design Requirements on Conceptual Tiltrotor Wing Weight', 55th Annual Forum of the American

Helicopter Society, Montreal, QC, Canada, Aircraft Design I/4, 25–27 May 1999.

Singleton, J.D.: 'Coupled Rotor – Fuselage Aeroelastic Analysis for Tiltrotor Configurations', 8th ARO Workshop on Aeroelasticity and Rotorcraft Systems, 18–20 October 1999, State College, PA, USA.

Soykasap, O.: 'Aeroelastic Optimization of a Composite Tiltrotor', Ph.D. Thesis, Georgia Institute of Technology, Atlanta, GA, USA, 1999.

Swanson, S.M., McCluer, M.S., Yamauchi, G.K. and Swanson, A.A.: 'Airloads Measurement from 1/4-Scale Tiltrotor Wind Tunnel Model', 25th European Rotorcraft Forum, Rome, Italy, 14–16 September 1999.

Wang, J.W., Jones, C.T. and Nixon, M.W.: 'A Variable Diameter Short Haul Civil Tiltrotor', 55th Annual Forum of the American Helicopter Society, Montreal, QC, Canada, 25–27 May 1999.

Young, L.A., Booth, E.R., Jr., Yamauchi, G.K., Botha, G. and Dawson, S.: 'Overview of the Testing of a Small-Scale Proprotor', 55th Annual Forum of the American Helicopter Society, Montreal, QC, Canada, 25–27 May 1999.

2000 Acree, C.W., Jr., Peyran, R.J. and Johnson, W.: 'Improving Tiltrotor Whirl – Mode Stability with Rotor Design Variations', 26th European Rotorcraft Forum, The Hague, Netherlands, September 2000.

Čečrdle, J.: Metodika výpočtu vířivého flatru pomocí programového systému MSC.NASTRAN (translation: Methodology of whirl flutter analysis by means of MSC.NASTRAN System), Report VZLU, No.R-3196/00, 2000.

Clements, T.M. and Rais-Rohani, M.: 'Design Optimization of a Composite Tilt-Rotor Wing with Stability Approximations', 41st AIAA/ASME/ASCE/AHS/ASC Structures, Structural Dynamics and Materials Conference, Atlanta, GA, USA, 3–6 April 2000.

Corso, L.M., Popelka, D.A. and Nixon, M.W.: Design, analysis, and test of a composite tailored tiltrotor wing, *Journal of the American Helicopter Society*, Vol.45, No.3, July 2000.

Donham R.E. and Watts, G.A.: 'Lessons Learned from Fixed and Rotary Wing Dynamic and Aeroelastic Encounters', AIAA/ASME/ASCE/AHS/ASC Structures, Structural Dynamics and Materials Conference, Atlanta, GA, USA, April 2000, AIAA 2000-1599.

Johnson, W.: 'Calculation of Tiltrotor Aeroacoustic Model (TRAM DNW) Performance, Airloads and Structural Loads', American Helicopter Society Aeromechanics Specialists' Meeting, Atlanta, GA, USA, November 2000

Kvaternik, R.G., Juang, J. and Bennett, R.L.: 'Exploratory Studies in Generalized Predictive Control for Active Aeroelastic Control of Tiltrotor Aircraft', American Helicopter Society Northeast Region Specialists' Meeting on Active Controls Technology, Bridgeport, CT, USA, 4–5 October 2000.

Maisel, M.D., Giulianetti, D.J. and Dugan, D.C.: The History of the XV-15 Tilt Rotor Research Aircraft: From Concept to Flight. NASA SP-2000-4517.

Nixon, M.W., Piatak, D.J., Corso, L.M. and Popelka, D.A.: Aeroelastic tailoring for stability augmentation and performance enhancements of

tiltrotor aircraft, *Journal of the American Helicopter Society*, Vol.45, No.4, October 2000.

Rand, O. and Peyran, R.J.: Experimental demonstration of the influence of wing couplings on whirl–flutter instability, *Journal of Aircraft*, Vol.37, No.5, pp. 859–864, September–October 2000.

Veldhuis, L.L.M., and Heyma, P.M.: Aerodynamic optimisation of wings in multi-engined tractor propeller arrangements, *Aircraft Design*, No.3, 2000, pp. 129–149.

Yeager, W.T., Jr. and Kvaternik, R.G.: 'Contributions of the Langley Transonic Dynamics Tunnel to Rotorcraft Technology and Development', AIAA Dynamics Specialists' Conference, Atlanta, GA, USA, 5–6 April 2000.

2001 Acree, C.W., Jr., Johnson, W. and Peyran, R.J.: Rotor design options for improving tiltrotor whirl flutter stability margins, *Journal of the American Helicopter Society*, Vol.46, No.2, 2001, pp. 87–95.

Acree, C.W., Jr.: 'Effects of Rotor Design Variations on Tiltrotor Whirl–Mode Stability', American Helicopter Society Tiltrotor / Runway Independent Aircraft Meeting, Arlington, TX, USA, March 2001.

Čečrdle, J.: Aircraft Whirl Flutter Analysis by means of MSC. NASTRAN Program System, MSC.Software Users' Conference 2001, Paper No.6, Brno, Czech Republic, May 23–24, 2001, ISBN 80-238-7111-0.

Čečrdle, J.: Vliv porušení prutu motorového lože na vřivý flatr, (translation: Influence of Engine Mount Failure to Whirl Flutter), Report VZLU, No.R-3299/01, 2001.

Čečrdle, J.: Výpočet vířivého flatru letounu Ae 270 (translation: Whirl Flutter Analysis of Ae 270 Aircraft) Report VZLU, No. AC0465CZ, 2001.

Johnson, W.: 'Calculation of the Aerodynamic Behavior of the Tilt Rotor Aeroacoustic Model (TRAM) in the DNW', American Helicopter Society Forum, May 2001.

Kvaternik, R.G., Piatak, D.J., Nixon, M.W., Langston, Ch.V., Singleton, J.D., Bennett, R.L. and Brown, R.K.: 'An Experimental Evaluation of Generalized Predictive Control of Tiltrotor Aeroelastic Stability Augmentation in Airplane Mode of Flight', American Helicopter Society 57th Annual Forum, Washington, DC, 9–11 May 2001.

Nannoni, F., Giancamilli, G. and Cicale, M.: 'ERICA: The European Advanced Tiltrotor', 27th European Rotorcraft Forum, Moscow, Russia, 11–14 September 2001.

Nixon, M.W., Langston, C.W., Singleton, J.D., Piatak, D.J., Kvaternik, R.G., Corso, L.M. and Brown, R.: 'Aeroelastic Stability of a Soft-Inplane Gimballed Tiltrotor Model in Hover', 42nd AIAA/ASIvIE/ASCE/AHS/ASC Structures, Structural Dynamics, and Materials Conference, Seattle, WA, USA, 16–19 April 2001.

Piatak, D.J., Kvaternik, R.G., Nixon, M.W., Langston, Ch.V., Singleton, J.D., Bennett, R.L. and Brown, R.K.: 'A Wind-Tunnel Parametric Investigation of Tiltrotor Whirl-Flutter Stability Boundaries', American Helicopter Society 57th Annual Forum, Washington, DC, 9–11 May 2001.

Yeager, W.T., Jr. and Kvaternik, R.G.: A Historical Overview of Aeroelasticity Branch and Transonic Dynamics Tunnel Contributions to Rotorcraft Technology and Development, NASA Langley, NASA TM-2001-211054 ARL-TR-2564.

2002 Acree, C.W.: 'Rotor Design Options for Improving V-22 Whirl-Mode Stability', Proceedings 58th Forum of the American Helicopter Society, Montreal, QC, Canada, 11–13 June 2002.

Botasso, C.L., Trainelli, L., Abdel-Nour, P. and Labo, G.: 'Tilt-rotor Analysis and Design Using Finite Element Multibody Procedures', 28th European Rotorcraft Forum, Bristol, UK, 17–20 September 2002.

Čečrdle, J.: Výpočet vířivého flatru pomocí programového systému MSC. NASTRAN (translation: Aircraft Whirl – Flutter Analysis by Means of the MSC.NASTRAN System), *Journal Czech Aerospace Proceedings*, No.4, pp. 26–30, December 2002, ISSN 1211-877X.

Čečrdle, J.: Výpočet vířivého flutteru letounu Ae 270 HP (translation: Whirl Flutter Analysis of Ae 270 HP Aircraft), Report VZLU, No.BC0670CZ, 2002.

Donham, R.E.: 'Twin Piston Engine Aircraft Whirl Flutter Accident / Analysis', Aerospace Flutter and Dynamics Council Meeting, Sedona, AZ, USA, May, 2002.

Johnson, W.: *CAMRAD II Comprehensive Analytical Model of Rotorcraft Aerodynamics and Dynamics*, Johnson Aeronautics, Palo Alto, CA, USA, 2002.

Johnson, W.: 'Influence of Wake Models on Calculated Tiltrotor Aerodynamics', American Helicopter Society Aerodynamics, Acoustics and Test Evaluation Technical Specialists' Meeting, San Francisco, CA, USA, January 2002.

Kunz, D.: 'Analysis of Prop-Rotor Whirl Flutter: Review and Update', 43rd AIAA/ASME/ASCE/AHS/ASC Structures, Structural Dynamics and Materials Conference, Denver, CO, USA, 22–25 April 2002.

Kvaternik, R.G., Piatak, D.J., Nixon, M.W., Langston, C.W., Singleton, J.D., Bennett, R.L. and Brown, R.K.: An experimental evaluation of generalized predictive control for tiltrotor aeroelastic stability augmentation in airplane mode of flight, *Journal of the American Helicopter Society*, Vol.47, No.3, July 2002.

Manley, D.J. and Von Klein, W.: 'Design and Development of a Super-Short Take-off and Landing Transport Aircraft', AIAA-2002-6023, International Powered Lift Conference, Williamsburg, VA, USA, 5–7 November 2002.

Piatak, D.J., Kvaternik, R.G., Nixon, M.W., Langston, C.W., Singleton, J.D., Bennett, R.L. and Brown, R.K.: A parametric investigation of whirl-flutter stability on the WRATS tiltrotor model, *Journal of the American Helicopter Society*, Vol.47, No.3, July 2002.

Reber, R.R.: Tiltrotor development to meet public acceptability targets, *Aeronautical Journal*, January 2002, pp. 33–38.

2003 Hathaway, E.L. and Gandhi, F.S.: 'Design Optimization for Improved Tiltrotor Whirl Flutter Stability', 29th European Rotorcraft Forum, Friedrichshafen, Germany, 16–18 September 2003.

Hathaway, E.L. and Gandhi, F.S.: Modeling refinements in simple tiltrotor whirl flutter analyses, *Journal of the American Helicopter Society*, Vol.48, No.3, 2003, pp. 186–198.

Manimala, B., Padfield, G.D., Walker, D., Naddei, M., Verde, L., Ciniglio, U., Rollet, P. and Sandri, F.: 'Load Alleviation in Tilt Rotor Aircraft through Active Control; Modelling and Control Concepts', American Helicopter Society 59th Annual Forum, Phoenix, AZ, USA, 6–8 May 2003

Massarati, P., Quaranta, G., Lanz, M. and Mantegazza, P.: *Dynamic Characterization and Stability of a Large Size Multibody Tiltrotor Model by POD Analysis*, ASME 2003.

Nixon, M.V., Langston, Ch.W., Singleton, J.D., Piatak, D.J., Kvaternik, R.G., Corso, L.M. and Brown, R.: 'Aeroelastic Stability of a Four-bladed Semi-articulated Soft-inplane Tiltrotor Model', American Helicopter Society 59th Forum, 6–8 May 2003, Phoenix, AZ.

Nixon, M.W., Langston, C.W., Singleton, J.D., Piatak, D.J., Kvaternik, R.G., Corso, L.M. and Brown, R.K.: Hover test of a soft-inplane gimballed tiltrotor model, *Journal of the American Helicopter Society*, Vol.48, No.1, January 2003.

Sanjurjo, E., De la Iglesia, F., Maderuelu, C., Climent, H. and Rodden, W.P.: 'Effect of Propeller 1P Loads on Aircraft Dynamic Response', International Forum on Aeroelasticity and Structural Dynamics (IFASD), Amsterdam, Netherlands 2003.

Singh, B. and Chopra, I.: Whirl flutter stability of two-bladed proprotor / pylon systems in high speed flight, *Journal of the American Helicopter Society*, Vol.48, No.2, 2003, pp. 99–107.

2004 Acree, C. W., Jr.: 'Effects of Blade Sweep on V-22 Whirl Flutter and Loads', American Helicopter Society 4th Decennial Specialist's Conference on Aeromechanics, San Francisco, CA, 21–23 January 2004.

Acree, C.W., Jr., Peyran, R.J. and Johnson, W.: Rotor Design Options for Improving XV-15 Whirl-Flutter Stability Margins, NASA Technical Paper, TP-2004-212262, AFDD/TR-04-001, 2004.

Acree, C.W., Jr.: A CAMRAD II Model of the V-22 Rotor for Whirl-Flutter Analysis, NASA TM-2004-212801, July 2004.

Acree, C.W.: 'Whirl Flutter Studies for a SSTOL Transport Demonstrator', AHS 4th Decennial Specialists' Conference on Aeromechanics, San Francisco, CA, 21–23 January 2004.

Bianchi, E., Russo, A., Kiessling, F., Ferrer, R., Dietrich, O., Frosoni, M., Bakker, R., Riziotis, V., Petot, D. and Lanz, M.: 'Numerical Whirl-flutter Investigation of the European Tiltrotor Concept: Current Status and Future Prospects', European Rotorcraft Forum, Marseille, France, 14–16 September 2004.

Donham, R.E.: 'Bending Stall flutter and Classical Flutter of Horizontal Axis Wind Turbines, Helicopters and Fixed Wing Systems', Aerospace Flutter and Dynamics Council, Spring Meeting 2004, NASA Langley Research Center.

Krueger, W.R. and Spieck, M.: Aeroelastic effects in multibody dynamics, *Vehicle Systems Dynamics*, Vol.41, No.5, pp. 383–399, 2004.

Mueller, J.P., Gourinat, Y., Ferrer, R., Krzsinski, T. and Kerdreux, B.: 'A Numerical Study on Active Control for Tiltrotor Whirl Flutter Stability Augmentation', Revised version of the paper: 'A Multibody Study on Single- and Multi-Variable Control Algorithms for Tiltrotor Whirl Flutter Stability Augmentation', American Helicopter Society 4th Decennial Specialist's Conference on Aeromechanics, Fisherman's Wharf, San Francisco, CA, USA, 21–23 January 2004.

Mueller, J.P.: 'Méthodologie d'Optimisation Aéroélastique Active d'une Voilure de Convertible – Flottement Gyroscopique', Ph.D. Thesis, Université Paul Sabatier (Toulouse III), Toulouse, France, October 2004.

2005 Acree, C.W., Jr.: Effects of Swept Tips on V-22 Whirl Flutter and Loads, NASA TM-2005-213458, 2005.

Čečrdle, J.: Výpočet vířivého a křidélkového flatru křídla s motorem aeroelastického modelu letounu L-610 (translation: Aileron and Whirl Flutter Analysis of L-610 Aircraft Aeroelastic Model Wing Engine Component), report VZLU, No.V-1839/3210/05, 2005.

Donham, R.E.: 'Effect of Propeller Blade Bending Dynamics on 1P Loads and Whirl Flutter', International Forum on Aeroelasticity and Structural Dynamics, Munich, Germany, 28 June–1 July 2005.

Dugeai, A.: 'Aeroelastic Developments in the elsA Code and Unsteady RANS Applications', International Forum on Aeroelasticity and Structural Dynamics, 28 June–1 July 2005, Munich, Germany.

Hathaway, E.L.: 'Active and Passive Techniques for Tiltrotor Aeroelastic Stability Augmentation', Ph.D. Thesis, The Graduate School College of Engineering, The Pennsylvania State University, 2005.

Singh, R. and Gandhi, F.: 'Wing Flaperon and Swashplate Control for Whirl flutter Stability Augmentation of a Softinplane Tiltrotor', 31st European Rotorcraft Forum, Florence, Italy, 13–15 September 2005.

Somenath M. and Deepak K.N.: 4-DOF Whirl Flutter Analysis of Tractor and Pusher (SARAS) Type Propeller Nacelle System of Aircraft, National Aerospace Laboratories, Bangalore, India, Report No.PD-ST-05-08, March 2005.

Veldhuis, L.: 'Propeller Wing Aerodynamic Interference', Ph.D. Thesis, Delft Technical University, June 2005.

2006 Arnold, J., Elinarson, G. and Krueger, W.R.: 'Multibody Simulation of an Oscillating Aeroelastic Wing Model', 3rd NAFEMS CFD Seminar, Wiessbaden, Germany, 2006.

Čečrdle, J.: Metodika výpočtu vířivého flatru turbovrtulového letounu dvoumotorové koncepce (translation Methodology of Twin Engine Aircraft Whirl Flutter Analysis), Report VZLU, No.R-3929, 2006.

Čečrdle, J.: 'Whirl Flutter Analysis of Commuter Aircraft Aeroelastic Model Wing–Engine Component', Engineering Mechanics 2006 National Conference with International Participation, 15.-18.5.2006, Svratka, Czech Republic, paper no.119, book of extended abstracts pp. 42–43, full text on CD-ROM, ISBN 80-86246-27-2.

2007 Čečrdle, J.: Metodika stanovení kritických parametrů stability letadlové konstrukce z hlediska vířivého flatru pro zadanou certifikační rychlost s využitím optimalizačního řešení (translation: Methodology of

Determination of Aircraft Structure Critical Parameters with Respect to Whirl Flutter for Considered Certification Speed by Means of Optimization), Report VZLU, No.R-4212, 2007.

Čečrdle, J.: 'Whirl Flutter Analysis of Small Transport Aircraft', International Forum on Aeroelasticity and Structural Dynamics (IFASD), Stockholm, Sweden, 18–20 June 2007.

Donham, R.E. and Osterholt, D.J.: 'Utilizing Test Results to Show Adding Flexibility of Propeller Blades is More Representative than the Classical Rigid Blade Propeller Whirl Flutter Analysis', International Forum on Aeroelasticity and Structural Dynamics (IFASD), Stockholm, Sweden, 18–20 June 2007.

Dugeai, A.: 'Turbomachinery Aeroelastic Developments and Validations Using ONERA elsA Solver', International Forum on Aeroelasticity and Structural Dynamics (IFASD), Stockholm, Sweden, 18–20 June 2007.

Krueger, W.R.: 'Multibody Dynamics for the Coupling of Aeroelasticity and Flight Mechanics of Highly Flexible Structures', International Forum on Aeroelasticity and Structural Dynamics (IFASD), Stockholm, Sweden, 18–20 June 2007.

Paik, J. and Gandhi, F.: 'Design Optimization for Soft-Inplane Tiltrotor Whirl Flutter Stability Improvement', American Helicopter Society 63rd Annual Forum, Virginia Beach, VA, USA, 1–3 May 2007.

2008 Čečrdle, J.: 'Determination of Aircraft Structure Whirl Flutter Stability Boundaries by Means of Optimization Based Solution', Engineering Mechanics 2008, National Conference with International Participation, 12–15 May 2008, Svratka, Czech Republic, book of extended abstracts pp. 42–43, full text on CD-ROM, ISBN 978-80-87012-11-6.

Čečrdle, J.: 'Exploitation of Optimization Solution for Determination of Whirl Flutter Stability Boundaries', 26th Congress of the International Council of the Aeronautical Sciences (ICAS 2008), 14–19 September 2008, Anchorage, AK, USA, ISBN 0-9533991-9-2.

Čečrdle, J.: 'Utilization of NASTRAN Optimization Solver 200 for Whirl Flutter Analysis', EMEA Aerospace Summit 2008, MSC.Software, 7.-8.10.2008, Toulouse, France, http://www.mscsoftware-marketing-eu.com/Newsletter/en/download.

2009 Arnold, J.: 'Using Multibody Dynamics for the Simulation of Flexible Rotor Blades – Getting the Mechanical Coupling Right', European Rotorcraft Forum, Hamburg, Germany, 2009.

Čečrdle, J.: Optimization solution for determination of whirl flutter stability boundaries, *Journal Czech Aerospace Proceedings*, No.3, pp. 23–32, ISSN 1211-877X, 2009.

Čečrdle, J.: Program 'PROPFM' (verze 1.0) - Výpočet aerodynamických matic tuhosti a tlumení vrtule pro analýzu vřivého flatru, (translation: Software 'PROPFM' (version 1.0) - Calculation of Propeller Aerodynamic Stiffness and Damping Matrices for Whirl Flutter Analysis), Report VZLU, No.R-4429, 2009.

Čečrdle, J.: Contribution to Whirl Flutter Analysis and Certification Procedure, Report VZLU, No.P-PK-0062/09, 2009.

Čečrdle, J.: Výpočet vířivého flatru letounu EV-55 (translation: Whirl Flutter Analysis of EV-55 Aircraft), Report VZLU, No.R-4496,2009.
Kim, T., Shin, S.J. and Kim, T.: Analysis of tiltrotor whirl flutter in time and frequency domain, *Journal of Mechanical Science and Technology*, pp. 3281–3291, 2009.
Krueger, W.R.: 'Analysis of Whirl Flutter Dynamics on a Tiltrotor Wind Tunnel Model', International Forum of Aeroelasticity and Structural Dynamics, Seattle, WA, USA, 21–25 June 2009.
Ortun, B.: 'CSM / CFD Coupling for the Dynamic Analysis of Helicopter Rotors', Ph.D. Thesis, December 2008, ONERA.
Rezaeian, A.: *Stability Analysis of Timeperiodic Systems Using Multibody Simulation for Application to Helicopters*, Deutscher Luft- und Raumfahrtkongress, 2009, Aachen.
2010 Čečrdle, J.: 'Determination of Twin Turboprop Utility Aircraft Whirl Flutter Stability Boundaries', 27th Congress of the International Council of the Aeronautical Sciences (ICAS 2010), 19–24 September 2010, Nice, France, ICAS2010-9.10.5, ISBN 978-0-9565333-0-2.
Čečrdle, J.: 'Whirl Flutter Analysis of Twin Turboprop Utility Aircraft', Engineering Mechanics Institute 2010 (EMI 2010), International Conference, 8–11 August 2010, Los Angeles, CA, USA.
Rezaeian, A.: 'Helicopter Ground Resonance Analysis Using Multibody Dynamics', 36th European Rotorcraft Forum, 2010, Paris.
2011 Čečrdle, J.: Výpočet vířivého flatru letounu L-410 – verze letounu L-410 UVP-E a L-410 UVP-E20 H-80 (translation: Whirl Flutter Analysis of L-410 Aircraft, Specifications L-410 UVP-E and L-410 UVP-E20 H-80), Report VZLU, No.MOSTA.0508.V.S.PD, 2011.
Dugeai, A., Mauffrey, Y. and Sicot, F.: 'Aeroelastic Capabilities of the elsA Solver for Rotating Machines Applications', International Forum on Aeroelasticity and Structural Dynamics (IFASD), International Conference, 26–30 June 2011, Paris, France.
Placzek, A. – Dugeai, A.: Numerical Prediction of the Aeroelastic Damping Using 'Multi-modal Dynamically Coupled Simulations on a 360° Fan Configuration', International Forum on Aeroelasticity and Structural Dynamics (IFASD), International Conference, 26–30 June 2011, Paris, France.
Rezaeian, A.: 'Whirl Flutter Analysis of a Wind Tunnel Model Using Multidisciplinary Simulation and Multibody Dynamics', 37th European Rotorcraft Forum, 2011, Italy.
Rodden, W.P.: *Theoretical and Computational Aeroelasticity*, Crest Publishing, CA, USA, 2011.
Sicot, F. and Dugeai, A.: 'Numerical Investigation of Propellers Whirl Flutter Using elsA', International Forum on Aeroelasticity and Structural Dynamics (IFASD), International Conference, 26–30 June 2011, Paris, France.
2012 Čečrdle, J. and Maleček, J.: 'Conceptual Design of Aeroelastic Demonstrator for Whirl Flutter Simulation', World Academy of Science, Engineering and Technology (WASET), International Conference, 13–14

August 2012, Oslo, Norway. Proceedings: WASET, Issue 68, pp. 132–136, pISSN 2010-376X, eISSN 2010-3778. Also: International Science Index, International Journal of Mechanical, Industrial Science and Engineering, Vol. 6, No 8, 2012.

Čečrdle, J.: Analysis of twin turboprop aircraft whirl-flutter stability boundaries, *Journal of Aircraft*, Vol.49, No.6, pp. 1718–1725, Nov–Dec 2012, ISSN 0021-8669, E-ISSN 1533-1013.

Ruiz-Calavera, L.P. and Perdones-Diaz, D.: 'CFD Based Aerolastic Calculation of Propeller Loads', 28th Congress of the International Council of the Aeronautical Sciences (ICAS 2012), 23–28 September 2012, Brisbane, QLD, Australia, ISBN 978-0-9565333-1-9.

2013 Čečrdle, J.: PROPFM - Software for Calculation of Propeller Aerodynamic and Gyroscopic Terms for Whirl Flutter Analysis (Version 2.0), Report VZLU, No.R-5656, 2013.

Čečrdle, J.: WHOUT - Software for MSC.NASTRAN Whirl Flutter Output Data Postprocessing, Report VZLU, No.R-5656, 2013.

Rezaeian, A.: 'Stability Assessment of a Propeller–Wing Wind Tunnel Model Based on Analysis Using Measured Structural Data', International Forum of Aeroelasticity and Structural Dynamics, Bristol, UK, 24–26 June 2013.

Verley, S. and Dugeai, A.: 'Counter-rotating Open Rotor Whirl Flutter Phenomenon Investigations Using elsA Solver', International Forum of Aeroelasticity and Structural Dynamics, Bristol, UK, 24–26 June 2013.

2014 Čečrdle, J. and Maleček, J.: 'Design and Development of New Whirl Flutter Aeroelastic Demonstrator', AIAA Science and Technology Forum and Exposition 2014: 55th AIAA/ASME/ASCE/AHS/SC Structures, Structural Dynamics and Materials Conference, National Harbor, MD, USA, 13–17 January 2014, AIAA-2014-0678.

Čečrdle, J.: Aeroelastic Certification of L 410 UVP-EPT and L 410 UVP-E20PT Aircraft with PT6A-42 Engines and AV-725 Propellers, Part 3: Whirl Flutter Analysis, Report VZLU, No.R-5617, 2014.

Čečrdle, J.: Influence of Propeller Blade Lift Distribution on Whirl Flutter Stability Characteristics, World Academy of Science, Engineering and Technology (WASET), International Conference, April 22–23, 2014, Istanbul, Turkey, pp. 757–763; Also: International Science Index, International Journal of Mechanical, Industrial Science and Engineering, Vol.8, No.4, 2014.

Čečrdle, J.: Influence of Propeller Blade Force Spanwise Distribution on Whirl Flutter Characteristics, Engineering Mechanics 2014, 20th International Conference, May12–15, 2014, Svratka, Czech Republic, pp. 124–127, ISBN 978-80-214-4871-1, ISSN 1805–8248, CD-ROM, ISBN 978-80-214-4872-8, ISSN 1805–8256.

Čečrdle, J.: Improved Solution of Whirl Flutter Using MSC.NASTRAN, MSC.Software Users' Conference 2014, MSC.Software s.r.o., Brno, Czech Republic, June 11–12, 2014, ISBN 978-80-260-6033-8.

Index of Authors

Index of Subjects

This page intentionally left blank